TRANSVERSE SINGLE-SPIN ASYMMETRIES IN PION-INDUCED DRELL-YAN AND J/ψ PRODUCTION AT COMPASS

BY

APRIL TOWNSEND

DISSERTATION

Submitted in partial fulfillment of the requirements
for the degree of Doctor of Philosophy in Physics
in the Graduate College of the
University of Illinois Urbana-Champaign, 2022

Urbana, Illinois

Doctoral Committee:

Professor Jen-Chieh Peng, Chair
Associate Research Professor Caroline Riedl, Co-Director of Research
Professor Matthias Grosse Perdekamp, Co-Director of Research
Assistant Professor Jaki Noronha-Hostler
Professor Jun Song

Abstract

A three-dimensional picture of the nucleon is gradually developing through experimental studies related to generalized parton distributions (GPDs) and transverse momentum dependent (TMD) parton distribution functions (PDFs). There are eight TMD PDFs which describe the nucleon at leading order. Four in particular will be discussed in this thesis. The Sivers and Boer-Mulders functions are predicted to be process-dependent and change sign when measured in semi-inclusive deep inelastic scattering (SIDIS) compared to Drell-Yan scattering (DY). In contrast, the pretzelosity and transversity functions are predicted to be truly universal. TMD PDFs are accessed experimentally through the extraction of transverse spin-(in)dependent azimuthal asymmetries.

COMPASS is a fixed target experiment located in the North Area of CERN with a broad physics program. It is uniquely capable of taking SIDIS and DY data under almost identical conditions, and therefore well suited for testing the (non-)universality of the TMD PDFs. It is also one of few experiments capable of probing TMD PDFs with the DY process. In 2015 and 2018 COMPASS collected Drell-Yan data using a 190 GeV/c negative pion beam and a transversely polarized proton target. This thesis focuses on extracting transverse spin-dependent azimuthal asymmetries (TSAs) from dimuon events resulting from DY. The first TSA results from the full COMPASS DY 2015+2018 data sample are presented. The new TSAs favor the predicted sign change for the Sivers function and the universality of transversity and pretzelosity.

During the 2015 and 2018 COMPASS runs, dimuons were also produced by the decay of J/ψ mesons. In pion-proton collisions, J/ψ mesons can be produced via quark-antiquark annihilation or via gluon-gluon fusion. TSAs extracted from these J/ψ events can be compared to different theoretical predictions to help determine which production mechanism is dominant at COMPASS kinematics. The TSAs can then be used to learn more about quark or gluon TMD PDFs depending on the production mechanism. The first J/ψ TSA results from pion-proton collisions at COMPASS are presented in this thesis. The small size of the Sivers, pretzelosity and transversity TSAs suggest that gluon-gluon fusion is the dominant production mechanism, and that the gluon TMDs are small or possibly zero. New information about the gluon TMDs is extremely valuable as they are so far not very well studied.

To my parents, for their continual guidance, support, encouragement, and love.

Acknowledgments

First I want to thank my advisors Caroline Riedl and Matthias Perdekamp. You welcomed me into the COMPASS group early in my graduate career, and have provided support, guidance, and encouragement ever since, no matter how busy your schedules became. Thank you for teaching me how to be a physicist, and for always treating me as a whole person.

I also want to thank the other members of the UIUC group who have supported me and taught me over the years. Robert, during our year of overlap you passed on to me what you had learned as a graduate student, including physics understanding, technical knowledge, and general advice. Riccardo, you taught me many things, including how to use the COMPASS software and how to manage data productions. Thank you for continuing to invest in me even when your responsibilities mostly lay outside of COMPASS. Marco, you taught me much about supercomputing and data production. Thank you for supporting me as I used ESCALADE, even after you had graduated. Vincent, you have helped me understand physics, software, and hardware. Thank you for the continual support and advice you have provided throughout my time as a graduate student. Finally, I want to thank Jen-Chieh Peng. In addition to being my committee chair, you have taught me many things about physics, encouraged me to think outside the box and ask creative questions, and demonstrated to me how exciting and diverse a physics career can be.

Next I want to thank all the other members of the COMPASS collaboration who I have worked with and learned from. In particular, I want to thank Bakur Parsamyan for collaborating with me on my analysis and for teaching me many things about physics, analysis strategies, how to present results clearly, and how to make sure one has tested everything before being satisfied with one's results.

Finally, I want to thank everyone else in my life who has supported me as I have worked to reach this point. To my husband Ted: you have been my daily support and encouragement, someone to celebrate with and a shoulder to cry on when needed. To my parents: you were the ones who helped me develop my interests and talents from a young age, and you have never ceased to support and encourage me. To my graduate student friends: thank you for helping me survive graduate classes, especially my first year, and for being nerdy and genuine friends since then. To my first research advisor when I was an undergraduate, Dr.

Darren Craig: thank you for advising me as I first entered the world of physics research, and for mentoring me as a whole person. Finally, thank you to my many other friends, family members, and professors who have lived life with me, invested in me, and encouraged me.

Table of Contents

List of Figures

List of Tables

Chapter 1

Introduction

Over 100 years ago, in 1911, Rutherford discovered that atoms contain a small but massive nuclei in his famous scattering experiment [1]. By 1932 it was known that nuclei are composed of protons and neutrons [2, 3], collectively referred to as nucleons. As time progressed, higher energy scattering experiments led to the discovery that nucleons are themselves composite particles. In 1964, Gell-Mann and Zweig developed the quark model to describe the structure of nucleons [4, 5]. In this simple quark model, the nucleons are each composed of three quarks with fractional electric charge and a spin of 1/2. Later in that decade, Feynman proposed the parton model to explain the results of deep inelastic scattering (DIS) experiments, in which high energy leptons are scattered off nucleons [6]. In the parton model, each nucleon is moving very fast and can be modeled as a distribution of independent partons that each carry some fraction of the total longitudinal momentum of the nucleon. The term 'longitudinal' means along the direction of motion of the nucleon. These two models were unified in the 1970's in quantum chromodynamics (QCD), the quantum field theory of strong nuclear interactions [7, 8, 9, 10, 11, 12]. In QCD, nucleons and other quark-composite particles, collectively referred to as hadrons, are composed of quarks held together by force-carrying gluons. There are valence quarks which are responsible for the charge and other quantum numbers of the hadron. Nucleons have three valence quarks. Surrounding the valence quarks is a 'cloud' of gluons and sea quarks. Sea quarks are short-lived quarks that appear in quark-antiquark pairs so that the net quantum numbers of the hadron do not change.

After determining the makeup of hadrons, experiments began to study the relationship between the quantum numbers of hadrons and the quarks and gluons they are made of. In 1988, the EMC collaboration discovered that only a small fraction of the total spin of a nucleon can be attributed to the quark spin [13]. This led to the 'proton spin crisis' and the understanding that the spin of nucleons arises from multiple sources. The spin sum rule illustrates the possible sources of spin of the nucleon [14, 15]:

$$\frac{1}{2} = \frac{1}{2}\Delta\Sigma + \Delta G + L_q + L_g. \tag{1.1}$$

In Eq. 1.1, $\Delta\Sigma$ is the contribution due to quark spin, ΔG is the contribution due to gluon spin, and $L_{q(g)}$ is related to the orbital momentum of the quarks (gluons). Following the EMC experiment, multiple other experiments measured $\Delta\Sigma$, establishing an approximate contribution of 30% due to quark spin [16]. Some experiments have also attempted to measure ΔG. Current results suggest that the contribution due to gluon spin is very small [17], but the uncertainties of the experiments are still very large. Various experiments are working to better understand the impact of the L_q and L_g contributions.

It is vital to study nucleon substructure experimentally because not all properties of bound states of quarks and gluons can be derived from QCD first principles. High-energy scattering processes involving hadrons are factorized into a hard scattering process which can be calculated with perturbative QCD, and a soft non-perturbative scattering process. The soft process is parametrized with experimentally determined parton distribution functions (PDFs) describing bound hadron structure, and fragmentation functions (FFs) describing the probability for quarks to fragment into hadrons.

Many experiments have studied the longitudinal momentum structure of the proton so that it is quite well understood. Much less is known about the transverse momentum-dependent structure. The transverse structure began to be studied in earnest after significant azimuthal asymmetries were measured in polarized proton collisions at the CERN Proton Synchrotron in 1975 [18]. Gradually, a three dimensional tomographic image of nucleon substructure is emerging [19]. Generalized parton distributions (GPDs) provide access to the transverse position of quarks and gluons, and transverse momentum dependent (TMD) PDFs contain information about the transverse momentum of the nucleon constituents.

Two of the most useful scattering processes for learning more about TMDs are semi-inclusive deep inelastic scattering (SIDIS) and the Drell-Yan (DY) process [20]. In SIDIS, a lepton is scattered off a nucleon target, and at least one outgoing hadron is detected in addition to the scattered lepton. The DY process is a hadron-hadron scattering process in which a quark from one hadron annihilates with an antiquark from the other hadron into a virtual photon. The virtual photon then decays into a dilepton. These processes allow access to TMDs through measuring various spin-(in)dependent azimuthal asymmetries.

This thesis will study TMD PDFs through the extraction of azimuthal asymmetries from data taken at the COMPASS experiment at CERN. It will look at Drell-Yan scattering data as well as data involving J/ψ production in hadron-hadron collisions. Chapter 2 will provide a theoretical introduction and give a brief review of current experimental results related to TMD PDFs. Chapter 3 will describe the COMPASS experiment and spectrometer setup, including the DC05 detector which the author has performed calibrations for and helped repair. The chapter will also explain the data production process by which the digital spectrometer output is reconstructed into useful physics quantities. The author was the Drell-Yan data production manager responsible for the newest reconstructions of the 2015 and 2018 DY data. Chapter 4 will introduce the methods by which transverse spin dependent azimuthal asymmetries (TSAs) are extracted from data. Chapter 5 will present the first TSA results extracted from the full COMPASS Drell-Yan data set. Chapter 6 will present the first TSA results extracted from J/ψ production events in the full 2015 and 2018 data sets. Finally, Chapter 7 will give a summary and outlook.

Chapter 2

Theoretical and Experimental Overview

2.1 Deep Inelastic Scattering

Nucleon substructure was first probed in deep inelastic scattering (DIS) experiments. In DIS, a lepton is scattered off a nucleon:

$$\ell(k) + N(P) \to \ell(k') + X(P_X), \tag{2.1}$$

where ℓ is a lepton with four-momentum $k = (E, \vec{k})$ in the initial state and $k' = (E', \vec{k}')$ in the final state, N is a nucleon with initial four-momentum P, and X refers to all undetected products of the experiment with combined four-momentum P_X. The Feynman diagram of this process is shown in Fig. 2.1. The lepton interacts with the nucleon by exchanging a virtual photon with four-momentum $q = k' - k$.

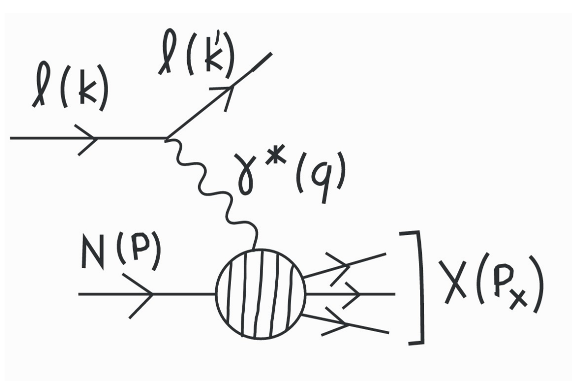

Figure 2.1: Feynman diagram for deep inelastic scattering.

In most of the experiments that will be mentioned in this chapter, DIS occurs in a fixed target setup where $P = (M, \vec{0})$. It is assumed that the lepton and quark masses are negligible compared to the other energy scales in the process. The Lorentz-invariant kinematic variables that can describe fixed-target DIS are:

$$\begin{aligned} Q^2 &= -q^2 = -(k'-k)^2, & x &= \frac{Q^2}{2P\cdot q}, \\ \nu &= \frac{P\cdot q}{M}, & y &= \frac{P\cdot q}{P\cdot k}, \\ W^2 &= (P+q)^2. \end{aligned} \tag{2.2}$$

Q^2 is the hard scale of the reaction; x is called Bjorken-x and can be interpreted as the nucleon longitudinal momentum fraction carried by the struck quark, ranging from 0 to 1; ν is the energy of the virtual photon; y is the fraction of initial lepton energy carried by the virtual photon and ranges from 0 to 1; and W^2 is the combined invariant mass of the final state hadrons. The scattering process is 'deeply inelastic' if $\nu, Q^2 \to \infty$ with fixed x. DIS can be completely parametrized using two of the above variables, usually x and Q^2.

The cross section for DIS is written as [21]

$$d^3\sigma = \frac{1}{4P\cdot k}\frac{e^4}{Q^4}L_{\mu\nu}W^{\mu\nu}2\pi\frac{d^3k'}{(2\pi)^3 2E'}, \tag{2.3}$$

where e is the charge of an electron, $L_{\mu\nu}$ is the leptonic tensor, and $W^{\mu\nu}$ is the hadronic tensor. The tensors can be broken into a symmetric portion describing the spin-independent part of the scattering and an antisymmetric portion describing the spin-dependent scattering:

$$\begin{aligned} L_{\mu\nu} &= L^{(S)}_{\mu\nu}(k,k') + iL^{(A)}_{\mu\nu}(k, s_\ell; k'), \\ W_{\mu\nu} &= W^{(S)}_{\mu\nu}(q,P) + iW^{(A)}_{\mu\nu}(q; P, S), \end{aligned} \tag{2.4}$$

where s_ℓ is the spin of the incoming lepton and S is the spin of the incoming hadron. The leptonic tensor can be calculated exactly using quantum electrodynamics (QED). However, the hadronic tensor encodes information about the bound states of quarks and gluons which cannot be calculated using perturbative QCD. It must instead be parametrized using structure functions which can only be determined experimentally. The DIS differential cross section with a longitudinally-polarized nucleon can then be written as

$$\begin{aligned} \frac{\mathrm{d}^2\sigma}{\mathrm{d}x\mathrm{d}y} = \frac{8\pi\alpha^2}{Q^2}\Bigg[&\frac{y}{2}F_1(x,Q^2) + \frac{1}{2xy}\left(1 - y - \frac{y^2\gamma^2}{4}\right)F_2(x,Q^2) \\ &+ c_1(y,\gamma,s_\ell,S)g_1(x,Q^2) + c_2(y,\gamma,s_\ell,S)g_2(x,Q^2)\Bigg], \end{aligned} \tag{2.5}$$

where α is the electromagnetic coupling constant; $\gamma = 2Mx/Q$; c_1 and c_2 are functions depending on the

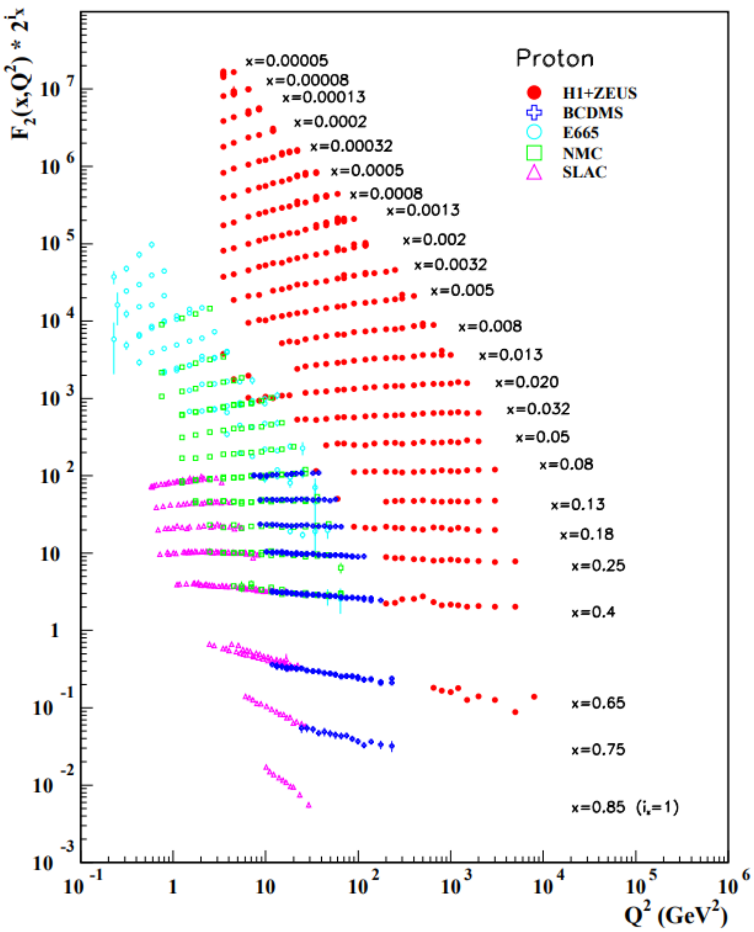

Figure 2.2: The structure function $F_2(x, Q^2)$ as measured by various experiments. From [23].

target and beam polarizations; and $F_1(x, Q^2)$, $F_2(x, Q^2)$, $g_1(x, Q^2)$, and $g_2(x, Q^2)$ are dimensionless structure functions. $F_1(x, Q^2)$ and $F_2(x, Q^2)$ describe the spin-independent structure of the nucleon, while $g_1(x, Q^2)$ and $g_2(x, Q^2)$ describe the spin-dependent nucleon structure.

2.2 Parton Model

The first experimental measurement of F_1 and F_2 was performed at SLAC in 1969. They observed that F_1 and F_2 did not depend strongly on Q^2 [22]. This was originally theorized by Bjorken [8]. A sample of experimental results for F_2 of the proton is shown in Fig. 2.2 taken from [23]. The initial experiments took data in the mid-x range where Fig. 2.2 shows no dependence of F_2 on Q^2. This phenomena is referred to as Bjorken scaling and led to the development of the parton model by Feynman [6]. (The dependence on Q^2 at high and low x will be discussed at the end of this section.)

The parton model describes a hadron in the infinite-momentum frame as a composition of free, point-like, massless partons. The inifinite momentum frame is a good approximation for a process where, in the center-

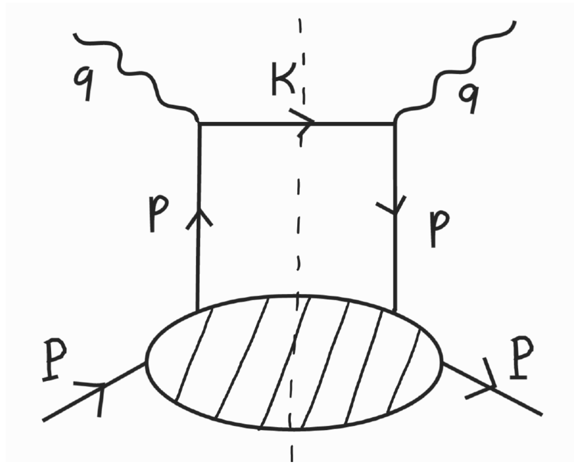

Figure 2.3: The ‘handbag diagram’ depicting the hadronic tensor in the parton model. The virtual photon with momentum q scatters incoherently off a free quark with momentum p. Note that only momentum is labeled in this diagram.

of-mass frame, the nucleon momentum is much larger than its invariant mass. In this limit, the strong force binding the nucleon together becomes asymptotically small. Therefore the partons appear to the incoming lepton to be free particles.

In this model, the hadronic tensor is represented by the ‘handbag diagram’ shown in Fig. 2.3. Then, the hadronic tensor of Eq. 2.4 can be written in terms of a quark-quark correlator as [21]:

$$W^{\mu\nu} = \sum_q e_q^2 \int \frac{\mathrm{d}^4 p}{(2\pi)^4} \delta\left((p+q)^2\right) \mathrm{tr}\left[\Theta\gamma^\mu(\not{p}+\not{q})\gamma^\nu\right], \tag{2.6}$$

where lower-case p is the momentum of the struck quark and Θ is the quark-quark correlation matrix. The elements of Θ are defined as

$$\Theta_{ij}(p,P,S) = \int d^4\xi e^{ip\cdot\xi} \langle PS| \bar{\psi}_j(0)\psi_i(\xi) |PS\rangle\,, \tag{2.7}$$

where $\psi(\xi)$ is the quark field.

In cases where the nucleon is unpolarized or longitudinally polarized, the symmetric and anti-symmetric pieces of the hadronic tensor can be written as [21]

$$\begin{aligned} W_{\mu\nu}^{(S)} &= \frac{1}{P\cdot q}\sum_q e_q^2 \left[(p_\mu+q_\mu)P_\nu + (p_\nu+q_\nu)P_\mu - g_{\mu\nu}\right] f_1^q(x), \\ W_{\mu\nu}^{(A)} &= \frac{1}{P\cdot q}\lambda\epsilon_{\mu\nu\rho\sigma}\left(p^\sigma+q^\sigma\right)P^\rho \sum_q e_q^2 g_{1L}^q(x), \end{aligned} \tag{2.8}$$

where λ is the longitudinal polarization of the nucleon relative to the momentum direction, the superscript and subscript q refer to the quark flavor, e_q is the electric charge of the quark with flavor q, $f_1(x)$ is the spin-independent quark number density and $g_{1L}(x)$ is the helicity distribution. The helicity distribution describes the net number of quarks longitudinally polarized in the same direction as the parent nucleon. To clarify the distinction between f_1 and g_{1L} we can write

$$\begin{aligned} f_1 &= f_1^+ + f_1^-, \\ g_{1L} &= f_1^+ - f_1^-, \end{aligned} \tag{2.9}$$

where the superscripts + and − refer to the longitudinal polarization of the quarks relative to that of the parent hadron. The functions f_1 and g_{1L} are examples of parton distribution functions (PDFs).

The structure functions in Eq. 2.5 can be written in terms of the PDFs f_1 and g_{1L}. In the naive parton model, where only the leading order QCD terms are considered, F_1 and F_2 of spin 1/2 quarks are related to each other via the Callan-Gross relation [24] and can be written in terms of f_1 as

$$F_2(x) = 2xF_1(x) = \sum_q e_q^2 x \left(f_1^q(x) + f_1^{\bar{q}}(x) \right). \tag{2.10}$$

Here the antiquark ($\bar{q}$) distributions (coming from the sea quarks in a nucleon) have been included along with the quark distributions. If the nucleon is longitudinally polarized, the structure function g_1 is related to g_{1L} by

$$g_1(x) = \frac{1}{2} \sum_q e_q^2 \left(g_{1L}^q(x) + g_{1L}^{\bar{q}}(x) \right). \tag{2.11}$$

The structure function $g_2(x) = 0$ in the naive parton model.

Various DIS experiments have measured f_1 and g_{1L}. Fig. 2.4 shows results for $xf_1(x)$ based on a global analysis of data from several CERN experiments [25]. Fig. 2.5 shows results for $xg_{1L}(x)$ based on an analysis of Hermes [26], SMC [27], and COMPASS [28] results from DIS with longitudinally polarized targets.

As mentioned earlier, Fig. 2.2 shows that $F_2(x, Q^2)$ is only independent of Q^2 when x ranges from about 0.02 to 0.4. As $x \to 0$, $F_2(x, Q^2)$ begins increasing with Q^2 while as $x \to 1$, $F_2(x, Q^2)$ begins decreasing with Q^2. This is shown more clearly in Fig. 2.6. These trends arise from the fact that the strong coupling constant α_s is dependent on Q^2 because the force-carrying gluons also carry the color charge of the strong force. The parton model can be improved by adding Q^2 evolution which takes the dependence on Q^2 into account. The DGLAP equations [29, 30, 31] are used to describe the Q^2 evolution of quark and gluon PDFs.

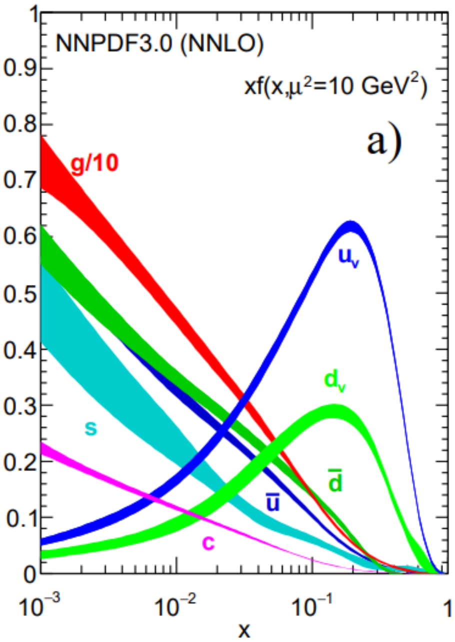

Figure 2.4: The first moment of the unpolarized parton distribution function $f_1(x)$ for various quark flavors and for gluons inside the proton. From [23].

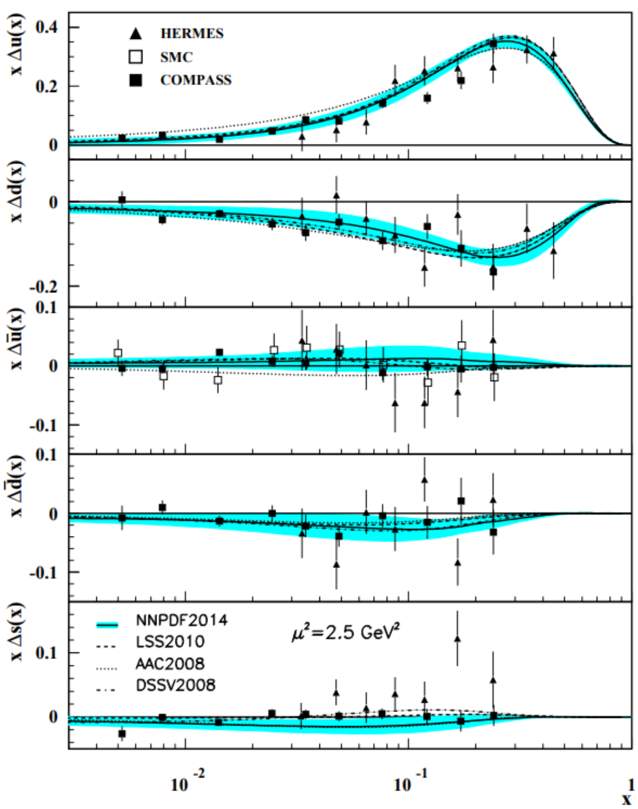

Figure 2.5: The first moment of the helicity distribution $g_{1L}(x)$ for various quark flavors in the longitudinally-polarized proton. From [23].

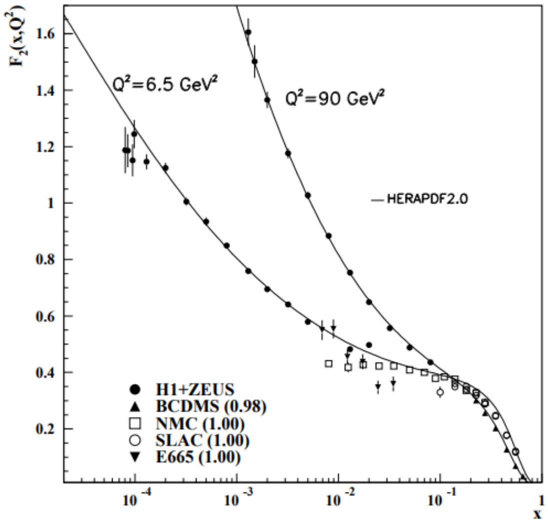

Figure 2.6: The structure function $F_2(x, Q^2)$ at two different Q^2 values. The dependence of $F_2(x, Q^2)$ on Q^2 at low x is clearly observable. From [23].

2.3 Transverse Momentum Dependence

So far only spin-independent and longitudinal-spin-dependent PDFs have been introduced. The DIS process as drawn in Fig. 2.1 is an inclusive process because no outgoing hadrons are detected. In this process the transverse momentum of the partons is integrated over. However, if more outgoing particles are detected, the parton transverse momentum can be probed. In semi-inclusive DIS (SIDIS), one or more outgoing hadrons are detected in addition to the scattered lepton. This process is often used to probe transverse momentum-dependent nucleon substructure and will be discussed further in Sect. 2.4. Another process that can be used is Drell-Yan (DY) scattering. This process will be described in Sect. 2.5. In addition to SIDIS and DY, the parton transverse momentum can be probed in electron-positron annihilation and in proton-proton collisions with a transversely-polarized proton.

The processes sensitive to transverse momentum are of order $1/Q$ [32], also called 'twist-2'. To this order, the quark-quark correlation matrix of Eq. 2.7 can be written as [32, 33]

$$\begin{aligned}\Theta = \frac{1}{2}\Bigg\{ & f_1(x, p_T^2)\not{P} + \frac{1}{M} f_{1T}^{\perp}(x, p_T^2)\left[\epsilon_{\mu\nu\rho\sigma}\gamma^\mu P^\nu + p_T^\rho S_T^\sigma\right] \\ & + \left[\lambda g_{1L}(x, p_T^2) + \frac{p_T \cdot S_T}{M} g_{1T}(x, p_T^2)\right]\gamma_5 \not{P} + h_1(x, p_T^2) i\sigma_{\mu\nu}\gamma^5 P^\mu S_T^\nu \\ & + \frac{1}{M} h_{1L}(x, p_T^2)\lambda i\sigma_{\mu\nu}\gamma^5 P^\mu p_T^\nu + \frac{1}{M} h_1^{\perp}\sigma_{\mu\nu} p_T^\mu P^\nu \\ & + \frac{1}{M^2} h_{1T}^{\perp}(x, p_T^2) i\sigma_{\mu\nu}\gamma^5 P^\mu \left[p_T^\nu p_T \cdot S_T - \frac{1}{2} p_T^2 S_T^\nu\right]\Bigg\},\end{aligned} \tag{2.12}$$

where p_T is the transverse momentum of the struck quark, λ is the longitudinal nucleon polarization, and

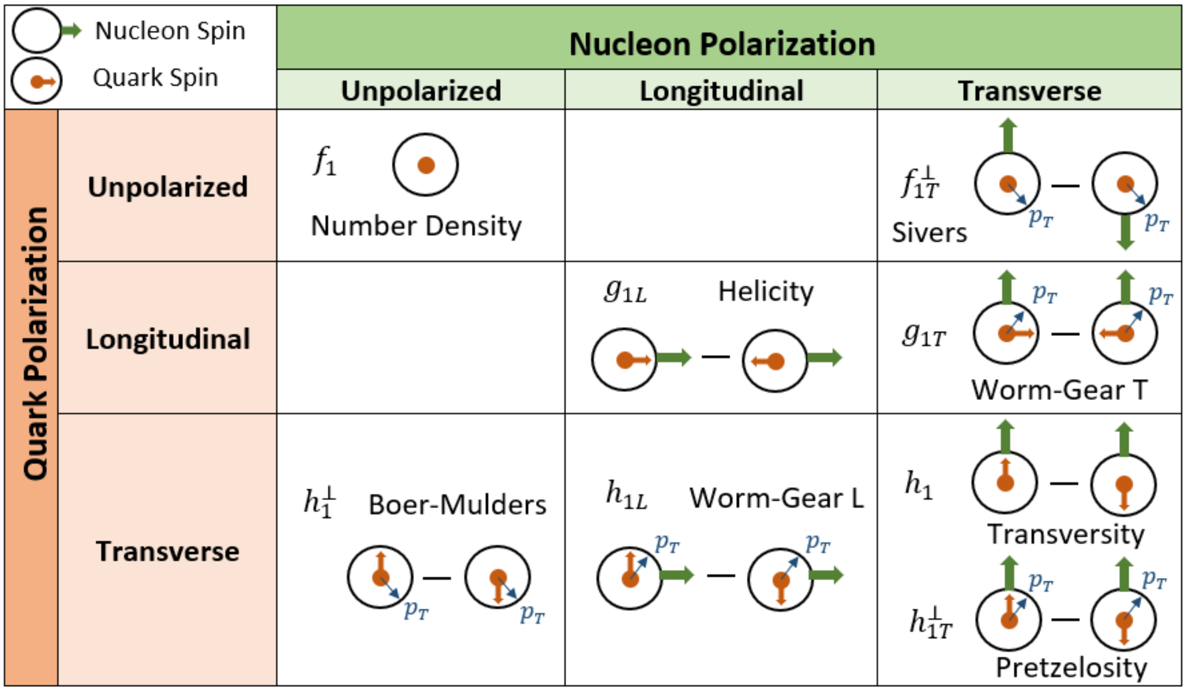

Figure 2.7: The eight leading-order (twist-2) quark TMDs organized by nucleon and quark polarization. The green arrows represent nucleon spin, the orange arrows represent quark spin, and the blue arrows represent quark transverse momentum.

S_T is the transverse nucleon polarization. There are eight quark transverse momentum dependent (TMD) PDFs in Eq. 2.12 that are functions of x and the quark p_T. These TMDs describe correlations between nucleon spin, quark spin, and quark transverse momentum. They are arranged into a table in Fig. 2.7 based on the associated nucleon and quark polarizations. A similar table exists for gluon TMDs.

As Fig. 2.7 shows, the symbols representing the TMDs indicate which type of quark they are related to: the f functions are related to unpolarized quarks, the g functions are related to longitudinally polarized quarks, and the h functions are related to transversely polarized quarks. The number density f_1, helicity distribution g_{1L}, and transversity distribution h_1 are the only functions to survive p_T integration. The functions f_1 and g_{1L} were already seen in Eq. 2.8. The four TMDs found in the leading twist cross sections of transversely polarized SIDIS and DY are the Sivers function, Boer-Mulders function, transversity function, and pretzelosity function.

The quark Sivers function $f_{1T}^{\perp}$ describes the correlations between the transverse momentum of an unpolarized quark and the transverse spin of the parent hadron. It was proposed to explain large spin-dependent asymmetries observed in $p^{\uparrow}p$ collisions [34]. The Boer-Mulders function $h_1^{\perp}$ describes the correlations between the transverse spin and transverse momentum of a quark inside an unpolarized nucleon [32]. The most interesting fact about the Sivers and Boer-Mulders functions is that they change sign under time reversal and therefore are 'T-odd' functions. Because of this, it was originally supposed that these functions could not be non-zero. However, it was later shown that the sign change under time reversal could be caused by soft gluon exchange in initial or final state interactions without violating time reversal invariance [35, 36]. Then, a non-zero Sivers or Boer-Mulders function should have opposite sign when measured in SIDIS compared to Drell-Yan [37]. This is because gluon exchange occurs in the initial state in DY and in the final state in SIDIS.

The transversity distribution h_1 is the analog of the helicity function g_{1L} for transverse polarization. That is, it describes the difference between the number of quarks transversely polarized in the same direction as the parent hadron and the number transversely polarized in the opposite direction. The function was first proposed in 1979 in the context of DY production with polarized beams [38]. The pretzelosity TMD $h_{1T}^{\perp}$ describes the correlation between the transverse polarization of a quark and its transverse momentum in a transversely polarized hadron. The name 'pretzelosity' refers to the predicted effect the function should have on the proton shape in transverse momentum space if it is non-zero [39]. These functions are even under time-reversal and therefore are predicted to be truly universal. It is important to experimentally validate the (non-)universality of the TMDs in order to verify this TMD framework of QCD.

2.4 Semi-Inclusive Deep Inelastic Scattering

Semi-inclusive DIS is one important experimental probe of hadron TMD structure. As Fig. 2.8 shows, it is like inclusive DIS (Fig. 2.1) except that at least one outgoing hadron is detected in addition to the scattered lepton:

$$\ell(k) + N(P) \rightarrow \ell(k') + H(P_h) + X(P_X), \tag{2.13}$$

where H refers to the detected hadron with four-momentum P_h. The process can be described fully using three independent kinematic variables (an increase from the two needed for inclusive DIS). In addition to

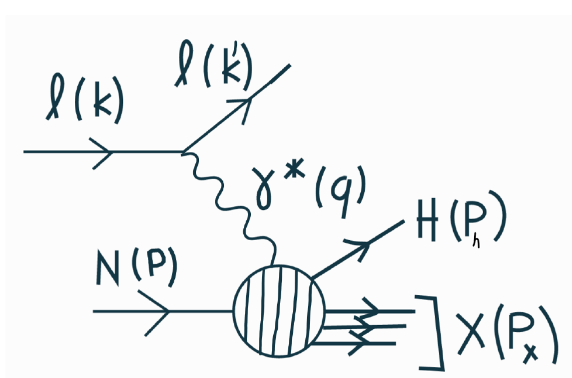

Figure 2.8: Leading order Feynman diagram for semi-inclusive deep inelastic scattering.

the kinematic variables in Eq. 2.2, the variable

$$z = \frac{P \cdot P_h}{P \cdot q}, \tag{2.14}$$

is often used to describe SIDIS. It describes the fraction of energy the detected hadron obtains.

The SIDIS cross section of a polarized lepton beam scattering off a transversely-polarized nucleon target can be written in terms of structure functions as [40]

$$\begin{aligned}
\frac{\mathrm{d}^5\sigma}{\mathrm{d}x\,\mathrm{d}y\,\mathrm{d}\phi_\mathrm{S}\,\mathrm{d}\phi_\mathrm{h}\,\mathrm{d}P_{hT}^2} = {} & \frac{\alpha^2}{xyQ^2}\frac{y^2}{2(1-\varepsilon)}\left(1+\frac{\gamma^2}{2x}\right)\Big\{F_{UU,T} + \varepsilon F_{UU,L} + \sqrt{2\epsilon(1+\varepsilon)}\cos(\phi_\mathrm{h})F_{UU}^{\cos(\phi_\mathrm{h})} \\
& + \varepsilon\cos(2\phi_\mathrm{h})F_{UU}^{\cos(2\phi_\mathrm{h})} + \lambda_\ell\sqrt{2\varepsilon(1-\varepsilon)}\sin(\phi_\mathrm{h})F_{LU}^{\sin(\phi_\mathrm{h})} \\
& + |S_T|\Big[\sin(\phi_\mathrm{h}-\phi_\mathrm{S})\left(F_{UT,T}^{\sin(\phi_\mathrm{h}-\phi_\mathrm{S})} + \varepsilon F_{UT,L}^{\sin(\phi_\mathrm{h}-\phi_\mathrm{S})}\right) \\
& \quad + \varepsilon\sin(\phi_\mathrm{h}+\phi_\mathrm{S})F_{UT}^{\sin(\phi_\mathrm{h}+\phi_\mathrm{S})} + \varepsilon\sin(3\phi_\mathrm{h}-\phi_\mathrm{S})F_{UT}^{\sin(3\phi_\mathrm{h}-\phi_\mathrm{S})} \\
& \quad + \sqrt{2\varepsilon(1+\varepsilon)}\left(\sin(\phi_\mathrm{S})F_{UT}^{\sin(\phi_\mathrm{S})} + \sin(2\phi_\mathrm{h}-\phi_\mathrm{S})F_{UT}^{\sin(2\phi_\mathrm{h}-\phi_\mathrm{S})}\right)\Big] \\
& + |S_T|\lambda_\ell\Big[\sqrt{1-\varepsilon^2}\cos(\phi_\mathrm{h}-\phi_\mathrm{S})F_{LT}^{\cos(\phi_\mathrm{h}-\phi_\mathrm{S})} + \sqrt{2\varepsilon(1-\varepsilon)}\cos(\phi_\mathrm{S})F_{LT}^{\cos(\phi_\mathrm{S})} \\
& \quad + \sqrt{2\varepsilon(1-\varepsilon)}\cos(2\phi_\mathrm{h}-\phi_\mathrm{S})F_{LT}^{\cos(2\phi_\mathrm{h}-\phi_\mathrm{S})}\Big]\Big\},
\end{aligned} \tag{2.15}$$

where λ_ℓ is the longitudinal polarization of the incoming lepton, S_T is the transverse polarization of the target nucleons, P_{hT} is the transverse momentum of the detected hadron, $\gamma = 2Mx/Q$, and

$$\varepsilon = \frac{1 - y - \gamma^2 y^2/4}{1 - y + y^2/2 + \gamma^2 y^2/4} \tag{2.16}$$

is the ratio of longitudinally-to-transversely polarized virtual photon flux. The angles ϕ_h and ϕ_S are defined in the target rest frame as shown in Fig. 2.9. The functions F are structure functions. The first, second, and third (if present) subscripts of F refer to the beam polarization, target polarization, and virtual photon polarization respectively. The subscripts U, L, and T mean unpolarized, longitudinally-polarized, and transversely-polarized respectively. If you integrate Eq. 2.15 over P_{hT} and sum over all the final hadron states, you end up back at the cross section for inclusive DIS (Eq. 2.5).

In the TMD regime ($P_{hT} \ll Q$), the structure functions can be interpreted as convolutions of TMD PDFs and fragmentation functions (FFs). Fragmentation functions describe the probability for a quark to hadronize into a particular hadron. The two fragmentation functions that appear in the leading twist SIDIS cross section, with a transversely polarized target and an unpolarized detected hadron, are D_1 and $H_1^\perp$. D_1 describes the probability for an unpolarized quark to fragment into an unpolarized hadron. $H_1^\perp$ is called the Collins FF and describes the probability for a transversely-polarized quark to fragment into an unpolarized

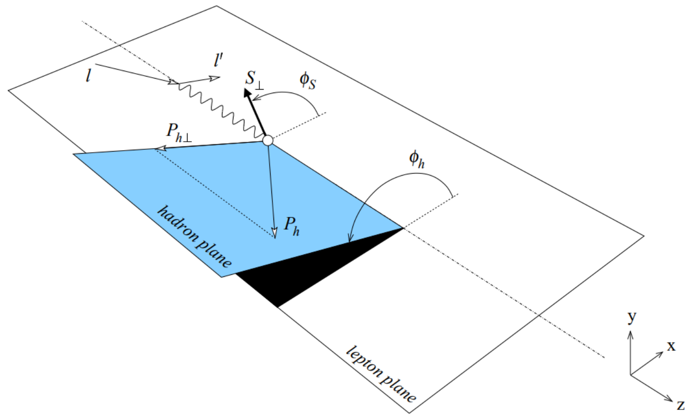

Figure 2.9: Definition of azimuthal angles for semi-inclusive deep inelastic scattering in the target rest frame. Taken from [40]. Some labeling is different than in the text: l is the lepton momentum (rather than k) and $\perp$ refers to transverse (rather than T).

hadron.

At leading twist with a transversely polarized target, $F_{UT,L}^{\sin(\phi_\mathrm{h}-\phi_\mathrm{S})}$ and $F_{UU,L}$ are equal to zero. Then, there are six remaining structure functions associated with only twist-2 TMDs and FFs [40]:

$$F_{UU,T} \propto f_1 \otimes D_1, \tag{2.17}$$

$$F_{UT,T}^{\sin(\phi_\mathrm{h}-\phi_\mathrm{S})} \propto f_{1T}^{\perp} \otimes D_1, \tag{2.18}$$

$$F_{UU}^{\cos(2\phi_\mathrm{h})} \propto h_1^{\perp} \otimes H_1^{\perp}, \tag{2.19}$$

$$F_{UT}^{\sin(\phi_\mathrm{h}+\phi_\mathrm{S})} \propto h_1 \otimes H_1^{\perp}, \tag{2.20}$$

$$F_{UT}^{\sin(3\phi_\mathrm{h}-\phi_\mathrm{S})} \propto h_{1T}^{\perp} \otimes H_1^{\perp}, \tag{2.21}$$

$$F_{LT}^{\cos(\phi_\mathrm{h}-\phi_\mathrm{S})} \propto g_{1T} \otimes D_1. \tag{2.22}$$

These structure functions are probed experimentally by extracting spin-independent ('unpolarized') asymmetries (UAs) and transverse-spin-dependent asymmetries (TSAs) from the data. These asymmetries are defined as

$$A_{\mathrm{BeamTarget}}^{w_i(\phi_\mathrm{h},\phi_\mathrm{S})} = \frac{F_{\mathrm{BeamTarget}}^{w_i(\phi_\mathrm{h},\phi_\mathrm{S})}}{F_{UU,T} + \varepsilon F_{UU,L}}, \tag{2.23}$$

where $w_i(\phi_\mathrm{h}, \phi_\mathrm{S})$ is the azimuthal modulation associated with the asymmetry and 'Beam' and 'Target' represent the beam and target polarizations (U, L, or T). The cross section in Eq. 2.15 can be rewritten in terms of these asymmetries. Including only the leading-twist asymmetries, the cross section becomes

$$\begin{aligned}\frac{\mathrm{d}^5\sigma}{\mathrm{d}x\,\mathrm{d}y\,\mathrm{d}\phi_\mathrm{S}\,\mathrm{d}\phi_\mathrm{h}\,\mathrm{d}P_{hT}^2} = {} & \frac{\alpha^2}{xyQ^2}\frac{y^2}{2(1-\varepsilon)}\left(1+\frac{\gamma^2}{2x}\right)(F_{UU,T}+\varepsilon F_{UU,L})\Big\{1+\varepsilon A_{UU}^{\cos(2\phi_\mathrm{h})}\cos(2\phi_\mathrm{h}) \\ & + S_T\Big[A_{UT}^{\sin(\phi_\mathrm{h}-\phi_\mathrm{S})}\sin(\phi_\mathrm{h}-\phi_\mathrm{S})+\varepsilon A_{UT}^{\sin(\phi_\mathrm{h}+\phi_\mathrm{S})}\sin(\phi_\mathrm{h}+\phi_\mathrm{S}) \\ & +\varepsilon A_{UT}^{\sin(3\phi_\mathrm{h}-\phi_\mathrm{S})}\sin(3\phi_\mathrm{h}-\phi_\mathrm{S})+\lambda\sqrt{1-\varepsilon^2}A_{LT}^{\cos(\phi_\mathrm{h}-\phi_\mathrm{S})}\cos(\phi_\mathrm{h}-\phi_\mathrm{S})\Big]\Big\}.\end{aligned} \tag{2.24}$$

The first four asymmetry amplitudes in Eq. 2.24 are single-spin asymmetries (SSAs) because they only depend on the target spin. $A_{LT}^{\cos(\phi_\mathrm{h}-\phi_\mathrm{S})}$ is a double-spin asymmetry because it is also dependent on the lepton beam polarization.

The relationship between the asymmetries and TMD PDFs and FFs can be determined using Eqs. 2.18-2.22. The asymmetry amplitude $A_{UU}^{\cos(2\phi_\mathrm{h})}$ gives access to the Boer-Mulders TMD and the Collins FF. It also includes a large contribution from a higher-twist effect called the Cahn effect [41] which complicates the interpretation of the asymmetry. The amplitude $A_{UT}^{\sin(\phi_\mathrm{h}-\phi_\mathrm{S})}$ is related to the Sivers TMD and the ordinary FF (D_1). The amplitude $A_{UT}^{\sin(\phi_\mathrm{h}+\phi_\mathrm{S})}$ receives contributions from the transversity TMD and the Collins FF and is often called the 'Collins TSA'. The amplitude $A_{UT}^{\sin(3\phi_\mathrm{h}-\phi_\mathrm{S})}$ is related to the pretzelosity TMD and the Collins FF. Finally, the amplitude $A_{LT}^{\cos(\phi_\mathrm{h}-\phi_\mathrm{S})}$ gives access to the worm-gear-T TMD and the ordinary FF. Experimental results regarding the single-spin asymmetries will be shown in Sect. 2.6.

2.5 Drell-Yan

Drell-Yan scattering (DY) is another important probe of TMD structure and will be the experimental focus of this thesis. It is a form of hadron-hadron scattering where a quark from one hadron annihilates with an anti-quark from the other hadron into a virtual neutral boson such as a virtual photon. The virtual boson then decays into a dilepton (a lepton-antilepton pair). Assuming only the target hadron (H_b) is polarized with spin S, the leading order process can be written as

$$H_a(P_a)+H_b(P_b,S)\to\gamma^*(q)+X\to\ell(k)+\bar{\ell}(k')+X \tag{2.25}$$

and is illustrated in Fig. 2.10.

The DY cross section can be written in terms of structure functions and azimuthal modulations in a similar way to the SIDIS cross section. In this case, the angles are defined in the target rest frame and the Collins-Soper (CS) frame as shown in Fig. 2.11. The leading order DY cross section for the case with a

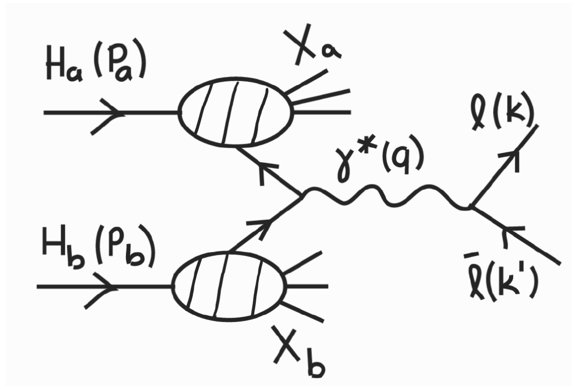

Figure 2.10: Leading order Feynman diagram for Drell-Yan scattering, where the virtual neutral boson is a virtual photon.

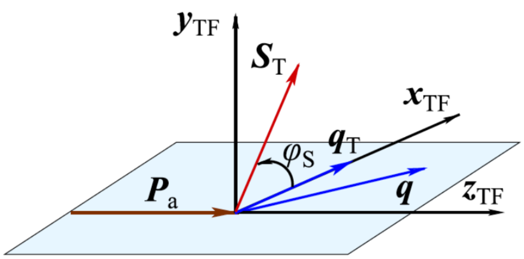

(a) The target rest frame defined so that the beam momentum P_a lies on z-axis and the virtual photon transverse momentum q_T lies on the x-axis.

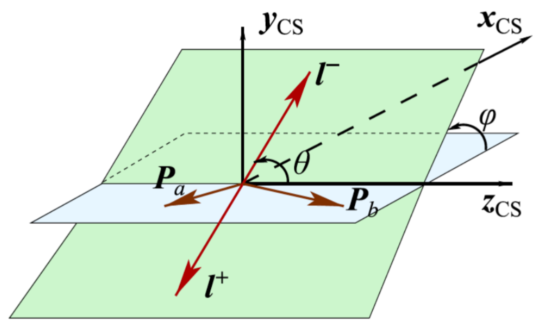

(b) The Collins-Soper frame is the rest frame of the virtual photon, achieved by boosting the target rest frame first along the z-axis then along the x-axis.

Figure 2.11: Definition of azimuthal angles for Drell-Yan scattering in the (a) target rest frame and the (b) Collins-Soper frame.

transversely-polarized target nucleon and unpolarized hadron beam is [42, 43]

$$
\begin{aligned}
\frac{\mathrm{d}^5\sigma}{\mathrm{d}^4q\mathrm{d}\Omega} = \frac{\alpha^2}{Fq^2}\Big\{&\left(1+\cos^2(\theta)\right)F_U^1 + \left(1-\cos^2(\theta)\right)F_U^2 \\
&+\sin(2\theta)F_U^{\cos(\phi)}\cos(\phi) + \sin^2(\theta)F_U^{\cos(2\phi)}\cos(2\phi) \\
&+|S_T|\Big[\Big(F_T^{\sin(\phi_S)} + \cos^2(\theta)\tilde{F}_T^{\sin(\phi_S)}\Big)\sin(\phi_S) \\
&\quad+\sin(2\theta)\Big(F_T^{\sin(\phi+\phi_S)}\sin(\phi+\phi_S) + F_T^{\sin(\phi-\phi_S)}\sin(\phi-\phi_S)\Big) \\
&\quad+\sin^2(\theta)\Big(F_T^{\sin(2\phi+\phi_S)}\sin(2\phi+\phi_S) + F_T^{\sin(2\phi-\phi_S)}\sin(2\phi-\phi_S)\Big)\Big]\Big\},
\end{aligned}
\tag{2.26}
$$

where $F = 4\sqrt{(P_a\cdot P_b)^2 - M_a^2M_b^2}$ is the flux of incoming hadrons, Ω is the solid angle of the lepton, and S_{T} is the transverse polarization of the target hadron. The subscripts U and T on the structure functions refer to an unpolarized or transversely-polarized target hadron respectively.

Drell-Yan can be described in the TMD regime if $q^2 \gg M_a^2, M_b^2$ and $q_T \ll q$, where q is the momentum of the virtual photon with transverse component q_{T}. Similar to DIS, $Q^2 \equiv -q^2$. Then, the structure functions can be interpreted as convolutions of two TMD PDFs, one associated with each hadron. The process probes the TMD PDFs related to the particular quark and antiquark that annihilate in the reaction. At twist-2 with a transversely-polarized target and unpolarized beam, the following structure functions are equal to zero: F_U^2, $F_U^{\cos(\phi)}$, $F_T^{\sin(\phi+\phi_{\mathrm{S}})}$, and $F_T^{\sin(\phi-\phi_{\mathrm{S}})}$. Also at leading twist $F_T^{\sin(\phi_{\mathrm{S}})} \approx \tilde{F}_T^{\sin(\phi_{\mathrm{S}})}$. The remaining structure functions are related to the following convolutions of TMDs [42]:

$$F_U^1 \propto f_a \otimes \tilde{f}_a, \tag{2.27}$$

$$F_U^{\cos(2\phi)} \propto h_1^\perp \otimes \tilde{h}_1^\perp, \tag{2.28}$$

$$F_T^{\sin(\phi_{\mathrm{S}})} \propto f_1 \otimes \tilde{f}_{1T}^\perp, \tag{2.29}$$

$$F_T^{\sin(2\phi+\phi_{\mathrm{S}})} \propto h_1^\perp \otimes \tilde{h}_{1T}^\perp, \tag{2.30}$$

$$F_T^{\sin(2\phi-\phi_{\mathrm{S}})} \propto h_1^\perp \otimes \tilde{h}_1, \tag{2.31}$$

where the first TMD is related to the nucleons in the beam and the second TMD, with a tilde over the symbol, is related to the nucleons in the target.

The structure functions can again be related to spin (in)dependent azimuthal asymmetries using the following definition:

$$A_{\mathrm{Target}}^{w_i(\phi,\phi_{\mathrm{S}})} = \frac{F_{\mathrm{Target}}^{w_i(\phi,\phi_{\mathrm{S}})}}{F_U^1 + F_U^2}, \tag{2.32}$$

where as before 'Target' refers to the target polarization and $w_i(\phi, \phi_{\mathrm{S}})$ is the angular modulation associated with the asymmetry. Then, the leading order DY cross section becomes

$$\begin{aligned} \frac{\mathrm{d}^5\sigma}{\mathrm{d}^4q\mathrm{d}\Omega} = \frac{\alpha^2}{Fq^2}\left(F_U^1 + F_U^2\right)\left(1 + A_U^1\cos^2(\theta)\right)\Big\{1 + D_{[\sin^2(\theta)]}A_U^{\cos(2\phi)}\cos(2\phi) \\ + |S_T|\Big[D_{[1+\cos^2(\theta)]}A_T^{\sin(\phi_{\mathrm{S}})}\sin(\phi_{\mathrm{S}}) \\ + D_{[\sin^2(\theta)]}\left(A_T^{\sin(2\phi+\phi_{\mathrm{S}})}\sin(2\phi+\phi_{\mathrm{S}}) + A_T^{\sin(2\phi-\phi_{\mathrm{S}})}\sin(2\phi-\phi_{\mathrm{S}})\right)\Big]\Big\}, \end{aligned} \tag{2.33}$$

where

$$D_{[f(\theta)]} = \frac{f(\theta)}{1 + A_U^1\cos^2(\theta)} \tag{2.34}$$

and will be referred to as 'depolarization factors'.

Eqs. 2.27-2.31 can be used to determine which TMDs each asymmetry is related to. The amplitude A_U^1 is related to the number density of each hadron. The amplitude $A_U^{\cos(2\phi)}$ is related to the Boer-Mulders function

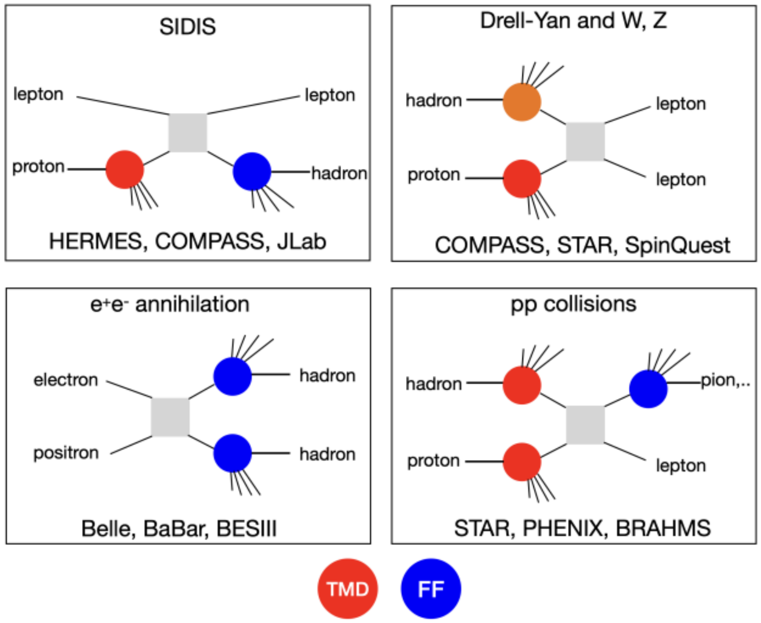

Figure 2.12: A comparison of the four primary TMD probes. The red and orange circles represent TMD PDFs, the blue circles represent FFs, and the gray boxes represent the perturbative part of the process. From [45].

of each hadron. Similar to the case in SIDIS, this asymmetry also receives non-negligible contributions from higher-twist QCD effects. The unpolarized asymmetries are often written in an alternate notation in the literature [44]: $\lambda = A_U^1$, $\nu = 2A_U^{\cos(2\phi)}$, and $\mu = A_U^{\cos(\phi)}$. Note that $A_U^{\cos(\phi)}$ is a twist-3 amplitude and so was not written in Eq. 2.33. The spin-dependent amplitude $A_T^{\sin(\phi_S)}$ is related to the Sivers function of the target and the number density of the beam. The amplitude $A_T^{\sin(2\phi+\phi_S)}$ receives contributions from the pretzelosity function of the target and the Boer-Mulders function of the beam. Finally, the amplitude $A_T^{\sin(2\phi-\phi_S)}$ gives access to the transversity function of the target and the Boer-Mulders function of the beam. Some experimental results for these amplitudes will be shown in the next section.

2.6 Experimental Results for Quark TMD PDFs

In this section, experimental results related to quark TMD PDFs will be presented. The focus will be results from SIDIS and DY experiments, though complementary results from e^+e^- annihilation and $p^\uparrow p$ collisions will also be mentioned. In addition to standard DY, results from W and Z boson production in hadron-hadron collisions will be presented. This process is the same as Fig. 2.10 except that a weak boson is exchanged instead of a virtual photon. A comparison of the information available in each of the four studied processes is shown in Fig. 2.12. Most of the presented results will be related to valence u and d quark PDFs in the proton or neutron.

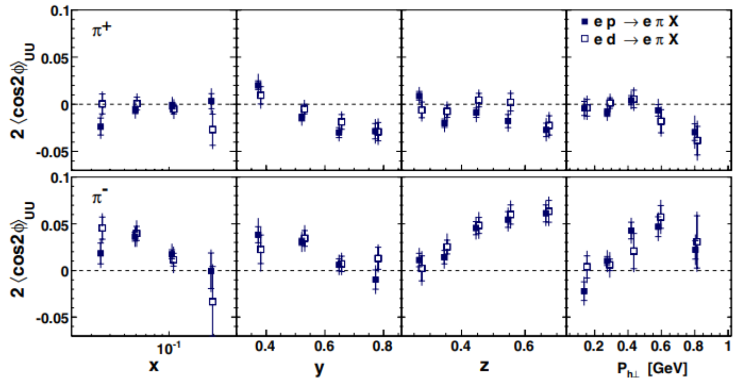

Figure 2.13: HERMES results for the $\cos(2\phi_\mathrm{h})$ amplitude from SIDIS off a proton (black closed) and deuteron (blue open) target where the detected hadron is a pion. From [46].

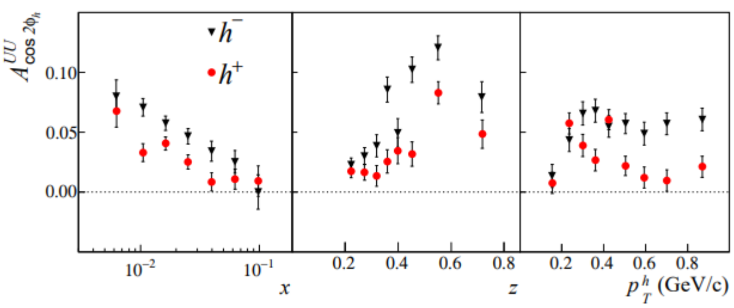

Figure 2.14: COMPASS results for $A_{UU}^{\cos(2\phi_\mathrm{h})}$ from SIDIS off a deuteron target where the detected outgoing hadron has positive (red circle) or negative (black triangle) electric charge. From [47].

2.6.1 Boer-Mulders function

As described in Sect. 2.3, the Boer-Mulders TMD PDF $h_1^\perp$ describes the correlation of the transverse polarization and transverse momentum of a quark in an unpolarized hadron. In SIDIS, the Boer-Mulders function is related to the spin-independent asymmetry $A_{UU}^{\cos(2\phi_\mathrm{h})}$ (Sect. 2.4). This asymmetry amplitude has been measured in SIDIS by the HERMES [46] and COMPASS [47, 48] collaborations. The CLAS collaboration also performed some measurements related to the Boer-Mulders function, but their uncertainties were very large so as to make the results inconclusive [49].

The HERMES results for the $\cos(2\phi_\mathrm{h})$ amplitude are shown in Fig. 2.13. In particular, Fig. 2.13 shows the results from both a proton and deuteron target where the outgoing detected hadron is a pion. As explained in Ref. [46], the sign difference between the amplitude for positive and negative pions is likely due to the Collins FF of the u quark having opposite sign depending on the electric charge of the fragmented hadron [50]. At first glance, there appears to be good consistency between the proton and deuteron results. However, the deuteron π^+ results are systematically shifted towards zero compared to the proton results,

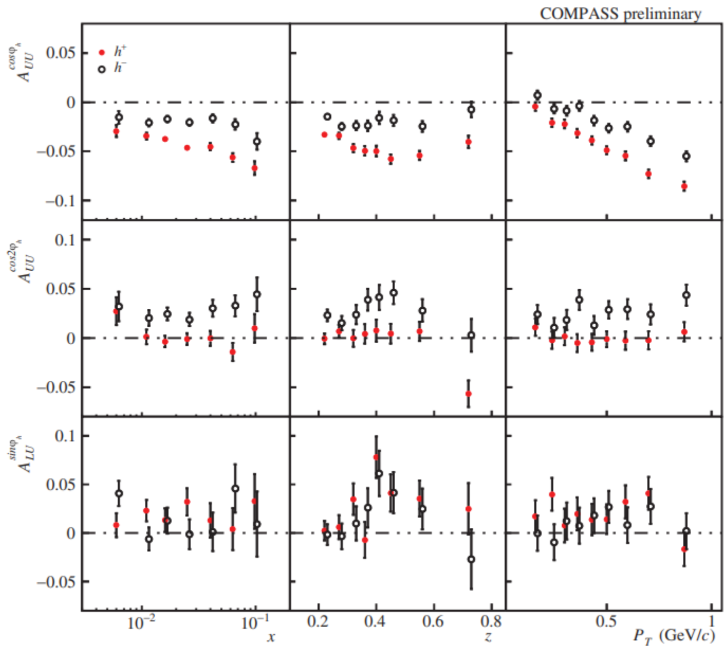

Figure 2.15: Preliminary COMPASS results for $A_{UU}^{\cos(2\phi_h)}$ from SIDIS off a proton target where the detected outgoing hadron has positive (red closed) or negative (black open) electric charge. From [48].

suggesting that the Boer-Mulders function is different for the u and d quarks.

The COMPASS results for $A_{UU}^{\cos(2\phi_h)}$ from SIDIS with a deuteron target are shown in Fig. 2.14. They have some similarities to the HERMES results, but the COMPASS asymmetries tend to be larger, especially for positively-charged hadrons. This could be influenced by the higher-twist Cahn effect [41] which is predicted to be stronger at COMPASS kinematics than HERMES kinematics.

There are also new preliminary results from COMPASS for $A_{UU}^{\cos(2\phi_h)}$ in SIDIS with a proton target shown in Fig. 2.15 (along with $A_{UU}^{\cos(\phi_h)}$ and $A_{LU}^{\sin(2\phi_h)}$) [48]. The asymmetry tends to be smaller in the proton case than in the deuteron case (Fig. 2.14), which suggests that the Boer-Mulders function is different for the u and d quark. This conclusion is consistent with the HERMES results.

The Boer-Mulders function can also be probed in DY scattering by extracting the asymmetry $A_U^{\cos(2\phi)} \equiv \nu/2$ (Sect. 2.5). The NA10 [51] and E615 [52] collaborations extracted this quantity in the past. Preliminary COMPASS results for ν [53] are also consistent with NA10 and E615. The results are shown in Fig. 2.16 along with the prediction from NNLO perturbative QCD (pQCD) [54]. Both the pQCD and data results increase with q_T, but the data results appear to scale faster. Divergences between the data and pQCD predictions suggest the presence of non-perturbative effects such as the Boer-Mulders function. However, as in the case of SIDIS, higher-twist effects can also have a significant contribution, making the interpretation of the results complicated. There is still much room for further studies of the Boer-Mulders function in both

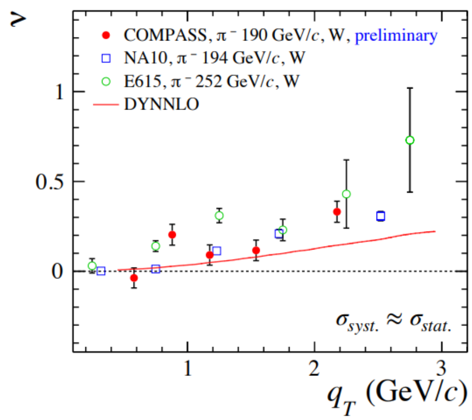

Figure 2.16: Preliminary COMPASS results for the asymmetry amplitude ν in DY, along with results from NA10 [51] and E615 [52] and the prediction from pQCD [54]. The experimental results are consistent with each other and vary from the pQCD prediction, hinting at a non-zero Boer-Mulders effect. From [53].

SIDIS and DY. This thesis will not study spin-independent asymmetries and so will not provide further results related to the Boer-Mulders function.

2.6.2 Pretzelosity function

The pretzelosity TMD $h_{1T}^{\perp}$ describes the correlation between transverse polarization and transverse momentum of a quark inside a transversely-polarized hadron (Sect. 2.3). The amplitude $A_{UT}^{\sin(3\phi_{\mathrm{h}}-\phi_{\mathrm{S}})}$ has been extracted from SIDIS (Sect. 2.4) by HERMES [55], COMPASS [56, 57, 58, 59], and JLab-E06-010 [60] to study pretzelosity. A sample of these results are shown in Figs. 2.17-2.19a. The results are all consistent with zero. This is not surprising because the asymmetry $A_{UT}^{\sin(3\phi_{\mathrm{h}}-\phi_{\mathrm{S}})}$ is supprssed in SIDIS at low q_{T}, and the pretzelosity TMD is expected to be small based on phenomenological fits [61, 62].

The TSA amplitude $A_{T}^{\sin(2\phi+\phi_{\mathrm{S}})}$ in Drell-Yan scattering is related to the pretzelosity TMD (Sect. 2.5) and can be extracted from COMPASS DY data. The first published result with about 40% of the total COMPASS DY data sample was published in 2017 [64] and is shown in Fig. 2.20 along with the transversity

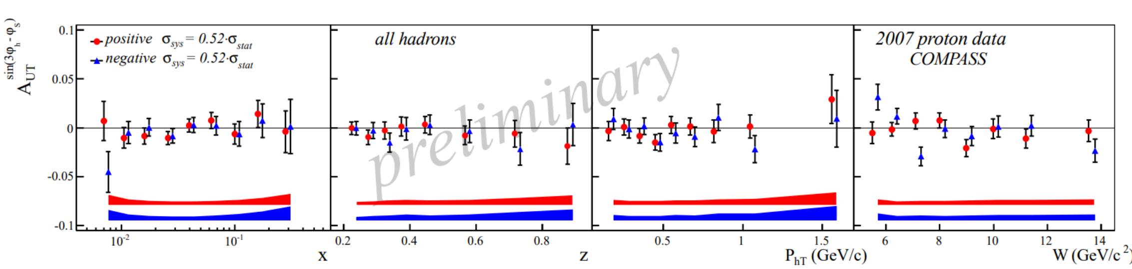

Figure 2.17: Preliminary COMPASS results for $A_{UT}^{\sin(3\phi_{\mathrm{h}}-\phi_{\mathrm{S}})}$ from SIDIS off a transversely polarized proton target where the detected hadron is a positively (red circle) or negatively (blue triangle) charged hadron. From [57].

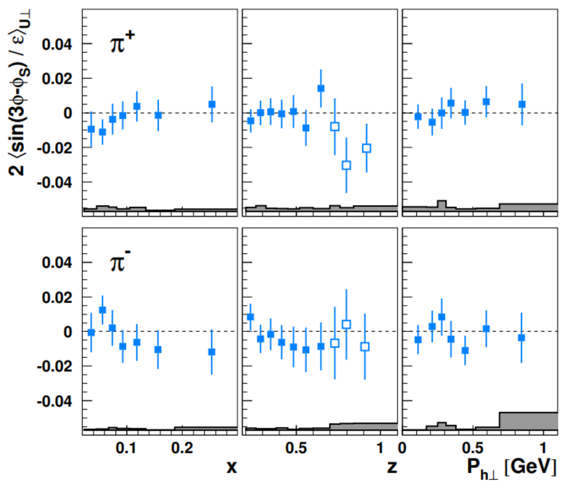

Figure 2.18: The final HERMES results for the $\sin(3\phi_{\mathrm{h}} - \phi_{\mathrm{S}})$ amplitude from SIDIS off a transversely polarized proton target where the detected hadron is a charged pion. From [55].

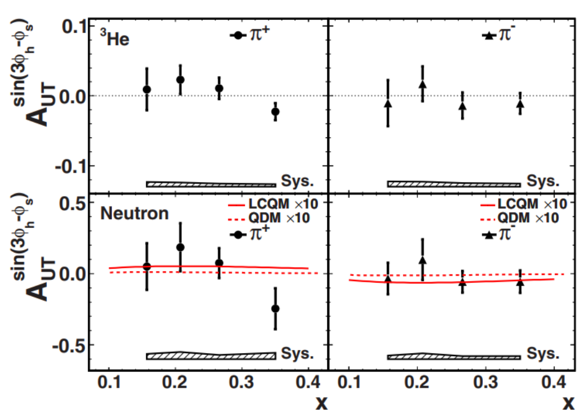

(a) From [60].

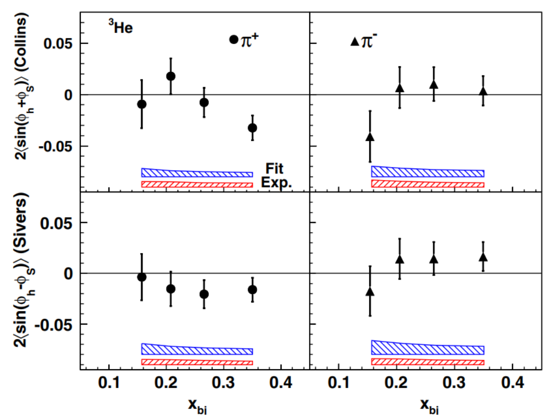

(b) From [63].

Figure 2.19: JLab Hall A results for (a) the pretzelosity TSA and (b) the Collins (top) and Sivers (bottom) TSAs measured in SIDIS off a transversely polarized ^{3}He target. The meson label indicates which outgoing hadron is detected. The second row of (a) is the neutron-only contribution to $A_{UT}^{\sin(3\phi_{\mathrm{h}}-\phi_{\mathrm{S}})}$.

and Sivers TSA amplitudes. This thesis will focus on the extraction of the pretzelosity, transversity, and Sivers TSAs from the total COMPASS DY data sample.

2.6.3 Transversity function

The transversity TMD PDF h_1 describes the correlation bewteen the transverse spin of a quark and the transverse polarization of the parent hadron (Sect. 2.3). In SIDIS, the single-spin asymmetry amplitude $A_{UT}^{\sin(\phi_{\mathrm{h}}+\phi_{\mathrm{S}})}$ is called the Collins asymmetry and is related to the transversity TMD convoluted with the Collins FF (Sect. 2.4). The Collins TSA has been extracted by HERMES [55], COMPASS [65, 66], and JLab Hall A [63].

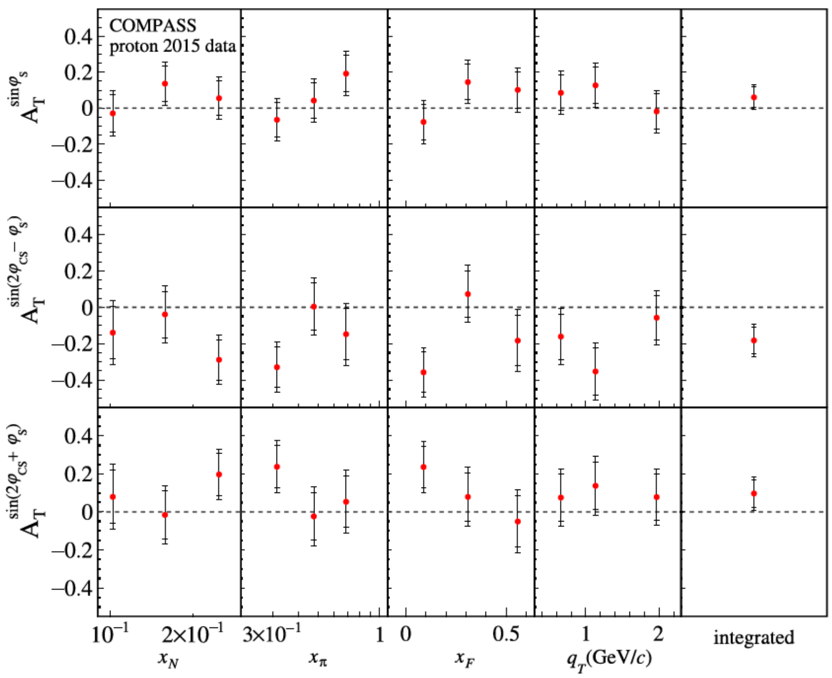

Figure 2.20: The first DY TSA results published by the COMPASS collaboration [64]. The first row is the Sivers TSA, the second is the transversity TSA, and the third is the pretzelosity TSA.

The HERMES Collins asymmetry extracted from SIDIS off a transversely-polarized proton target is shown in Fig. 2.21a for the case where the detected hadron is a charged pion. The opposite sign for positive and negative pions comes from the same Collins FF behavior mentioned in Sect. 2.6.1: the Collins FF has opposite sign when it is favored (e.g. u quark fragmenting into π^-) compared to when it is disfavored (e.g. u quark fragmenting into π^+). The increase in magnitude of the Collins TSA with increasing x makes sense if the transversity effect is primarily carried by valence quarks.

COMPASS extracted the Collins asymmetry from SIDIS off a deuterium target [65] and off a proton target [66]. The results with the proton target are shown in Fig. 2.22a and are consistent with the HERMES results in Fig. 2.21a. The results with the deuterium target are shown in Fig. 2.22b to be consistent with zero. This suggests that the transversity effect for the d quark is opposite to that for the u quark so that they cancel out in a deuterium target.

JLab Hall A extracted the Collins asymmetry from SIDIS off a polarized ^{3}He target. The results in Fig. 2.19b show that the Collins TSA is suppressed compared to the proton case, which is consistent with the COMPASS deuterium results.

The transversity TMD can also be probed by extracting the TSA $A_T^{\sin(2\phi-\phi_S)}$ from DY (Sect. 2.5). The published COMPASS result for this amplitude is shown in the middle row of Fig. 2.20. The STAR collaboration has also measured the Collins asymmetry in the distribution of charged pions in jets from $p^\uparrow p$

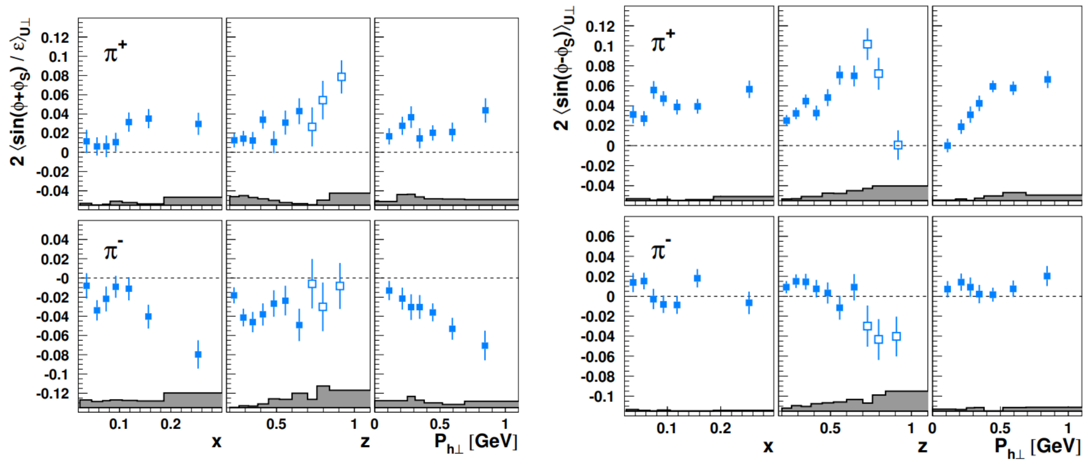

(a) (b)

Figure 2.21: The final HERMES results for the (a) Collins TSA and (b) Sivers TSA from SIDIS off a trasnversely-polarized proton target. From [55].

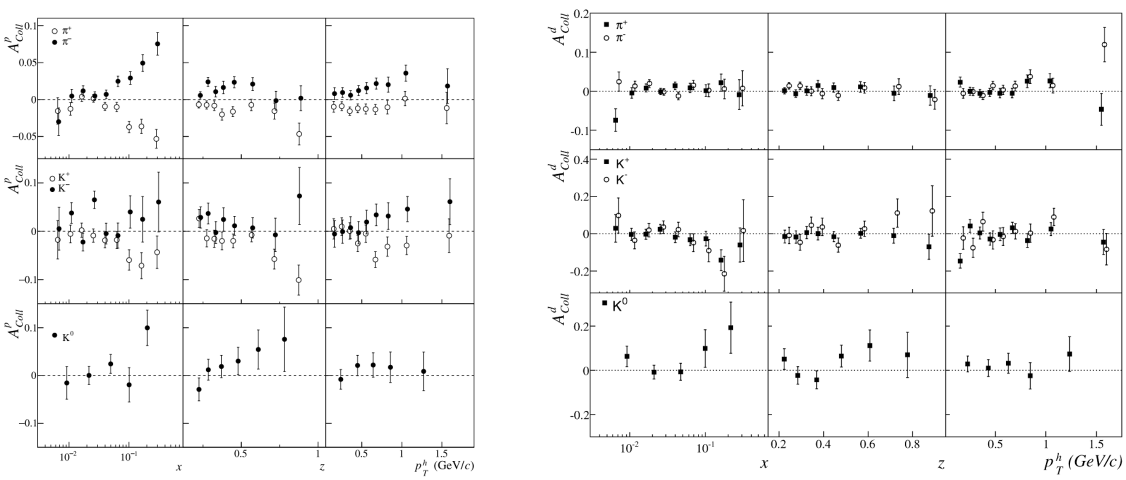

(a) (b)

Figure 2.22: COMPASS results for the Collins TSA from SIDIS off a trasnversely-polarized (a) proton target [66] and (b) deuterium target [65]. The meson label indicates the outgoing hadron detected.

collisions [67], shown in Fig. 2.23.

The JAM collaboration performs phenomenological fits for TSAs and FFs taking into account data from all four processes shown in Fig. 2.12. In addition to SIDIS, DY, and $p^{\uparrow}p$ data from the experiments already mentioned in this section, data on the Collins FF from electron-positron collisions at BELLE [69, 70], BABAR [71, 72], and BESIII [73] are also included. JAM published results in 2020 [68] for the transversity PDF, Sivers PDF, and Collins FF for the up and down quark using experimental data available at the time. The results are shown in Fig. 2.24. As discussed in Ref. [68], the fit was used to predict some other SSA amplitudes that were not initially included, and the prediction was found to agree well with experimental

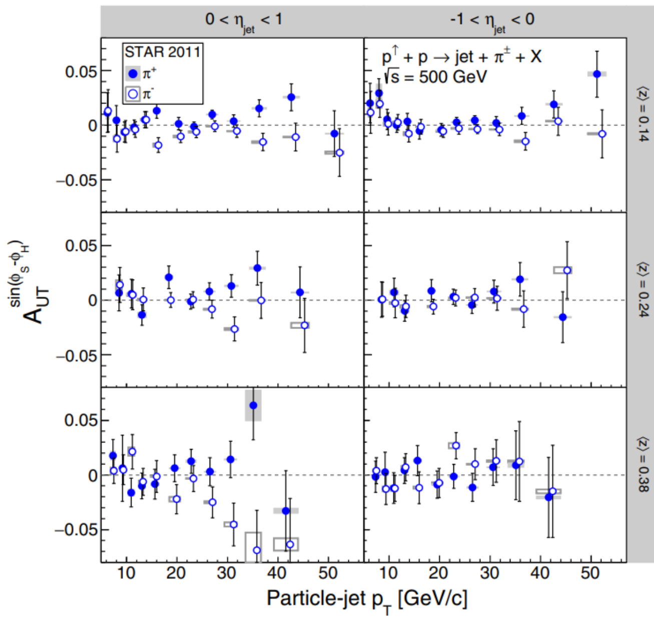

Figure 2.23: STAR results for the Collins TSA in charged pion production in $p^\uparrow p$ collisions. From [67].

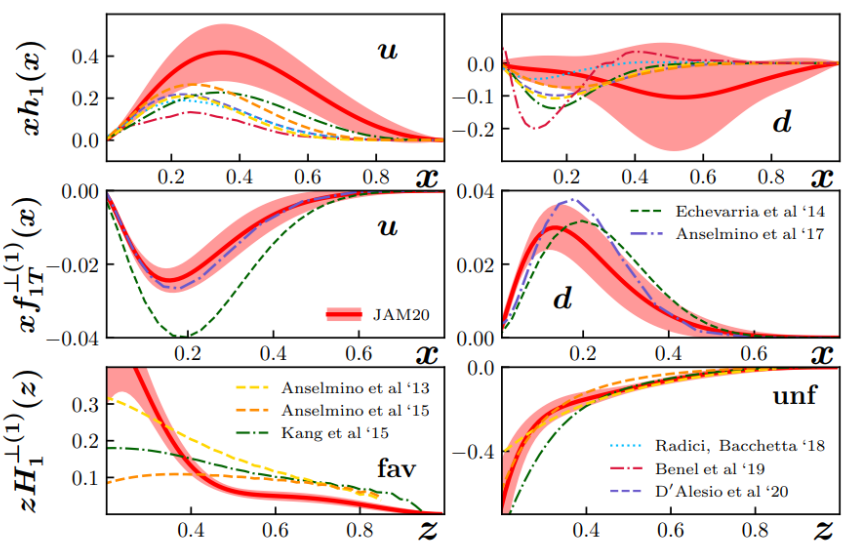

Figure 2.24: Published phenomenological fits of the first moment of the transversity TMD (first row), the Sivers TMD (second row), and the Collins FF (third row) by the JAM collaboration. The first column is for the up quark and the second column is for the down quark. The dashed lines are past global fits by other groups. From [68].

data. This gives evidence that the SSAs in the various processes all have a common origin. JAM is working on improving the fit and decreasing the uncertainties by incorporating new data from STAR, the final results from HERMES, and some lattice QCD results [74].

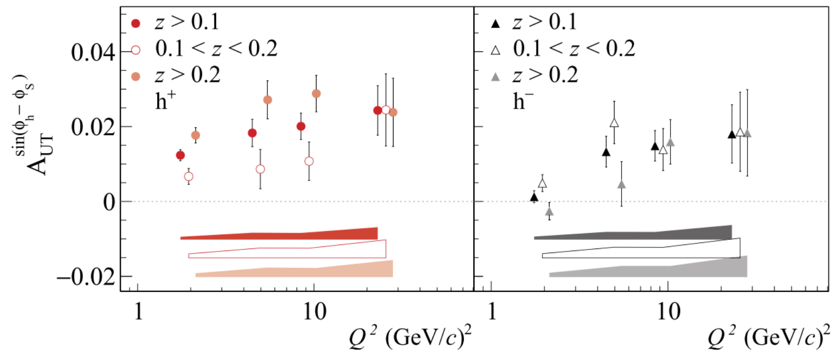

Figure 2.25: COMPASS SIDIS results for the Sivers TSA, where the detected hadron is positively charged (left) or negatively charged (right). From [59].

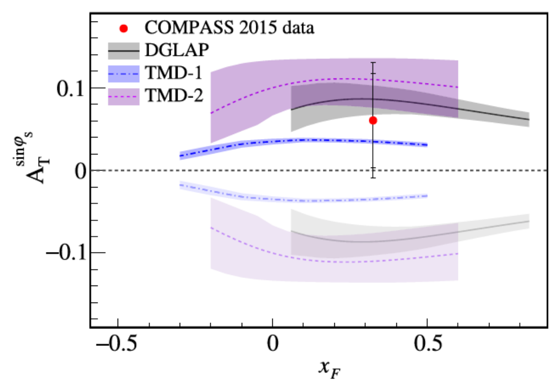

Figure 2.26: Published COMPASS DY result for the Sivers TSA along with phenomenological predictions. The curves where $A_T^{\sin(\phi_S)} > 0$ are the predictions if the sign change hypothesis holds, while the faded curves where $A_T^{\sin(\phi_S)} < 0$ are the predictions if the sign change hypothesis does not hold. From [64].

2.6.4 Sivers function

All the experiments described in Sect. 2.6.3 also measured SSAs related to the Sivers function $f_{1T}^{\perp}$, which describes the correlation between the transverse momentum of an unpolarized quark and the transverse spin of the parent hadron (Sect. 2.3). The final HERMES results for the Sivers TSA $A_{UT}^{\sin(\phi_h-\phi_S)}$ measured in SIDIS (Sect. 2.4) off a transversely-polarized proton target are shown in Fig. 2.21b [55]. The TSA signal in π^+ production is very clearly positive, while it is around zero for π^- production. This can be explained if the Sivers TMD has an opposite sign for up and down quarks, since π^+ production is dominated by u quark scattering while π^- production involves significant contributions from both u and d quark scattering. JLab Hall A measured the Sivers TSA in SIDIS off a neutron target and also found an amplitude consistent with zero as shown in Fig. 2.19b [63].

COMPASS results for the Sivers TSA in SIDIS off a transversely-polarized proton target are shown

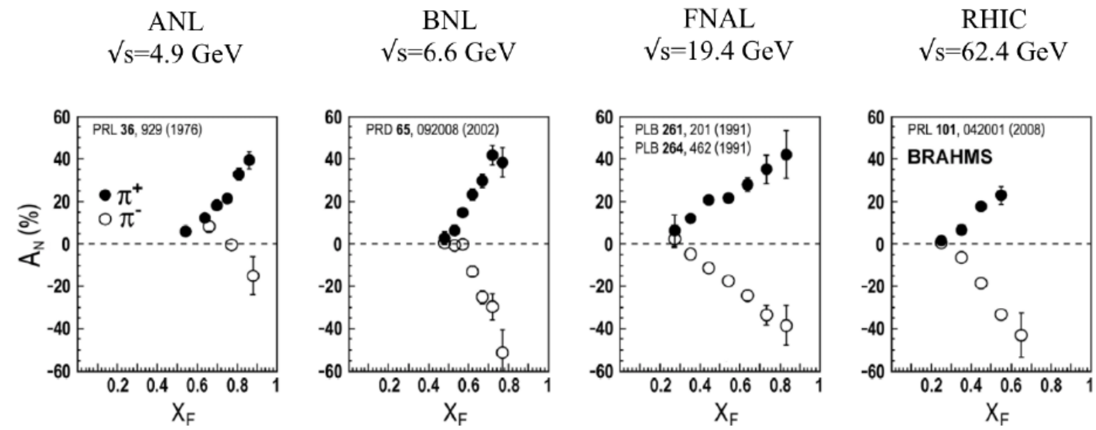

Figure 2.27: Large results for A_{N} from experiments at ANL (1976) [75], BNL (2002) [76], FNAL (1991) [77, 78], and RHIC (2008) [79].

in Fig. 2.25 [59]. The asymmetries are clearly positive, particularly at high Q^2. The highest Q^2 point corresponds to essentially the same kinematic region where the COMPASS DY TSAs were extracted [64] and so can be directly compared to the DY Sivers TSA $A_T^{\sin(\phi_{\mathrm{S}})}$ (Sect. 2.5) in the first row of Fig. 2.20. Because of the way the angles are defined in the two measurements, having a positive $A_{UT}^{\sin(\phi_{\mathrm{h}}-\phi_{\mathrm{S}})}$ amplitude in SIDIS and a positive $A_T^{\sin(\phi_{\mathrm{S}})}$ amplitude in DY corresponds to a Sivers TMD PDF of opposite sign in the two processes. Thus the published COMPASS results favor the sign change hypothesis for the Sivers TMD (see Sect. 2.3). This is illustrated in Fig. 2.26, where the integrated DY Sivers TSA is shown along with phenomenological curves based on SIDIS data. The curves with $A_T^{\sin(\phi_{\mathrm{S}})} > 0$ are the predictions if the sign change hypothesis holds, while the faded curves where $A_T^{\sin(\phi_{\mathrm{S}})} < 0$ are the predictions if the sign change hypothesis does not hold. The published DY result favors the sign change hypothesis, but the statistical certainty is less than 2σ. This thesis will present updated COMPASS DY TSA results for the Sivers, transversity, and pretzelosity TSAs with the entire DY data set.

In collider experiments, a left-right asymmetry amplitude labeled A_{N} can be measured and is directly related to the Sivers TMD. Here 'left' and 'right' are defined based on the azimuthal angles of outgoing particles. This A_{N} has been observed to be large in various experiments with different center-of-mass energies, as illustrated in Fig. 2.27. In fact, it was this experimental signature that led to the proposal of the Sivers TMD PDF.

The STAR collaboration has measured A_{N} in W and Z boson production in collisions of transversely polarized protons [80, 81]. This process is very similar to the process shown in Fig. 2.10, but with the virtual photon replaced by a weak boson. Because of the similarities, A_{N} measured in this process should provide complementary information about the Sivers TMD. The most recent preliminary STAR results [81]

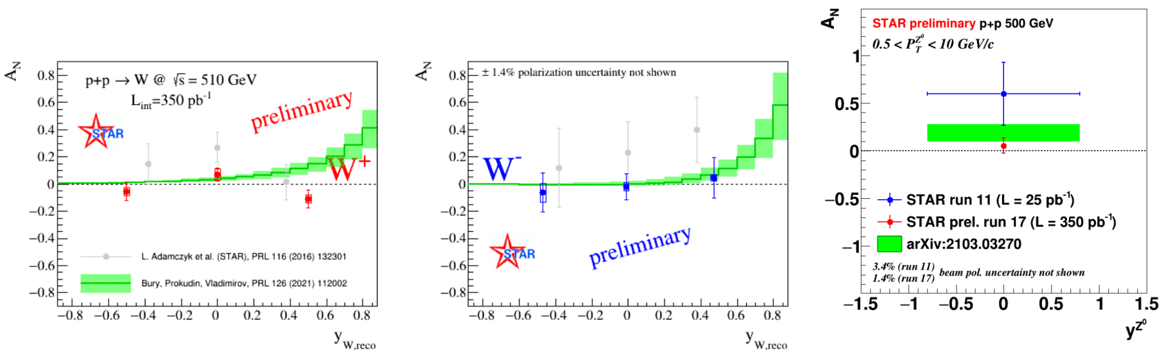

(a) (b)

Figure 2.28: STAR results for A_{N} in (a) $W^{\pm}$ and (b) Z^0 production in $p^{\uparrow}p$ collisions [81]. The (a) faded points and (b) blue point are the previously published results [80], and the green boxes are the phenomenological predictions from [82].

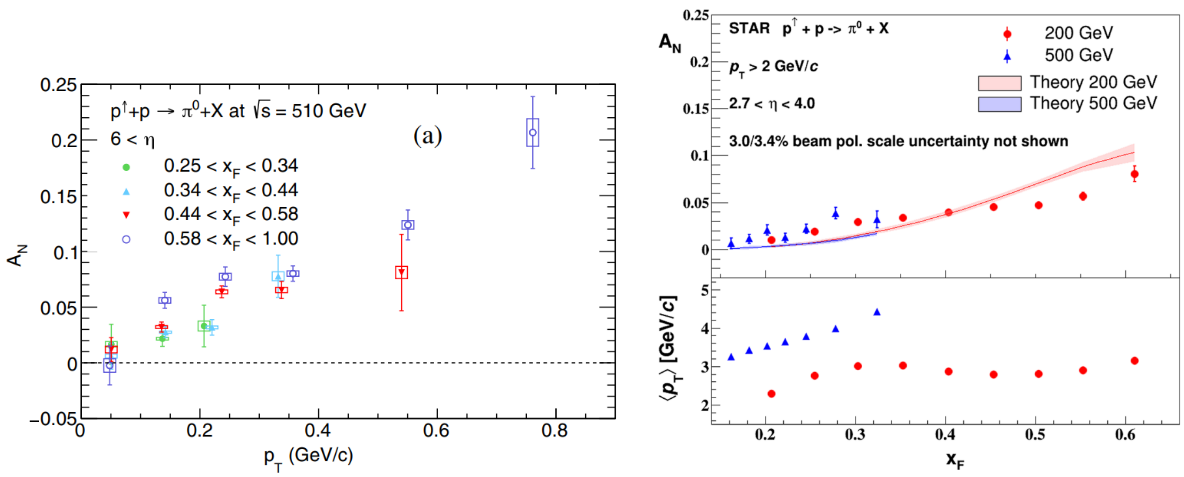

(a) From [83]. (b) From [84].

Figure 2.29: Results for A_{N} in forward π^0 production in $p^{\uparrow}p$ collisions as measured by (a) RHICf and (b) STAR.

are shown in Fig. 2.28. The new amplitudes are closer to zero than the published STAR results [80], shown as faded points in Fig. 2.28.

Other A_{N} measurements in different kinematic regions have recently been performed by several experiments at RHIC. RHICf [83] and STAR [84] have measured A_{N} in forward π^0 production with detectors at different distances from the interaction point, as shown in Fig. 2.29. PHENIX has measured A_{N} in forward neutron production [85] as shown in Fig. 2.30. In all cases the asymmetry amplitudes are large.

Global fits have been performed by multiple groups to extract the Sivers function taking into account data from the various processes described above. The published results from JAM [68], described in Sect. 2.6.3, are shown in Fig. 2.24. Their results for the Sivers function of the up and down quark are also shown along with three other global extractions [86, 87, 88] in Fig. 2.31. As in the case of the Collins TSA, the predictive

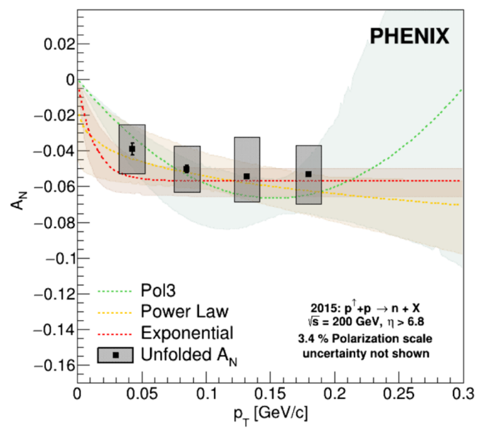

Figure 2.30: Results from PHENIX for $A_{\rm N}$ in forward neutron production in $p^{\uparrow}p$ collisions. From [85].

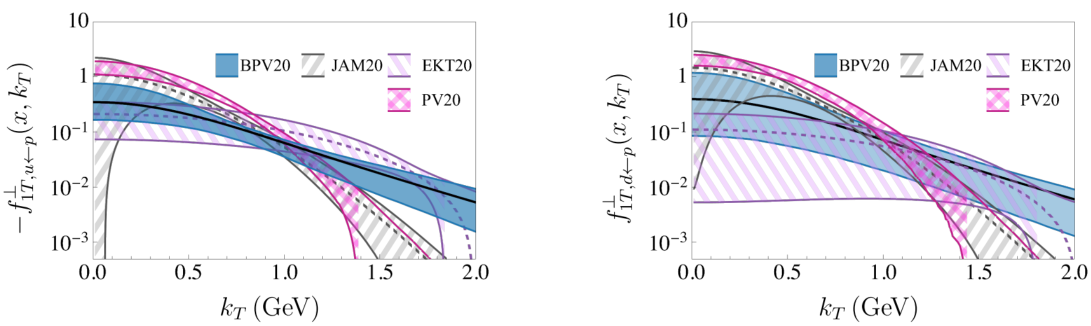

Figure 2.31: Results for the Sivers function for the up (left) and down (right) quarks from four different global fits: BPV20 [86], JAM20 [68], EKT20 [87] and PV20 [88]. Figure from [86].

power of the global fits supports the proposition that the SSAs in the various different processes arise from the same underlying mechanism. More data related to the Sivers TMD needs to be studied in order to conclusively determine if the sign change hypothesis holds.

2.7 J/ψ production

J/ψ production in hadron-hadron collisions may also be sensitive to TMD PDFs. Generally, J/ψ production proceeds as follows: A $c\bar{c}$ pair is produced in the collisions and hadronizes into a J/ψ meson. The meson then decays into a dilepton. In equation form this is

$$\pi^- + p^{\uparrow} \to c\bar{c} \to J/\psi \to \mu^-\mu^+. \tag{2.35}$$

The J/ψ events, like DY events, can be identified by the dilepton signature. There are three models commonly used to describe quarkonia production in general, specifically the non-perturbative hadronization of a produced heavy $q\bar{q}$ pair into a specific quarkonium state [89].

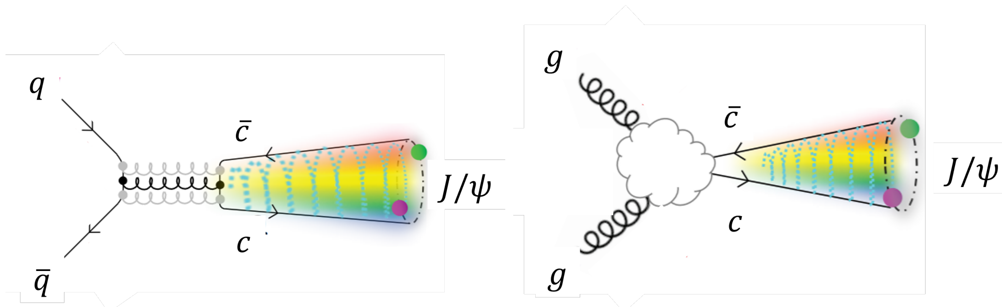

Figure 2.32: Leading order J/ψ production processes in hadron-hadron collisions: quark-antiquark annihilation (left) and gluon-gluon fusion (right). From an internal COMPASS presentation by P. Faccioli.

The color singlet model (CSM) assumes that gluon emission from heavy quarks is suppressed so that the quantum numbers of a $q\bar{q}$ do not change when the pair hadronizes into a quarkonium. The quarkonium cross section is therefore equivalent to the cross section for producing a color singlet $q\bar{q}$. The CSM can describe many experiments reasonably well, including photoproduction data at HERA [90] and e^+e^- data at B factories [91]. However, higher-order corrections are often required, particularly at high p_{T}. Additionally, this model can sometimes be affected by infrared divergences. One of the biggest issues with the CSM is the fact that it does not well explain observed absolute cross sections, for example of the J/ψ and ψ' charmonium mesons [92].

Many of these issues are addressed in the more general non-relativistic QCD (NRQCD) model. In NRQCD, there is an expansion in powers of the velocity of the heavy quarks in addition to the usual expansion in powers of the strong coupling constant α_S. This allows the $q\bar{q}$ states to be produced as color octet states which then transition to color singlet physical mesons. The non-perturbative behavior is encoded in long-distance matrix elements (LDMEs) which are determined from fits to data. The LDMEs are dependent on the quark color, spin, and angular momentum, but are otherwise assumed to be universal. While the NRQCD model is more rigorous and theoretically successful than the simple CSM, it does not always describe experimental data satisfactorily [93]. In particular, it has often failed when attempting to describe fixed-target data [94].

The color evaporation model (CEM) is the simplest model and differs in approach from the other two. The CEM uses quark-hadron duality to assume that there is a constant probability for a given heavy $q\bar{q}$ pair to hadronize into a specific quarkonium state. This probability is independent of kinematics and the subprocess by which the $q\bar{q}$ pair is produced in the collision. The fractions are determined from fits to experimental data. Though the CEM cannot calculate absolute cross sections, it has described well some collider data [95, 96] and is particularly useful for describing fixed-target data where the other models fail.

The perturbative processes by which a $q\bar{q}$ pair can be produced are generally model independent. In

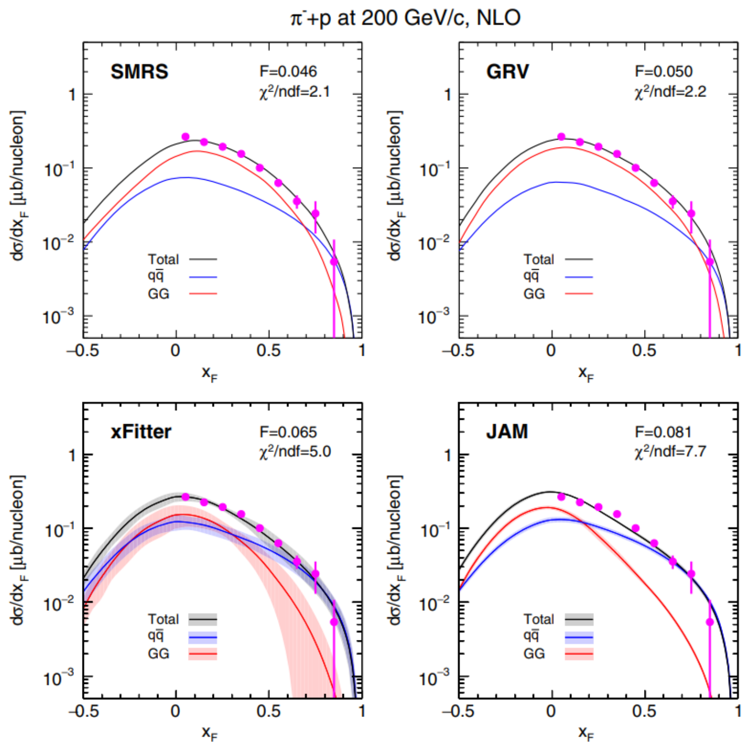

Figure 2.33: Fits of CEM predictions for the x_F distribution of the J/ψ differential cross section in 200 GeV/c pion-proton collisions. Each panel shows the fit with a different pion PDF scheme. The fits in the top panels with wider gg distributions have better χ^2 values than the bottom fits. From [97].

particular, the two leading order production processes in hadron-hadron collisions are quark-antiquark annihilation and gluon-gluon fusion. For the specifc case of J/ψ production, these processes are illustrated in Fig. 2.32.

The process by which the J/ψ is produced would determine whether the data is sensitive to quark or gluon TMDs. In the case of $q\bar{q}$ annihilation, there is a probable duality between the J/ψ production process and the DY process because the spin and parity of a J/ψ are the same as for a photon. If this duality holds, transverse-spin-dependent asymmetries in J/ψ production would provide complementary information about quark TMDs to that provided by DY.

On the other hand, if gg fusion dominates, then TSAs in J/ψ production would probe gluon TMDs. A couple of recent studies have suggested that gg fusion dominates in many fixed-target collisions. Reference [97] has shown that using NLO CEM, gg fusion is the dominant J/ψ production mechanism in fixed target experiments with a pion beam where the beam momentum is at least 125 GeV/c. This is exemplified in Fig. 2.33, where the pion PDF schemes with wider gluon distributions better describe the x_F distribution of the J/ψ differential cross section in pion-proton collisions at 200 GeV/c. In line with this, Ref. [102] has shown that NRQCD predictions better fit fixed-target data if the used pion PDF has higher gluon content

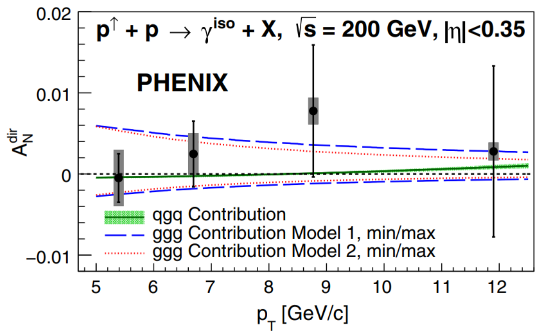

(a) From [98].

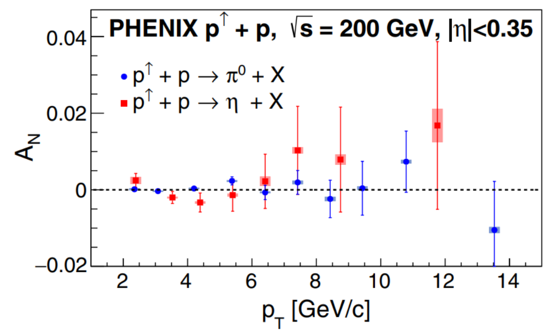

(b) From [99].

Figure 2.34: PHENIX A_{N} measurements in mid-rapidity (a) direct photon production and (b) π^0 and η production in $p^{\uparrow}p$ collisions.

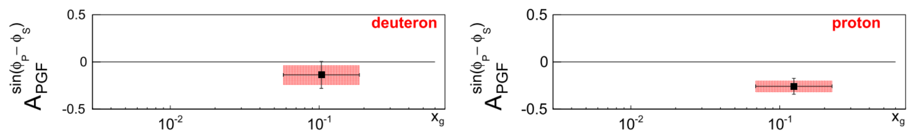

(a) From [100].

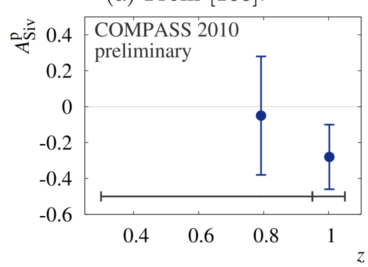

(b) From [101].

Figure 2.35: COMPASS results for Sivers TSA amplitudes in (a) photon-gluon fusion and (b) J/ψ leptoproduction. The data was collected during SIDIS runs with a proton (a right, b) or deuteron (a left) target.

at medium to large x. These results suggest that at COMPASS, J/ψ production in 190 GeV/c pion-proton collisions can be used to probe gluon TMDs.

There is much less data related to gluon TMDs compared to quark TMDs. Of specific interest is the gluon Sivers function, which describes the transverse momentum carried by gluons in a transversely polarized hadron. PHENIX has taken several A_{N} measurements in $p^{\uparrow}p$ collisions at mid-rapidity which are related to the gluon Sivers function [103, 104]. They have measured A_{N} in direct photon production [98], π^0 production [105, 99], and η production [99]. In all three cases, the asymmetry amplitude is consistent with zero, as shown in Fig. 2.34.

COMPASS has also measured Sivers asymmetry amplitudes in processes involving gluon interactions. They found negative non-zero amplitudes for $A^{\sin(\phi_{\mathrm{h}}-\phi_{\mathrm{S}})}$ in photon-gluon fusion in SIDIS interactions [100], as

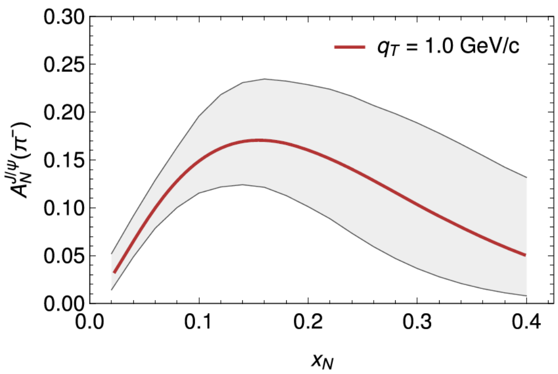

Figure 2.36: Prediction for A_{N} in π^--induced J/ψ production at COMPASS, assuming $q\bar{q}$ as the dominant J/ψ production mechanism. From [106].

shown in Fig. 2.35a. They have also found a negative Sivers TSA amplitude in exclusive J/ψ leptoproduction at high z [101], as shown in Fig. 2.35b. The PHENIX and COMPASS results appear to disagree, but it must be kept in mind that the kinematic coverage of the two experiments is not identical. Additionally the interpretation, and in the case of COMPASS the extraction, of these asymmetries is very model dependent. Further experimental data is needed to clarify and expand our understanding of gluon TMDs.

COMPASS has collected many J/ψ events from 190 GeV/c $\pi^- + p^\uparrow$ collisions during their DY data-taking runs. This thesis will also present TSA results extracted from these J/ψ events. It must then be determined how to interpret the TSA results, as related to quark TMDs or gluon TMDs. Reference [106] has predicted a large A_{N} amplitude in these J/ψ events assuming quark-antiquark annihilation as the dominant production mechanism. The prediction is shown in Fig. 2.36. However, as described earlier, more recent work has suggested that gluon-gluon fusion should be the dominant production mechanism at COMPASS kinematics. The A_{N} extracted from pion-induced J/ψ events at COMPASS can be compared to the prediction from Ref. [106]. This can contribute to our understanding of which production mechanism is dominant and give insight into how to interpret the TSA results. Whether the TSAs are related to quark or gluon TMDs, the additional data will be valuable for improving our understanding of the TMD structure of the proton and the pion.

Chapter 3

COMPASS Experiment

The COmmon Muon Proton Apparatus for Structure and Spectroscopy (COMPASS) experiment is a fixed-target experiment located in the North Area of CERN. COMPASS first started taking data in 2002 and has had a broad physics program over the years. Many types of measurements have been taken including polarized inclusive and semi-inclusive deep inelastic scattering (DIS and SIDIS respectively), Primakoff reactions, deeply virtual Compton scattering (DVCS), deeply virtual meson production, and polarized Drell-Yan (DY) and other dilepton production. The year this thesis is completed, 2022, will be the last year the COMPASS collaboration collects new data. This thesis is focused on analyzing polarized DY data taken in 2015 and 2018.

COMPASS receives beam from the M2 beamline of the Super Proton Synchotron (SPS). The M2 beamline can provide either a secondary hadron beam or a tertiary muon beam. The beam then impinges on the polarized or unpolarized COMPASS target. During the DY runs in 2015 and 2018, a 190 GeV/c negative pion beam impinged on a transversely polarized NH_3 target. The particles coming out of collisions at the target pass through a two-stage spectrometer. Both stages have a dipole magnet used to measure the momentum of particles, then contain a series of tracking detectors and calorimeters. The first stage is called the Large Angle Spectrometer (LAS) and contains the dipole magnet SM1 which provides an integrated field of 1 Tm. The second stage is called the Small Angle Spectrometer (SAS) and contains the dipole magnet SM2 which provides an integrated field of 4.4 Tm. Looking along the direction of the beam, the left side of the spectrometer is called the 'Jura' side and the right side is called the 'Saleve' side after the two mountain ranges to the west and east of CERN. A schematic of the COMPASS setup during the 2015 and 2018 DY runs is shown in Fig. 3.1.

In this chapter, Sect. 3.1 will describe the COMPASS setup during the 2015 and 2018 DY data-taking

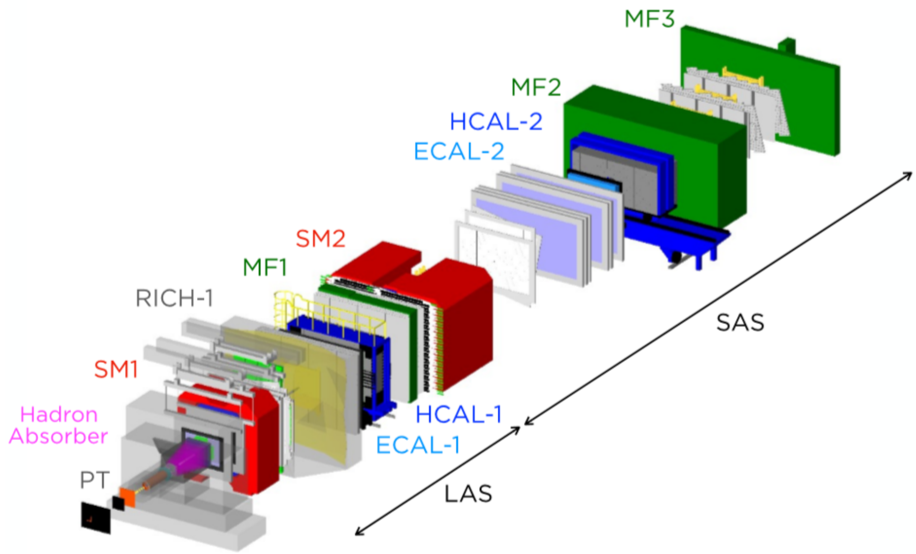

Figure 3.1: Diagram of the COMPASS spectrometer setup during the 2015 and 2018 DY data-taking runs. The different components are discussed in Sect. 3.1. Diagram from [107].

runs, including the polarized target and the various tracking detectors. Sect. 3.2 will give further details about one specific drift chamber detector called DC05 that was built and is maintained by the UIUC group. It will include information about the detector calibrations performed by the author, and the repairs the author was involved in. Finally, Sect. 3.3 will describe the reconstruction process by which the raw data from the COMPASS spectrometer is converted into physics quantities that can be used for analysis. The author managed the newest large-scale reconstructions of the 2015 and 2018 data using supercomputing resources.

3.1 Experimental Setup

In this section, the COMPASS beam, target, and spectrometer setup will be described. More details about the setup can be found in Ref. [108], [109], and [110].

3.1.1 Beam

The SPS can accelerate protons to an energy of 450 GeV. At the beginning of the M2 beamline, these protons impinge on the T6 beryllium production target, and the proton beam is converted to a secondary hadron beam. The T6 target length can be adjusted to change the intensity of the beam. After the T6 target, various dipole, quadropole, and toroidal magnets are used to select beam particles with the desired momentum. A schematic of the M2 beamline is shown in Fig. 3.2. In 2015 and 2018, the selected beam that was sent to the COMPASS target was a 190 GeV/c negative pion beam, with about 2% contamination from

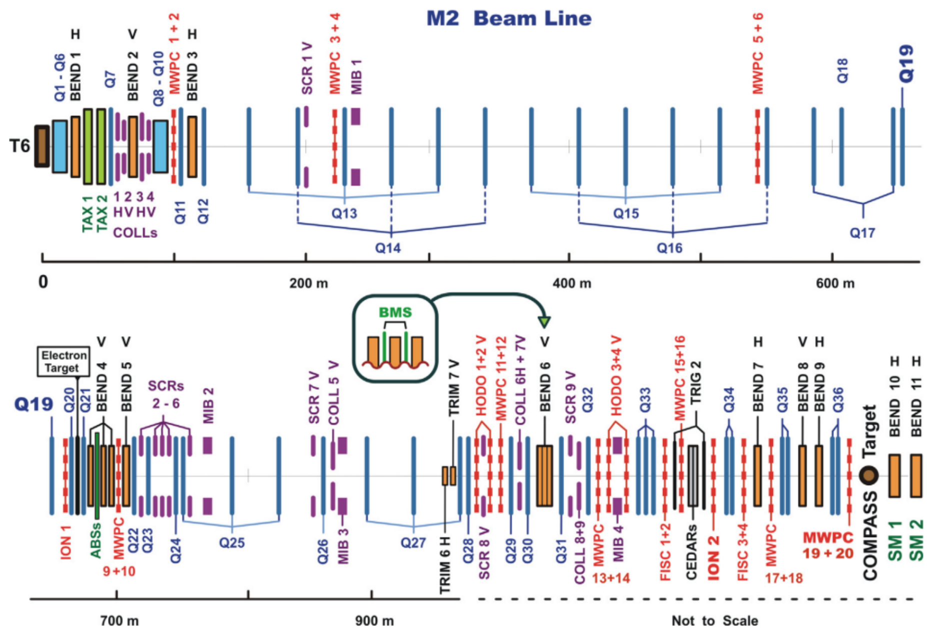

Figure 3.2: Diagram of the CERN M2 beamline, beginning at the T6 beryllium target and ending at the COMPASS target. Image from [109].

negative kaons and 1% contamination from antiprotons.

While traveling, many pions and kaons in the beam decay into muons and antineutrinos. These muons are longitudinally polarized because anti-neutrinos always have left-handed helicity. Absorbers can be added to remove the remaining hadrons and create a tertiary muon beam. A 160 GeV/c muon beam was used during some of the other COMPASS measurements, including SIDIS. (In the hadron beam, the decay muons are removed using magnets since they have lower momenta than the hadrons.)

The SPS and the beginning of the M2 beamline are underground, while the COMPASS target and spectrometer are above ground. Therefore, the beam must be bent upward and then once at ground level, bent to be horizontal again. The beam is bent up to ground level in a 250 m long tunnel of alternating focusing and defocusing (FODO) quadrupole magnets. It arrives at ground level 100 m before the COMPASS target, where it is bent to be horizontal again using a series of three dipole magnets called Bend 6. Before and after Bend 6 are tracking detectors that can determine the beam momentum to a precision of 1%. These detectors comprise the beam momentum station (BMS), a diagram of which is shown in Fig. 3.3. In 2015 and 2018, the intensity of the hadron beam was too high for the BMS to work accurately. Therefore, in 2014 a low intensity negative pion beam was sent through the BMS in order to measure the momentum distribution. The result is shown in Fig. 3.4. The average momentum was found to be 190.9 $\pm$ 3.2 GeV/c. The momentum distribution should be independent of the beam intensity and therefore was assumed to be the same in 2015 and 2018 as it was in 2014.

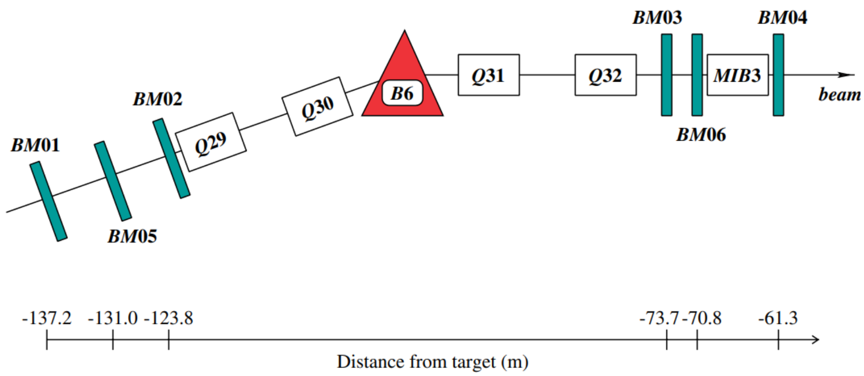

Figure 3.3: Diagram of the COMPASS BMS, including six tracking detectors (blue) and the Bend 6 (B6) magnets that bend the beam to the horizontal. From [108].

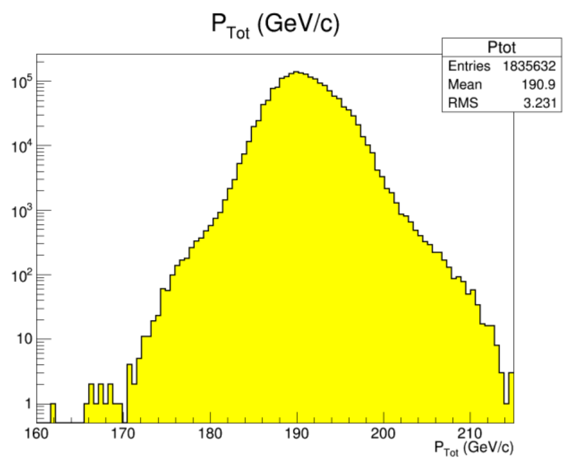

Figure 3.4: Momentum distribution of the COMPASS negative pion beam, determined during a low intensity beam run in 2014. From a COMPASS internal presentation.

Downstream of the BMS and about 30 m before the COMPASS target, there are two Cherenkov counter detectors (CEDARs) designed for particle identification. The operating principle of the CEDARs is as follows. When particles travel faster than the speed of light in a given medium, they emit Cherenkov radiation. The angle of radiation is larger when the particle velocity is faster. In the hadron beam, the momentum of each hadron will be approximately the same, so lighter particles will have higher velocity. Thus the angle of the Cherenkov radiation can be used to determine the mass and therefore the identity of the particles. During the DY runs in 2015 and 2018, many of the beam particles diverged from the optical axis of the CEDARs, making the particle identification process much more difficult. There is a method to overcome this difficulty [111], but because the beam contamination from kaons and antiprotons was only a few percent, the effect on the DY physics analysis was negligible and the CEDAR data was therefore neglected.

Downstream of the CEDARS, one more set of magnets are positioned immediately in front of the target in order to fine-tune the beam direction. In runs with a transversely-polarized target, such as the 2015 and

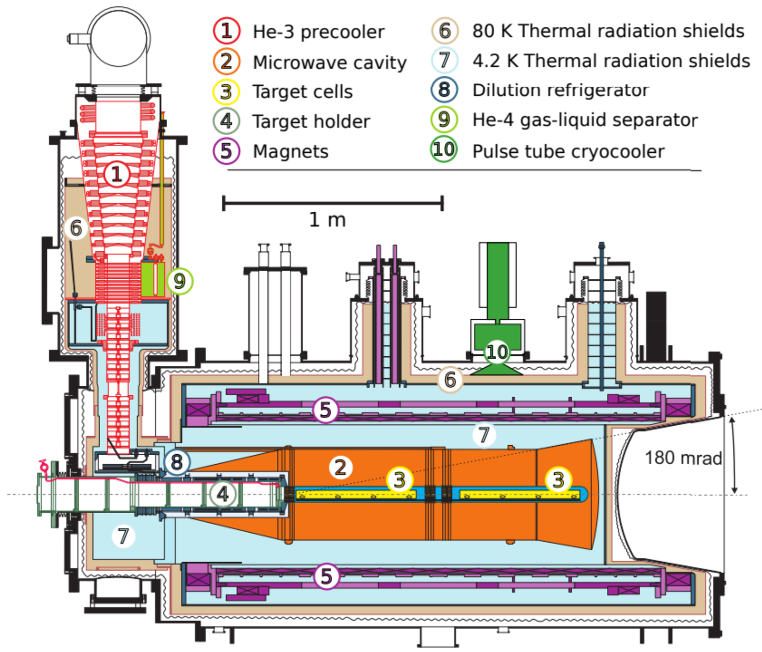

Figure 3.5: Diagram of the COMPASS polarized target in 2015 and 2018, including the magnets and liquid helium dilution refrigerator. From [112].

2018 runs, these magnets can compensate for the impact on the beam of the magnetic field used to maintain the target polarization.

3.1.2 Polarized Target

The COMPASS polarized target is composed of two or three cells filled with deuterated lithium (^{6}LiD) or solid state ammonia (NH_3). In the 2015 and 2018 runs, the target was filled with solid state NH_3. A diagram of the target is shown in Fig. 3.5.

The target cells are surrounded by a longitudinal superconducting magnet that can create a uniform field of up to 2.5 T. This magnet is responsible for the longitudinal polarization of the target. The polarization is achieved using the process of dynamic nuclear polarization (DNP) [113], in which the polarization of electrons is transferred to the nucleons in the target using microwave radiation. The achieved polarization is maintained by immersing the target in a dilution refrigerator filled with liquid helium at approximately 60 mK. To achieve transverse polarization, the nucleon spin is rotated 90 degrees using a 0.63 T dipole magnet. The transverse polarization cannot be maintained because of the weak field and the fact the field is not uniform, so the polarization exponentially decays over time. The relaxation time in 2015 and 2018 is about 1000 hours. The average achieved transverse polarization in 2015 and 2018, including the gradual polarization relaxation, is 73%.

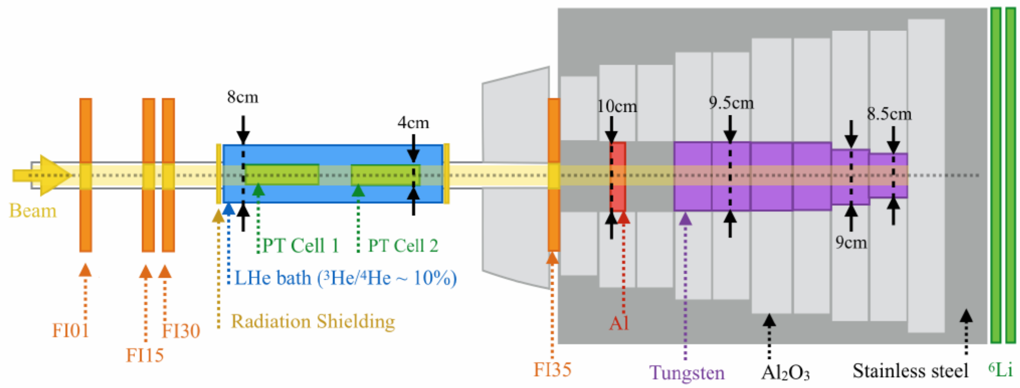

Figure 3.6: A diagram of the polarized target (PT) and the hadron absorber including the aluminum and tungsten targets. The FI detectors are scintillating fiber detectors used for beam and event vertex reconstruction. From [114].

In the NH_3 target, only the protons can be polarized. Therefore, a dilution factor quantifying the fraction of the target that can be polarized must be included whenever the target polarization is used in calculations (e.g. in the DY cross-section in Eq. 2.33). Naively, the dilution factor is expected to be near 3/17 in NH_3, but it can be calculated more precisely by taking into account the cross-section of the desired process (e.g. DY) off a hydrogen atom compared to the cross-section off of other nucleons in the target. In 2015 and 2018, the dilution factor ranges from 0.14 to 0.18.

In 2015 and 2018, the target was composed of two 55 cm long cells filled with solid state NH_3. The cells had a radius of 2 cm and were separated by 20 cm. The two target cells were polarized in opposite directions. Each data-taking period was divided into sub-periods. Between sub-periods, the polarization of each target cell was flipped in order to reduce the impact of luminosity and spectrometer acceptance effects. In order to flip the polarization between sub-periods, the polarization was first destroyed then recreated.

3.1.3 Hadron Absorber

During the Drell-Yan data-taking runs in 2015 and 2018, it was only important to track the leptons coming out of the target collisions (see the Feynman diagram for the DY process in Fig. 2.10). Therefore, a hadron absorber was added after the polarized target to remove the majority of the hadrons coming out of collisions. It was also used to contain radiation levels from the high intensity hadron beam.

A diagram of the hadron absorber with the polarized target is shown in Fig. 3.6. It is made of Al_2O_3 slabs held in a stainless steel frame. Within the slabs, near the front of the absorber, is a cylindrical aluminum plug 7 cm long and 10 cm in diameter. Behind this is a tungsten plug made of three cylinders that are 80 cm, 20 cm, and 20 cm in length and 9.5 cm, 9 cm, and 8.5 cm in diameter. These plugs can act as nuclear targets to collect spin-independent DY data and study nuclear-dependent effects. Typically only the first 10 cm of tungsten is used in physics studies because the beam is highly contaminated by secondary particles after this point.

3.1.4 Triggers

Many particles pass through the COMPASS spectrometer, and the front end electronics on the detectors cannot process all the information. Additionally, in 2015 and 2018 only possible Drell-Yan events needed to be recorded. A trigger system is used to signal which events are important and which can be ignored. During the 2015 and 2018 runs, the signal of a DY event was a dimuon. Muons rather than electrons were chosen because muons travel farther through material and are therefore easier to identify and track. There were three single-muon triggers used in 2015 and 2018: the LAS trigger (LAST), outer trigger (OT), and middle trigger (MT). Each trigger is made of at least two scintillating hodoscopes located at different positions along the spectrometer. The triggers use the target pointing technique illustrated in Fig. 3.7. If a particle passes through both hodoscopes in coincidence as defined by a coincidence matrix, the signal is recorded (unless a veto signal is also received as discussed below).

The LAST is the only trigger in the LAS portion of the spectrometer between SM1 and SM2. It is composed of two hodoscope planes H1 and H2, each with 32 slabs. The OT and MT are located in the SAS portion of the spectrometer. The first OT hodoscope plane H3O is located immediately downstream of SM2, while the second plane H4O is located downstream of the second muon wall. H3O is composed of 18 slabs, while H4O is composed of 32 slabs. Finally, the MT is composed of two planes, H4M between the second and third muon walls, and H5M after the third muon wall. Each are made of 32 slabs.

The three single muon triggers can be combined to create dimuon triggers. COMPASS uses three dimuon triggers: LASTxLAST, LASTxOT, and LASTxMT. The LASTxLAST trigger covers events with smaller polar angles and therefore higher Q^2 values compared to the other two. The LASTxLAST trigger requires two LAST coincidences to occur. The LASTxOT and LASTxMT require one coincidence in the LAST and one in the OT or MT respectively.

There is also a veto trigger system located upstream of the target. This veto system is centered on the beam axis and is used to reject muons resulting from beam decay that were not removed by the M2 absorber. If the veto trigger signals at the same time as a muon trigger, the event is not saved. As will be mentioned in Chapter 5, the LASTxMT trigger was also used as a veto in the 2015 and 2018 data analyses in order to remove additional contamination from beam decay muons.

Finally, there is a random trigger (RT) set up outside of the spectrometer region which records signals

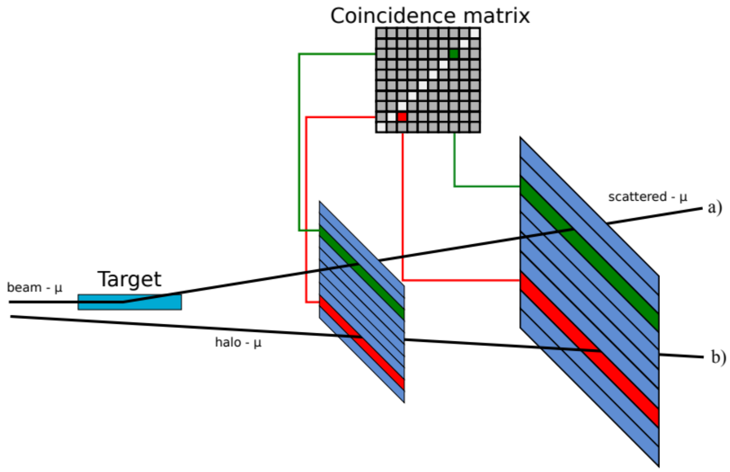

Figure 3.7: Target pointing technique for the single muon triggers at COMPASS. Image from a COMPASS internal note by J. Barth et.al.

based the radioactive beta decay of ^{22}Na rather than based on what is passing through the spectrometer. The RT is not affected by the veto trigger and is used to study the beam flux.

3.1.5 Tracking Detectors

The COMPASS spectrometer is designed to cover a large angular phase space, from 8 mrad to 165 mrad. For this reason, multiple different types of tracking detectors are used in order to determine the position and timing information of particles coming out of the target. These can be divided into three categories: very small area trackers (VSAT), small area trackers (SAT), and large area trackers (LAT). The detectors track position in up to four orientations: X and Y which are the horizontal and vertical orientations respectively, and U and V which are rotated at different angles from the X and Y axes.

Very Small Area Trackers

Very small area trackers must be able to handle the highest rates of incoming particles, up to 5×10^7 Hz. There are two types of VSATs that were used during the DY runs: scintillating fiber (SciFi) detectors and pixelized micromesh gaseous structure (pixelized micromega) detectors. Four SciFi detectors were used for tracking during 2015 and 2018. FI01, FI15, and FI03 are upstream of the target (see Fig. 3.6) and make up what is referred to as the 'beam telescope'. FI04 was located in the LAS region in 2015, but was moved to the beam telescope in 2018 to help with beam reconstruction. The active areas range from 3.9×3.9 cm^2 to 12.3×12.3 cm^2. These detectors use multiple staggered layers of scintillating fibers to determine particle position as illustrated in Fig. 3.8a, and the nominal spacial resolutions are 130 μm, 170 μm or 210 μm

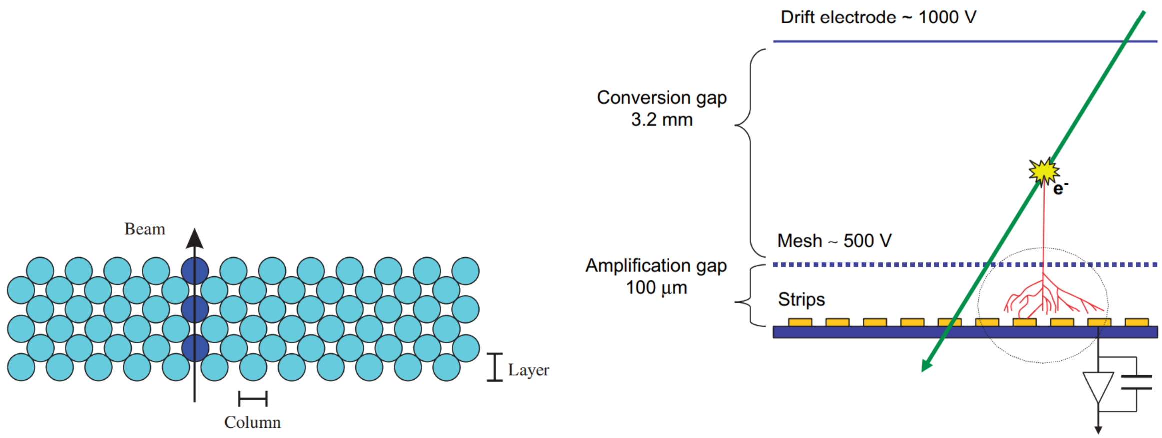

(a) (b)

Figure 3.8: (a) Fiber configuration of a SciFi plane. The actual number of fiber layers per plane is 8, 12, or 14. (b) Basic operating principle of the micromega detectors. In 2015 and 2018, two GEM foils were added to the conversion gap. Both figures are from [108].

depending on the diameters of the fibers (0.5 mm, 0.75 mm, or 1 mm respectively). The nominal timing resolution of the SciFis is 400 ps. The SciFi stations track in the X, Y, and sometimes the U orientations.

The pixelized micromegas are special sensitive areas in the center of the regular small area tracker micromega detectors which will be described below. The pixels are 2.5×0.4 mm^2 or 6.25×0.4 mm^2 in size and cover an active region of 50×50 mm^2. The spacial resolution of the pixel region is 80 μm and the timing resolution is 9 ns.

Small Area Trackers

The small area trackers cover the region 5 to 40 cm from the beam and receive particles at a rate of about 10^5 Hz. There are two types of SATs: gas electron multipliers (GEMs) and micromesh gaseous structure (micromega) detectors.

There are eleven GEM detectors spread throughout the COMPASS spectrometer, as well as two pixel GEMs. The GEMs are mounted on the dead zone areas of the large area trackers that will be described below. Each GEM has an active area of 31×31 cm^2 with a 5 cm diameter dead zone. The operating principle of the GEMs is shown in Fig. 3.9. Each GEM contains three layers of 50 μm polymide foil coated on both sides with copper. Holes are drilled in the foil at a density of 10^4 cm^{-1}. An electric potential of a few hundred volts is applied between each layer. The electron signal from the drift gap is amplified as it passes through holes in each foil layer until it reaches the readout strips. The presence of three layers of foil rather than just one reduces the total drift time and allows a higher detection rate. The nominal spacial and timing resolution of the GEMs is 110 μm and 10 ns respectively.

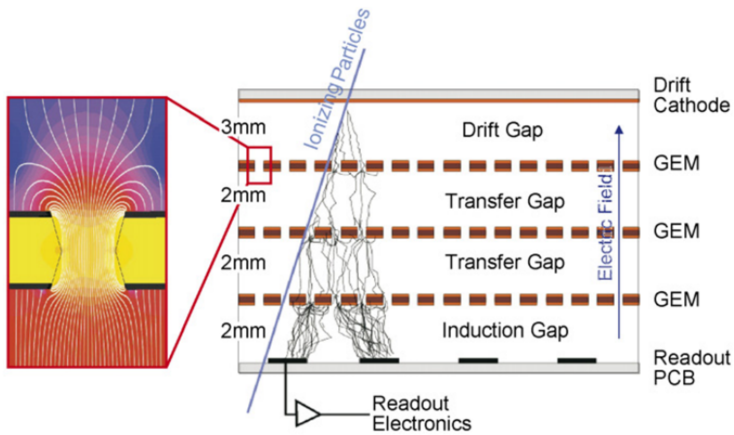

Figure 3.9: Operating principle of the GEM detectors. From [108].

There are three micromega detectors that are located downstream of one another between the target and the first spectrometer magnet SM1. Each detector has an active area of 40×40 cm^2 and tracks all four coordinates (X, Y, U, and V). In the center of the active area is a 5 cm diameter circular dead zone where the particles are not tracked because the flux is too high. As described above, the middle 50×50 mm^2 area of this region contains a special pixelized section used as a VSAT. The operating principle of the micromegas is shown in Fig. 3.8b. Charged particles traveling through the gas (Ne/C_2H_6/CF_4 at a ratio of 80/10/10) in the conversion region will produce electrons. An electric field of 1 kV/cm causes the electrons to drift toward the amplification region where the field is 50 kV/cm. This higher field leads to an electron avalanche and the amplified signal is picked up by readout strips. The amplification region is very narrow, only 100 μm, which keeps the electron avalanche narrow and allows a good spacial resolution of about 110 μm. A micromesh is placed between the conversion and amplification regions to prevent the electric field from being distorted, therefore allowing the drift time of the electrons to be quicker and the possible readout rate to be higher. The micromesh also keeps slowly drifting ions close to the avalanche. The nominal timing resolution of the micromegas is 9 ns. During the DY runs, two GEM foils were added to the micromegas to help the amplification to be more gradual as in the GEM detectors and reduce the discharge rate.

Large Area Trackers

The large area trackers cover a large planar area and do not have to process high fluxes like the SATs and VSATs. Because of the large areas, the position and timing resolutions are not as good as the smaller trackers. The LATs use five different types of drift chamber technologies.

There are four traditional drift chambers in or before the LAS region: DC00, DC01, DC04, and DC05. DC00 and DC01 are just upstream of SM1, and DC04 and DC05 are downstream of SM1. DC00 and DC01

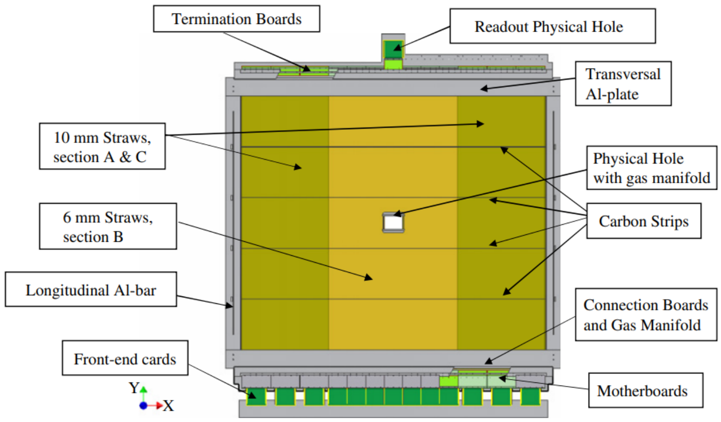

Figure 3.10: Frontal schematic of a straw tube detector at COMPASS. From [108].

must process a higher flux of particles than DC04 and DC05 because SM1 bends many low energy particles out of the acceptance region. DC00 and DC01 have active areas of 180×127 cm^2 and 30 cm diameter circular dead zones. DC04 and DC05 have larger active areas of 240×204 cm^2 with 30 cm diameter dead zones. Each of the four drift chambers is made of eight detector layers, two for each coordinate (X, Y, U, and V). More details about these drift chambers, particularly DC05, will be given in Sect. 3.2. The spacial resolution of these DCs is 300-400 μm.

The next type of LAT is a straw tube detector. During the DY runs only one straw detector was used: ST03 located in the LAS downstream of DC05. A straw detector is composed of many circular tubes. At the center of each tube is a gold-plated tungsten anode wire. The tube wall acts as a cathode. When a charged particle passes through the gas in the detector, the electrons drift toward the anode wires where they are detected. ST03 is made of six double layers, each with straw tubes at different orientations. Each detector plane has two sections. The straws in the inner section have a diameter of 6.1 mm while the straws in the outer section have a diameter of 9.6 mm. A schematic of a straw plane is shown in Fig. 3.10. The nominal spacial resolution of ST03 is 400 μm.

The Rich Wall detector is in the LAS immediately downstream of the RICH (Sect. 3.1.6), which is downstream of ST03, and is similar to a straw tube detector. It is composed of eight layers of mini drift tubes as shown in Fig. 3.11. Aluminum combs act as the cathodes and gold-plated tungsten wires in the center act as the anodes. The Rich Wall has an active area of 527×391 cm^2 and a square dead zone of 102×51 cm^2. Its nominal resolution is 600 μm.

Another type of large angle tracker is a multi-wire proportional chamber (MWPC). There are six MWPCs in the LAS and eight in the SAS. There are three categories of MWPCs. Types A and B measure the X, U, and V coordinates, while type A* measures the X, U, V, and Y coordinates. Type A and A* have an active

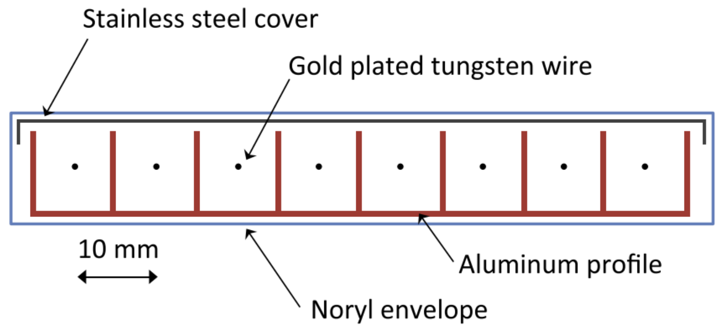

Figure 3.11: A diagram of a mini drift tube in the Rich Wall. From [109].

area of 178×120 cm^2, while type B is smaller with an active area of 178×90 cm^2. The dead zones of type A, A*, and B have a diameter of 16 cm, 20 cm, and 22 cm respectively. There are seven type A, one type A*, and six type B MWPCs. The MWPCs operate similar to the DCs, but there is no calibrated relationship between the position and time of drifting electrons (see Sect. 3.2). The spacial resolution of the MWPCs is about 600 μm.

Downstream of SM2 is a final large size drift chamber called W45. W45 has six stations, each with two different orientations. The active area of W45 is 520×260 cm^2 and the dead zone is 50 or 100 cm in diameter. The nominal spacial resolution is 500-600 μm.

It is interesting to note the gas mixtures used in the different types of LATs. The DCs use a mixture of $Ar/C_2H_6/CF_4$ at a ratio of 45/45/10 in order to have good spacial resolution and a linear position-time relationship. The MWPCs use a mixture of $Ar/CO_2/CF_4$ at a ratio of 74/6/20 in order to have a fast counting rate, and ST03 uses the same gasses at a ratio of 80/10/10. The Rich Wall uses an Ar/CO_2 mixture at a ratio of 70/30. Finally, W45 uses $Ar/CF_4/CO_2$ at a ratio of 85/10/5 in order to increase the drift velocity of electrons.

3.1.6 Particle Identification

The COMPASS spectrometer uses four types of detectors for particle identification (PID): a ring imaging Cherenkov (RICH) detector, electromagnetic calorimeters (ECAL), hadron calorimeters (HCAL), and muon walls (MW). The RICH detector distinguishes between types of hadrons, specifically pions, kaons, and protons. It operates similarly to the CEDARs along the beamline (Sect. 3.1.1), distinguishing particles based on the angle of the emitted Cherenkov radiation. There are two ECALs and two HCALs, one each in the LAS and SAS. The ECALs measure the energy of photons and electrons, while the HCALs measure the energy of hadrons. In each case, the material in the calorimeters stops the desired particles, and the resulting electromagnetic or hadronic showers are detected by photomultiplier tubes.

The muon walls were the only important PID detectors during the DY runs, because as mentioned in Sect. 3.1.4, COMPASS identifies a DY event by a dimuon. There are two important muon filters (MFs) in the spectrometer during the DY runs: MF1 is positioned at the end of the LAS before SM2, and MF2 is positioned near the end of the SAS before W45. These muon filters are absorbers which stop most particles except for muons. MF1 is a 60 cm thick iron absorber, while MF2 is a 2.4 m thick concrete absorber. Behind MF1 and MF2 are two muon walls, MW1 and MW2. These are responsible for tracking the muons that pass through the MFs. MW1 is made of mini drift tubes similar to the Rich Wall, and MW2 is made of drift tubes with a wire in the center similar to the straw detectors. MW1 is made of eight planes and has an active area of 480×410 cm^2 with a deadzone of 140×80 cm^2. MW2 is made of twelve planes and has an active area of 450×450 cm^2 with a dead zone of 90×70 cm^2.

3.1.7 Data Acquisition

In total there are over 250,000 detector channels at COMPASS. The information from these channels is collected by the data acquisition system (DAQ) and transferred to the CERN magnetic storage tape called CASTOR. Even with the trigger system that selects only events of interest, the events are read out at a rate of about 30 kHz. Each event is about 45 kB in size. In total, about 820 terabytes of raw data were collected in 2015 and 1000 terabytes in 2018.

The signals produced in detectors by passing particles (e.g. light in scintillating fibers) must first be converted to digital signals. This is done using time-to-digital converters (TDCs) or analog-to-digital converters (ADCs). The TDCs and ADCs are on the front end electronic cards or on the second stage specialized COMPASS electronic cards called GANDALF (Generic Advanced Numerical Device for Analog and Logic Functions), GeSiCA (GEM and Silicon Control and Acquisition) or CATCH (COMPASS Accumulate Transfer and Control Hardware). The special electronic cards send the digitized data to FPGA (Field Programmable Gate Array) multiplexers, where it is sorted by event and spill. Then it is sent to multiplexer slaves where the final processing is performed. Finally, the data is transferred to CASTOR.

3.2 Drift Chamber DC05

This section will give more details on the UIUC-built drift chamber DC05. The operating principle and many of the more specific details are true for the other COMPASS drift chambers as well (see Sect. 3.1.5).

DC05 is made of alternating layers of wires and cathodes. There are two wire planes with each orientation: X (vertical wires), Y (horizontal wires), U, and V ($\pm10^\circ$ respectively from the vertical). The wire planes are made of alternating anode or 'sense' wires with radii of 20 μm and cathode or 'field' wires with radii of 100 μm. The wires in the two planes with the same orientation or 'view', referred to as X and X' for example,

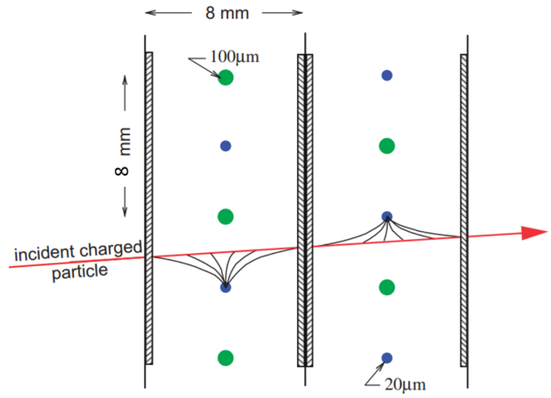

Figure 3.12: Operating principle of the COMPASS drift chambers. Modified from [108].

are offset from each other by half a drift cell. The X and Y planes each have 256 sense wires, and the U and V planes each have 320 sense wires. In between the wire layers are cathode layers made of carbon-painted mylar. Square drift cells with a width of 8 mm are formed with the anode wire in the center and cathodes on all sides, as shown in Fig. 3.12. Charged particles traveling through the gas mixture ($Ar/C_2H_6/CF_4$ at a ratio of 45/45/10) in the chamber ionize the argon atoms, producing electrons. As the electrons drift, they ionize other argon atoms creating an avalanche. This electron avalanche is detected by the sense wire. The ethane (C_2H_6) acts as a quencher to control the size of the electron avalanche. The CF_4 prevents aging of the detector by breaking up long molecular carbon chains.

In the DC05 gas mixture, drifting electrons have a mostly linear position-time or RT relationship. The drift time is determined by comparing the time the trigger fires (Sect. 3.1.4) to the time the sense wire detects the drifting electron. This timing information combined with tracking information from other detectors can be used to determine a so-called RT calibration relationship, which gives the distance between the passing particle and the sense wire. The direction of the particle relative to a sense wire is determined by combining information from all the wire planes. The half-cell offset between the two planes of the same view is critical in this determination.

The author of this thesis performed RT calibrations of DC05 for COMPASS 2018 data, which were used in official COMPASS data productions (see Sect. 3.3). Each of the eight wire planes were calibrated independently for each of the data-taking periods of 2018. A sample RT relation for the U' plane in the 2018 period P05 is shown in Fig. 3.13. The calibration values relating position (R) and time (T) should lie along the center of each 'branch'. This center value was found by projecting the 2D histogram onto the R axis in each bin of T, then fitting the projections with Gaussian curves. Note that the two branches are symmetric, so only one branch needs to be fit. The preliminary and updated calibrations of the U' plane in 2018 P05 is shown as red dots in Fig. 3.13. As the calibration improves, the resolution of the DC05 measurement should

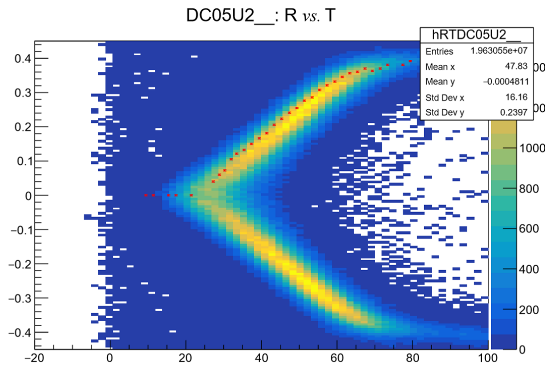

(a)

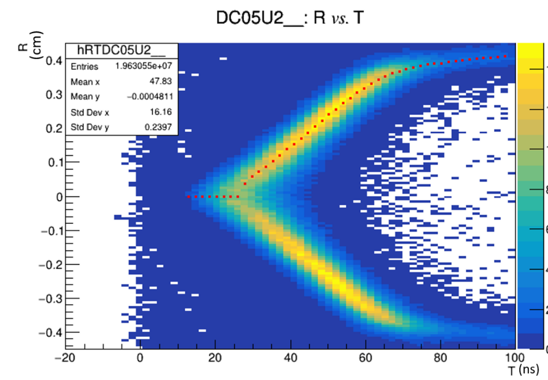

(b)

Figure 3.13: The (a) preliminary and (b) updated RT calibration curves for the U' plane of DC05, using data from 2018 P05. The red dots show the calibration points and should lie along the center of the branch of the RT curve. Note that the linear RT relationship degrades at large T. This is an effect of the CF_4 gas.

also improve. Indeed, for the plane shown in Fig. 3.13, the resolution improved from 434 ± 2 μm to 350 ± 1 μm.

The UIUC group is responsible for maintaining DC05. The author of this thesis has been part of the team which repaired DC05 on three different occasions. In September 2019, a team went to repair broken wires in the Y' plane which prevented the Y-view from operating during most of the 2018 data-taking run. Two wires in the Y' plane were replaced, as was the nylon wire in the Y plane that is responsible for holding the sense wires in place. After repairing the broken wires, it was necessary to check that all sense wires in the Y planes were still pulled to the proper tension so as to prevent wire oscillations in the high voltage field and sagging due to gravity. The sense wires are so thin (20 μm) that it is usually not possible to tell if a wire is loose by eye, so an alternate test was used. When AC current is passed through a wire lying in a transverse magnetic field, the wire will oscillate when the current frequency is equal to the resonant frequency f of the wire. The resonant frequency is related to the tension of the wire via

$$f = \frac{1}{2L}\sqrt{\frac{T}{\rho}}, \tag{3.1}$$

where L is the wire length, ρ is the linear density of the wire, and T is the tension. The length and linear density of the wires were known from when DC05 was constructed. In order to determine the tension of a wire, it was grounded on one side and connected to a function generator which could provide AC current on the other. All other wires were grounded on both sides. A magnet was placed under the wire, and the AC current was turned on. The wire was monitored (by eye) to determine the frequency at which it oscillated at maximum amplitude. This frequency was then plugged into Eq. 3.1 to determine the tension of each wire.

All sense wires in both Y planes were tested, and no additional wires were loose enough to require repair.

After repairing the Y planes, DC05 was reassembled. During the subsequent tests to ensure DC05 was functioning properly, it was found that certain planes were not receiving voltage correctly. Therefore in January 2020 the UIUC team returned to CERN. The high voltage connections on the faulty planes were repaired, then the detector was again reassembled. The tests after this repair all went well, and DC05 was returned to its normal location in the COMPASS spectrometer in preparation for the 2021 data-taking run. However, sometime between January 2020 and the beginning of the 2021 COMPASS run, another wire broke, this time in the Y plane. In February 2022, the team returned once again and removed the broken wire. Additionally, the metal pins holding the wire plane frames in place were replaced with newer, slightly thicker pins to help keep the frames at the proper tension and prevent further wire breakages.

3.3 Data Production

The digitized data coming out of the DAQ (Sect. 3.1.7) must be reconstructed into physical quantities in order to perform physics analysis. COMPASS uses CORAL (COMPASS Reconstruction and AnaLysis Libraries) to reconstruct the raw data. The steps CORAL takes are as follows. First, timing, calibration, and alignment information is combined to determine the positions of particles causing 'hits' in the detectors. The hits are combined into continuous tracks using knowledge of the experimental setup, including the magnetic fields and the material budgets of the detectors. Using this same information, the momentum and charge of the particles is determined. Each track has an associated χ^2 value based on the quality of the fit to the hits. After this, the tracks are extrapolated to the target region, and the points where multiple tracks cross are assigned as vertices. If a beam particle track is associated to a vertex, it is defined to be a primary vertex. If not, it is a secondary vertex. The information coming out of the CORAL reconstruction is written to data structure trees (DSTs). Once the data is in DSTs, the COMPASS data analysis tool called PHAST (PHysics Analysis Software Tool) can be used to perform further analysis. Both CORAL and PHAST are written in C++.

COMPASS data is generally reconstructed period by period until an entire year of data has been reconstructed under the same conditions. This large-scale reconstruction is referred to as a data production. Improvements of the various inputs to the reconstruction, such as detector calibrations, can lead to reproductions of the data. Multiple data productions have occurred for the 2015 and 2018 data. The 2015 data is composed of nine periods called W07-W15, and the 2018 data is composed of nine periods called P00-P08. The newest 2015 and 2018 productions differ from the older ones in several ways, including hodoscope alignment, MWPC and DC calibrations, and optimization of the hit association algorithm in CORAL.

Because of the quantity of raw data, large-scale parallel computing resources are necessary for running

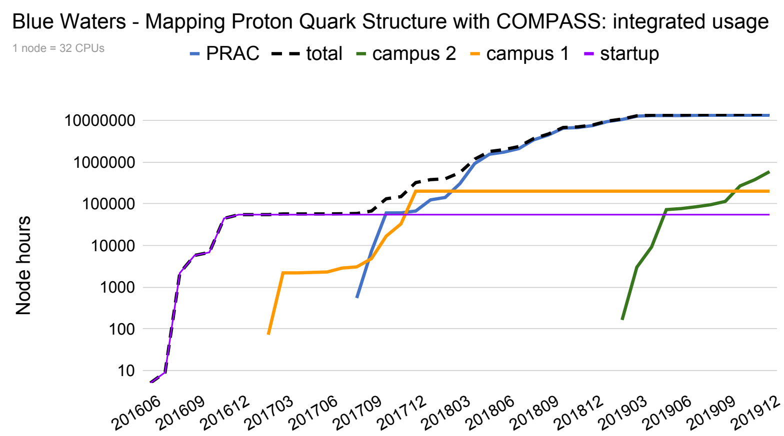

(a)

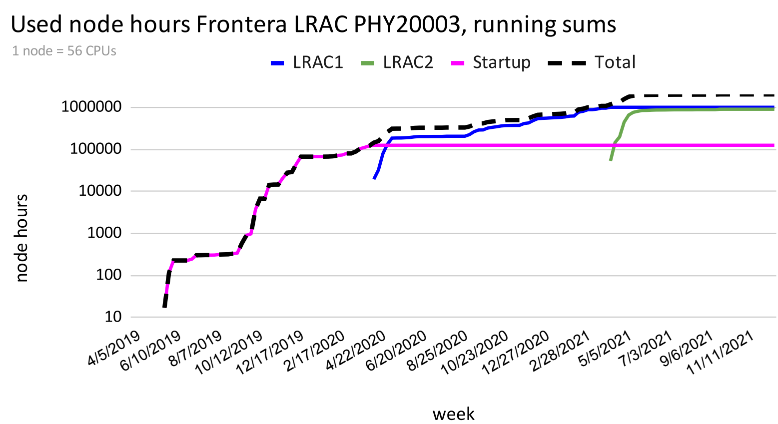

(b)

Figure 3.14: Graphs illustrating the usage overtime of the UIUC allocations on the (a) Blue Waters and (b) Frontera supercomputers. Note that the y-axis is on a log scale. The solid lines correspond to different allocations, and the dashed black lines show the total usage. From [115].

COMPASS data productions. The UIUC group has secured allocations on two US-based supercomputers to help with this. The first was the NSF-funded petascale supercomputer Blue Waters. From 2016 through 2020, UIUC received a total allocation of 14 million node hours on Blue Waters, with node corresponding to 32 CPUs. The allocation on Blue Waters allowed COMPASS to finish the first 2018 data production in record time after the completion of the 2018 run. In 2020, Blue Waters was replaced by another NSF-funded computer called Frontera located at the Texas Advanced Computing Center (TACC). From 2020-2022, UIUC receivd a total allocation of over 2 million node hours on Frontera, where each node corresponds to 56 CPUs. The author of this thesis was the Drell-Yan data production manager from fall 2019 through summer 2020, utilizing both Blue Waters and Frontera. The author used about one fourth of the total allocated node hours on Frontera to manage the most recent 2015 and 2018 productions. The total usage overtime of the Blue

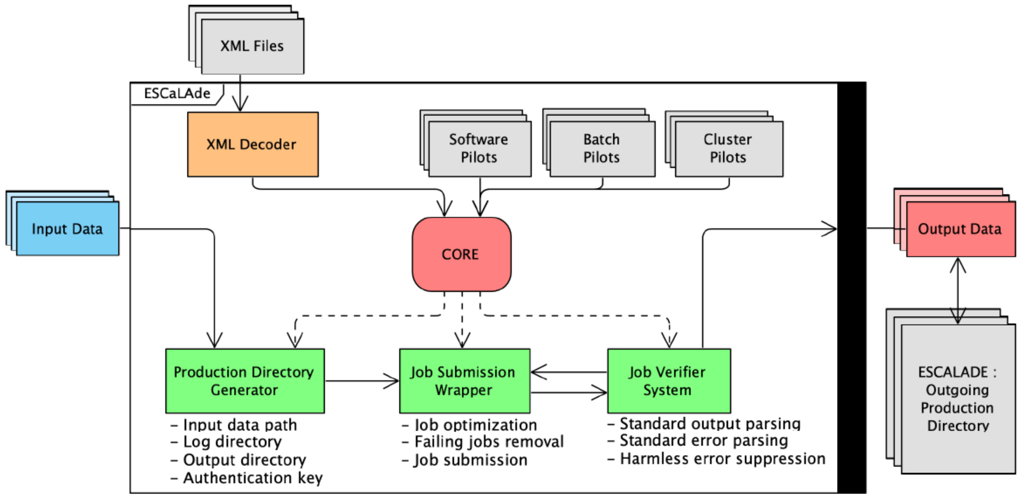

Figure 3.15: Basic architecture of the ESCALADE production framework. From [114].

Waters and Frontera allocations is illustrated in Fig. 3.14.

A production framework is needed to manage the data productions. The production framework is responsible for running the necessary software, submitting jobs, organizing input and output data and files, and checking the integrity of the final outputs. The primary production framework that was used on Blue Waters and Frontera is called ESCALADE and was written by former COMPASS member Marco Meyer [114]. The basic architecture of ESCALADE is depicted in Fig. 3.15. The so called 'pilot' scripts responsible for running the software and interacting with the supercomputer environment sometimes need to be modified to work on different machines. For example, Blue Waters used the workload manager TORQUE to submit jobs to nodes, while Frontera uses SLURM. The author of this thesis helped to update ESCALADE during the transition from Blue Waters to Frontera.

Chapter 4

Methods of Transverse Spin Asymmetry Extraction

As discussed in Sects. 2.4 and 2.5, the experimental observables related to TMD PDFs are transverse-spin asymmetries (TSAs). There are various methods that are used to extract TSAs from COMPASS DY data. In all of them, it is important to be aware of the role of acceptance in the formula or method, so that acceptance effects are not mistaken for physical asymmetries. In general, the methods are designed to cancel out acceptance as much as possible. False asymmetries can be used to determine the relative size of any remaining acceptance effects on the final extracted asymmetries.

Section 4.1 will explain a simple method of TSA extraction called the one-dimensional double ratio method, where a ratio of experimental counts is formed and fit with an angular modulation associated with a particular TSA. This method relies on the "reasonable assumption" that the COMPASS spectrometer acceptance is stable during each data-taking period. When this is not true, this method can be biased.

A more robust method is the Unbinned Maximum Likelihood (UML) method, in which a likelihood function is constructed based on the DY cross-section, with the fit parameters being the TSAs and spin-independent asymmetries. The negative log of this likelihood function is minimized to extract all the asymmetries at once. This method will be described in Sect. 4.2.

In addition to the traditional TSAs, the left-right asymmetry A_{N} (also sometimes called the analyzing power) will be extracted to further study the Sivers TMD. Normally A_{N} is measured in collider experiments rather than fixed target experiments (see Sect. 2.6.4). However, it is interesting to extract it from COMPASS data because it can complement the standard UML method by dealing with systematics in a different way. This quantity was first extracted from COMPASS data in Ref [116]. A naive left-right asymmetry can be very dependent on acceptance effects. Section 4.3 will explain how the two-target geometric mean method can be used to minimize these effects.

4.1 One-Dimensional Double Ratio Method

The expected number of DY events from a given target cell can be written as a function of angle as

$$N(\Phi) \propto B\, l\, a(\Phi)(\sigma_0 \pm \sigma_\pm(\Phi)) = B\, l\, a(\Phi)\sigma_0(1 \pm \epsilon(\Phi)), \tag{4.1}$$

where N is the number of events, Φ is some azimuthal angle (e.g. ϕ_S), B is the beam flux, l is the target cell length, $a(\Phi)$ encodes the acceptance and efficiency of the spectrometer, σ_0 is the spin-independent cross section, and $\sigma_\pm(\Phi)$ is the transverse-spin-dependent portion of the cross section. The $\pm$ refers to target cell polarization, and $\epsilon(\Phi) = \sigma_\pm(\Phi)/\sigma_0$ is assumed to be much less than one.

Using the events from both target cells and both polarization configurations (see Sect. 3.1.2), a "double ratio" of event counts can be constructed to access the TSAs. This is defined as

$$F_\mathrm{DR} = \frac{N_{1+}N_{2+}}{N_{1-}N_{2-}}, \tag{4.2}$$

where the subscript 1(2) refers to the upstream(downstream) target cell and $\pm$ refers to the corresponding cell polarization. Plugging Eq. 4.1 into Eq. 4.2 gives

$$F_\mathrm{DR}(\Phi) = \frac{B_{1+}B_{2+}a_{1+}(\Phi)a_{2+}(\Phi)l^2\sigma_0^2(1+\epsilon(\Phi))^2}{B_{1-}B_{2-}a_{1-}(\Phi)a_{2-}(\Phi)l^2\sigma_0^2(1-\epsilon(\Phi))^2} \tag{4.3}$$

The l and σ_0 terms cancel exactly. The beam flux is approximately the same during an entire period of data taking, so $B_{1+} \approx B_{1-}$ and $B_{2+} \approx B_{2-}$. Therefore Eq. 4.3 becomes

$$F_\mathrm{DR}(\Phi) = \frac{a_{1+}(\Phi)a_{2+}(\Phi)(1+\epsilon(\Phi))^2}{a_{1-}(\Phi)a_{2-}(\Phi)(1-\epsilon(\Phi))^2} \simeq \frac{a_{1+}(\Phi)a_{2+}(\Phi)}{a_{1-}(\Phi)a_{2-}(\Phi)}(1+4\epsilon(\Phi)+8\epsilon^2(\Phi)+O(\epsilon^3)), \tag{4.4}$$

where the last approximation holds because $\epsilon \ll 1$. It is reasonable to assume that the COMPASS spectrometer is stable during each data-taking period because the positions and setups of the detectors are not changed during single periods. This "reasonable assumption" means that

$$\frac{a_{1+}(\Phi)a_{2+}(\Phi)}{a_{1-}(\Phi)a_{2-}(\Phi)} \simeq \text{constant}. \tag{4.5}$$

In this assumption, any angular modulations in the double ratio come from $\epsilon(\Phi)$ and give access to the asymmetry in the DY cross section (Eq. 2.33) associated with the angle Φ.

To extract the asymmetry, the binned ratio $F_{\mathrm{DR}}(\Phi)$ is fit with a function based on the series expansion in Eq. 4.4. To first order the fit function is

$$f_1 = p_0(1 + 4p_1 g(\Phi)), \tag{4.6}$$

where $g(\Phi)$ is the angular modulation associated with Φ in the DY cross section (Eq. 2.33), and p_1 is the so called "raw asymmetry" associated with Φ. For the Sivers asymmetry $A_{\mathrm{T}}^{\sin(\phi_{\mathrm{S}})}$, $g(\Phi) = \sin(\phi_{\mathrm{S}})$. For the pretzelosity TSA $A_{\mathrm{T}}^{\sin(2\phi_{\mathrm{CS}}+\phi_{\mathrm{S}})}$, $g(\Phi) = \sin(2\phi_{\mathrm{CS}} + \phi_{\mathrm{S}})$. Finally, for the transversity TSA $A_{\mathrm{T}}^{\sin(2\phi_{\mathrm{CS}}-\phi_{\mathrm{S}})}$, $g(\Phi) = \sin(2\phi_{\mathrm{CS}} - \phi_{\mathrm{S}})$. For the definitions of these angles see Fig. 2.11. The parameter p_1 is called the raw asymmetry because the appropriate nuclear polarization value, dilution factor, and depolarization factor must be divided out to isolate the asymmetry (see Sect. 2.5 and 3.1.2). That is, $A_T = p_1/(S_{\mathrm{T}} f D)$, where S_{T} is the magnitude of the target polarization (as a percentage), f is the dilution factor describing the fraction of the target material that can be polarized, and D is the depolarization factor associated with the TSA (Eq. 2.34).

The statistical error of the double ratio can be determined using the fact that each N is sufficiently large so that its error is $\sqrt{N}$. Then the uncertainty of the double ratio becomes

$$\begin{aligned}\sigma_{F_{\mathrm{DR}}} &= F_{\mathrm{DR}}\sqrt{\left(\frac{\sqrt{N_{1+}}}{N_{1+}}\right)^2 + \left(\frac{\sqrt{N_{1-}}}{N_{1-}}\right)^2 + \left(\frac{\sqrt{N_{2+}}}{N_{2+}}\right)^2 + \left(\frac{\sqrt{N_{2-}}}{N_{2-}}\right)^2} \\ &= F_{\mathrm{DR}}\sqrt{\frac{1}{N_{1+}} + \frac{1}{N_{1-}} + \frac{1}{N_{2+}} + \frac{1}{N_{2-}}}.\end{aligned} \tag{4.7}$$

Since, $F_{\mathrm{DR}} - 1 \simeq 0$, Eq. 4.7 can be approximated as

$$\sigma_{F_{\mathrm{DR}}} = \sqrt{\frac{1}{N_{1+}} + \frac{1}{N_{1-}} + \frac{1}{N_{2+}} + \frac{1}{N_{2-}}}. \tag{4.8}$$

The double ratio is plotted in different angular bins with statistical errors determined by Eq. 4.8. Then the points are fit with a function of the form of Eq. 4.6 to extract the appropriate asymmetry. The error of the asymmetry is determined based on the error of the fit parameters.

4.2 Unbinned Maximum Likelihood Method

The 1D double ratio method can be very sensitive to acceptance if the reasonable assumption (Eq. 4.5) is not a valid approximation. In that case, the modulations may be partly due to acceptance effects. Then, the amplitude extracted from the fit does not reflect the true asymmetry size. The Unbinned Maximum

Likelihood (UML) method is a more robust option which is less sensitive to acceptance effects. The UML method is particularly attractive because all asymmetries can be extracted at once, and correlations between the amplitudes can be evaluated. Additionally, higher order components of the DY cross section can easily be included in the calculations if desired.

Consider the general case where $x = \{x_1, x_2, \ldots, x_N\}$ is a set of N independent measurements which obey the normalized probability density function (abbreviated by lowercase 'pdf' to differentiate from the parton distribution function 'PDF') $f(x, \vec{A})$, where $\vec{A}$ is the vector of unknown parameters to be extracted. A likelihood function can be constructed as

$$\mathcal{L}(x, \vec{A}) = \prod_{i=1}^{N} f(x_i, \vec{A}). \tag{4.9}$$

The parameter values $\vec{A}_{\text{best}}$ which maximize $\mathcal{L}(x, \vec{A})$ are the best-fit parameters to the data. For ease of computation, typically the negative natural log of the likelihood function,

$$-\ln \mathcal{L}(x, \vec{A}) = -\sum_{i=1}^{N} \ln f(x_i, \vec{A}), \tag{4.10}$$

is minimized to find the best fit parameters.

For DY data, the appropriate pdfs are based on the DY cross section. For the UML method, some higher-twist terms are used in the fit in addition to the leading order terms from Eq. 2.33 (see Sect. 2.5). The pdfs for each target cell and each polarization are thus

$$\begin{aligned} f(\phi_{\mathrm{S}}, \phi, \theta, \vec{A}) = 1 &+ D_{[\sin(2\theta)]} A_{\mathrm{U}}^{\cos(\phi)} \cos(\phi) + D_{[\sin^2(\theta)]} A_{\mathrm{U}}^{\cos(2\phi)} \cos(2\phi) \\ &\pm |S_{\mathrm{T}}| f \left[A_{\mathrm{T}}^{\sin(\phi_{\mathrm{S}})} \sin(\phi_{\mathrm{S}}) \right. \\ &+ D_{[\sin^2(\theta)]} \left(A_{\mathrm{T}}^{\sin(2\phi+\phi_{\mathrm{S}})} \sin(2\phi + \phi_{\mathrm{S}}) + A_{\mathrm{T}}^{\sin(2\phi-\phi_{\mathrm{S}})} \sin(2\phi - \phi_{\mathrm{S}}) \right) \\ &\left. + D_{[\sin(2\theta)]} \left(A_{\mathrm{T}}^{\sin(\phi+\phi_{\mathrm{S}})} \sin(\phi + \phi_{\mathrm{S}}) + A_{\mathrm{T}}^{\sin(\phi-\phi_{\mathrm{S}})} \sin(\phi - \phi_{\mathrm{S}}) \right) \right], \end{aligned} \tag{4.11}$$

where S_{T} is the target polarization, f is the target dilution factor, and $D_{[f(\theta)]}$ are the depolarization factors defined by Eq. 2.34. There are four different pdfs, one for each target cell configuration. The likelihood function will involve a sum of the four pdfs, each weighted by a constant $C_{j\pm}$ where j is the target cell and $\pm$ is the cell polarization. In total, then, the likelihood function will have 11 unknown parameters: 2 UAs, 5 TSAs, and 4 constants.

The likelihood function needs to be normalized. This is often accomplished by using normalized pdfs. However, in this case the integral $I_{j\pm} = \int f_{j\pm}(x, \vec{A}) \mathrm{d}x$ equals the number of events $N_{j\pm}$ from the appropriate target cell. Therefore, the Extended UML method must be used, where the likelihood function is normalized with a Poissonian distribution term. Now, instead of Eq. 4.9, the likelihood function will be of the form

$$\mathcal{L}(\vec{A}) = \frac{I^N \exp\{-I\}}{N!} \prod_{i=1}^{N} \frac{f(x_i, \vec{A})}{I}, \tag{4.12}$$

where $I = \int f(x, \vec{A})\mathrm{d}x$. The negative log likelihood function becomes

$$-\ln \mathcal{L}(\vec{A}) = \ln(N!) + I - \sum_{i=1}^{N} \ln f(x_i, \vec{A}). \tag{4.13}$$

The term $\ln(N!)$ is a constant which does not depend on $\vec{A}$, so it is irrelevant in the minimization procedure and can be dropped.

Thus the negative log-likelihood function in the DY case, with events from each target cell considered, is

$$\begin{aligned} -\ln \mathcal{L}(\vec{A}) = I_{1+} - \sum_{i=1}^{N_{1+}} \ln C_{1+} f_{1+}(\phi_{\mathrm{S},i}, \phi_i, \theta_i, \vec{A}) + I_{1-} - \sum_{i=1}^{N_{1-}} \ln C_{1-} f_{1-}(\phi_{\mathrm{S},i}, \phi_i, \theta_i, \vec{A}) \\ + I_{2+} - \sum_{i=1}^{N_{2+}} \ln C_{2+} f_{2+}(\phi_{\mathrm{S},i}, \phi_i, \theta_i, \vec{A}) + I_{2-} - \sum_{i=1}^{N_{2-}} \ln C_{2-} f_{2-}(\phi_{\mathrm{S},i}, \phi_i, \theta_i, \vec{A}), \end{aligned} \tag{4.14}$$

where as a reminder $C_{j\pm}$ are the relative normalization constants and $I_{j\pm} = \int C_{j\pm} f_{j\pm}(\phi_{\mathrm{S}}, \phi, \theta)\, \mathrm{d}\phi_{\mathrm{S}}\, \mathrm{d}\phi\, \mathrm{d}\theta$. The integral must be taken over all of phase space. If the phase space has no holes in it, then the integral can easily be calculated analytically and found to be $I_{j\pm} = 8\pi^2 C_{j\pm}$.

A finite data sample can cause biased results. For example, if the number of events from each target cell differs significantly, some terms in the likelihood function may have too much weight compared to others. To correct for this, each term is reweighted by $\bar{N}/N_{j\pm}$, where $\bar{N} = \frac{1}{4}(N_{1+} + N_{1-} + N_{2+} + N_{2-})$ is the average number of events per cell. Applying this reweighting to Eq. 4.14 and plugging in the result for $I_{j\pm}$, the negative log likelihood function to minimize becomes

$$-\ln \mathcal{L}(\vec{A}) = \sum_{(j=1,2)} \sum_{(\mathrm{sign}=+,-)} \frac{\bar{N}}{N_{j,\mathrm{sign}}} \left(I_{j,\mathrm{sign}} - \sum_{i=1}^{N_{j,\mathrm{sign}}} \ln C_{j,\mathrm{sign}} f_{j,\mathrm{sign}}(\phi_{\mathrm{S},i}, \phi_i, \theta_i, \vec{A}) \right). \tag{4.15}$$

When calculating the negative log likelihood function in Eq. 4.15, the dilution factor and depolarization factors in Eq. 4.11 are considered on an event-by-event basis. This is so that each event is weighted based on the confidence that the polarization of the target is actually affecting the trajectory of the outgoing particles. The more diluted the target polarization is, the less the angular dependence of that event should influence the construction of the likelihood function. The polarization is not considered event-by event. Rather, the average polarization of all the included events is calculated and divided out of the TSAs after the minimization has been performed. Therefore, this method is referred to as the fD-weighted Extended Unbinned Maximum Likelihood (EWUML) method by the COMPASS collaboration, where f refers to dilution factor and D to depolarization factor.

4.3 Left-Right Asymmetry Extraction Method

The left-right asymmetry A_{N} is also related to the Sivers TMD. A basic definition for a left-right asymmetry is:

$$A_{\ell\mathrm{r}} = \frac{1}{|S_{\mathrm{T}}|fD}\frac{\sigma_{\ell} - \sigma_{\mathrm{r}}}{\sigma_{\ell} + \sigma_{\mathrm{r}}}, \tag{4.16}$$

where S_{T} is the target polarization, f is the dilution factor, D is the depolarization factor, σ is the cross-section of events, ℓ indicates left and r indicates right. At COMPASS, "left" and "right" are defined in the target rest frame (see Fig. 2.11a) as

$$\begin{aligned} \text{Left} : \hat{q_{\mathrm{T}}} \cdot \left(\hat{S_{\mathrm{T}}} \times \hat{P}_{\pi}\right) > 0 \Rightarrow 0 < \phi_{\mathrm{S}} < \pi \\ \text{Right} : \hat{q_{\mathrm{T}}} \cdot \left(\hat{S_{\mathrm{T}}} \times \hat{P}_{\pi}\right) < 0 \Rightarrow -\pi < \phi_{\mathrm{S}} < 0, \end{aligned} \tag{4.17}$$

where $\hat{S}_{\mathrm{T}}$ is the target polarization vector, $\hat{P}_{\pi}$ is the pion momentum vector, and $\hat{q}_{\mathrm{T}}$ is the virtual photon transverse momentum vector. The left-right asymmetry in Eq. 4.16 is related to the amplitudes of all of the $\sin(n\phi_{\mathrm{S}})$ modulations in the DY cross-section for odd values of n. Assuming the only sizeable amplitude is the physical $\sin(\phi_{\mathrm{S}})$ amplitude, the DY differential cross-section can be approximated to be

$$\frac{\mathrm{d}\sigma}{\mathrm{d}^4q\mathrm{d}\phi_{\mathrm{S}}} \propto \hat{\sigma}_{\mathrm{U}}\left(1 + |S_{\mathrm{T}}|fDA_{\mathrm{N}}\sin(\phi_{\mathrm{S}})\right) \tag{4.18}$$

after integrating over all other angular modulations. The depolarization factor should then be the one associated with the $\sin(\phi_{\mathrm{S}})$ amplitude in the DY cross-section (Eq. 2.33): $D = (1+\cos^2(\theta))/(1+A_U^1\cos^2(\theta))$. Plugging Eq. 4.18 into Eq. 4.16 gives

$$\begin{aligned} A_{\ell\mathrm{r}} &= \frac{1}{|S_{\mathrm{T}}|fD}\frac{\int_0^{\pi}\frac{\mathrm{d}\sigma}{\mathrm{d}^4q\mathrm{d}\phi_{\mathrm{S}}}\,\mathrm{d}\phi_{\mathrm{S}} - \int_{-\pi}^{0}\frac{\mathrm{d}\sigma}{\mathrm{d}^4q\mathrm{d}\phi_{\mathrm{S}}}\,\mathrm{d}\phi_{\mathrm{S}}}{\int_0^{\pi}\frac{\mathrm{d}\sigma}{\mathrm{d}^4q\mathrm{d}\phi_{\mathrm{S}}}\,\mathrm{d}\phi_{\mathrm{S}} + \int_{-\pi}^{0}\frac{\mathrm{d}\sigma}{\mathrm{d}^4q\mathrm{d}\phi_{\mathrm{S}}}\,\mathrm{d}\phi_{\mathrm{S}}} \\ &= \frac{1}{|S_{\mathrm{T}}|fD}\frac{\left(\phi_{\mathrm{S}} - |S_{\mathrm{T}}|fDA_{\mathrm{N}}\cos(\phi_{\mathrm{S}})\right)\Big|_0^{\pi} - \left(\phi_{\mathrm{S}} - |S_{\mathrm{T}}|fDA_{\mathrm{N}}\cos(\phi_{\mathrm{S}})\right)\Big|_{-\pi}^{0}}{\left(\phi_{\mathrm{S}} - |S_{\mathrm{T}}|fDA_{\mathrm{N}}\cos(\phi_{\mathrm{S}})\right)\Big|_0^{\pi} + \left(\phi_{\mathrm{S}} - |S_{\mathrm{T}}|fDA_{\mathrm{N}}\cos(\phi_{\mathrm{S}})\right)\Big|_{-\pi}^{0}} \\ &= \frac{2A_{\mathrm{N}}}{\pi}. \end{aligned} \tag{4.19}$$

So, the basic left-right asymmetry definition should be scaled by $\pi/2$ when defining A_{N}.

The simplest way to extract a left-right asymmetry from data is to use the definition

$$A_{\mathrm{N}} = \frac{\pi}{2}\frac{1}{|S_{\mathrm{T}}|fD}\frac{N_{\ell} - N_{\mathrm{r}}}{N_{\ell} + N_{\mathrm{r}}}, \tag{4.20}$$

where $N_{\ell} = \int_0^{\pi} N(\phi_{\mathrm{S}})\,\mathrm{d}\phi_{\mathrm{S}}$ is the number of left events and $N_{\mathrm{r}} = \int_{-\pi}^{0} N(\phi_{\mathrm{S}})\,\mathrm{d}\phi_{\mathrm{S}}$ is the number of right events. As before, S_{T} is the magnitude of the target polarization, f is the target dilution factor, and D is depolarization factor. The definition of counts in Eq. 4.1 can be simplified to be the product of luminosity L, acceptance $a(\Phi)$, and cross-section $\sigma(\Phi)$,

$$N(\Phi) = L \times a(\Phi) \times \sigma(\Phi), \tag{4.21}$$

where luminosity is the ratio of the measured event rate and the cross-section. This means that the basic left-right asymmetry definition in Eq. 4.20 is dependent on spectrometer acceptance. To isolate the physics information, it is important to define A_{N} in a way that cancels the acceptance dependence as much as possible.

The geometric mean definition of the left-right asymmetry minimizes acceptance effects. The left-right geometric mean asymmetry for events from a single target cell is defined as

$$A_{\mathrm{N,geo}} = \frac{\pi}{2}\frac{1}{|S_{\mathrm{T}}|fD}\frac{\sqrt{N_{\ell}^{+}N_{\ell}^{-}} - \sqrt{N_{\mathrm{r}}^{+}N_{\mathrm{r}}^{-}}}{\sqrt{N_{\ell}^{+}N_{\ell}^{-}} + \sqrt{N_{\mathrm{r}}^{+}N_{\mathrm{r}}^{-}}}, \tag{4.22}$$

where as before the $\pm$ superscripts refer to the target polarization sign. Taking the definition of the number of events from Eq. 4.21, we can rewrite this as

$$\begin{aligned} A_{\mathrm{N,geo}} &= \frac{\pi}{2}\frac{1}{|S_{\mathrm{T}}|fD}\frac{\sqrt{(L^{+}a_{\mathrm{J}}^{+}\sigma_{\ell})(L^{-}a_{\mathrm{S}}^{-}\sigma_{\ell})} - \sqrt{(L^{+}a_{\mathrm{S}}^{+}\sigma_{\mathrm{r}})(L^{-}a_{\mathrm{J}}^{-}\sigma_{\mathrm{r}})}}{\sqrt{(L^{+}a_{\mathrm{J}}^{+}\sigma_{\ell})(L^{-}a_{\mathrm{S}}^{-}\sigma_{\ell})} + \sqrt{(L^{+}a_{\mathrm{S}}^{+}\sigma_{\mathrm{r}})(L^{-}a_{\mathrm{J}}^{-}\sigma_{\mathrm{r}})}} \\ &= \frac{\pi}{2}\frac{1}{|S_{\mathrm{T}}|fD}\frac{\kappa\sigma_{\ell} - \sigma_{\mathrm{r}}}{\kappa\sigma_{\ell} + \sigma_{\mathrm{r}}}, \end{aligned} \tag{4.23}$$

with

$$\kappa = \frac{\sqrt{a_J^{+}a_S^{-}}}{\sqrt{a_S^{+}a_J^{-}}}, \tag{4.24}$$

where the subscript J refers to the Jura side of the spectrometer, and S refers to the Saleve side of the spectrometer. As a reminder, 'Jura' and 'Saleve' refer to the absolute left and right sides of the COMPASS spectrometer when standing at the target and looking downstream. Just as the reasonable assumption

(Eq. 4.5) was made in the 1D double ratio method, it is reasonable to assume that $\kappa \sim 1$. False asymmetries can be used to check the confidence of this assumption and quantify a systematic uncertainty if needed.

The two-target geometric mean definition of the left-right asymmetry is even less sensitive to acceptance effects. This asymmetry considers events from both target cells:

$$A_{\mathrm{N,2T}} = \frac{\pi}{2}\frac{1}{|S_{\mathrm{T}}|fD}\frac{\sqrt[4]{N_\ell^{1+}N_\ell^{1-}N_\ell^{2+}N_\ell^{2-}} - \sqrt[4]{N_{\mathrm{r}}^{1+}N_{\mathrm{r}}^{1-}N_{\mathrm{r}}^{2+}N_{\mathrm{r}}^{2-}}}{\sqrt[4]{N_\ell^{1+}N_\ell^{1-}N_\ell^{2+}N_\ell^{2-}} + \sqrt[4]{N_{\mathrm{r}}^{1+}N_{\mathrm{r}}^{1-}N_{\mathrm{r}}^{2+}N_{\mathrm{r}}^{2-}}}. \tag{4.25}$$

Using the same method as the single-target geometric mean, this can be rewritten as

$$A_{\mathrm{N,2T}} = \frac{\pi}{2}\frac{1}{|S_{\mathrm{T}}|fD}\frac{\kappa_{2\mathrm{T}}\sigma_\ell - \sigma_{\mathrm{r}}}{\kappa_{2\mathrm{T}}\sigma_\ell + \sigma_{\mathrm{r}}} \tag{4.26}$$

with

$$\kappa_{2\mathrm{T}} = \frac{\sqrt[4]{a_{\mathrm{J}}^{1+}a_{\mathrm{S}}^{1-}a_{\mathrm{J}}^{2+}a_{\mathrm{S}}^{2-}}}{\sqrt[4]{a_{\mathrm{S}}^{1+}a_{\mathrm{J}}^{1-}a_{\mathrm{S}}^{2+}a_{\mathrm{J}}^{2-}}} = \sqrt[4]{\frac{a_{\mathrm{J}}^{1+}a_{\mathrm{S}}^{2-}}{a_{\mathrm{S}}^{1+}a_{\mathrm{J}}^{2-}}}\sqrt[4]{\frac{a_{\mathrm{S}}^{1-}a_{\mathrm{J}}^{2+}}{a_{\mathrm{J}}^{1-}a_{\mathrm{S}}^{2+}}}. \tag{4.27}$$

This ratio $\kappa_{2\mathrm{T}}$ is even more stable than the single-target ratio, as can be seen when the terms from each data-taking subperiod are separated like in Eq. 4.27. The acceptance ratio from the first subperiod is reciprocal to the ratio from the second subperiod, so most acceptance effects should cancel out. The statistical error of $A_{\mathrm{N,2T}}$ is

$$\begin{aligned} \delta A_{\mathrm{N,2T}} = \frac{\pi}{2}\frac{1}{2|S_{\mathrm{T}}|fD} & \frac{\sqrt[4]{N_\ell^{1+}N_\ell^{1-}N_\ell^{2+}N_\ell^{2-}N_{\mathrm{r}}^{1+}N_{\mathrm{r}}^{1-}N_{\mathrm{r}}^{2+}N_{\mathrm{r}}^{2-}}}{\left(\sqrt[4]{N_\ell^{1+}N_\ell^{1-}N_\ell^{2+}N_\ell^{2-}} + \sqrt[4]{N_{\mathrm{r}}^{1+}N_{\mathrm{r}}^{1-}N_{\mathrm{r}}^{2+}N_{\mathrm{r}}^{2-}}\right)^2} \\ & \times \sqrt{\frac{1}{N_\ell^{1+}} + \frac{1}{N_\ell^{1-}} + \frac{1}{N_\ell^{2+}} + \frac{1}{N_\ell^{2-}} + \frac{1}{N_{\mathrm{r}}^{1+}} + \frac{1}{N_{\mathrm{r}}^{1-}} + \frac{1}{N_{\mathrm{r}}^{2+}} + \frac{1}{N_{\mathrm{r}}^{2-}}}. \end{aligned} \tag{4.28}$$

The two-target geometric mean method (Eqs. 4.25-4.28) will be used to extract A_{N} in this analysis.

Chapter 5

High Mass Drell-Yan Transverse Spin Asymmetries

This chapter will present the COMPASS Drell-Yan TSA results extracted using the methods described in Chapter 4. Sect. 5.1 will describe the event selection process used to select DY dimuon events from the data. Sect. 5.2 will present the DY results for TSAs related to the Sivers, pretzelosity, and transversity TMDs, extracted using the 1D double ratio and EWUML methods. Additionally, the results for the left-right asymmetry A_{N} will be shown. Sect. 5.3 will describe the systematic studies performed on the data and quantify systematic uncertainties. Then the final TSA results will be presented with their total uncertainties. Finally, Sect. 5.4 will put these new COMPASS results in the context of the other experimental results discussed in Sect. 2.6.

5.1 Data Selection

The signature of a DY event in COMPASS data is a dimuon. In order to identify physical DY candidates, a multi-step event selection must be performed. The standard event selection steps that were used in the previous COMPASS publication of DY TSAs [64] are as follows:

1. The event contains two oppositely-charged tracks coming from the 'best' primary vertex. A primary vertex has an associated beam track (Sect. 3.3), and the 'best' is either chosen by CORAL algorithms or is the vertex with the lowest χ^2. Both particle tracks must cross at least 30 radiation lengths after the hadron absorber (Sect. 3.1.3) to ensure the particles are muons, not hadrons or electrons.

2. A dimuon trigger was fired when the event occurred. In particular, either the LASTxLAST or LASTxOT. The LASTxMT is used as a veto to reject beam decay muons. The trigger system was

discussed in Sect. 3.1.4.

3. The first measured point of each track is before 300 cm, and so upstream of the first spectrometer magnet SM1. The last measured point is after 1500 cm, and so downstream of the first muon wall.

4. The time of each muon track is defined.

5. The muon track times must be separated by less than 5 ns to ensure they are correlated.

6. The track fit has a reduced $\tilde{\chi}^2 < 10$.

7. The tracks pass through the hodoscopes of the dimuon trigger that was fired. This is to ensure the trigger was not activated by some other particle.

8. The event comes from a 'good spill', meaning the detector and beam behavior was stable when the event was recorded.

9. The Bjorken-x variables are within the physical ranges of $0 < x_{\rm N}, x_\pi < 1$ and $-1 < x_{\rm F} = x_\pi - x_{\rm N} < 1$.

10. The transverse momentum $q_{\rm T}$ of the virtual photon satisfies $0.4\ {\rm GeV}/c < q_{\rm T} < 5.0\ {\rm GeV}/c$. This ensures that the angular resolution is sufficient and that the TMD interpretation can be applied to the data (see Sect. 2.5).

11. The z-coordinate of the vertex lies within one of the NH_3 target cells. In 2015, the limits of the target cells were -294.5 cm $< z_{\rm vtx} < -239.3$ cm and -219.5 cm $< z_{\rm vtx} < -164.3$ cm. In 2018, the limits were -294.5 cm $< z_{\rm vtx} < -239.4$ cm and -219.1 cm $< z_{\rm vtx} < -163.9$ cm. The target was described in detail in Sect. 3.1.2.

12. The radial position of the vertex is within the target cell radius. In the past the cut $r < 1.9$ cm was made to ensure the event is well within the 2 cm radii of the target cells. However, it was found that in 2015, the target was off center, so the radial cut was reduced to $r < 1.8$ cm to ensure no events were kept where the beam scattered off the target holder rather than the ammonia. In 2018, the cut $r < 1.9$ cm was kept.

These 12 cuts were applied to the data. There were also several additional cuts that were added in this analysis:

13. Ensure the beam passed entirely through both target cells. This is verified by ensuring the radial location of the track is within the radius from Step 12 at the most upstream limit of the first target cell (-294.5 cm in both 2015 and 2018) and the most downstream limit of the second target cell (-164.3

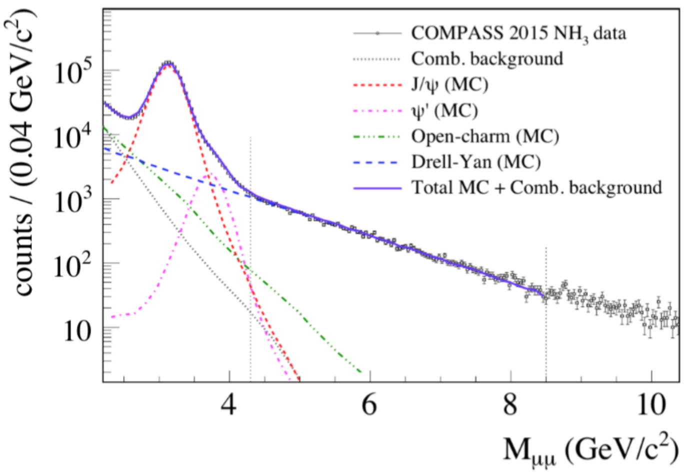

Figure 5.1: Dimuon invariant mass distribution in 2015 data after event selection. The vertical dashed lines indicate the 'high mass' range selected for DY analysis. From [64].

cm in 2015, -163.9 cm in 2018). The purpose of this cut is to equalize the flux of events from each target cell, to help eliminate bias in the asymmetry extraction.

14. Remove low momentum muon tracks by requiring $p_{\mu_\pm} < 7$ GeV/c. This is implemented to be consistent with the DY spin-independent asymmetry analysis performed by other COMPASS members. Monte-Carlo (MC) is used in the extraction of spin-independent asymmetries, and the MC/real data agreement is much worse for tracks with very low momentum.

15. Require $p_{\mu_+} + p_{\mu_-} < 180$ GeV/c in order to further minimize background from beam decay muons.

16. Lower the track reduced $\tilde{\chi}^2$ cut to $\tilde{\chi}^2 < 3.2$. This cut was found to reduce period dependence in 2018 (see Sect. 5.3.7 for more details). Many studies were performed, and the cut $\tilde{\chi}^2 < 3.2$ was chosen to minimize the loss of statistics while significantly reducing period dependence.

After performing the selection cuts, the selected dimuon events are plotted as a function of dimuon invariant mass. The resulting distribution from the published 2015 data is shown in Fig. 5.1. The processes producing the dimuons in each mass region, as reconstructed from Monte-Carlo (MC), are also shown. In addition to true DY events, there are events produced by the decay of J/ψ mesons, ψ' mesons, and so called 'open-charm' mesons, which are pairs of mesons produced from the decay of weakly-bound charmonium. Further, there is a combinatorial background made of oppositely-charged muon pairs that do not come from a common physics event but pass all the event selection cuts. The combinatorial background is estimated from experimental data by applying the above event selection to pairs of muons with the same electrical charge, since same-sign muon pairs do not come from a common physics events.

Cuts	2015 Events		2018 Events	
Dimuon, Best Primary Vertex, $4.3\ \mathrm{GeV}/c < M < 8.5\ \mathrm{GeV}/c$	1164945	100%	1427058	100%
Dimuon trigger fired (LAS-LAST or LAS-OT)	851491	73.1%	933602	65.4%
$z_{\mathrm{first}} < 300$ cm, $z_{\mathrm{last}} > 1500$ cm	838472	72.0%	919823	64.5%
Time defined	828797	71.1%	912876	64.0%
$\Delta t < 5$ ns	467287	40.1%	498956	35.0%
Track $\tilde{\chi}^2 < 10$	463697	39.8%	494650	34.7%
Trigger validation	180373	15.5%	202325	14.2%
Physical x_{N}, x_{π}, x_{F}	180245	13.5%	202119	14.2%
$0.4\ \mathrm{GeV}/c < q_{\mathrm{T}} < 5.0\ \mathrm{GeV}/c$	162210	12.1%	182201	12.8%
z_{vtx} inside NH_3 target cells	47684	3.6%	50762	3.6%
r_{vtx} cut	46058	3.5%	48033	3.4%
Beam through both NH_3 cells	45654	3.5%	47415	3.3%
$p_{\mu_{\pm}} > 7\ \mathrm{GeV}/c$	45594	3.5%	47354	3.3%
$p_{\mu_+} + p_{\mu_-} < 180\ \mathrm{GeV}/c$	40138	3.4%	46996	3.3%
Track $\tilde{\chi}^2 < 3.2$	40111	3.4%	40728	2.9%
Good spill	34729	3.0%	36869	2.6%

Table 5.1: High mass DY event selection on the 2015 and 2018 COMPASS data samples. (Note that P00 of 2018 is not included.)

It is important to isolate DY events from the rest of the background processes in order to perform the analysis on a true DY sample. The region between 4.3 GeV/c and 8.5 GeV/c minimizes background levels while maximizing statistics. Therefore, this region, referred to by COMPASS as the 'high mass' region, is selected for the DY analysis. It is depicted in Fig. 5.1 with vertical dashed lines. Studies on the background levels in different mass regions will be presented in Sect. 5.3.1. The numbers of high mass DY events after each event selection cut in the 2015 and 2018 data samples are shown in Table 5.1 (in a slightly shuffled order from how they were presented in the text). Note that all 9 periods of 2015 are included, but only 8 of the 9 periods of 2018 are included. The first period of 2018, referred to as P00, was removed from the analysis because the beam conditions were significantly different. Some important 1D and 2D kinematic distributions for the total selected high mass DY data sample are shown in Figs. 5.2 and 5.3.

5.2 Results

The 1D double ratio, EWUML, and A_{N} methods were applied to the high mass DY events that survived the event selection cuts. When extracting the DY asymmetries, A_U^1 is set equal to the leading twist value of 1 when defining the depolarization factors. The impact on the results of changing the value of A_U^1 will be quantified as a systematic uncertainty. The asymmetries are calculated for each period, then a weighted average over all periods is taken. The asymmetry results are presented in this section with their statistical uncertainties only. The sources and sizes of systematic uncertainties will be presented in Sect. 5.3.

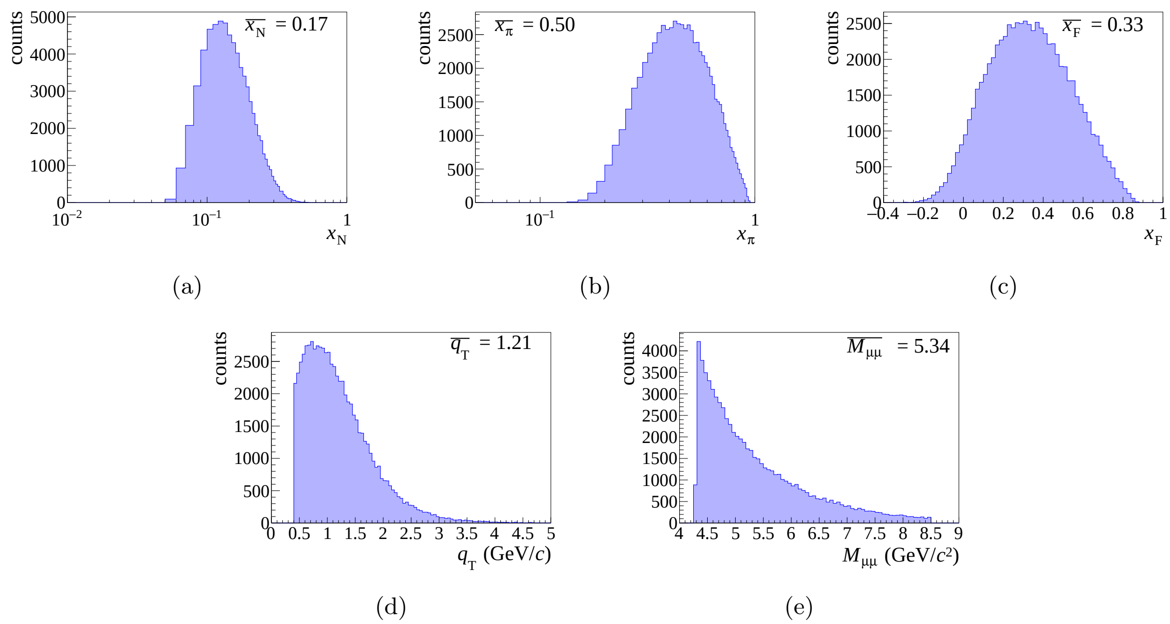

Figure 5.2: One-dimensional distributions of (a) x_{N}, (b) x_{π}, (c) x_{F}, (d) q_{T}, and (e) $M_{\mu\mu}$ for the selected COMPASS high mass DY data sample. Both 2015 and 2018 data are included. The mean kinematic values are printed on the plots.

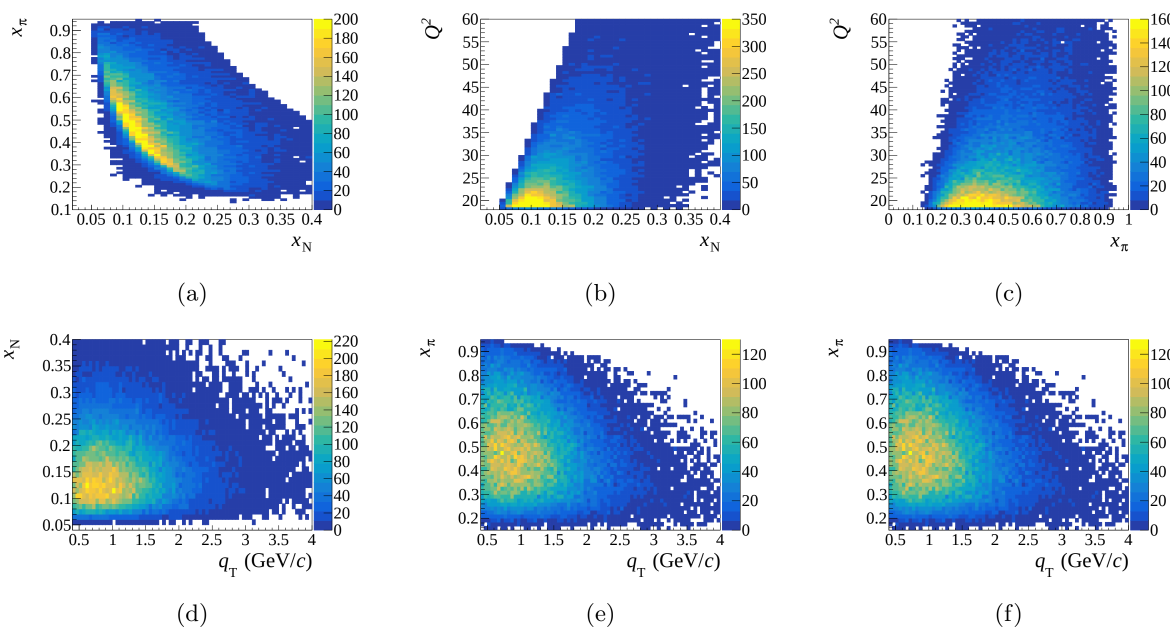

Figure 5.3: Two-dimensional distributions showing the correlations of (a) x_{N} and x_{π}, (b) x_{N} and $Q^2 = M_{\mu\mu}^2$, (c) x_{π} and Q^2, (d) q_{T} and x_{N}, (e) q_{T} and x_{π}, and (f) q_{T} and x_{F} for the selected COMPASS high mass DY data sample. Both 2015 and 2018 data are included.

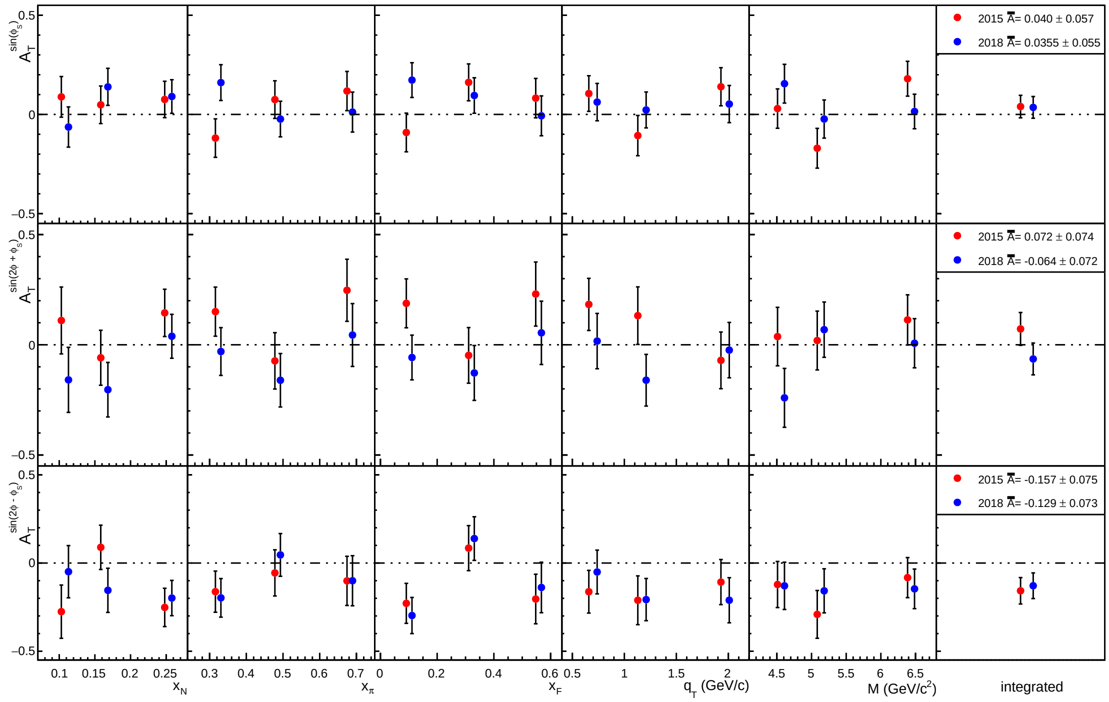

Figure 5.4: 1D Double Ratio TSA results from 2015 (red) and 2018 (blue) high mass DY events, binned in different kinematic variables and also extracted over the entire kinematic range. The first row is the Sivers TSA, the second is pretzelosity, and the third is transversity.

5.2.1 Standard TSA Results

The TSA amplitudes related to the Sivers, pretzelosity, and transversity TMDs were extracted using the 1D double ratio and the EWUML methods. The 1D results for each year are shown in Fig. 5.4, and the EWUML results are shown in Fig. 5.5. The average of the 2015 and 2018 results is shown for both methods in Fig. 5.6. The two methods give statistically compatible results. Because the EWUML method is in general more robust and reliable, the EWUML results alone will be shown from now on. Also, from now on the TSAs will simply be referred to by the TMD they are related to (e.g. Sivers TSA).

5.2.2 $A_{\rm N}$ Results

The results for $A_{\rm N}$, extracted using the two-target geometric mean left-right asymmetry formulation, are shown for each year in Fig. 5.7. In Fig. 5.8, the overall average $A_{\rm N}$ results are shown alongside the Sivers TSA $A_{\rm T}^{\sin(\phi_{\rm S})}$ results from the EWUML method. The results are not identical, especially when considering the fact that the input data is fully correlated. The difference between the two values may be influenced by the fact that $A_{\rm N}$ includes contributions from all $\sin(n\phi_{\rm S})$ amplitudes with odd n. This will be discussed further in Sect. 5.3.6.

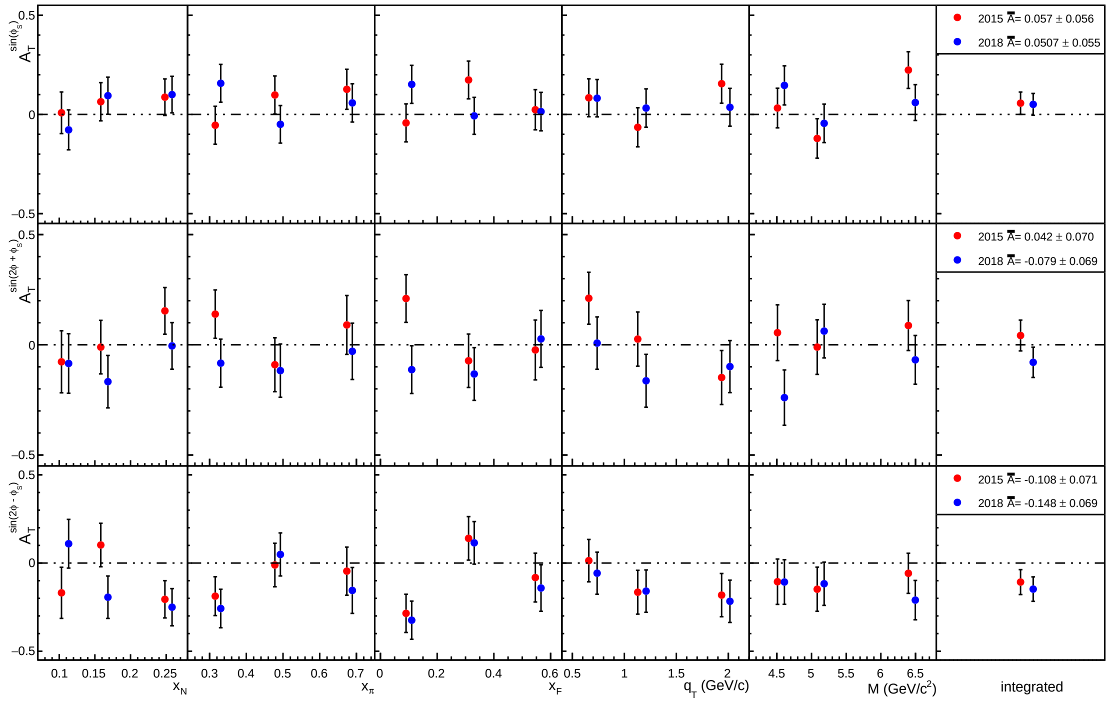

Figure 5.5: EWUML TSA results from 2015 and 2018 high mass DY events. Otherwise like Fig. 5.4.

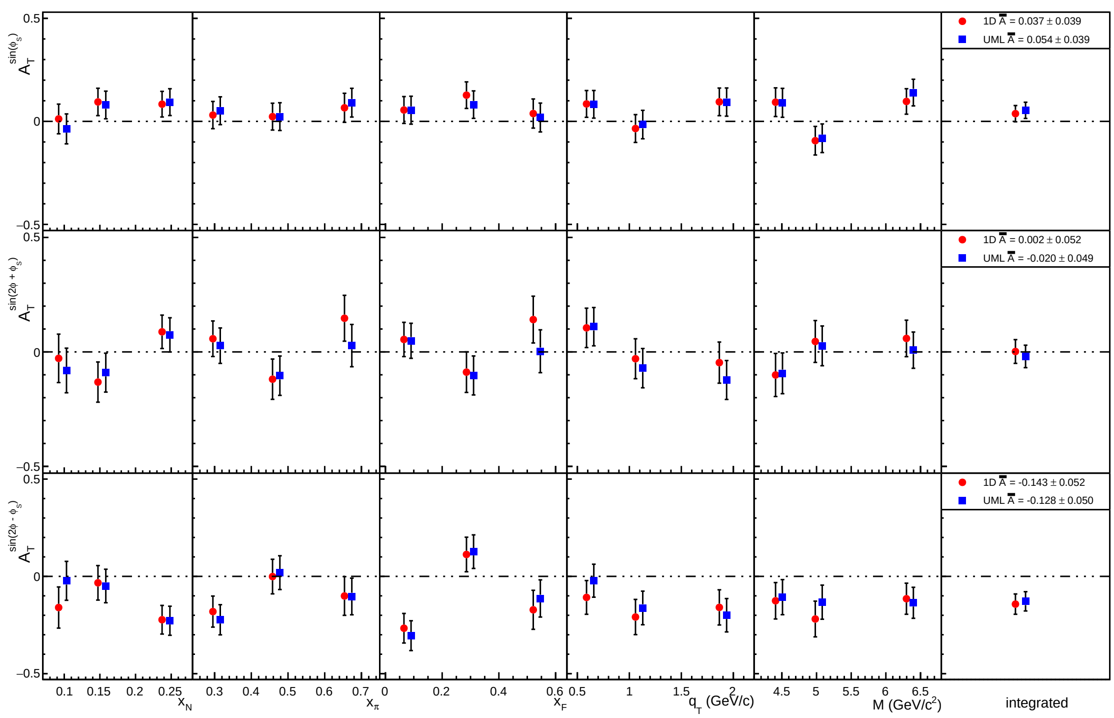

Figure 5.6: The average of the 2015 and 2018 high mass DY TSAs from both the 1D double ratio (red circle) and EWUML (blue square) methods. Otherwise like Fig. 5.4.

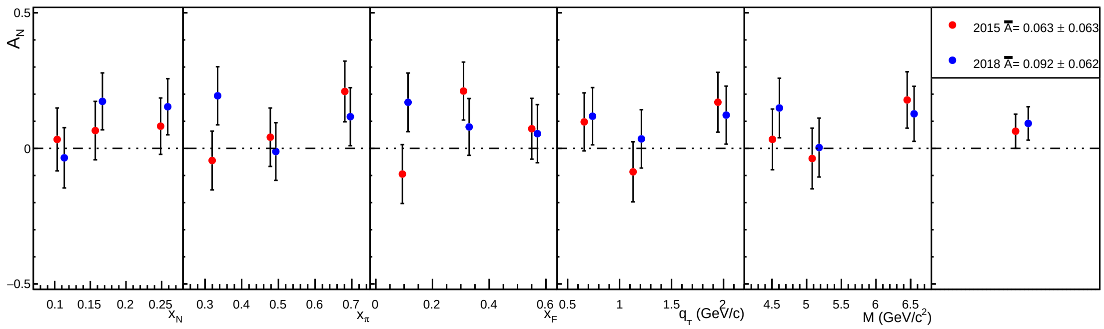

Figure 5.7: A_{N} results from 2015 (red) and 2018 (blue) high mass DY data samples, binned in different kinematic variables and also averaged over all kinematic bins.

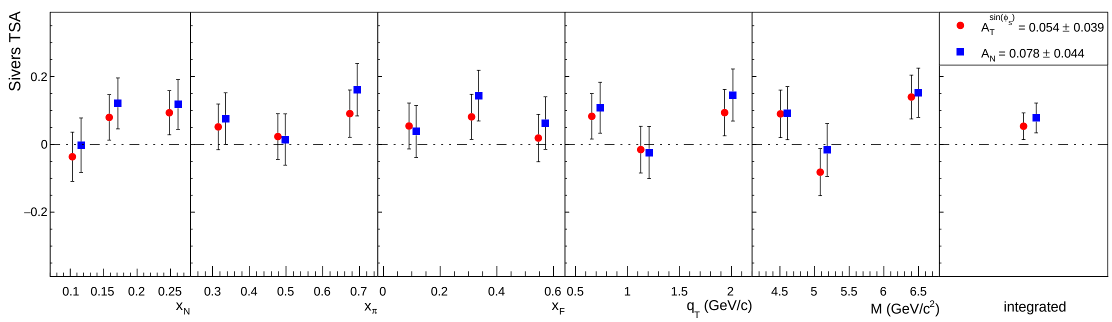

Figure 5.8: Average high mass DY A_{N} (blue square) and $A_{\mathrm{T}}^{\sin(\phi_{\mathrm{S}})}$ (red circle) results, binned in different kinematic variables and also averaged over all kinematic bins.

5.3 Systematic Studies

Various systematic studies are performed to better understand the data and test the robustness of the analysis results. Some of these studies reveal that other factors could be diluting or enhancing the TSA results, and thus a systematic uncertainty needs to be reported. This section will describe these sources of systematic uncertainty and report them as a fraction of the statistical uncertainty. Some studies do not add to the uncertainty but contribute to other areas of the analysis, for example determining event selection cuts. The first two sections will describe these types of studies.

5.3.1 Background Contamination

It is assumed when extracting the TSAs that all the 'high mass' events remaining after the selection described in Sect. 5.1 are true DY events. It is important to be aware of how much background contamination there is in the high mass range (4.3 to 8.5 GeV/c^2) in order to ensure that this assumption is reasonable. The ideal way to calculate background levels is with Monte-Carlo simulations. However, the most up-to-date COMPASS

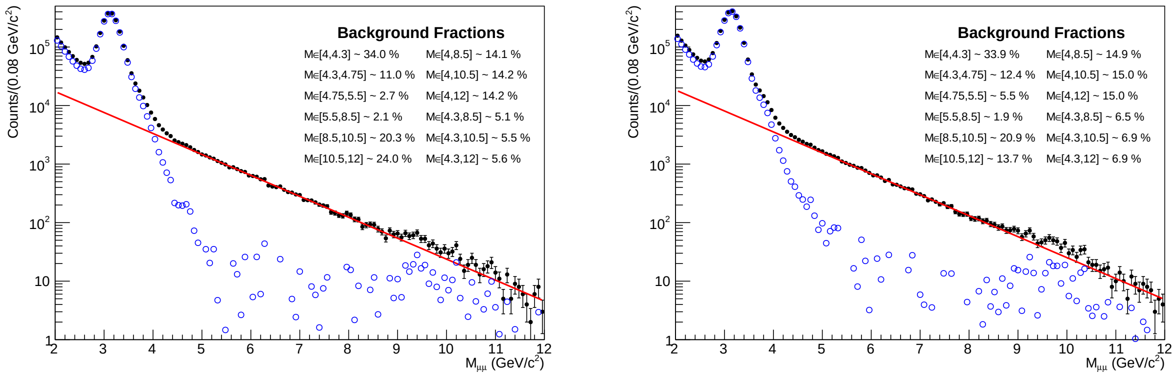

(a) (b)

Figure 5.9: Background contamination in different dimuon invariant mass ranges in (a) 2015 and (b) 2018 data. The black points are the data, the red is the exponential fit based on data between 5.5 and 8.5 GeV/c^2, and the blue is the background estimated by subtracting the fit from the data. Background percentages in different mass ranges are printed on the plots.

DY MC simulations do not currently describe all of the data well. For this reason, the background will be estimated by looking only at real data. It is known that the DY cross section is well modeled by an exponential decay curve [117]. Therefore, the high mass region of the real data invariant mass distribution will be fit with an exponential curve. This curve will be subtracted from the data to estimate the amount of background.

Figs. 5.9 shows the invariant mass distributions and background estimations for 2015 and 2018 data. The exponential is fit using data between 5.5 and 8.5 GeV/c^2, where based on Fig. 5.1 the DY process should be most pure, then extrapolated through the rest of the mass range. The background levels in different regions are printed on the figures. In particular, the percent background in the range 4.3 to 8.5 GeV/c^2 is approximately 5% in 2015 and 7% in 2018. This range gives the best balance of maximizing statistics while minimizing background contamination. The background levels are not high enough to significantly impact the TSA extraction, especially in comparison to other systematic effects that will be described below.

5.3.2 Target Cell Event Migration

When calculating TSAs, we need to separate events originating in the two different NH_3 target cells with opposite polarizations. Events are separated based on the reconstructed vertex location. However, the finite resolution of vertex reconstruction means that some vertices are reconstructed in the wrong target cell or outside both target cells. This migration between target cells due to incorrect reconstruction contributes an additional dilution factor, which is included directly in the TSA extraction formulas in Chapter 4. Using a Monte-Carlo sample, the generated and reconstructed vertex locations of high mass DY events can be

Kinematic Bin		DY Mixing Factors	
		Upstream	Downstream
x_{N}	[0.00, 0.13)	0.95	0.89
	[0.13, 0.19)	0.95	0.94
	[0.19, 1.00]	0.96	0.96
x_{π}	[0.00, 0.40)	0.95	0.94
	[0.40, 0.56)	0.95	0.93
	[0.56, 1.00]	0.96	0.91
x_{F}	[-1.0, 0.21)	0.95	0.95
	[0.21, 0.41)	0.96	0.94
	[0.41, 1.00]	0.95	0.90
q_{T}	[0.50, 0.90)	0.95	0.92
	[0.90, 1.40)	0.96	0.93
	[1.40, 5.00]	0.95	0.94
$M_{\mu\mu}$	[4.30, 4.75)	0.95	0.91
	[4.75, 5.50)	0.96	0.93
	[5.50, 8.50]	0.95	0.95

Table 5.2: Additional dilution factors due to cell-to-cell event migration in high mass DY data.

compared to estimate the size of the additional dilution factor.

The event migration seen in 2018 MC is shown in Fig. 5.10. The figure shows the fraction of reconstructed events generated in the correct target cell, the incorrect target cell, or outside or between the target cells. The overall distribution as well as the distributions in each kinematic bin are shown. The new dilution factor is determined bin by bin and is calculated to be the fraction of events reconstructed in the incorrect cell subtracted from the fraction of events reconstructed in the correct cell. In other words

$$d_{\mathrm{up(down)}} = f_{\mathrm{up(down)}} - f_{\mathrm{down(up)}}, \tag{5.1}$$

where $d_{\mathrm{up(down)}}$ is the new dilution factor in the upstream (downstream) target cell, and $f_{\mathrm{up(down)}}$ is the fraction of reconstructed events generated in the respective target cell.

In order for the dilution factors calculated from Fig. 5.10 to be trustworthy, the z-vertex distributions must agree reasonably well between MC and real data. In the high mass range the agreement is acceptable, as can be seen in Fig. 5.11. There is no up-to-date 2015 MC sample available at the time this thesis was written, but the z-vertex distribution in the 2015 data matches the 2018 MC distribution reasonably well as shown in Fig. 5.12. Because of the consistency between the two years and the fact that the MC is based on 2018, the dilution factors determined using 2018 real data were used for both 2015 and 2018 TSA extraction. These dilution factors due to target cell mixing are shown by bin in Table 5.2.

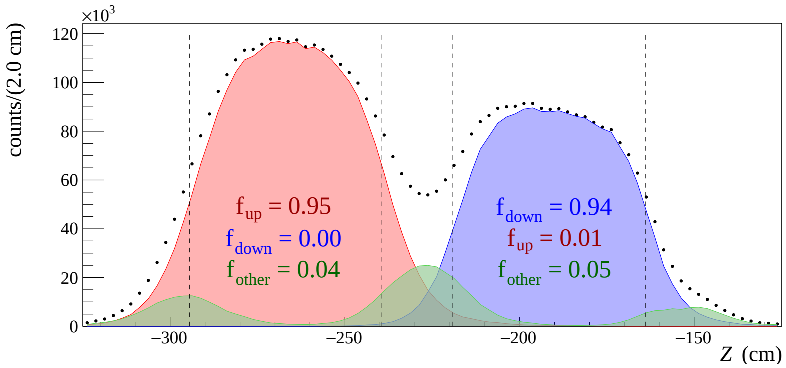

(a)

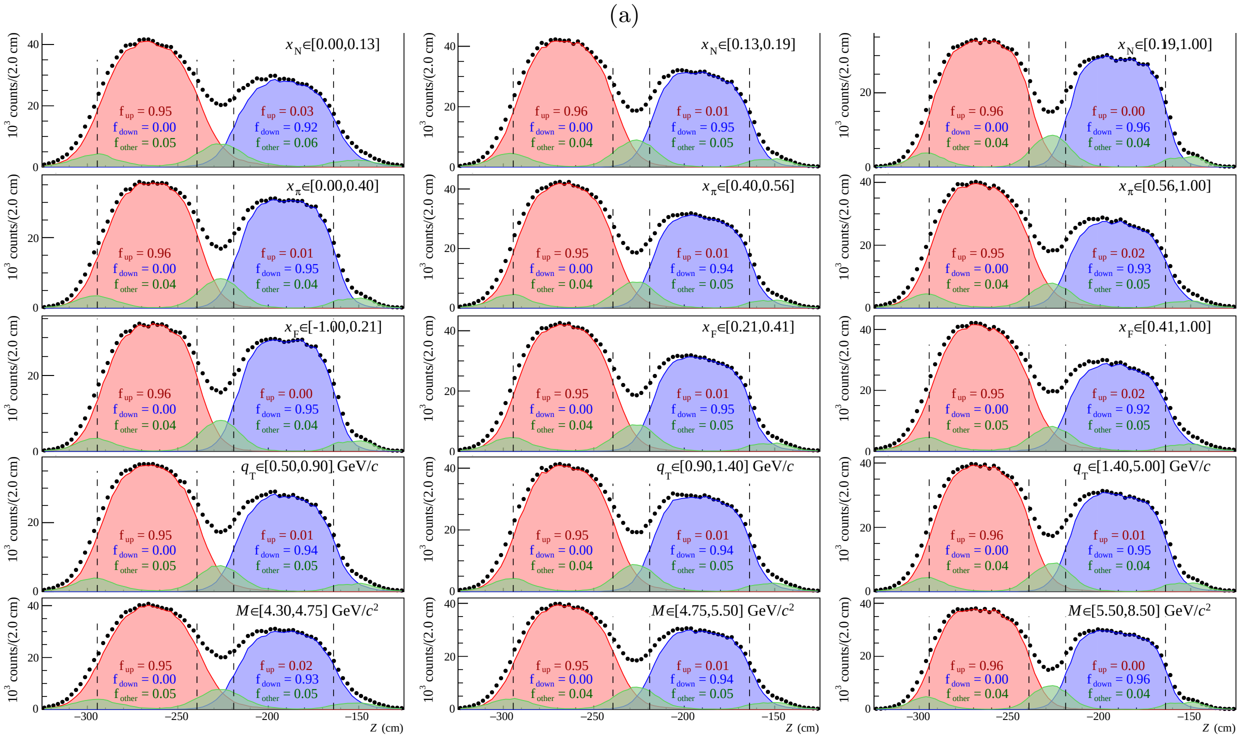

(b)

Figure 5.10: Target cell event migration in the high mass range 2018 MC sample, (a) overall and (b) binned in kinematic variables. The vertical dashed lines indicate the borders of the NH_3 target cells. Four z-vertex distributions are shown: reconstructed (black), generated in the upstream cell (red), generated in the downstream cell (blue), and generated outside or between the two cells (green). The fractions f written on the plots quantify the percentage of reconstructed events generated in each region. Where the f values do not add to one, it is due to rounding.

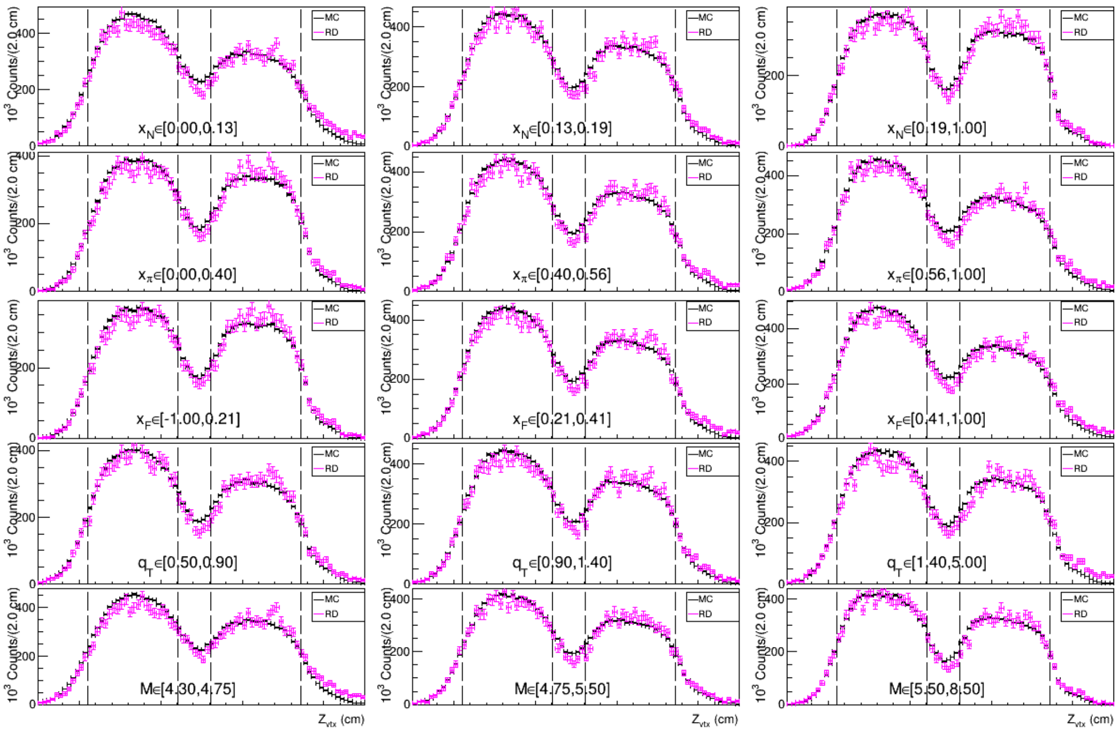

Figure 5.11: Comparison of the 2018 MC (black) and 2018 real data (magenta) z-vertex distributions in the high mass DY range, in different kinematic bins.

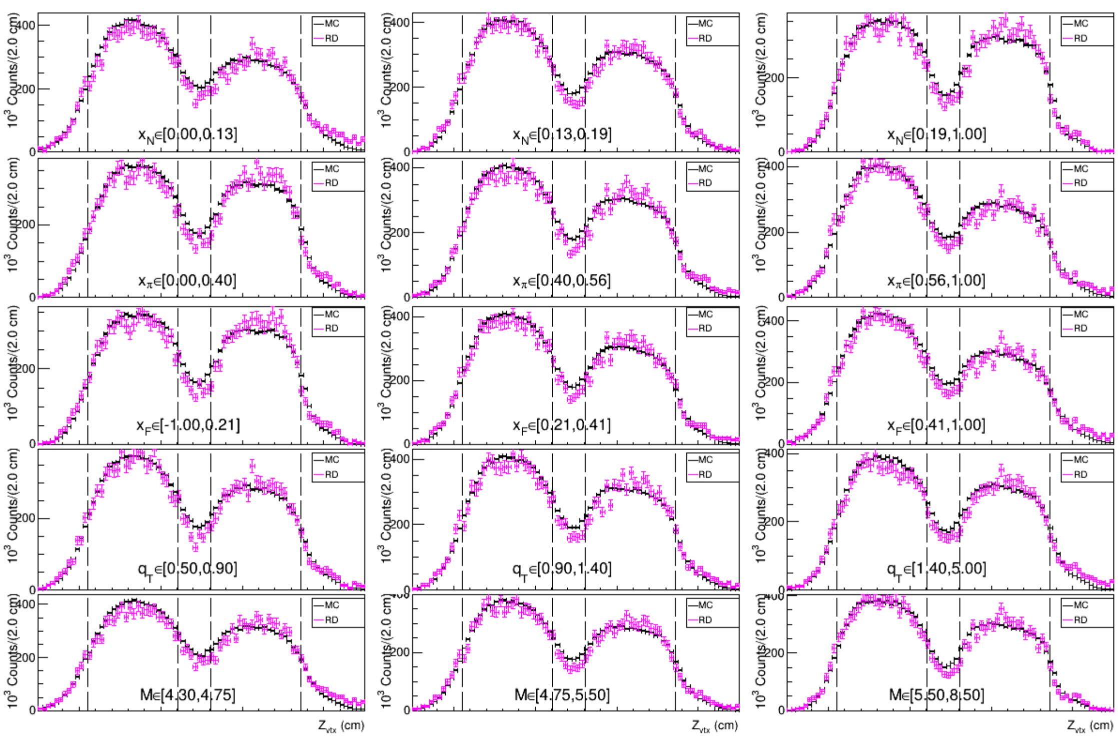

Figure 5.12: Comparison of the 2018 MC (black) and 2015 real data (magenta) z-vertex distributions in the high mass DY range, in different kinematic bins.

5.3.3 Left-Right Event Migration

When calculating the left-right asymmetry A_{N}, it is necessary to identify events as either 'left' ($0 < \phi_{\mathrm{S}} < \pi$) or 'right' ($-\pi < \phi_{\mathrm{S}} < 0$). Because of the finite angular resolution of the spectrometer, sometimes 'left' events can be reconstructed as 'right', and vice versa. This will dilute the measured asymmetry compared to the true asymmetry. Monte-Carlo can be used to determine the fraction of events reconstructed correctly, like in the previous section. Fig. 5.13 shows the fraction of reconstructed events generated in the correct and incorrect ϕ_{S} hemispheres. On average, about 3% of events are reconstructed in the incorrect hemisphere, and these events lie close to the border of 'left' and 'right'. The mixing could be removed by applying a cut on ϕ_{S} so that events near the border are not used. However, the A_{N} is related to the amplitude of the modulation $\sin(\phi_{\mathrm{S}})$. This means that the asymmetry amplitudes affected by the mixing are those that are near zero anyway, since $\sin(0) = \sin(\pi) = 0$. Therefore, the loss of statistics from a ϕ_{S} cut outweighs the benefits, so a systematic uncertainty will be assigned to A_{N} instead.

The systematic uncertainty of A_{N} due to this migration can be estimated using the simplified definition of the left-right asymmetry

$$A_{\ell\mathrm{r}} = \frac{N_\ell - N_\mathrm{r}}{N_\ell + N_\mathrm{r}}. \tag{5.2}$$

Fig. 5.13 shows that the fraction of events generated correctly vs incorrectly is approximately the same for the left and right hemispheres. Let ξ_1 be the average fraction of events reconstructed in the correct hemisphere, and ξ_2 the average fraction of events reconstructed in the incorrect hemisphere. Then

$$N_{\ell,\mathrm{reco}} = \xi_1 N_{\ell,\mathrm{gen}} + \xi_2 N_{\mathrm{r},\mathrm{gen}} \tag{5.3}$$

and

$$N_{\mathrm{r},\mathrm{reco}} = \xi_1 N_{\mathrm{r},\mathrm{gen}} + \xi_2 N_{\ell,\mathrm{gen}}, \tag{5.4}$$

where the subscript 'reco' refers to the reconstructed events and the subscript 'gen' refers to generated events. The measured $A_{\ell\mathrm{r}}$ is then

$$A_{\ell\mathrm{r},\mathrm{measured}} = \frac{N_{\ell,\mathrm{reco}} - N_{\mathrm{r},\mathrm{reco}}}{N_{\ell,\mathrm{reco}} + N_{\mathrm{r},\mathrm{reco}}} = \frac{(\xi_1 - \xi_2)(N_{\ell,\mathrm{gen}} - N_{\mathrm{r},\mathrm{gen}})}{(\xi_1 + \xi_2)(N_{\ell,\mathrm{gen}} + N_{\mathrm{r},\mathrm{gen}})} = (\xi_1 - \xi_2) A_{\ell\mathrm{r},\mathrm{true}}, \tag{5.5}$$

where the fact that $\xi_1 + \xi_2 = 1$ was used in the derivation. Thus left-right event migration causes the measured $A_{\ell\mathrm{r}}$ to be a few percent smaller than the true $A_{\ell\mathrm{r}}$. The shift due to the migration is

$$\Delta A_{\ell\mathrm{r}} = A_{\ell\mathrm{r},\mathrm{measured}} - A_{\ell\mathrm{r},\mathrm{true}} = \frac{1 - (\xi_1 - \xi_2)}{\xi_1 - \xi_2} A_{\ell\mathrm{r},\mathrm{measured}}. \tag{5.6}$$

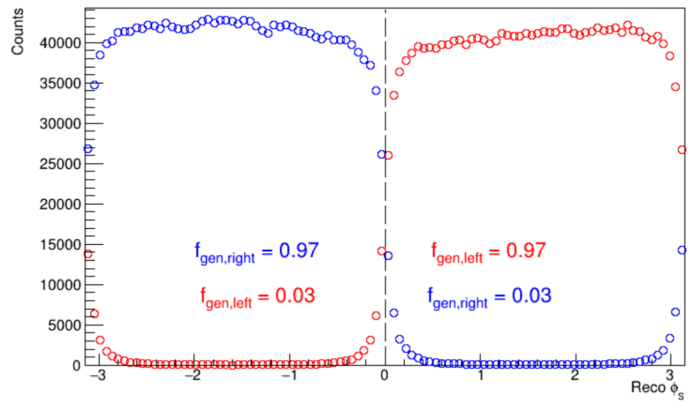

(a)

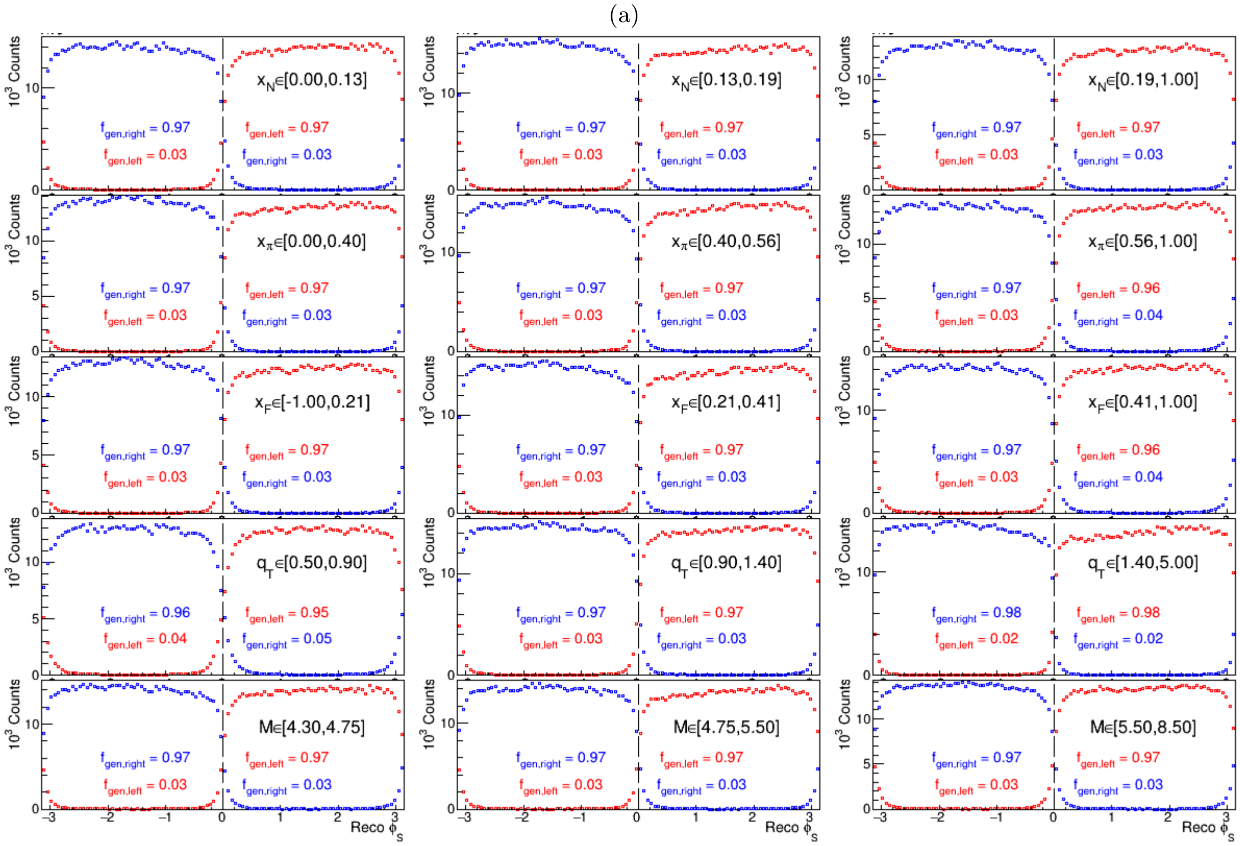

(b)

Figure 5.13: The 2018 MC-generated ϕ_S distributions plotted as a function of reconstructed ϕ_S in order to quantify the amount of left-right event migration in the high mass range (a) overall and (b) binned in kinematic variables. The blue points are events generated in the 'right' hemisphere, and the red points are events generated in the 'left'. The x-axis shows the reconstructed ϕ_S. Positive ϕ_S is 'left' and negative ϕ_S is 'right'.

Kinematic		$\sigma_{\text{sys}}/\sigma_{\text{stat}}$	
		2015	**2018**
x_{N}	[0.00, 0.13)	0.010	0.034
	[0.13, 0.19)	0.029	0.060
	[0.19, 1.00]	0.053	0.058
x_{π}	[0.00, 0.40)	0.025	0.059
	[0.40, 0.56)	0.004	0.044
	[0.56, 1.00]	0.13	0.079
x_{F}	[-1.0, 0.21)	0.053	0.052
	[0.21, 0.41)	0.11	0.016
	[0.41, 1.00]	0.015	0.018
q_{T}	[0.00, 0.90)	0.11	0.010
	[0.90, 1.04)	0.074	0.022
	[1.04, 5.00]	0.048	0.032
$M_{\mu\mu}$	[4.30, 4.75)	0.007	0.062
	[4.75, 5.50)	0.040	0.018
	[5.50, 8.50]	0.12	0.032

Table 5.3: Systematic uncertainty of A_{N} as a fraction of statistical uncertainty due to left-right event migration in high mass DY data.

A systematic uncertainty can be assigned based on this shift:

$$\frac{\sigma_{\text{sys}}}{\sigma_{\text{stat}}} = \frac{\Delta A_{\ell\text{r}}}{\sigma_{\text{stat}}}, \tag{5.7}$$

where σ_{stat} is the statistical uncertainty of $A_{\ell\text{r}}$. Eq. 5.7 is true for A_{N} as well since A_{N} is related to $A_{\ell\text{r}}$ by a scaling factor. The level of left-right migration can be safely assumed to be the same in 2015 and 2018, but the impact is different in each year based on the size of A_{N}. The uncertainty is calculated bin by bin using Eqs. 5.6 and 5.7, and the results are shown in Table 5.3. The systematic uncertainty calculated over the entire kinematic range due to left-right event migration, as a fraction of statistical uncertainty, comes to 4% in 2015 and 5% in 2018.

5.3.4 False Asymmetries

There may be external factors that can cause artificial, or 'false', asymmetries in the data, for example instabilities in certain detectors which were not significant enough to cause the data spill to be rejected (see step 8 of the event selection in Sect. 5.1). When attempting to extract physics asymmetries, these false asymmetries may dilute or amplify the true physics values. This section will describe the various tests performed to estimate the size of false asymmetry effects on the results presented in the previous section. The false asymmetries studied below are not independent of each other and so can not be naively added together.

UML TSAs

In the EWUML extraction of the standard TSAs, there are three false asymmetry tests performed. As a reminder, the COMPASS target is composed of two cells polarized in opposite directions (see Sect. 3.1.2). In the first false asymmetry test (FA1), the polarization of one of the target cells is flipped compared to the true polarization when defining the log-likelihood function (Eq. 4.15) so that the physics amplitudes cancel. In the second test (FA2), the events are randomly divided into two subperiods based on whether the run number is even or odd, rather than based on the cell polarization. Any physics asymmetries should average out to zero in this test. Finally, in the third test (FA3) each target cell is analyzed individually. Each cell is divided into an upstream and downstream half, and the two halves are treated as the two target cells in the EWUML calculation. Since the entire target cell has the same polarization in reality, there should be no physics asymmetries in this amplitude.

If there are no false asymmetry effects from the spectrometer or other sources, the false asymmetries just described should lie within a Gaussian distribution centered on zero, with a width equal to the statistical uncertainty. Therefore, if the values of the false asymmetries lie within $\pm 0.68\,\sigma_{\text{stat}}$ of zero (where σ_{stat} is the statistical uncertainty), no systematic uncertainty is assigned. If they lie outside that interval, then the distance from $0.68\,\sigma_{\text{stat}}$ is used as the percent systematic uncertainty. In equation form, this is written as:

$$\begin{aligned} \frac{\sigma_{\text{sys}}}{\sigma_{\text{stat}}} &= 0 && \text{if} \quad |A_{\text{false}}| < 0.68\,\sigma_{\text{stat}} \\ \frac{\sigma_{\text{sys}}}{\sigma_{\text{stat}}} &= \sqrt{\frac{A^2_{\text{false}}}{\sigma^2_{\text{stat}}} - 0.68^2} && \text{otherwise.} \end{aligned} \tag{5.8}$$

This systematic uncertainty is calculated period-by-period and bin-by-bin, and a weighted average of the periods is performed.

The period-averaged false asymmetries for 2015 and 2018 respectively are shown in Fig. 5.14 and 5.15. The systematic uncertainties in 2015 and 2018 from each false asymmetry, calculated by bin using Eq. 5.8, are shown in Fig. 5.16 and Fig. 5.17 respectively as a fraction of the statistical uncertainty. The false asymmetries presented here are not all independent of each other, and are also correlated with the RLTB test that will be presented in Sect. 5.3.5.

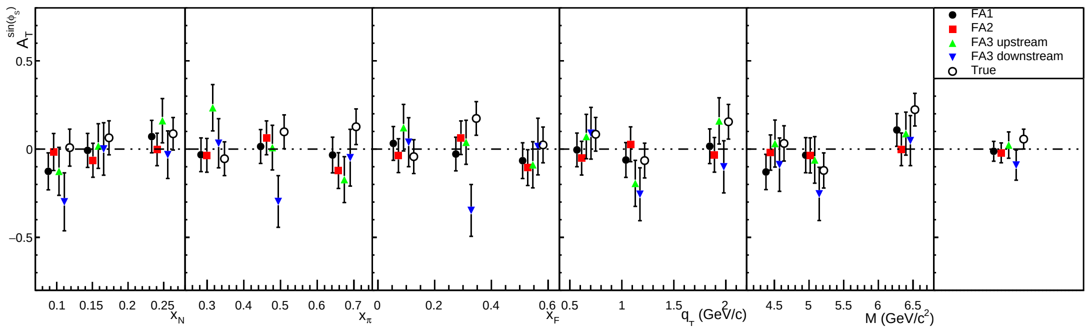

(a)

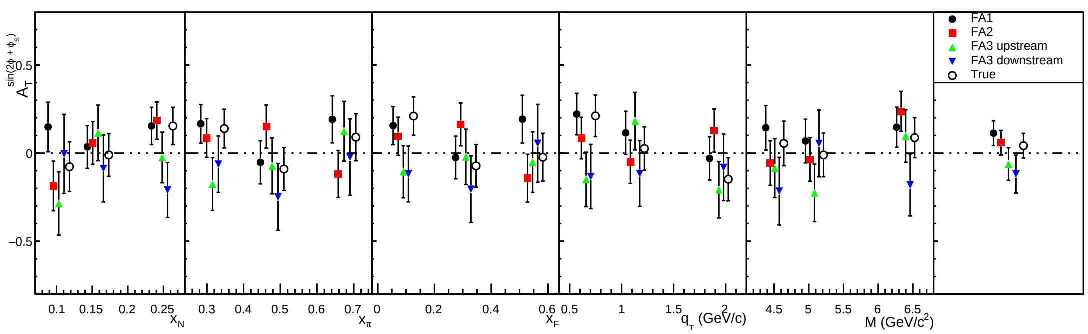

(b)

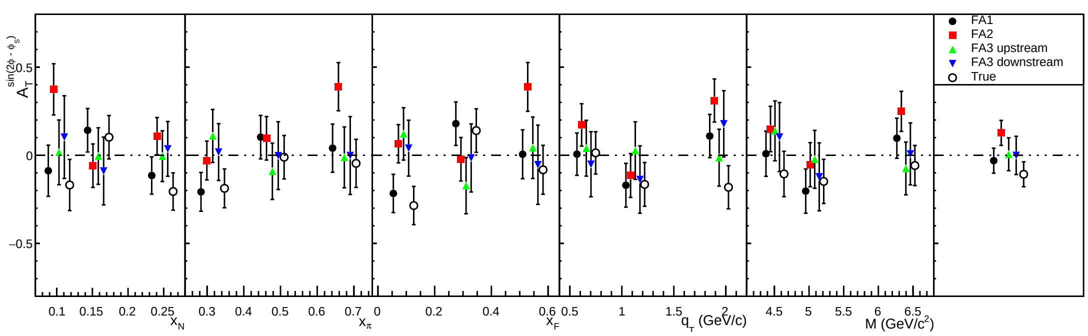

(c)

Figure 5.14: 2015 period-averaged high mass DY false asymmetries for the (a) Sivers, (b) pretzelosity, and (c) transversity TSAs. The extracted physics asymmetry is also shown for comparison.

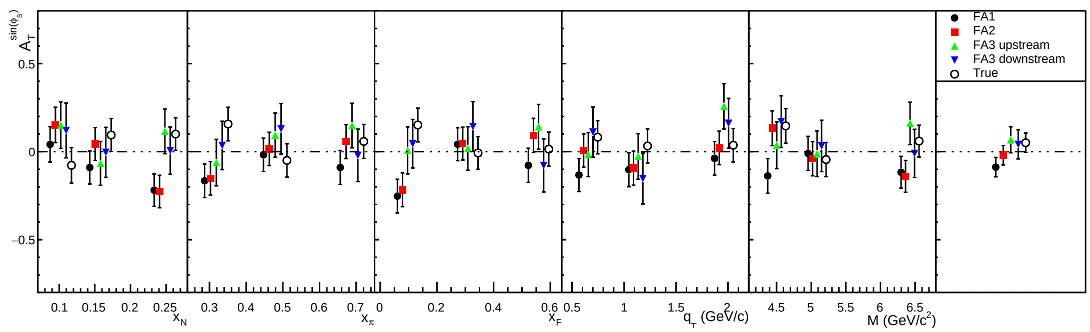

(a)

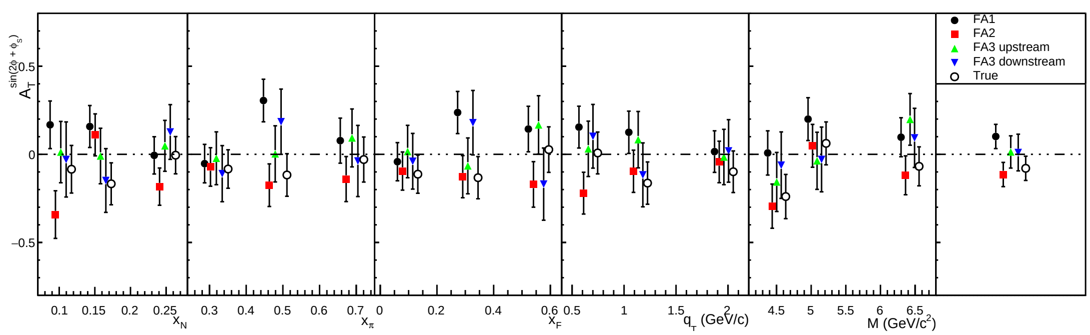

(b)

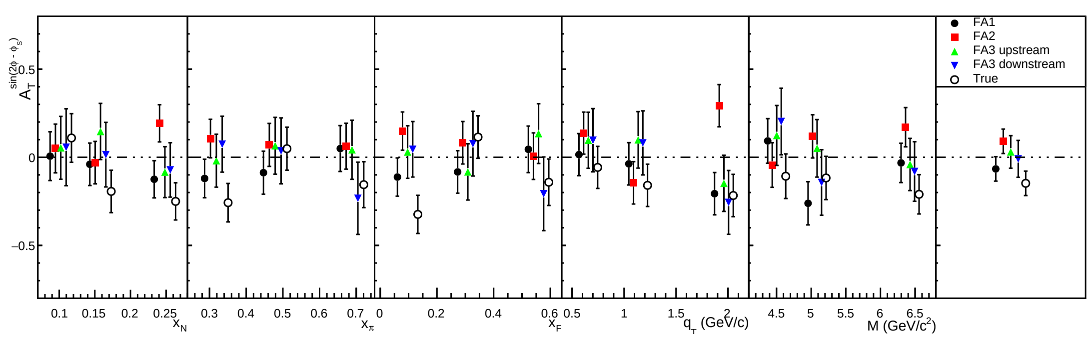

(c)

Figure 5.15: 2018 period-averaged high mass DY false asymmetries for the (a) Sivers, (b) pretzelosity, and (c) transversity TSAs. The extracted physics asymmetry is also shown for comparison.

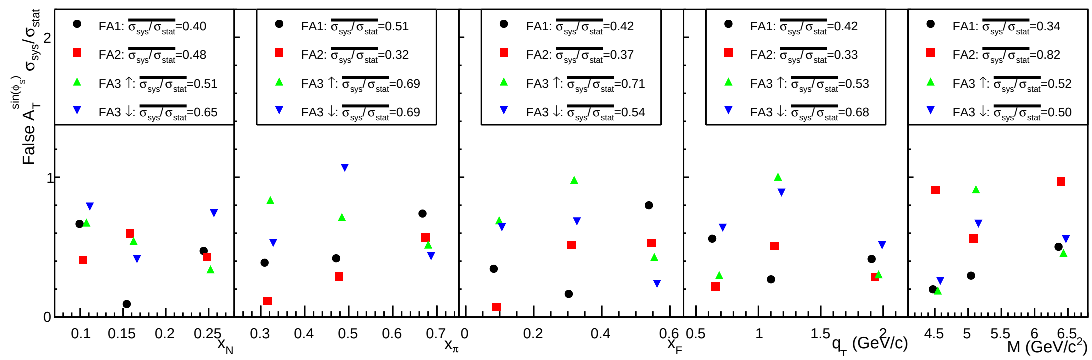

(a)

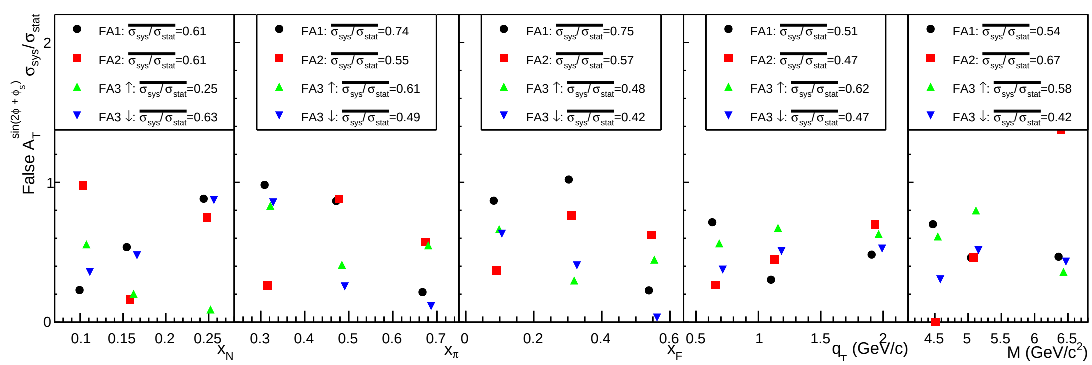

(b)

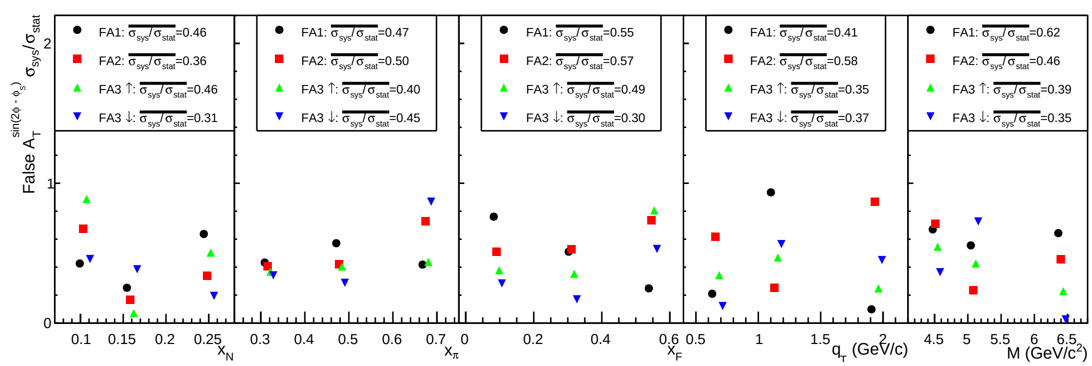

(c)

Figure 5.16: Systematic unceratinties as a fraction of statistical uncertainties from false asymmetry tests for 2015 high mass DY (a) Sivers, (b) pretzelosity, and (c) transversity.

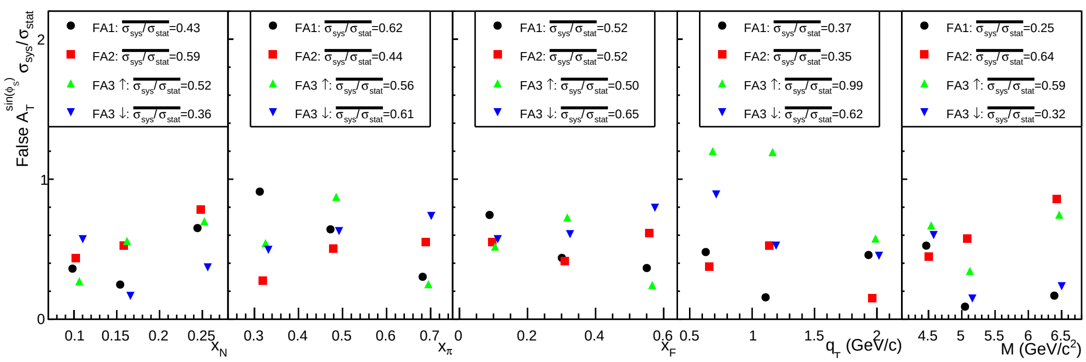

(a)

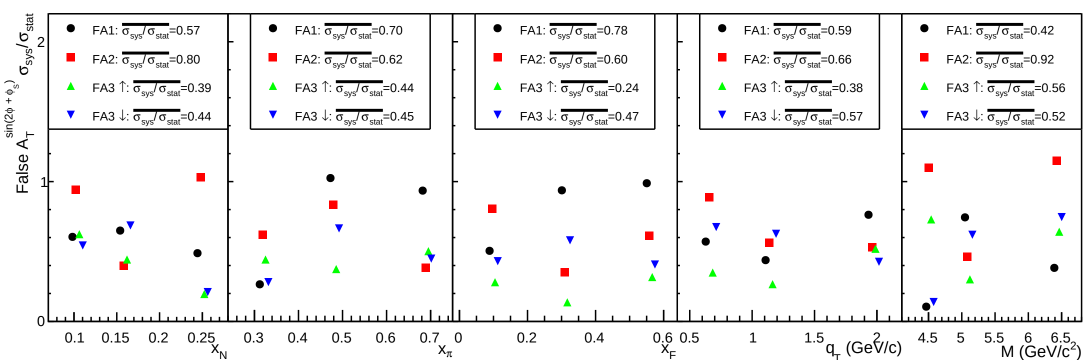

(b)

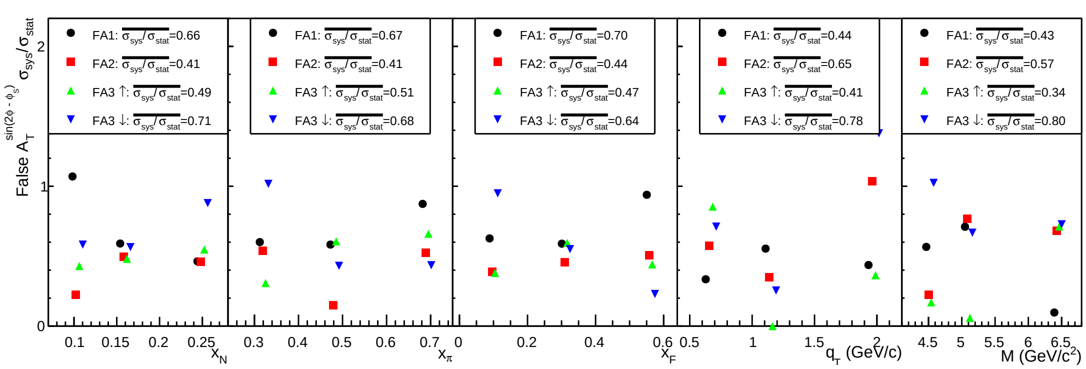

(c)

Figure 5.17: Systematic uncertainties as a fraction of statistical uncertainties from false asymmetry tests for 2018 high mass DY (a) Sivers, (b) pretzelosity, and (c) transversity.

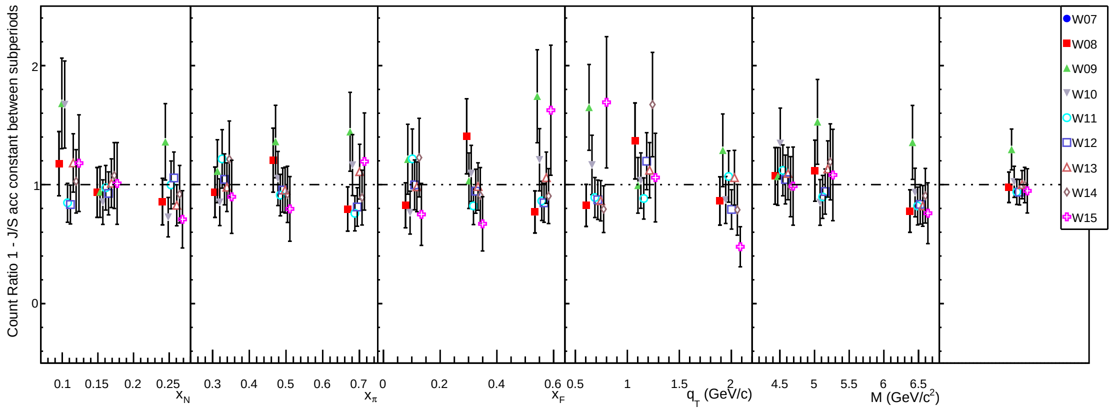

(a)

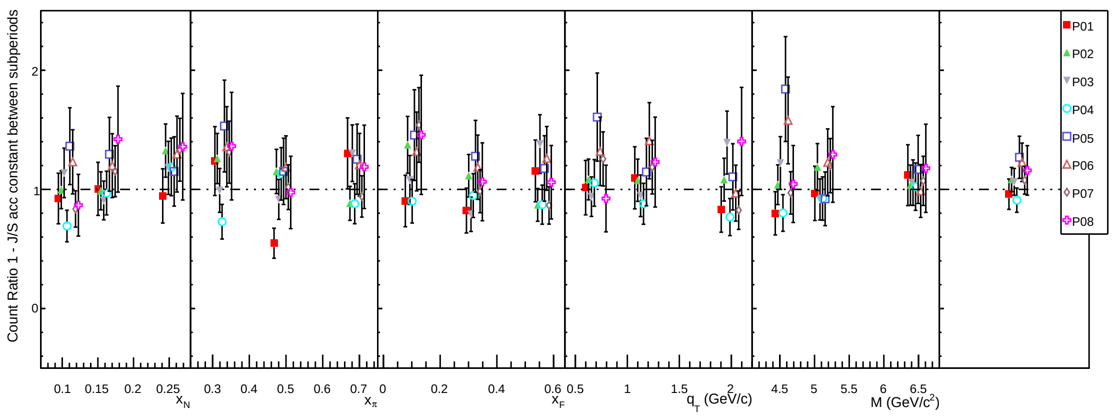

(b)

Figure 5.18: The false asymmetry ratio R_1 by period and kinematic bin from (a) 2015 and (b) 2018 high mass DY data. R_1 should equal one if the Jura/Saleve acceptance ratio is constant between subperiods.

Left-Right A_N

As derived in Sect. 4.3, the geometric mean definition of the left-right asymmetry A_N can be written as

$$A_\mathrm{N} = \frac{\pi}{2} \frac{1}{|S_\mathrm{T}| f D} \frac{\kappa_{2\mathrm{T}} \sigma_\ell - \sigma_\mathrm{r}}{\kappa_{2\mathrm{T}} \sigma_\ell + \sigma_\mathrm{r}} \tag{5.9}$$

with

$$\kappa_{2\mathrm{T}} = \frac{\sqrt[4]{a_\mathrm{J}^{1+} a_\mathrm{S}^{1-} a_\mathrm{J}^{2+} a_\mathrm{S}^{2-}}}{\sqrt[4]{a_\mathrm{S}^{1+} a_\mathrm{J}^{1-} a_\mathrm{S}^{2+} a_\mathrm{J}^{2-}}} = \sqrt[4]{\frac{a_\mathrm{J}^{1+} a_\mathrm{S}^{2-}}{a_\mathrm{S}^{1+} a_\mathrm{J}^{2-}}} \sqrt[4]{\frac{a_\mathrm{S}^{1-} a_\mathrm{J}^{2+}}{a_\mathrm{J}^{1-} a_\mathrm{S}^{2+}}}, \tag{5.10}$$

where as a reminder $a_{\mathrm{J(S)}}$ refers to the acceptance on the Jura (Saleve) side of the spectrometer, which is the absolute left (right) side. The assumption was made that $\kappa_{2\mathrm{T}}$ is equal to one. If this is not true, then the measured asymmetry includes some spectrometer acceptance effects rather than being a purely physical

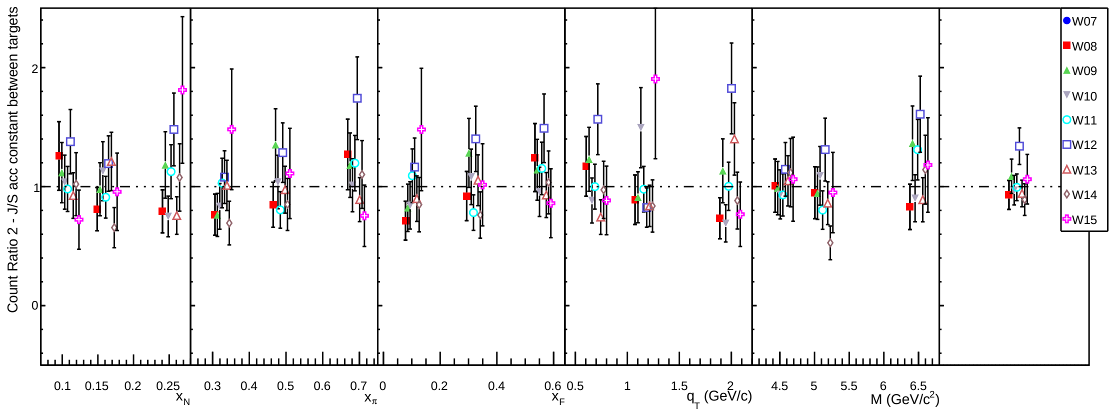

(a)

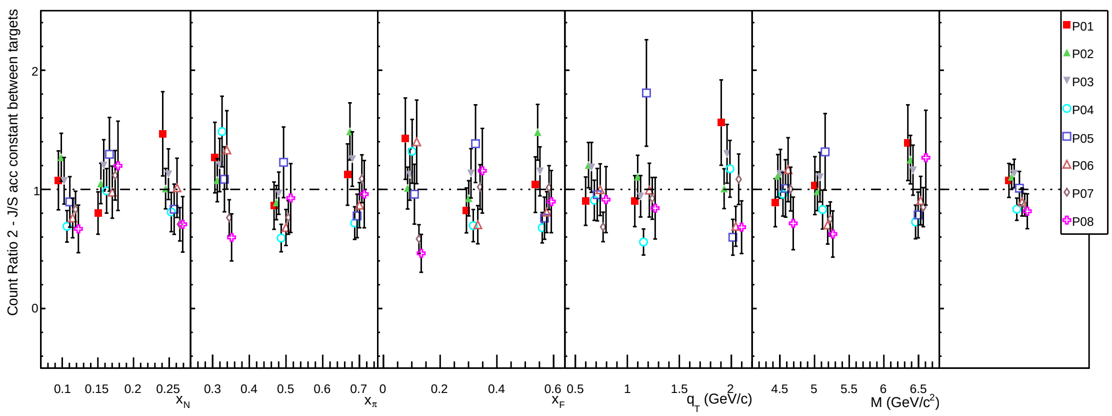

(b)

Figure 5.19: The false asymmetry ratio R_2 by period and kinematic bin from (a) 2015 and (b) 2018 high mass DY data. R_2 should equal one if the Jura/Saleve acceptance ratio is constant between target cells.

asymmetry.

Ratios of event counts can be formed that do not represent any physical asymmetries, and that will be equal to one unless there are asymmetric acceptance effects. The variation of the ratios from one can be used to estimate the size of possible spectrometer effects on A_{N}. Two such ratios will be calculated here. First,

$$R_1 = \frac{N_\ell^{1+} N_\mathrm{r}^{2-} N_\ell^{1-} N_\mathrm{r}^{2+}}{N_\mathrm{r}^{1+} N_\ell^{2-} N_\mathrm{r}^{1-} N_\ell^{2+}} = \frac{a_\mathrm{J}^{1+} a_\mathrm{J}^{2-}}{a_\mathrm{S}^{1+} a_\mathrm{S}^{2-}} \frac{a_\mathrm{S}^{1-} a_\mathrm{S}^{2+}}{a_\mathrm{J}^{1-} a_\mathrm{J}^{2+}}. \tag{5.11}$$

This R_1 will equal one if the Jura/Saleve acceptance ratio is equal between data-taking subperiods, or equivalently between target polarization configurations. The acceptance on the Jura and Saleve sides are not expected to be equal because of the spectrometer setup. However, the ratio of Jura and Saleve acceptances

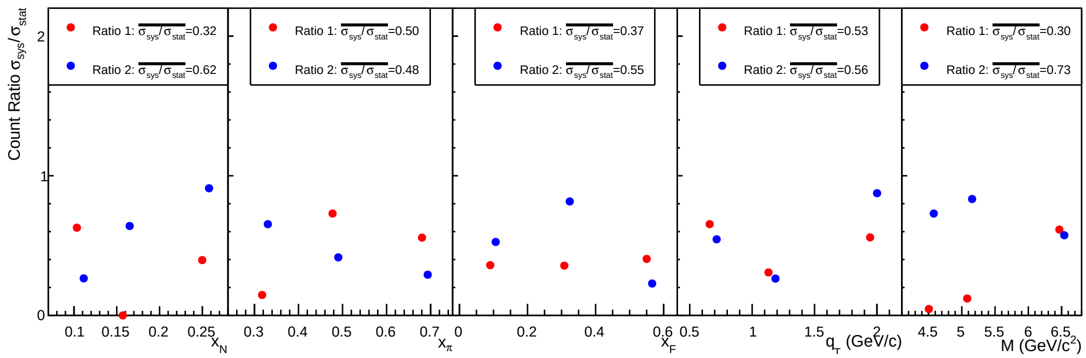

(a)

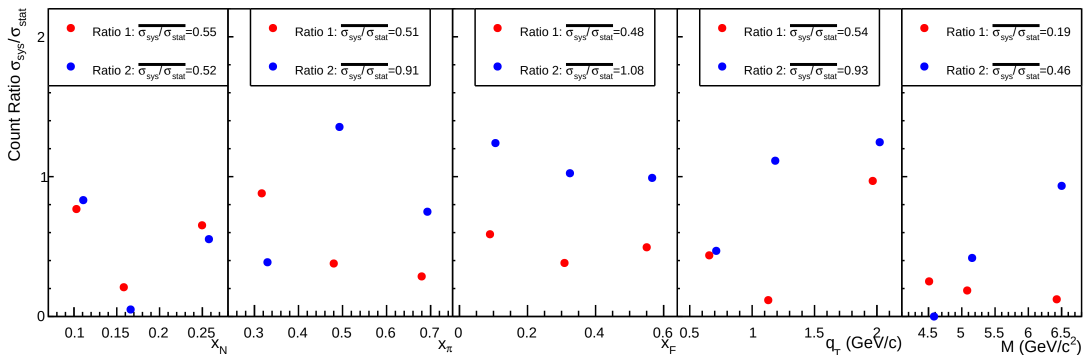

(b)

Figure 5.20: Systematic uncertainties as a fraction of statistical uncertainties due to false asymmetry ratios R_1 (red) and R_2 (blue) for high mass DY (a) 2015 and (b) 2018 A_{N} results.

should be constant regardless of the target polarization configuration. A second non-physical ratio is

$$R_2 = \frac{N_{\mathrm{r}}^{1+} N_{\ell}^{1-} N_{\ell}^{2+} N_{\mathrm{r}}^{2-}}{N_{\ell}^{1+} N_{\mathrm{r}}^{1-} N_{\mathrm{r}}^{2+} N_{\ell}^{2-}} = \frac{a_{\mathrm{S}}^{1+} a_{\mathrm{S}}^{1-}}{a_{\mathrm{J}}^{1+} a_{\mathrm{J}}^{1-}} \frac{a_{\mathrm{J}}^{2+} a_{\mathrm{J}}^{2-}}{a_{\mathrm{S}}^{2+} a_{\mathrm{S}}^{2-}}. \tag{5.12}$$

This ratio will equal one if the Jura/Saleve acceptance ratio is equal for each of the two target cells.

If there are no spectrometer effects, the values of R_1 and R_2 should lie within a Gaussian distribution centered on one, with a width equal to the statistical error of the ratios. Therefore, a systematic uncertainty is assigned using a similar method to that described above for the UML false asymmetries:

$$\begin{aligned} \frac{\sigma_{\mathrm{sys}}}{\sigma_{\mathrm{stat}}} &= 0 && \text{if} \quad |R_{1,2} - 1| < 0.68\,\sigma_{\mathrm{stat}} \\ \frac{\sigma_{\mathrm{sys}}}{\sigma_{\mathrm{stat}}} &= \sqrt{\frac{(R_{1,2}-1)^2}{\sigma_{\mathrm{stat}}^2} - 0.68^2} && \text{otherwise.} \end{aligned} \tag{5.13}$$

Again, this uncertainty is calculated period-by-period and bin-by-bin, and a weighted average of the periods is performed.

The ratios R_1 and R_2 are shown by period in Fig. 5.18 and 5.19. The systematic uncertainties for $A_{\rm N}$ calculated in each bin using Eq. 5.13 are shown in Fig. 5.20 as a fraction of statistical uncertainty. The two ratios are correlated, and they are also correlated with the $A_{\rm N}$ top-bottom test described in the next section.

5.3.5 Right-Left-Top-Bottom Test

The physics asymmetries should ideally be independent of what hemisphere of the spectrometer the outgoing muon tracks pass through. Another 'false asymmetry' study involves testing whether this is true. The azimuthal angle of the positive muon track in the laboratory frame is used to tag each event as 'top' ($\phi_{\mu_+} > 0$), 'bottom' ($\phi_{\mu_+} < 0$), 'left' ($\pi/2 < \phi_{\mu_+} < \pi$ or $-\pi < \phi_{\mu_+} < -\pi/2$) or 'right' ($0 < \phi_{\mu_+} < \pi/2$ or $-\pi/2 < \phi_{\mu_+} < 0$), where ϕ_{μ_+} ranges from $-\pi$ to π. The Sivers, pretzelosity, and transversity TSAs are calculated in each hemisphere.

$A_{\rm N}$ is just calculated in the top and bottom hemispheres since it is a left-right asymmetry measurement. The top and bottom asymmetry values are compared to each other, as are the left and right asymmetries. The difference between each is calculated, taking into account the size of the statistical error bars:

$$\alpha = \frac{|A_{\rm top(left)} - A_{\rm bottom(right)}|}{\sqrt{\sigma^2_{\rm top(left)} + \sigma^2_{\rm bottom(right)}}}. \tag{5.14}$$

This difference is then compared to zero and a systematic uncertainty is quantified using a similar method to Eq. 5.8:

$$\begin{aligned} \frac{\sigma_{\rm sys}}{\sigma_{\rm stat}} &= 0 && \text{if} \quad \alpha < 0.68 \\ \frac{\sigma_{\rm sys}}{\sigma_{\rm stat}} &= \sqrt{\alpha^2 - 0.68^2} && \text{otherwise.} \end{aligned} \tag{5.15}$$

Again this uncertainty is calculated period-by-period and then a weighted average over periods is found so that there is one uncertainty per kinematic bin. This check is called the Right-Left-Top-Bottom (RLTB) test.

Figure 5.21 shows the period-averaged differences of $A_{\rm N}$ calculated in the top and bottom hemispheres. Figure 5.23 and 5.24 shows period-averaged differences between the TSAs calculated in the top and bottom and right and left hemispheres in 2015 and 2018 respectively. The percent systematic uncertainties on $A_{\rm N}$ from the top-bottom test are shown in Fig. 5.22. The systematic uncertainties from the top-bottom and right-left comparisons are shown in Fig. 5.25 and Fig. 5.26 for the Sivers, pretzelosity, and transversity TSAs.

The RLTB test is correlated with the previously described false asymmetry tests. Therefore, summing all the false asymmetry uncertainties in quadrature would overestimate the systematic uncertainty. Instead, a different approach is taken. First, the uncertainties are averaged over each kinematic bin for each variable in order to average over statistical fluctuations. Then, the averages from each of the five kinematics are averaged together. Finally, the largest average is assigned to be the systematic uncertainty due to false asymmetries. The kinematic-averaged and final uncertainty values are shown for each TSA and A_{N} in Tables 5.4-5.7.

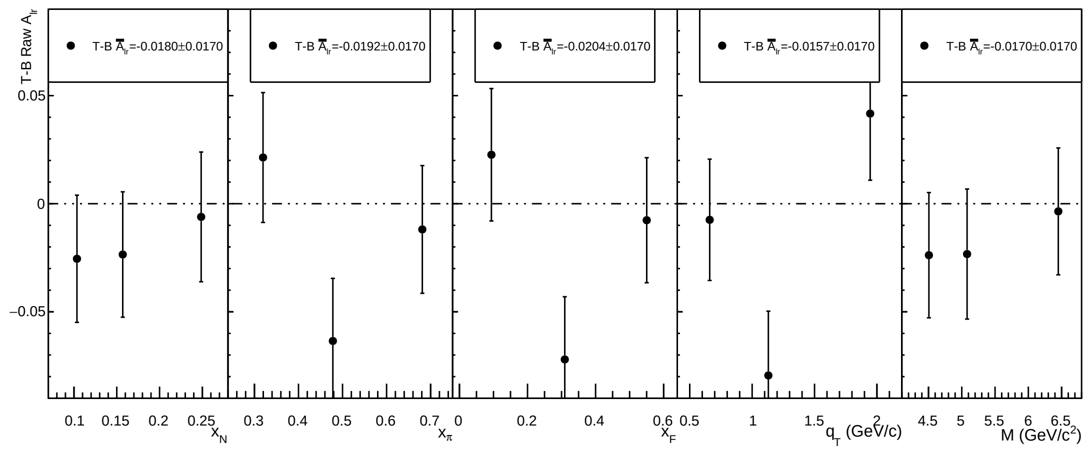

(a)

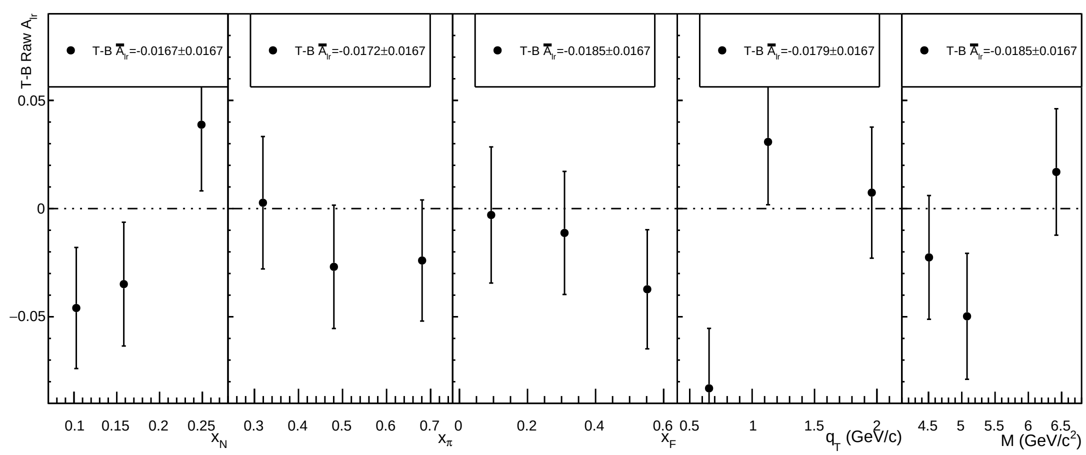

(b)

Figure 5.21: Period-averaged difference between A_N in the top and bottom hemispheres of the spectrometer for high mass DY (a) 2015 and (b) 2018 data.

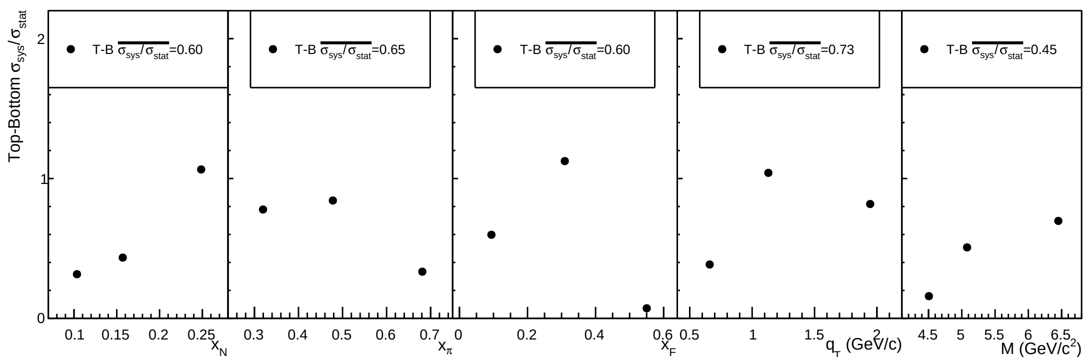

(a)

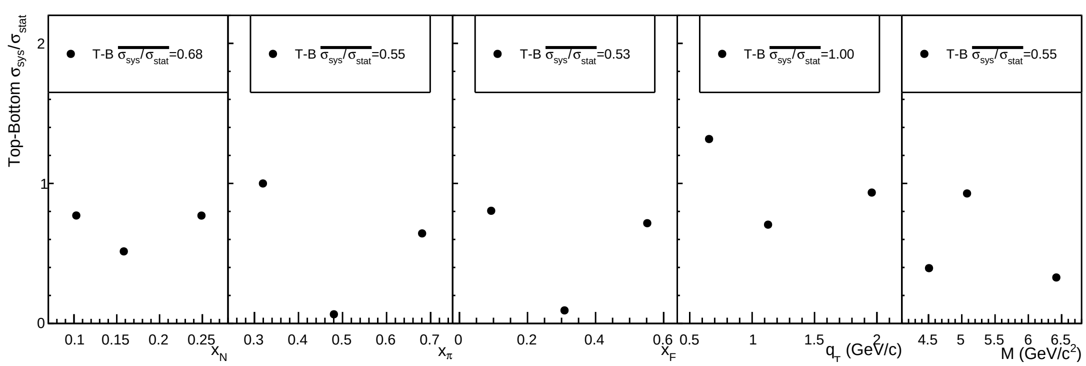

(b)

Figure 5.22: Systematic uncertainty for A_{N} due to the top-bottom test as a fraction of statistical uncertainty in high mass DY (a) 2015 and (b) 2018 data.

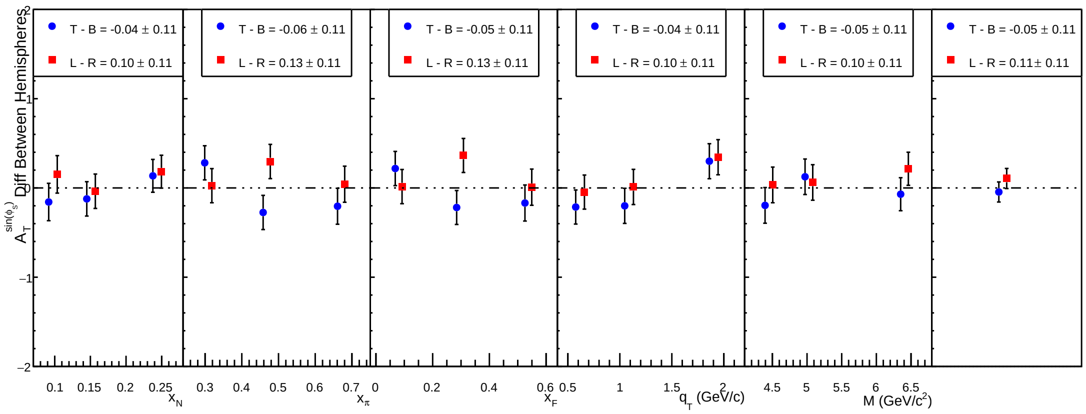

(a)

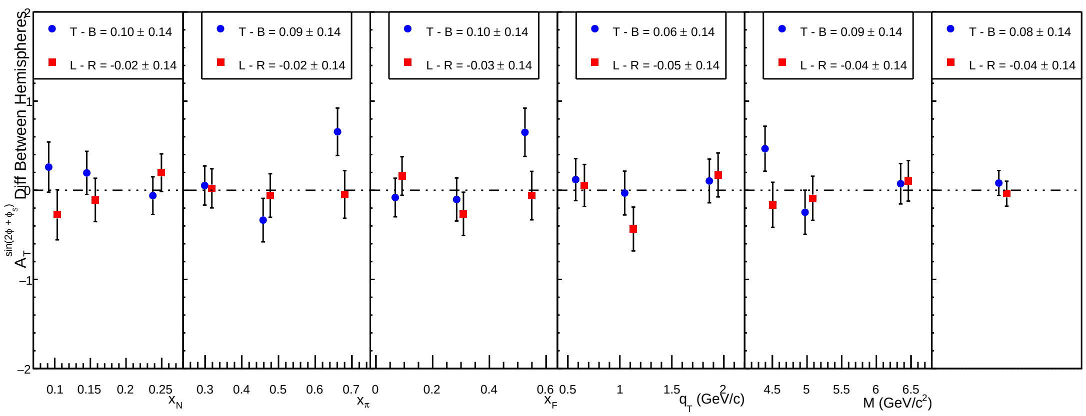

(b)

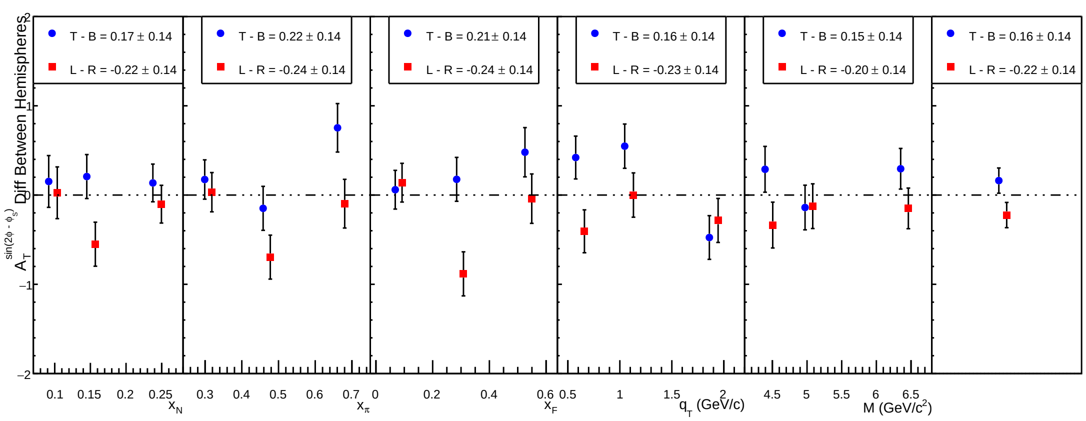

(c)

Figure 5.23: Period-averaged differences of the (a) Sivers, (b) pretzelosity, and (c) transversity TSAs between the top and bottom hemispheres (blue) and left and right hemispheres (red) in 2015 high mass DY data.

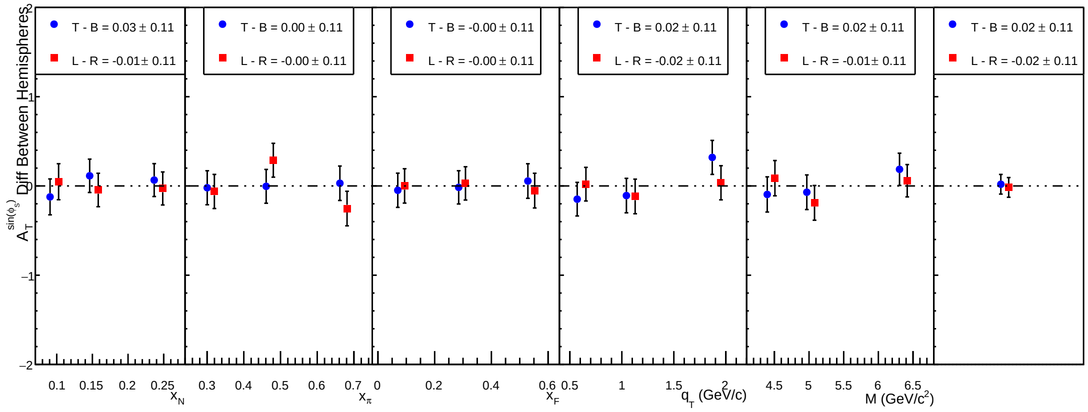

(a)

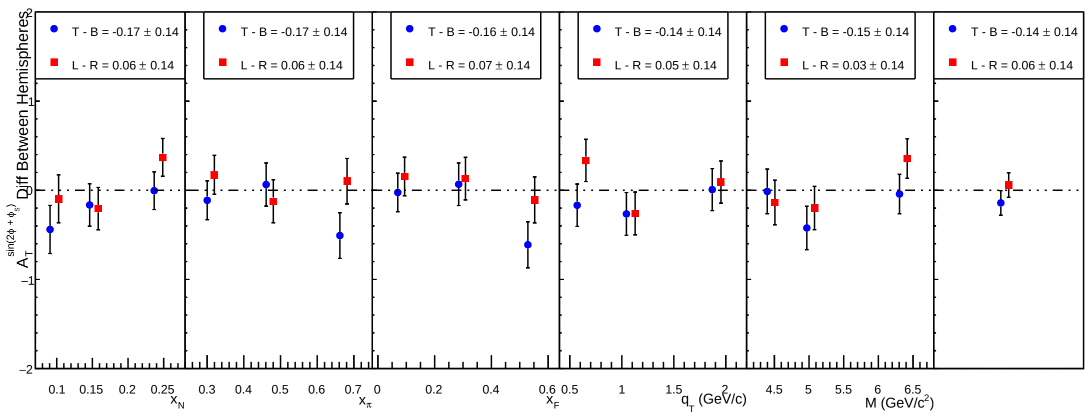

(b)

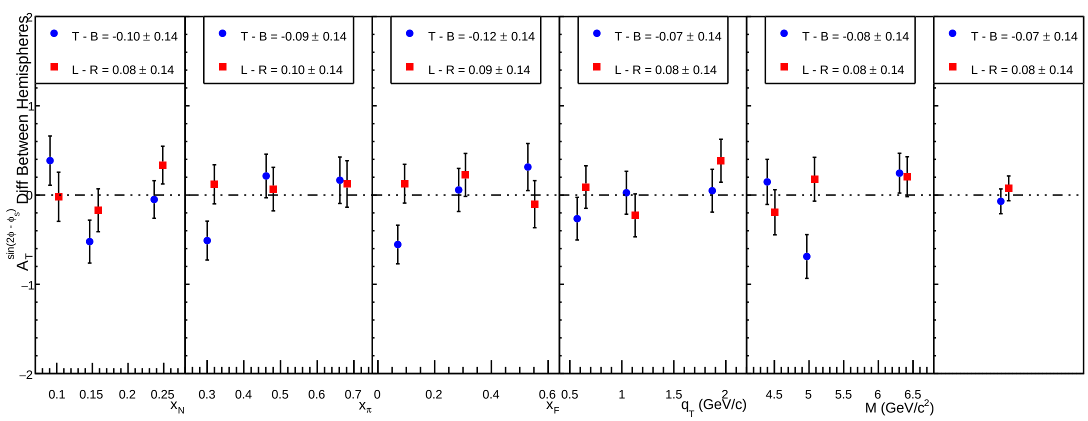

(c)

Figure 5.24: Period-averaged differences of the (a) Sivers, (b) pretzelosity, and (c) transversity TSAs between the top and bottom hemispheres (blue) and left and right hemispheres (red) in 2018 high mass DY.

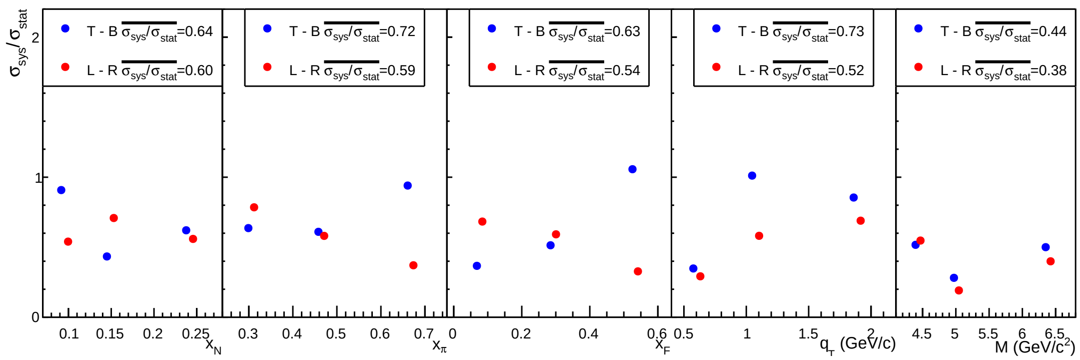

(a)

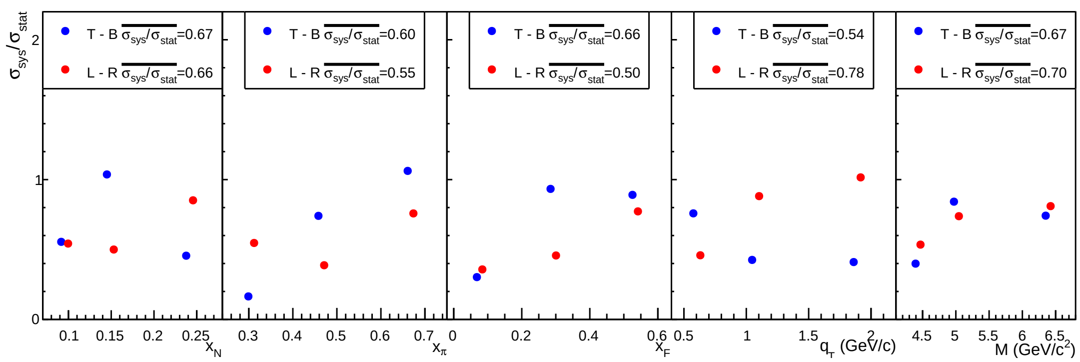

(b)

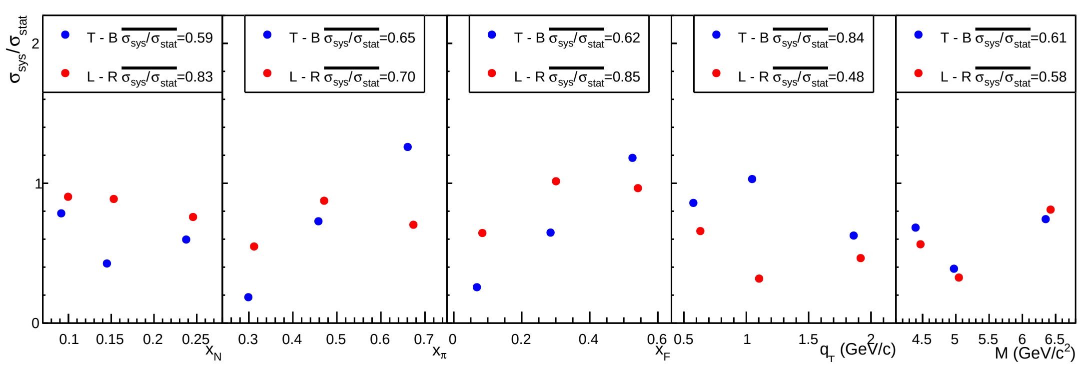

(c)

Figure 5.25: Systematic uncertainties for the (a) Sivers, (b) pretzelosity, and (c) transversity TSAs due to the RLTB test as a fraction of statistical uncertainties in 2015 high mass DY data.

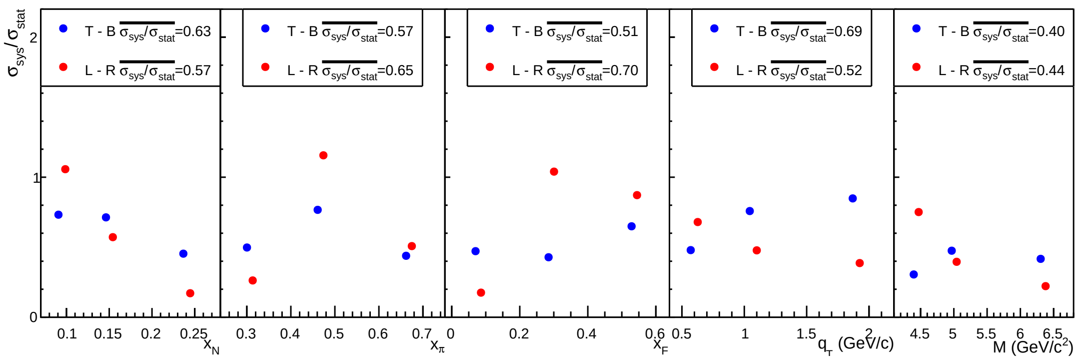

(a)

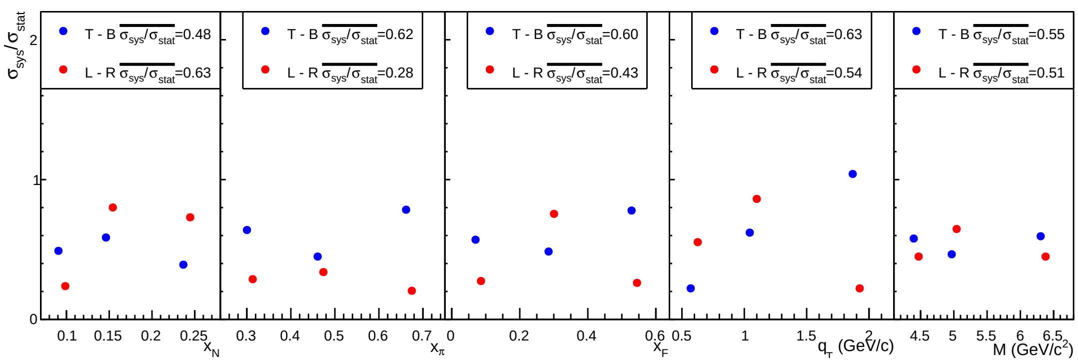

(b)

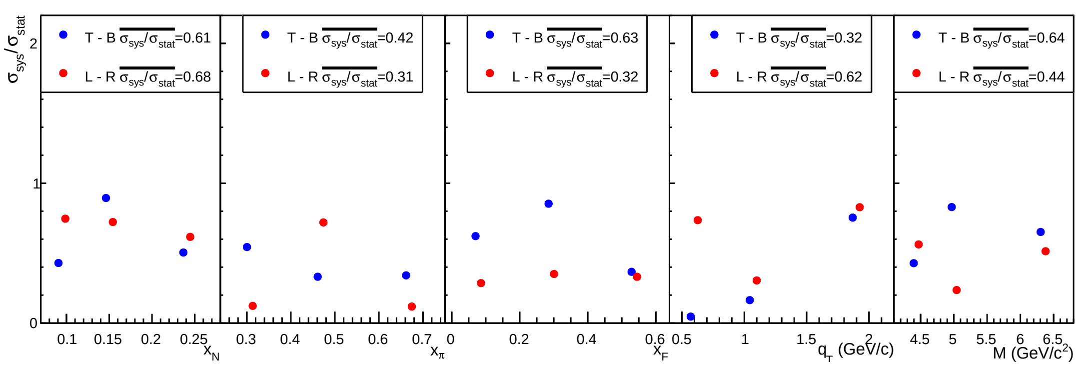

(c)

Figure 5.26: Systematic uncertainties for the (a) Sivers, (b) pretzelosity, and (c) transversity TSAs due to the RLTB test as a fraction of statistical uncertainties in 2018 high mass DY data.

Kinematic	**2015** $\sigma_{\text{sys}}/\sigma_{\text{stat}}$					
	FA1	FA2	FA3 1	FA3 2	RL	TB
x_N	0.40	0.48	0.51	0.65	0.60	0.64
x_π	0.51	0.32	0.69	0.69	0.59	0.72
x_F	0.42	0.37	0.71	0.54	0.54	0.63
q_T	0.42	0.33	0.53	0.68	0.52	0.73
$M_{\mu\mu}$	0.34	0.82	0.52	0.50	0.38	0.44
Average	0.42	0.46	0.59	0.61	0.53	***0.63***

Kinematic	**2018** $\sigma_{\text{sys}}/\sigma_{\text{stat}}$					
	FA1	FA2	FA3 1	FA3 2	RL	TB
x_N	0.43	0.59	0.52	0.36	0.57	0.63
x_π	0.62	0.44	0.56	0.61	0.65	0.57
x_F	0.52	0.52	0.50	0.65	0.70	0.51
q_T	0.37	0.35	0.99	0.62	0.52	0.69
$M_{\mu\mu}$	0.25	0.64	0.59	0.32	0.44	0.40
Average	0.44	0.51	***0.63***	0.51	0.58	0.56

Table 5.4: Average systematic uncertainty of DY TSAs due to various false asymmetries, as a fraction of statistical uncertainty, for the Sivers TSA $A_{\text{T}}^{\sin(\phi_{\text{S}})}$. The values presented here are the average over the three bins of the identified kinematic variable. The average from each type of kinematic is averaged together in the last row, and the largest value (in bold italics) is the systematic uncertainty assigned to the results.

Kinematic	**2015** $\sigma_{\text{sys}}/\sigma_{\text{stat}}$					
	FA1	FA2	FA3 1	FA3 2	RL	TB
x_N	0.61	0.61	0.25	0.63	0.66	0.67
x_π	0.74	0.55	0.61	0.49	0.55	0.60
x_F	0.75	0.57	0.48	0.42	0.50	0.66
q_T	0.51	0.47	0.62	0.47	0.78	0.54
$M_{\mu\mu}$	0.54	0.67	0.58	0.42	0.70	0.67
Average	0.63	0.57	0.51	0.49	***0.64***	0.63

Kinematic	**2018** $\sigma_{\text{sys}}/\sigma_{\text{stat}}$					
	FA1	FA2	FA3 1	FA3 2	RL	TB
x_N	0.57	0.80	0.39	0.44	0.63	0.48
x_π	0.70	0.62	0.44	0.45	0.28	0.62
x_F	0.78	0.60	0.24	0.47	0.43	0.60
q_T	0.59	0.66	0.38	0.57	0.54	0.63
$M_{\mu\mu}$	0.42	0.92	0.56	0.52	0.51	0.55
Average	0.61	***0.72***	0.40	0.49	0.48	0.58

Table 5.5: Average systematic uncertainty of DY TSAs due to various false asymmetries, as a fraction of statistical uncertainty, for the pretzelosity TSA $A_{\text{T}}^{\sin(2\phi+\phi_{\text{S}})}$. See the caption of Table 5.4 for more information.

Kinematic	**2015** $\sigma_{\text{sys}}/\sigma_{\text{stat}}$					
	FA1	FA2	FA3 1	FA3 2	RL	TB
x_N	0.46	0.36	0.46	0.31	0.83	0.59
x_π	0.47	0.50	0.40	0.45	0.70	0.65
x_F	0.55	0.57	0.49	0.30	0.85	0.62
q_T	0.41	0.58	0.35	0.37	0.48	0.84
$M_{\mu\mu}$	0.62	0.46	0.39	0.35	0.58	0.61
Average	0.50	0.49	0.42	0.36	***0.69***	0.66

Kinematic	**2018** $\sigma_{\text{sys}}/\sigma_{\text{stat}}$					
	FA1	FA2	FA3 1	FA3 2	RL	TB
x_N	0.66	0.41	0.49	0.71	0.68	0.61
x_π	0.67	0.41	0.51	0.68	0.31	0.42
x_F	0.70	0.44	0.47	0.64	0.32	0.63
q_T	0.44	0.65	0.41	0.78	0.62	0.32
$M_{\mu\mu}$	0.43	0.57	0.34	0.80	0.44	0.64
Average	0.58	0.50	0.44	***0.72***	0.47	0.52

Table 5.6: Average systematic uncertainty of DY TSAs due to various false asymmetries, as a fraction of statistical uncertainty, for the transversity TSA $A_{\mathrm{T}}^{\sin(2\phi-\phi_{\mathrm{S}})}$. See the caption of Table 5.4 for more information.

Kinematic	**2015** $\sigma_{\text{sys}}/\sigma_{\text{stat}}$		
	R1	R2	TB
x_N	0.32	0.88	0.60
x_π	0.17	0.43	0.65
x_F	0.26	0.32	0.60
q_T	0.87	0.83	0.73
$M_{\mu\mu}$	0.27	0.92	0.45
Average	0.38	***0.68***	0.61

Kinematic	**2018** $\sigma_{\text{sys}}/\sigma_{\text{stat}}$		
	R1	R2	TB
x_N	0.54	0.87	0.68
x_π	0.27	1.06	0.55
x_F	0.41	1.59	0.53
q_T	0.54	1.17	1.00
$M_{\mu\mu}$	0.22	0.90	0.55
Average	0.40	***1.1***	0.66

Table 5.7: Average systematic uncertainty of DY TSAs due to various false asymmetries, as a fraction of statistical uncertainty, for A_{N}. See the caption of Table 5.4 for more information.

5.3.6 Other $\sin(n\phi_S)$ Amplitudes with Odd n

As mentioned in Sect. 4.3, the left-right asymmetry A_N is related to all the $\sin(n\phi_S)$ amplitudes with odd n. Only the case where $n = 1$ should be physical, but it needs to be checked whether any of the other amplitudes are sizeable. This was done using the EWUML method, and the results are shown in Fig. 5.27 up to $n = 9$. Some amplitudes with $n > 1$ are non-zero in this extraction. This should not be turned into a systematic uncertainty because it is related to the very definition of the left-right asymmetry. However, it may be a reason why there is a difference observed between A_N and $A_T^{\sin(\phi_S)}$ in Fig. 5.8.

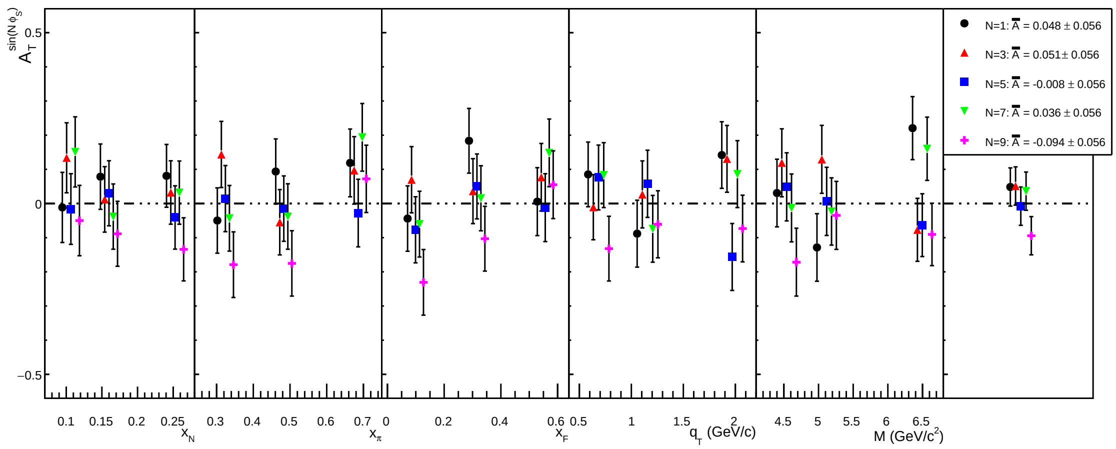

(a)

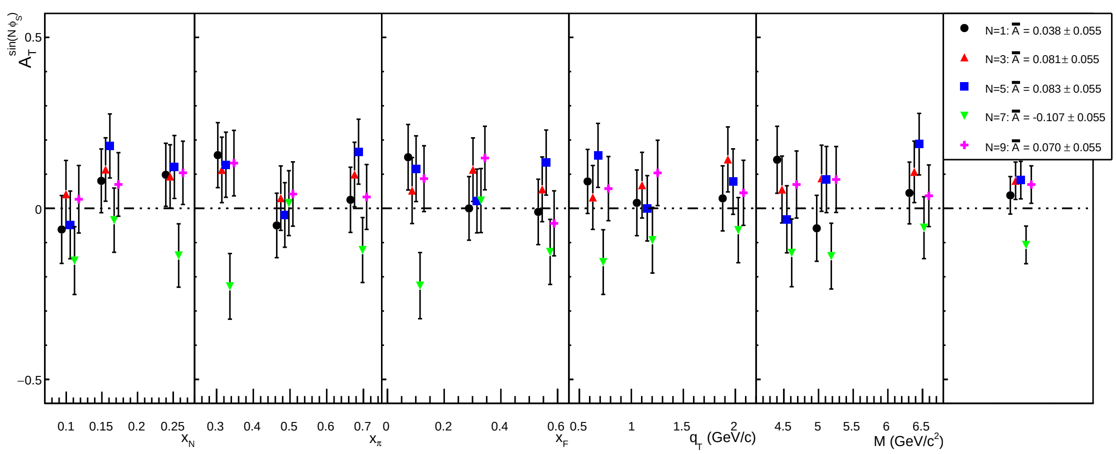

(b)

Figure 5.27: Different $\sin(n\phi_S)$ amplitudes with odd n up to $n = 9$ in high mass DY (a) 2015 and (b) 2018 data.

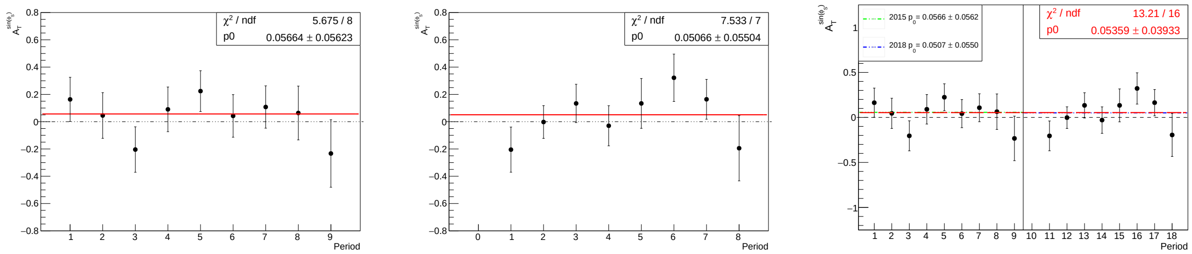

(a) (b) (c)

Figure 5.28: High mass DY Sivers TSA $A_{\mathrm{T}}^{\sin(\phi_S)}$ by period in (a) 2015, (b) 2018, and (c) both years combined. The χ^2 values of the constant fits indicate that the results within a single year as well as between years are statistically compatible.

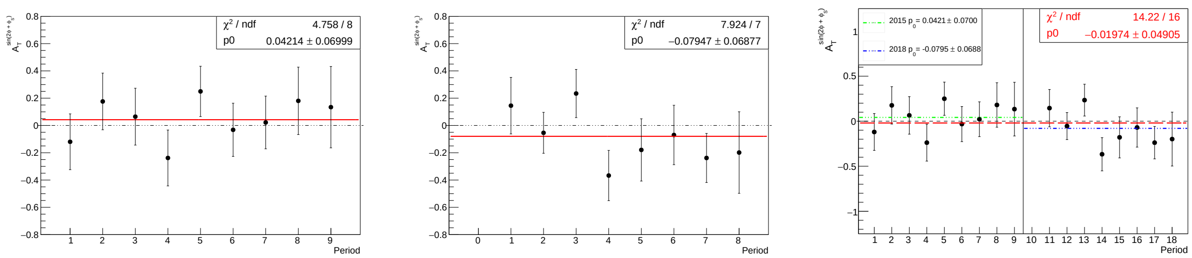

(a) (b) (c)

Figure 5.29: High mass DY pretzelosity TSA $A_{\mathrm{T}}^{\sin(2\phi+\phi_S)}$ by period in (a) 2015, (b) 2018, and (c) both years combined. The χ^2 values of the constant fits indicate that the results within a single year as well as between years are statistically compatible.

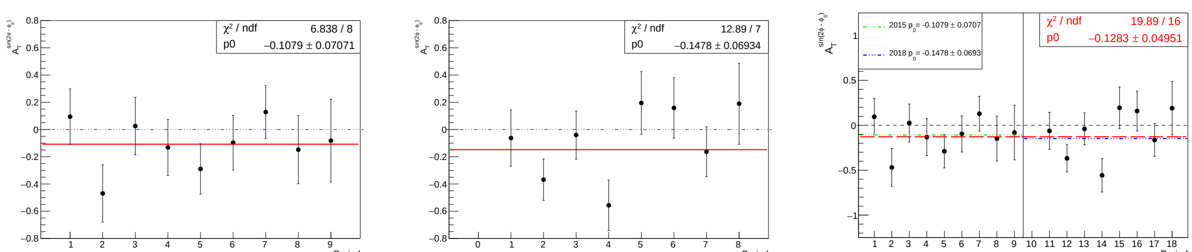

(a) (b) (c)

Figure 5.30: High mass DY transversity TSA $A_{\mathrm{T}}^{\sin(2\phi-\phi_S)}$ by period in (a) 2015, (b) 2018, and (c) both years combined. The χ^2 values of the constant fits suggest that the results within a single year as well as between years are statistically compatible.

5.3.7 Period Compatibility

As mentioned in Sects. 3.3, the COMPASS DY data was taken in periods of 2-4 weeks each. Each year, 2015 and 2018, was comprised of 9 periods, but the first period of 2018 (P00) was removed from the analysis due to significant differences in the beam and some detector settings. The TSAs shown in Sect. 5.2 are the

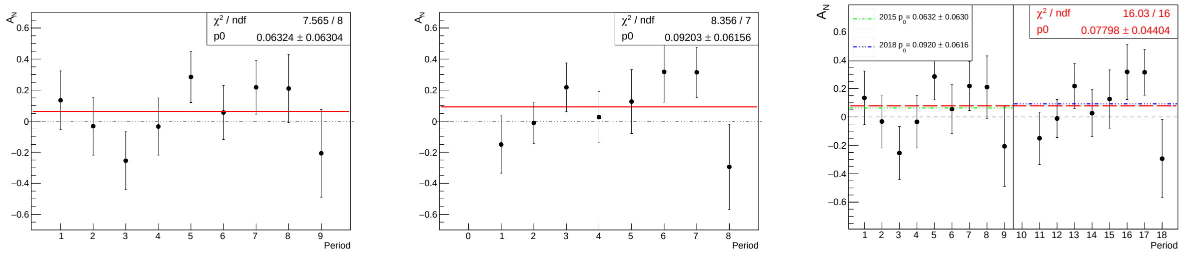

(a) (b) (c)

Figure 5.31: High mass DY A_{N} by period in (a) 2015, (b) 2018, and (c) both years combined. The χ^2 values of the constant fits indicate that the results within a single year as well as between years are statistically compatible.

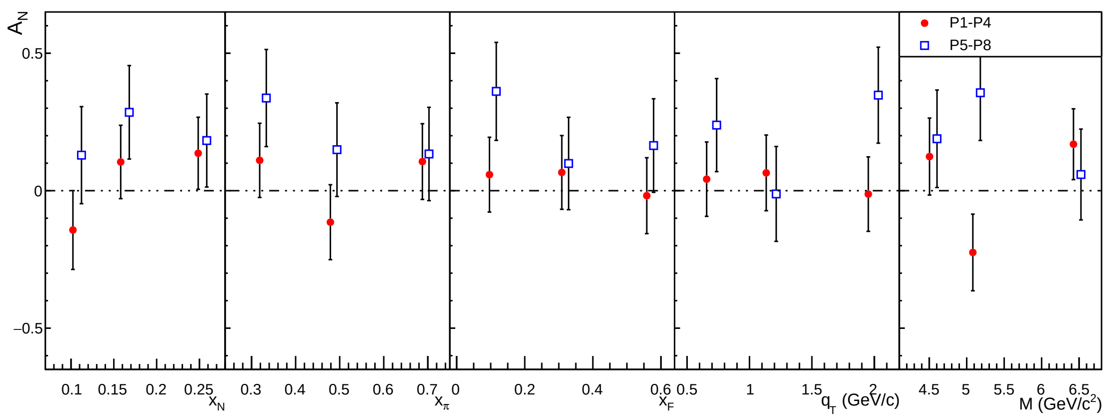

Figure 5.32: A_{N} averaged over each half of 2018 separately, in various kinematic bins.

weighted averages of the TSAs from each of the periods. One important test is to check whether the results from each period are statistically compatible. Period dependence would suggest that data-taking conditions or spectrometer acceptance are influencing the measurements.

Figs. 5.28-5.30 show the results of the Sivers, pretzelosity, and transversity TSAs respectively by period for 2015, 2018, and the combination of the two years. Fig. 5.31 shows the period-by-period results of A_{N}. In each case, the asymmetries from each period are fit with a constant to check if the points are statistically compatible. The reduced χ^2 of the fits indicate that there is no strong period dependence when you compare each individual period. However, in 2018, there is a discrepancy if you compare the average of the first half of the year to the average of the second half. This can be seen in Fig. 5.32 for A_{N} and Fig. 5.33 for the standard TSAs. Various tests were performed by COMPASS analyzers, including this author, to try to understand the source of this discrepancy. These included studying kinematic distributions of the muon tracks and checking the impact of other angular cuts on the TSA results. In the end, no cause could be identified. Therefore, a systematic uncertainty is assigned based on the difference between the two halves of 2018 using the same

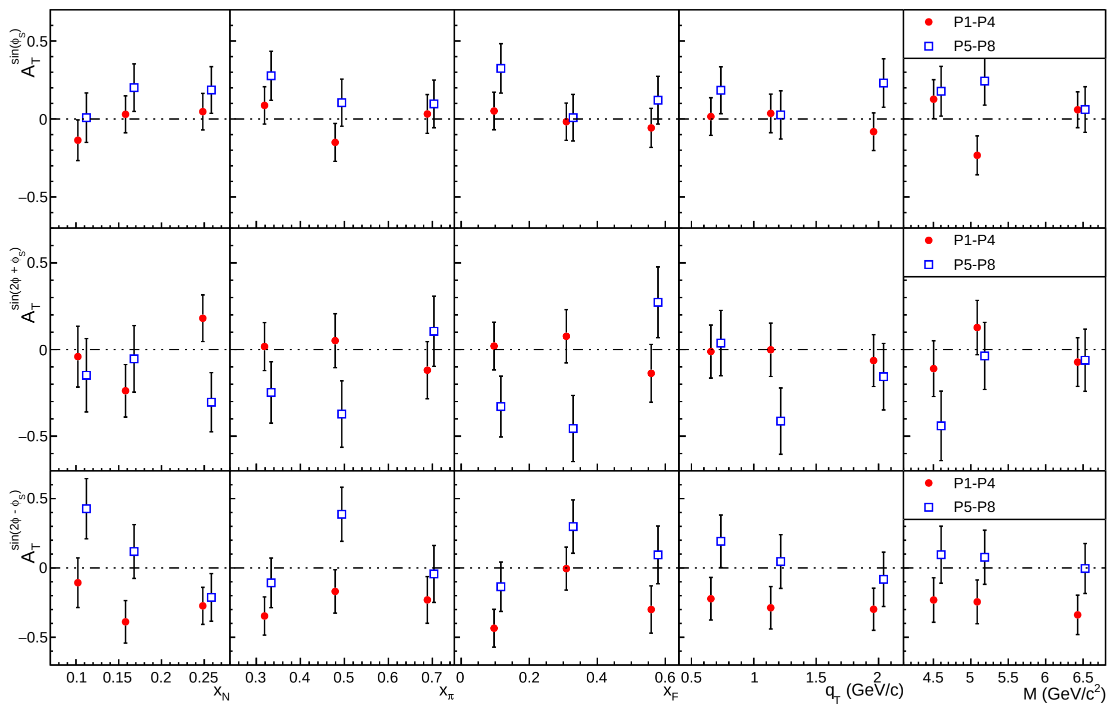

Figure 5.33: The TSAs averaged over each half of 2018 separately, in various kinematic bins. The first row is the Sivers TSA, the second row is the pretzelosity TSA, and the third row is the transversity TSA.

procedure that was used in the RLTB test (Eqs. 5.14 and 5.15). The resulting systematic uncertainty in 2018 in units of statistical uncertainty comes to 0.6 for Sivers and A_{N}, 0.9 for pretzelosity, and 1.1 for transversity. No systematic uncertainty due to time dependence is assigned in 2015 because no problematic behavior is observed.

5.3.8 Total Systematic Uncertainty

In addition to the systematic tests described above, some studies were performed by other COMPASS analyzers to quantify the impact of various data quality cuts on the extracted TSAs. This study was not performed specifically for A_{N}, so it is assumed that the level of systematic uncertainty is comparable to that for $A_{\mathrm{T}}^{\sin(\phi_{\mathrm{S}})}$. The systematic uncertainty from each additive source is shown in Table 5.8.

The dilution and polarization factors have inherent uncertainties resulting from the calculation methods. Additionally, because the value of A_U^1 is not known for certain, there is inherent uncertainty in the depolarization factors. These all contribute multiplicative systematic uncertainties that together come to 11%. This multiplicative uncertainty is not included in the systematic error bands, but is taken into account when summing 2015 and 2018 results together. The overall final TSA and A_{N} results with systematic uncertainty bands are shown in Fig. 5.34 and 5.35 respectively. The combined systematic uncertainty as a fraction of

Systematic Uncertainty	2015 $\langle \sigma_{\mathrm{sys}}/\sigma_{\mathrm{stat}} \rangle$			
	$A_{\mathrm{T}}^{\sin(\phi_S)}$	$A_{\mathrm{T}}^{\sin(2\phi+\phi_S)}$	$A_{\mathrm{T}}^{\sin(2\phi-\phi_S)}$	A_{N}
Period Compatibility	0.00	0.00	0.00	0.00
Left-Right Event Migration	N/A	N/A	N/A	0.04
Data Quality Cuts	0.4	0.5	0.45	0.4
False Asymmetries	0.6	0.65	0.7	0.7
Total	**0.7**	**0.8**	**0.8**	**0.8**

Systematic Uncertainty	2018 $\langle \sigma_{\mathrm{sys}}/\sigma_{\mathrm{stat}} \rangle$			
	$A_{\mathrm{T}}^{\sin(\phi_S)}$	$A_{\mathrm{T}}^{\sin(2\phi+\phi_S)}$	$A_{\mathrm{T}}^{\sin(2\phi-\phi_S)}$	A_{N}
Period Compatibility	0.6	0.9	1.1	0.6
Left-Right Event Migration	N/A	N/A	N/A	0.05
Data Quality Cuts	0.45	0.55	0.55	0.45
False Asymmetries	0.6	0.7	0.7	1.1
Total	**0.95**	**1.25**	**1.40**	**1.30**

Table 5.8: Overall systematic uncertainty percentages for each TSA from high mass DY data.

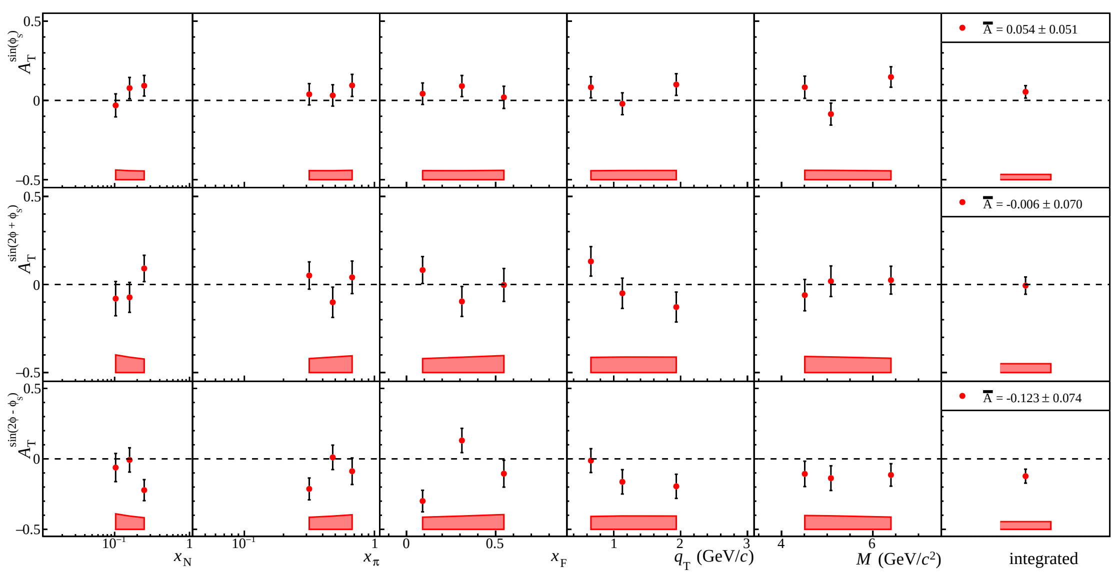

Figure 5.34: TSA high mass DY results averaged over 2015 and 2018 with systematic uncertainty bands, in various kinematic bins and extracted over the entire kinematic range. The first row is the Sivers TSA, the second is pretzelosity, and the third is transversity. The errors printed in the right-most panels are the combined systematic and statistical uncertainties.

statistical uncertainty comes to 0.8 for the Sivers TSA, 1.0 for the pretzelosity TSA, 1.1 for the transversity TSA, and 1.1 for A_{N}. Thus the contribution to the uncertainty from systematics is approximately equal to the contributions from statistics.

5.4 Interpretation of Results

The newest COMPASS DY TSA results in Figs. 5.34 and 5.35 will now be discussed in the context of the TSA results presented in Sect. 2.6. Firstly, the new pretzelosity TSA result in Fig. 5.34 is consistent

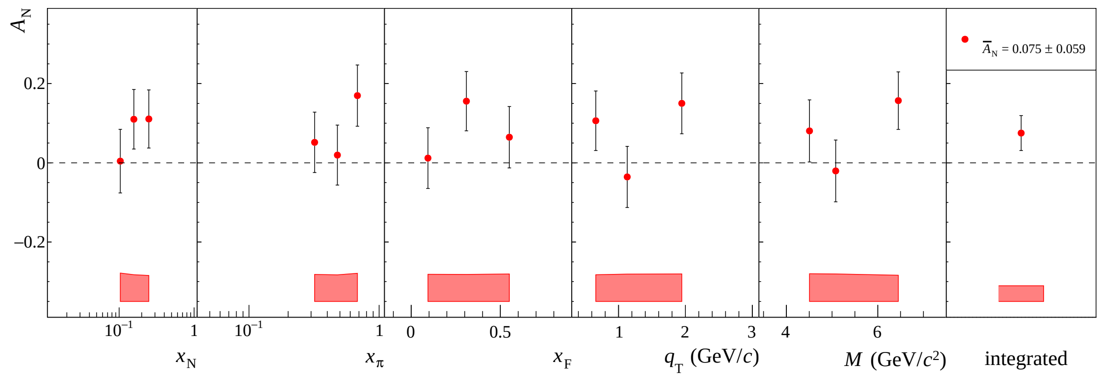

Figure 5.35: A_{N} high mass DY results averaged over 2015 and 2018 with systematic uncertainty bands, in various kinematic bins and also extracted over the entire kinematic range. The error printed in the right-most panel is the combined systematic and statistical uncertainty.

with zero. The amplitude has shifted towards zero compared to the initial published result in Fig. 2.20. The new integrated point is shown along with recent phenomenological predictions from Ref. [61] in Fig. 5.36a. It is interesting to note that a pretzelosity amplitude of zero has also been observed in multiple SIDIS experiments (Figs. 2.17, 2.18, 2.19a). The new DY result for the transversity TSA is 2σ below zero, similar to the original publication. It is shown to agree with phenomenological predictions [61] within error bars in Fig. 5.36b, suggesting that transversity is indeed universal.

The most important output of this analysis is information about the sign of the Sivers function in DY. The new DY Sivers amplitude $A_{\mathrm{T}}^{\sin(\phi_{\mathrm{S}})}$ and the left-right asymmetry A_{N} are both observed to be 1σ above zero. The significance is the same as the previously published COMPASS DY result in Fig. 2.20. Though the error bars are greatly reduced due to increased statistics, the data point itself has shifted closer to zero. The new result still favors the sign change hypothesis to a level of 1.5σ, as shown in Fig. 5.36c. However, it also leaves open the possibility of a zero amplitude. As shown in Fig. 2.28, the newest STAR results for A_{N} in DY-like W/Z boson production are also small and consistent with zero, though the kinematic coverage of STAR is different than COMPASS. In summary, the new COMPASS DY Sivers result favors the sign-change hypothesis between SIDIS and DY. The kinematic-integrated DY and SIDIS TSA results from similar kinematic regions at COMPASS are shown side-by-side for comparison in Fig. 5.37.

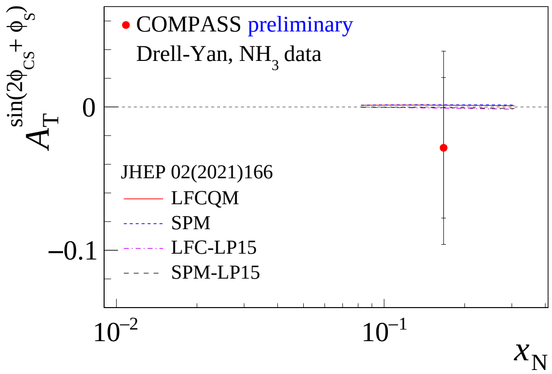

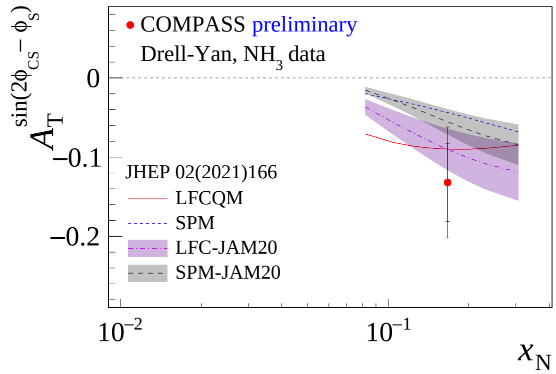

(a) (b)

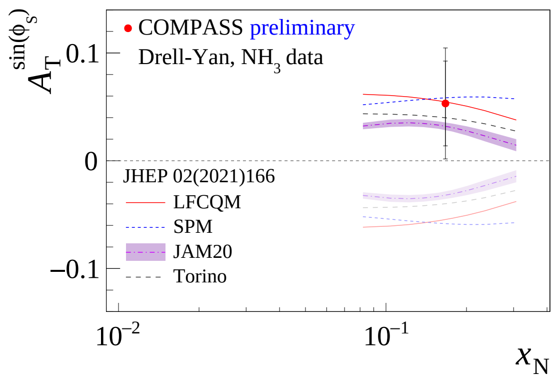

(c)

Figure 5.36: The newest COMPASS DY integrated results for the (a) pretzelosity, (b) transversity, and (c) Sivers TSA amplitudes along with recent phenomenological predictions from Ref. [61]. Note that in (c), the darker curves are for the case where the Sivers sign change prediction holds, and the faded curves are for the case where it does not. Plots are from the official COMPASS release of the 2015+2018 DY TSA results.

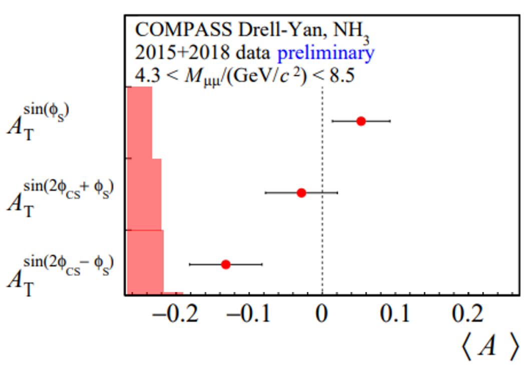

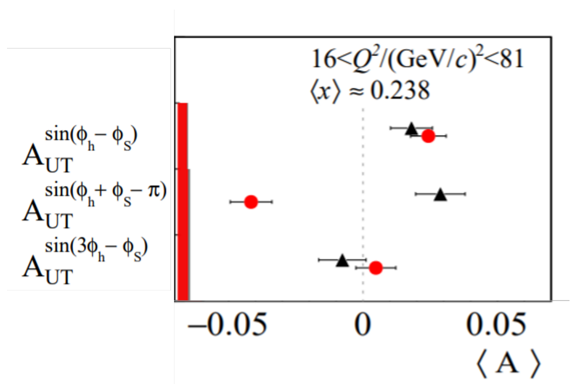

(a) (b)

Figure 5.37: The (a) newest COMPASS DY TSA results along with the (b) published SIDIS TSA results in the same kinematic region [59]. In (a) the top TSA is associated with the proton Sivers function, the middle is associated with the proton pretzelosity function, and the bottom is associated with the proton transversity function. In (b) the top TSA is associated with the proton Sivers function, the middle is associated with the proton transversity function, and the bottom is associated with the proton pretzelosity function. Because of the angle definitions, Sivers TSAs with the same sign in SIDIS and DY point to Sivers TMD functions with opposition signs.

Chapter 6

J/ψ Transverse Spin Asymmetries

This chapter will present the TSA results from COMPASS J/ψ data. It will follow the same basic outline as Chapter 5. The event selection process will be described in Sect. 6.1. The 1D double ratio, EWUML, and A_{N} results will be presented in Sect. 6.2. The various systematic studies will be explained in Sect. 6.3. Finally, in Sect. 6.4 the new results will be interpreted in the context of the other related experimental and theoretical results presented in Sect. 2.7.

6.1 Data Selection

The dimuons resulting from J/ψ decay (Eq. 2.35) are selected from the data using almost the same event selection described in Sect. 5.1. The low momentum cut is not included because it did not significantly impact the agreement between Monte-Carlo and real data in the J/ψ mass range. An additional requirement that $x_{\mathrm{F}} \geq 0$ is applied to the J/ψ data because the asymmetry extraction was found to be unstable when $x_{\mathrm{F}} < 0$ due to a high percentage of depolarization factors equaling zero. This was not a problem in the high mass DY case, probably for two reasons. First, there are relatively few negative x_{F} events in the high mass range (Fig. 5.2c). Second, a different value for A_U^1 was used in the J/ψ case as will be described below in Sect. 6.2. The mass range chosen for the J/ψ analysis is 2.85 GeV/c^2 $< M_{\mu\mu} <$ 3.4 GeV/c^2. As seen in Fig. 5.1, this selects the peak of J/ψ events centered around the true J/ψ mass of about 3.1 GeV/c^2. In the indicated mass range, background levels are less than 10%, as will be shown in Sect. 6.3.1. The number of J/ψ event candidates after each cut is shown in Table 6.1. Note that after all cuts are applied, there are about 43 times more J/ψ events than high mass DY events (Table 5.1). Some important 1D and 2D kinematic distributions for the total selected J/ψ data sample are shown in Figs. 6.1 and 6.2.

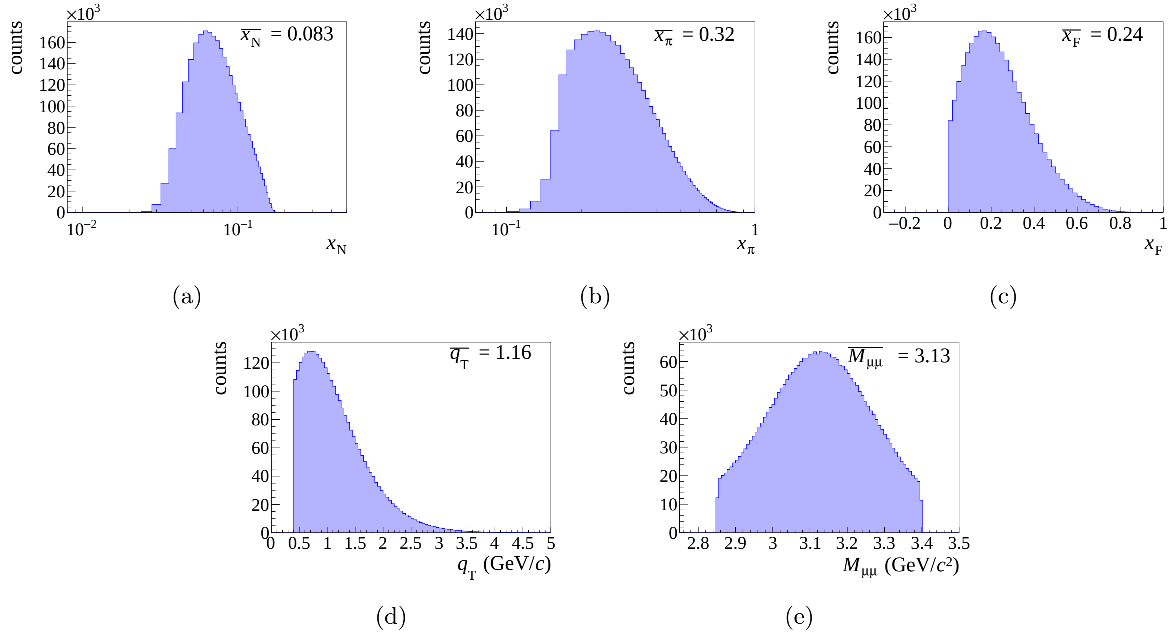

Figure 6.1: One-dimensional distributions of (a) $x_{\rm N}$, (b) x_π, (c) $x_{\rm F}$, (d) $q_{\rm T}$, and (e) $M_{\mu\mu}$ for the selected COMPASS J/ψ data sample. Both 2015 and 2018 data are included. The mean kinematic values are printed on the plots.

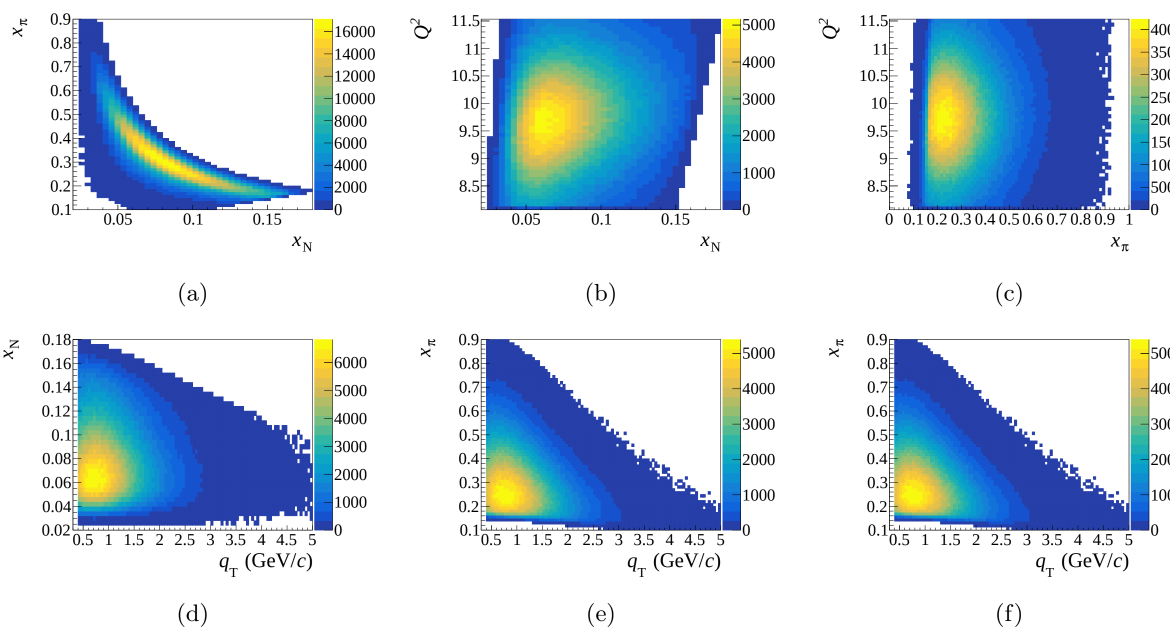

Figure 6.2: Two-dimensional distributions showing the correlations of (a) $x_{\rm N}$ and x_π, (b) $x_{\rm N}$ and $Q^2 = M^2_{\mu\mu}$, (c) x_π and Q^2, (d) $q_{\rm T}$ and $x_{\rm N}$, (e) $q_{\rm T}$ and x_π, and (f) $q_{\rm T}$ and $x_{\rm F}$ for the selected COMPASS J/ψ data sample. Both 2015 and 2018 data are included.

Cuts	2015 Events		2018 Events	
Dimuon, Best Primary Vertex, 2.85 GeV/$c < M <$ 3.4 GeV/c	10153449	100%	11808194	100%
Dimuon trigger fired (LAS-LAST or LAS-OT)	8412737	82.9%	9341801	79.1%
$z_{\text{first}} <$ 300 cm, $z_{\text{last}} >$ 1500 cm	8336815	82.1%	9255234	78.4%
Time defined	8313004	81.9%	7982554	67.6%
$\Delta t <$ 5 ns	7179887	70.7%	7918603	67.1%
Track $\tilde{\chi}^2 < 10$	7159399	70.5%	7891881	66.8%
Trigger validation	6069416	59.8%	6767919	57.3%
Physical x_{N}, x_π, x_{F}	6069404	59.8%	6767910	57.3%
0.4 GeV/$c < q_{\text{T}} <$ 5.0 GeV/c	5362240	52.8%	5982335	50.7%
z_{vtx} inside NH_3 target cells	2117881	20.9%	2284201	19.3%
r_{vtx} cut	2045946	20.2%	2162452	18.3%
Beam through both NH_3 cells	2028585	20.0%	2133010	18.1%
$p_{\mu_+} + p_{\mu_-} <$ 180 GeV/c	2028307	20.0%	2132737	18.1%
Track $\tilde{\chi}^2 < 3.2$	1820502	17.9%	1866642	15.8%
Good spill	1574976	15.5%	1683869	14.3%
$x_{\text{F}} \geq 0$	1494507	14.7%	1607471	13.6%

Table 6.1: J/ψ event selection on 2015 and 2018 COMPASS data samples. (Note that P00 of 2018 is not included.)

6.2 Results

The 1D double ratio, EWUML, and A_{N} methods were applied to the J/ψ event sample that survived the selection cuts. In this mass range, the value of A_U^1 is not close to 1 as it was in the DY case. Instead, a value of $A_U^1 = 0$ is used when calculating the depolarization factors. This is more consistent with extracted values of A_U^1 in J/ψ production [118]. As in the high mass DY case, the asymmetries are calculated period-by-period then averaged together. The sources of systematic uncertainty will be presented in Sect. 6.3.

6.2.1 Standard TSA Results

The 1D double ratio results for the Sivers, pretzelosity, and transversity TSAs are shown in Fig. 6.3, while the EWUML results are shown in Fig. 6.4. The overall averages of 2015 and 2018 results from both methods are shown in Fig. 6.5. The two methods give statistically compatible results, and only the EWUML results will be shown from now on.

6.2.2 A_{N} Results

The A_{N} results from the 2015 and 2018 J/ψ samples are shown in Fig. 6.6. The average results are shown alongside the Sivers TSA $A_{\text{T}}^{\sin(\phi_S)}$ results from the EWUML method in Fig. 6.7. The two amplitudes are more consistent in this mass range than they were in the high mass DY case (Fig. 5.8).

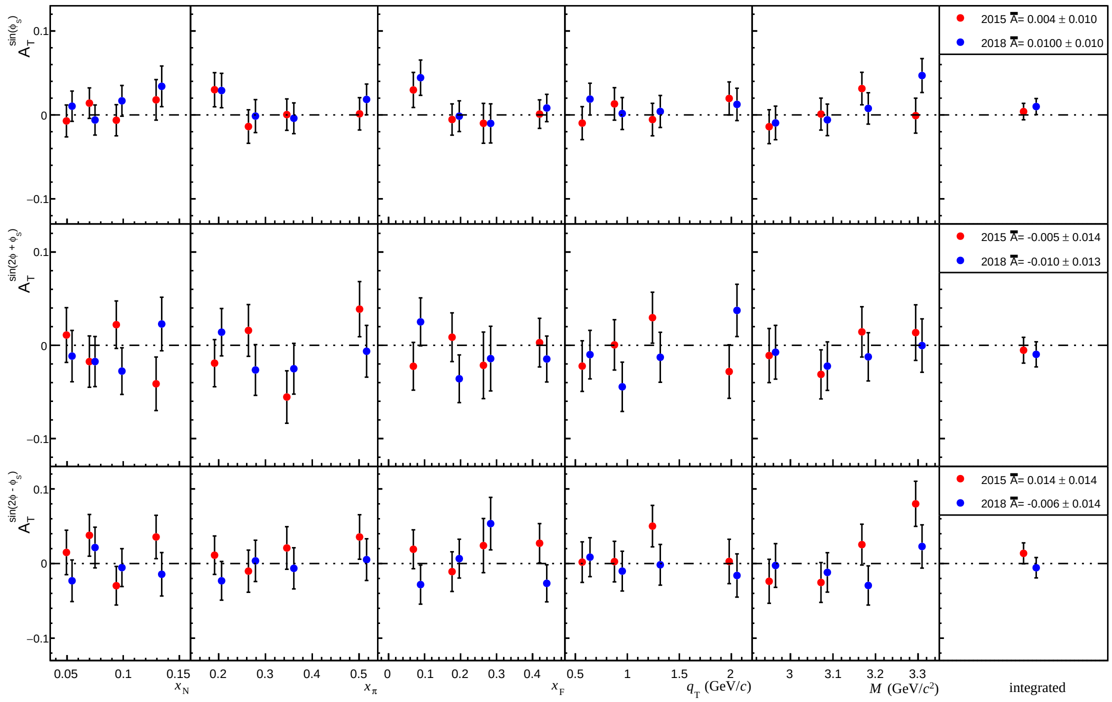

Figure 6.3: 1D Double Ratio TSA results from 2015 (red) and 2018 (blue) J/ψ events, binned in different kinematic variables and also extracted over the entire kinematic range. The first row is the Sivers TSA, the second is pretzelosity, and the third is transversity.

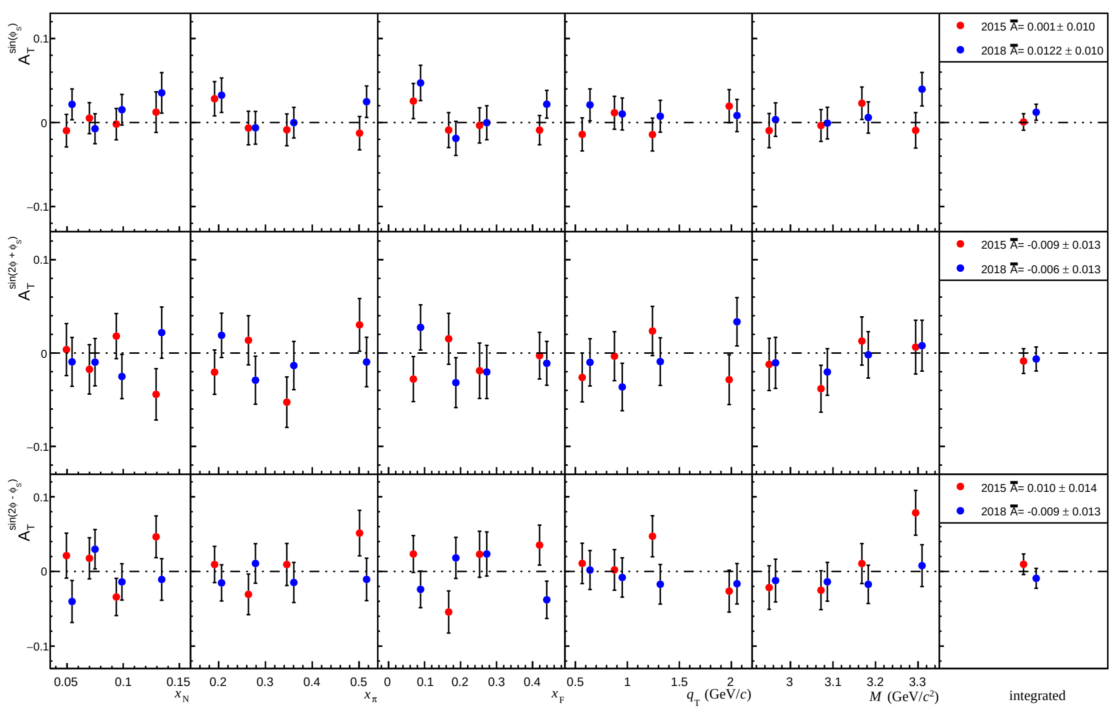

Figure 6.4: EWUML TSA results from 2015 and 2018 J/ψ events. Otherwise like Fig. 6.3.

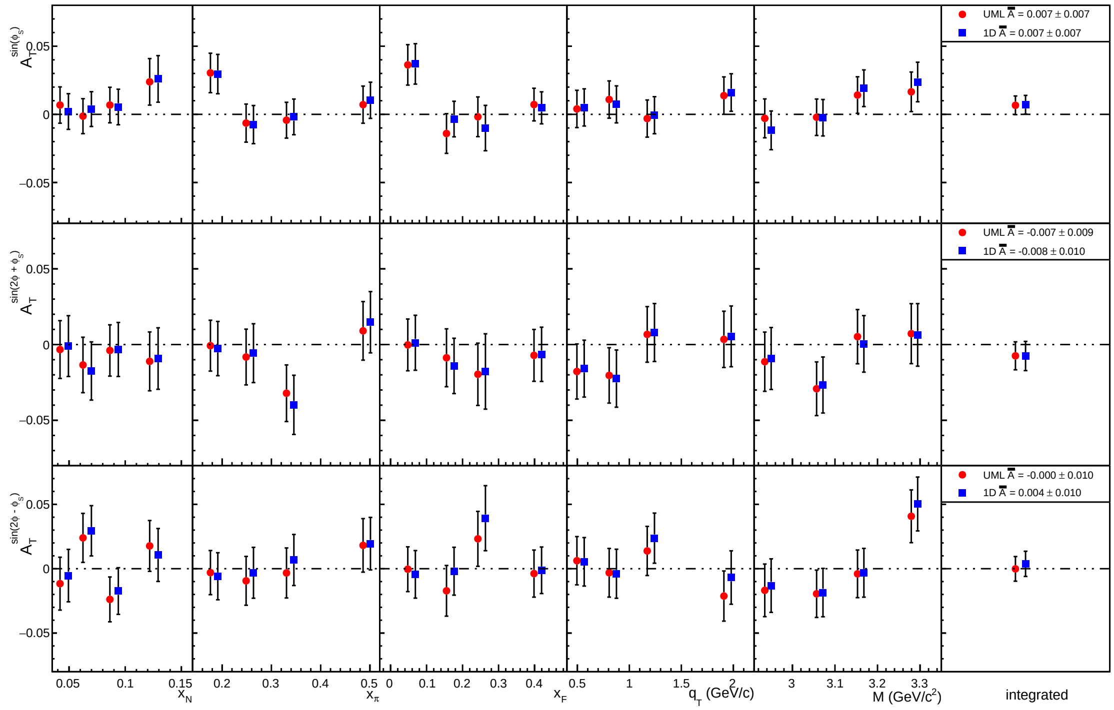

Figure 6.5: The average of the 2015 and 2018 J/ψ TSAs from both the 1D double ratio (red circle) and EWUML (blue square) methods. Otherwise like Fig. 6.3

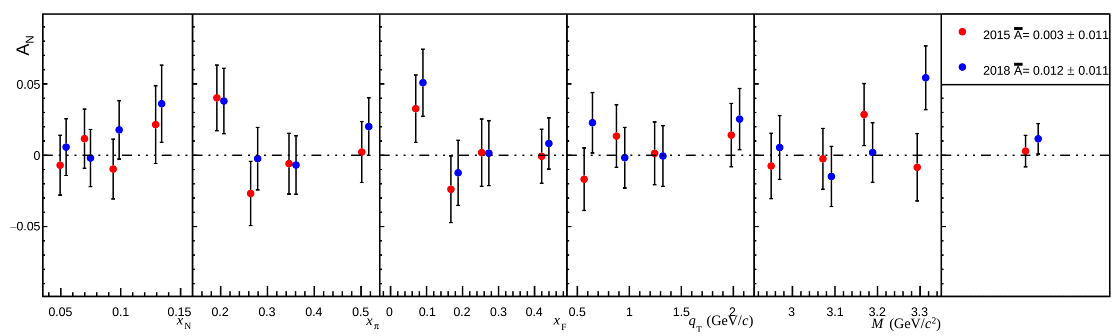

Figure 6.6: A_N results from the 2015 (red) and 2018 (blue) J/ψ data samples, binned in different kinematic variables and also extracted over the entire kinematic range.

6.3 Systematic Studies

The various systematic studies will be detailed in this section. The same tests performed in Sect. 5.3 on high mass DY data will be applied to J/ψ data.

6.3.1 Background Contamination

When extracting and interpreting the asymmetries, it is assumed that all events in the chosen mass range of 2.85 GeV/c^2 < $M_{\mu\mu}$ < 3.4 GeV/c^2 are J/ψ events. The background levels need to be estimated in order to

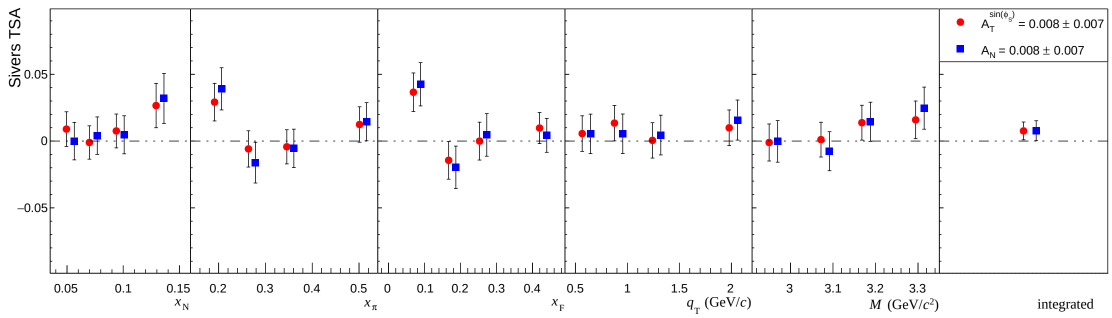

Figure 6.7: Average J/ψ $A_{\rm N}$ (blue square) and $A_{\rm T}^{\sin(\phi_{\rm S})}$ (red circle) results.

confirm that this assumption is reasonable. As mentioned in Sect. 5.3.1, there are currently some significant discrepancies between the dimuon invariant mass distributions in the most up-to-date COMPASS Monte Carlo and in the real data. For this reason, the MC cannot reliably be used to estimate the contamination in the chosen mass range. Instead, the background levels are estimated by applying a fitting routine to the real data invariant mass distributions.

The fit to real data is a sum of multiple functions. Two Gaussian functions are used, one modeling the J/ψ contribution and one modeling the ψ' contribution. The mean of the ψ' distribution is set to be 1.19 times the mean of the J/ψ distribution in order to stay consistent with the difference between the known true masses of the two mesons. Additionally, the width of the ψ' peak is constrained to differ from the width of the J/ψ peak by no more than 10%, because the resolution of the two resonances should be similar. The remaining background is modeled in two alternative ways: with a single curve defined as a

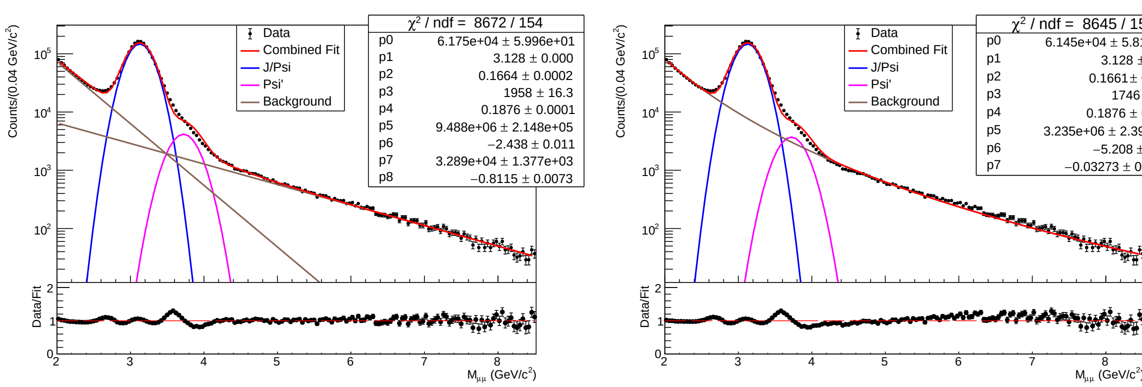

(a) (b)

Figure 6.8: The 2015 dimuon invariant mass distribution fit with a sum of two Gaussians and either (a) two exponential curves or (b) a polynomial multiplied by an exponential . In (a) the fit is of the form $f = p_0 e^{-(x-p_1)^2/2p_2^2} + p_3 e^{-(x-1.19p_1)^2/2p_4^2} + p_5 e^{p_6 x} + p_7 e^{p_8 x}$ and in (b) the fit is of the form $f = p_0 e^{-(x-p_1)^2/2p_2^2} + p_3 e^{-(x-1.19p_1)^2/2p_4^2} + p_5 x^{p_6} e^{p_7 x}$.

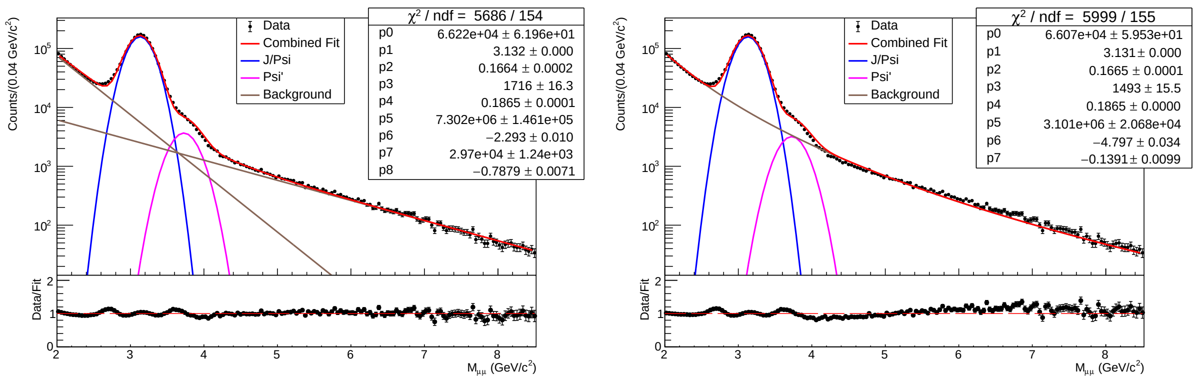

(a) (b)

Figure 6.9: The 2018 dimuon invariant mass distribution fit as described in the caption of Fig. 6.8.

2015				
Mass Range	Background polynomial×exponential		Background 2 exponentials	
(GeV/c^2)	J/ψ Purity (%)	Relative Number of Events (%)	J/ψ Purity (%)	Relative Number of Events (%)
[2.85,3.4]	92.4	100	92.9	100
[2.9,3.4]	93.0	96	93.5	96
[3.0,3.25]	94.4	61	94.8	61

2018				
Mass Range	Background polynomial×exponential		Background 2 exponentials	
(GeV/c^2)	J/ψ Purity (%)	Relative Number of Events (%)	J/ψ Purity (%)	Relative Number of Events (%)
[2.85,3.4]	92.5	100	92.6	100
[2.9,3.4]	93.1	96	93.3	96
[3.0,3.25]	94.5	61	94.6	61

Table 6.2: Estimated purity of J/ψ events in the given dimuon invariant mass region based on fits to real data, along with the change in the number of events due to narrowing the mass region.

polynomial multiplied by an exponential, or with two exponential curves, one modeling the low mass region and one modeling the high mass region. Both models were applied to the data and found to give consistent background estimates. The fits applied to the 2015 and 2018 data samples (including all periods except 2018 P00) are shown in Figs. 6.8 and 6.9.

After the fit has been applied to the data, the curves are integrated over the desired mass range and the percent contribution from the J/ψ peak is determined. The background levels in three different mass ranges are shown in Table 6.2. In the region chosen for the analysis (2.85 GeV/c^2 < $M_{\mu\mu}$ < 3.4 GeV/c^2), the contamination level is around 7.5% in both 2015 and 2018. This value decreases by a few percent as the mass range is narrowed, but the loss of statistics outweighs this small improvement in purity. Therefore, it is concluded that the selected mass range is satisfactory.

6.3.2 Target Cell Event Migration

As in the DY case (see Sect. 5.3.2), an additional dilution factor needs to be assigned due to some event vertices being reconstructed in the wrong target cell or outside both cells. Unlike the DY case, the z-vertex distributions for events in the J/ψ mass range do not agree very well between the 2018 MC and real data. This is shown by bin in Fig. 6.10a. In particular, the relative number of events in each target cell is different between MC and real data (RD). This difference can be mostly corrected by reweighting the MC to better match the data. The MC events are divided into three distributions based on the location of the MC-generated z-vertex: in the upstream cell, downstream cell, or outside the two cells. These distributions are plotted as a function of reconstructed vertex location and then are renormalized based on a fit to the real data z-vertex distribution. The three rescaled distributions are then summed together. The new reweighted MC distribution is shown in Fig. 6.10b to agree much better with the real data distribution. The additional dilution factors are estimated using the rescaled 2018 MC, as shown in Fig. 6.11. As in the DY case, the values from the 2018 MC are used for both 2015 and 2018 TSA extraction because of the consistency of the z-vertex distributions between the two years. The new dilution factors by bin are recorded in Table 6.3. Note that the overall dilution due to mixing is a few percent higher than in the high mass DY case.

Kinematic Bin		**J/ψ Mixing Factors**	
		Upstream	**Downstream**
x_{N}	[0.00, 0.06)	0.91	0.90
	[0.06, 0.08)	0.92	0.92
	[0.08, 0.11)	0.93	0.92
	[0.11, 1.00]	0.93	0.92
x_{π}	[0.00, 0.21)	0.93	0.93
	[0.21, 0.28)	0.93	0.93
	[0.28, 0.38)	0.92	0.92
	[0.38, 1.00]	0.92	0.89
x_{F}	[-1.0, 0.10)	0.93	0.93
	[0.10, 0.20)	0.93	0.93
	[0.20, 0.31)	0.92	0.92
	[0.31, 1.00]	0.91	0.89
q_{T}	[0.50, 0.72)	0.92	0.92
	[0.72, 1.04)	0.92	0.92
	[1.04, 1.48)	0.92	0.92
	[1.48, 5.00]	0.94	0.92
$M_{\mu\mu}$	[2.85, 3.02)	0.85	0.96
	[3.02, 3.12)	0.94	0.96
	[3.12, 3.22)	0.94	0.92
	[3.22, 3.40]	0.91	0.78

Table 6.3: Additional dilution factors due to cell-to-cell event migration in J/ψ events.

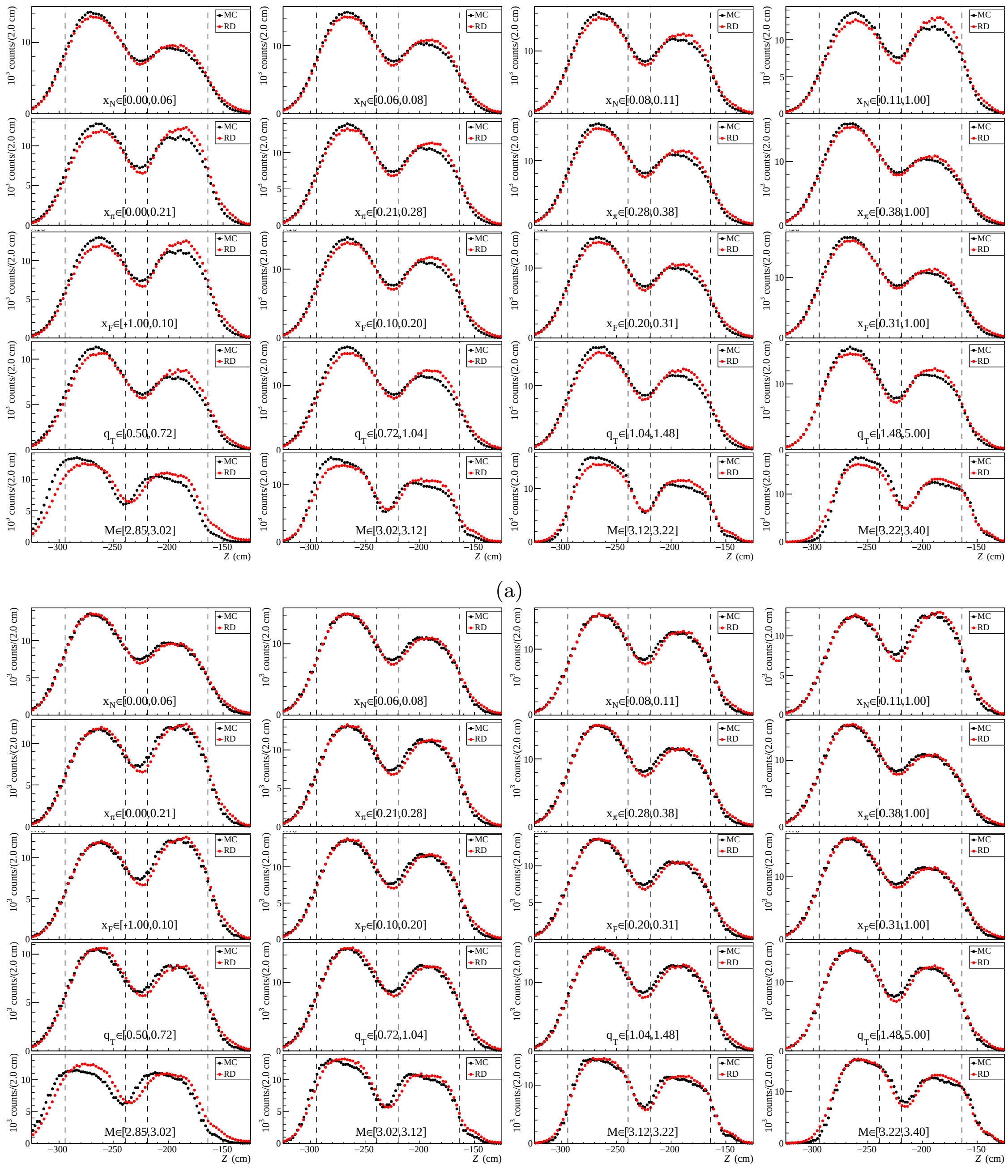

(a)

(b)

Figure 6.10: Comparison of real data and MC z-vertex distributions (a) before and (b) after rescaling.

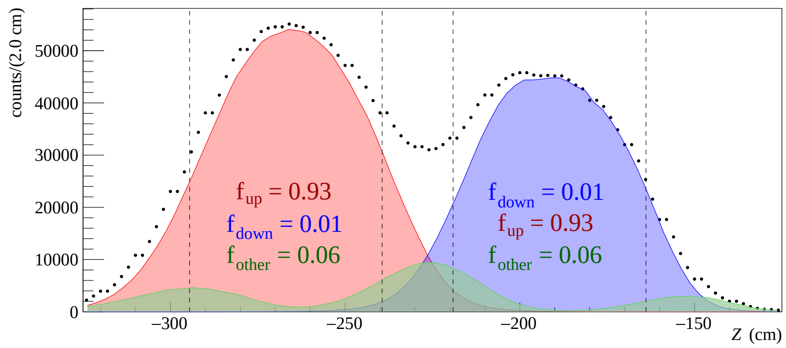

(a)

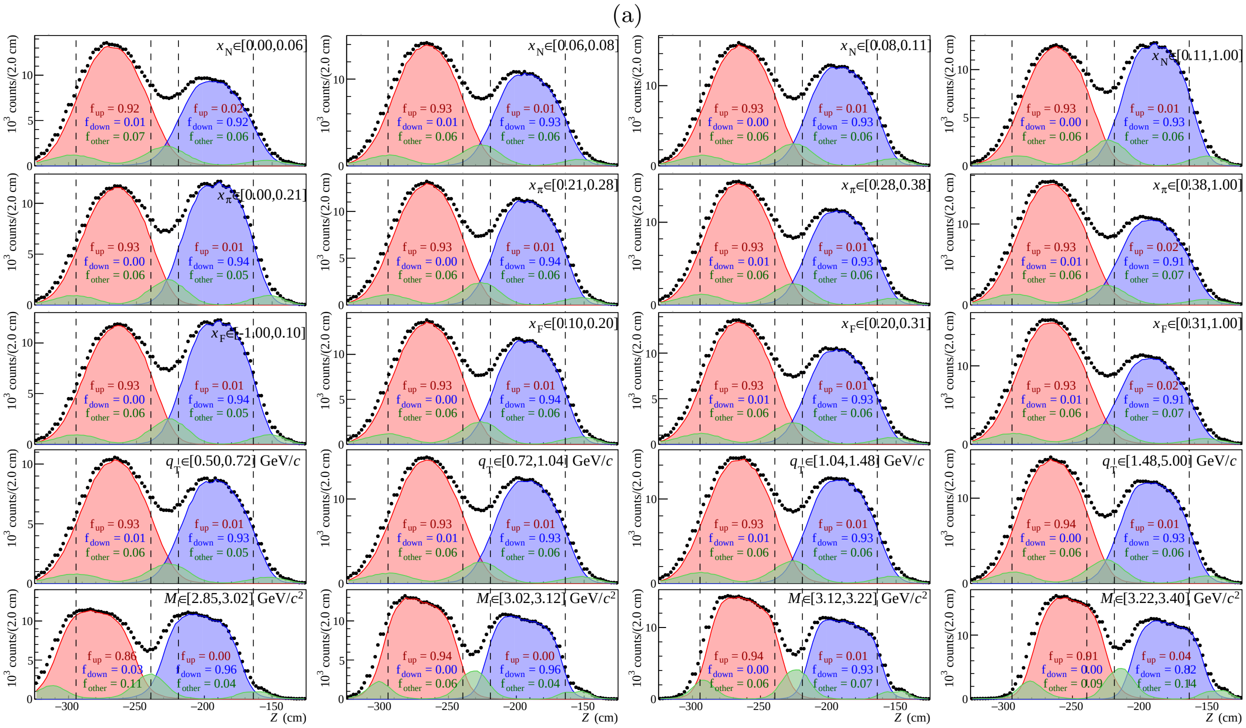

(b)

Figure 6.11: Target cell event migration in the J/ψ mass range estimated based on 2018 MC, (a) overall and (b) binned in kinematic variables. Layout and colors are the same as Fig. 5.10.

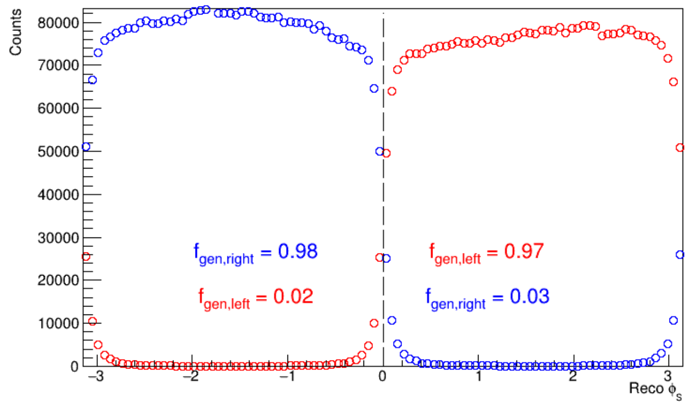

(a)

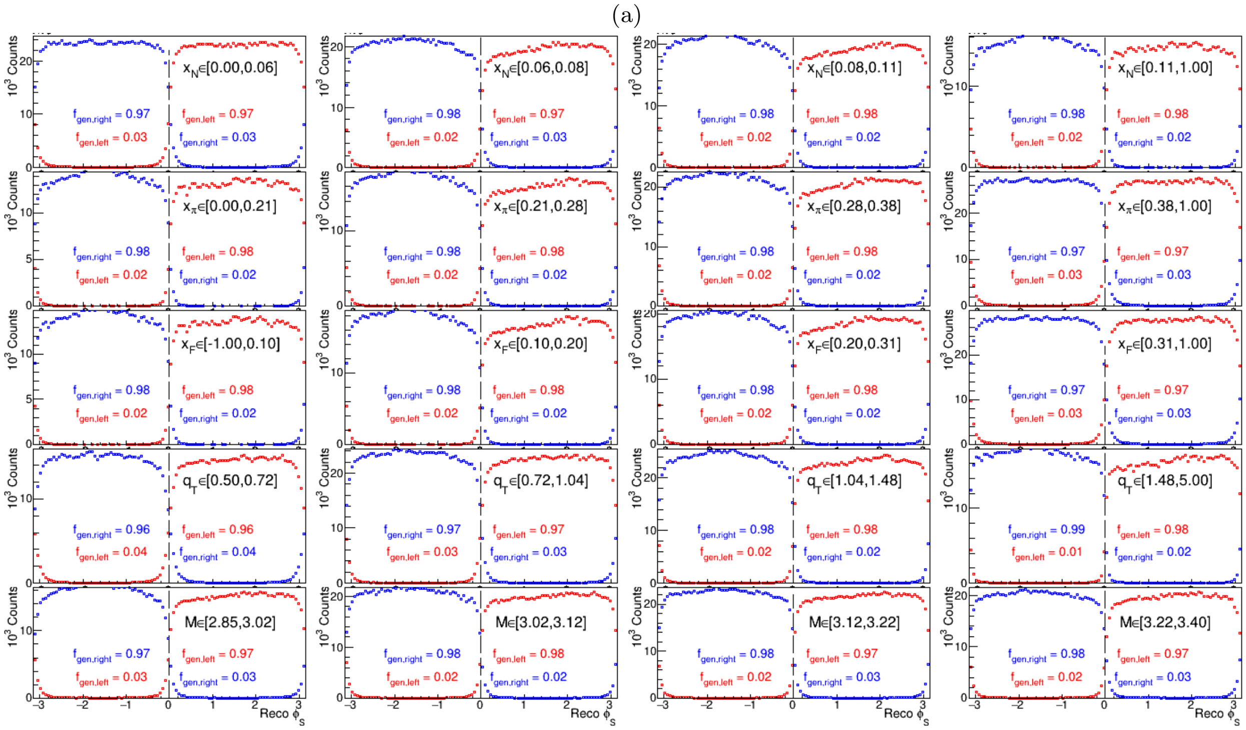

(b)

Figure 6.12: Left-right event migration in the J/ψ mass range estimated based on 2018 MC, (a) overall and (b) binned in kinematic variables. The layout and colors are the same as Fig. 5.13.

6.3.3 Left-Right Event Migration

The amount of left-right event migration due to finite angular resolution must also be recalculated in the J/ψ mass range. The results are shown in Fig. 6.12. The level of migration is 2-3%, about the same as in the high mass case. A systematic uncertainty on A_N is estimated using the same method described in

Kinematic		$\sigma_{\text{sys}}/\sigma_{\text{stat}}$	
		2015	**2018**
$x_{\rm N}$	[0.00, 0.06)	0.021	0.001
	[0.06, 0.08)	0.014	0.014
	[0.08, 0.11)	0.004	0.019
	[0.11, 1.00]	0.033	0.024
x_π	[0.00, 0.23)	0.046	0.039
	[0.23, 0.30)	0.017	0.031
	[0.30, 0.40)	0.012	0.008
	[0.40, 1.00]	0.037	0.032
$x_{\rm F}$	[-1.0, 0.125)	0.051	0.042
	[0.125, 0.21)	0.032	0.014
	[0.21, 0.30)	0.039	0.016
	[0.30, 1.00]	0.043	0.029
$q_{\rm T}$	[0.00, 0.72)	0.048	0.044
	[0.72, 1.04)	0.022	0.042
	[1.04, 1.48)	0.013	0.013
	[1.48, 5.00]	0.034	0.020
$M_{\mu\mu}$	[2.85, 3.02)	0.033	0.001
	[3.02, 3.12)	0.004	0.025
	[3.12, 3.22)	0.092	0.056
	[3.22, 3.40]	0.048	0.094

Table 6.4: Systematic uncertainty of $A_{\rm N}$ as a fraction of statistical uncertainty due to left-right event migration in J/ψ data.

Sect. 5.3.3. The change to $A_{\rm N}$ due to the migration is

$$\Delta A_{\rm N} = A_{\rm N,measured} - A_{\rm N,true} = \frac{1-(\xi_1-\xi_2)}{\xi_1-\xi_2} A_{\rm N,measured}, \tag{6.1}$$

and the size of the systematic uncertainty relative to the statistical error is

$$\frac{\sigma_{\rm sys}}{\sigma_{\rm stat}} = \frac{\Delta A_{\rm N}}{\sigma_{\rm stat}}. \tag{6.2}$$

Since the migration levels are about the same between high mass and J/ψ, but the statistical error bars are much smaller in the J/ψ case, the systematic uncertainty due to left-right migration is even more insignificant in the J/ψ mass range compared to the high mass range. The uncertainty in each bin is shown in Table 6.4. On average, the systematic uncertainty comes to 1.5% of the statistical error in 2015 and just 0.4% in 2018.

6.3.4 False Asymmetries

The same false asymmetry tests from Sect. 5.3.4 will be applied in the J/ψ mass range to test the potential impact of acceptance and other spectrometer effects on the TSA extraction. As before, the false asymmetries are not all independent of each other. The largest effect from the various false asymmetries and the RLTB test (Sect. 6.3.5) will be assigned as the systematic uncertainty.

UML TSAs

Here the three false asymmetry tests using the EWUML method described in Sect. 5.3.4 will be reviewed. In the first test (FA1), the polarization of one of the target cells is flipped when defining the log-likelihood function (Eq. 4.15) so that the physics amplitudes cancel. In the second test (FA2), the events are randomly divided into two subperiods based on whether the run number is even or odd, rather than based on the cell polarization. Any physics asymmetries should average out to zero in this test. Finally, in the third test (FA3) each target cell is analyzed individually. Each cell is divided into an upstream and downstream half, and the two halves are treated as the two target cells in the EWUML calculation. Since the entire target cell has the same polarization in reality, there should be no physics asymmetries in this amplitude.

If there are no false asymmetry effects from the spectrometer or other sources, the false asymmetries just described should lie within a Gaussian distribution centered on zero, with a width equal to the statistical error. Therefore the systematic uncertainty is assigned using the following formula:

$$\begin{aligned} \frac{\sigma_{\mathrm{sys}}}{\sigma_{\mathrm{stat}}} &= 0 && \text{if} \quad |A_{\mathrm{false}}| < 0.68\,\sigma_{\mathrm{stat}} \\ \frac{\sigma_{\mathrm{sys}}}{\sigma_{\mathrm{stat}}} &= \sqrt{\frac{A_{\mathrm{false}}^2}{\sigma_{\mathrm{stat}}^2} - 0.68^2} && \text{otherwise.} \end{aligned} \tag{6.3}$$

This systematic uncertainty is calculated period-by-period and bin-by-bin, and a weighted average of the periods is performed. The period-averaged false asymmetries for 2015 and 2018 respectively are shown in Fig. 6.13 and 6.14. The systematic uncertainties in 2015 and 2018 from each false asymmetry, calculated by bin using Eq. 6.3, are shown in Fig. 6.15 and Fig. 6.16 respectively as a fraction of the statistical uncertainty.

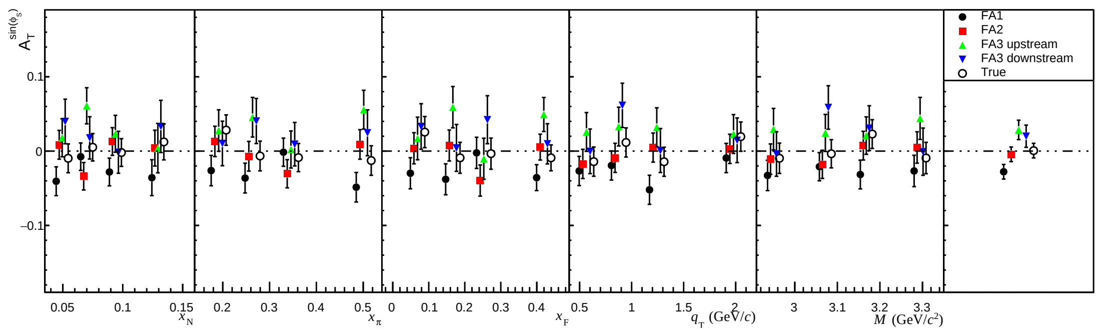

(a)

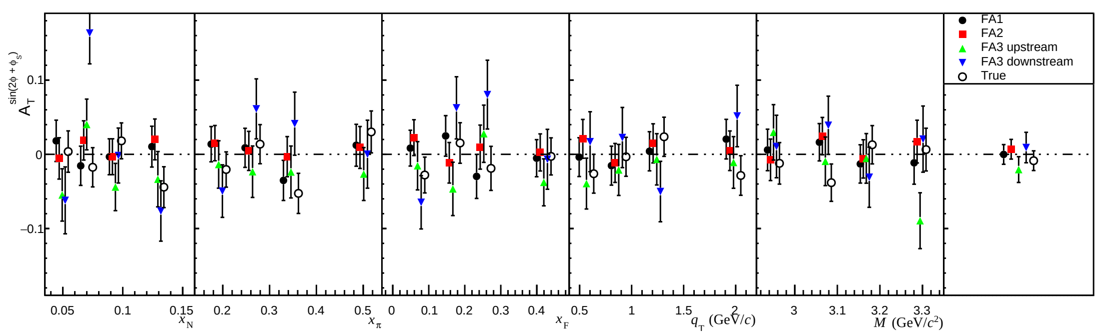

(b)

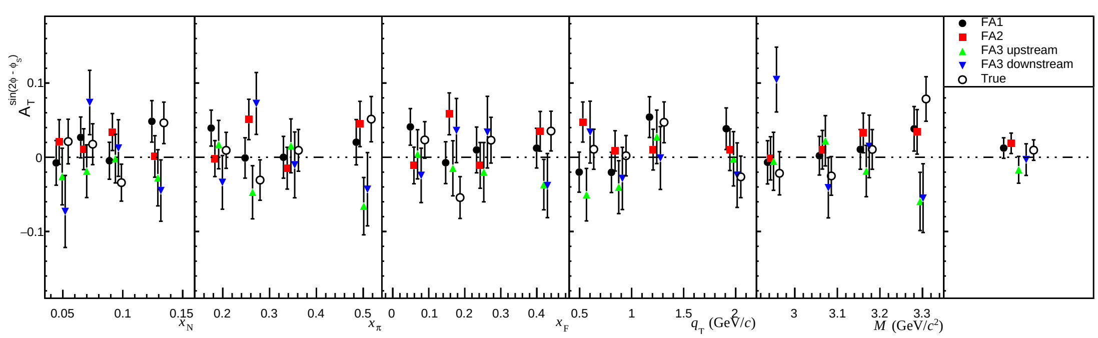

(c)

Figure 6.13: 2015 period-averaged J/ψ false asymmetries for the (a) Sivers, (b) pretzelosity, and (c) transversity TSAs. The extracted physics asymmetry is also shown for comparison.

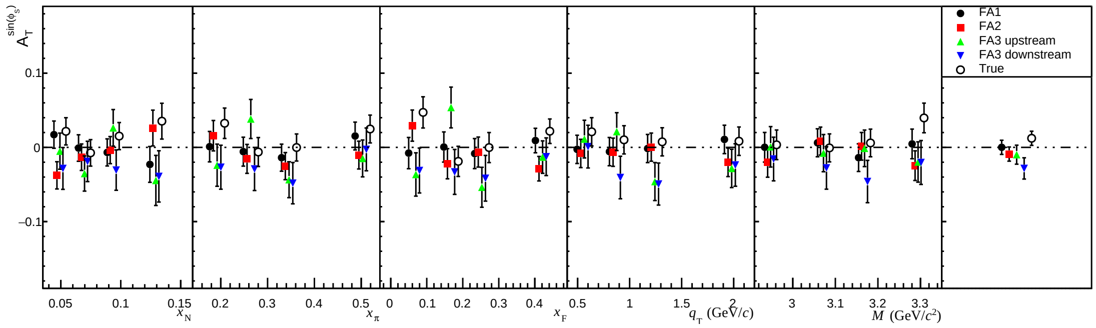

(a)

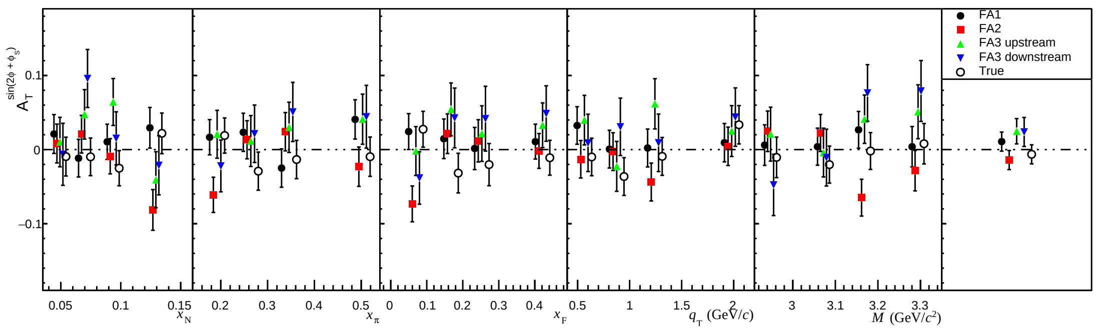

(b)

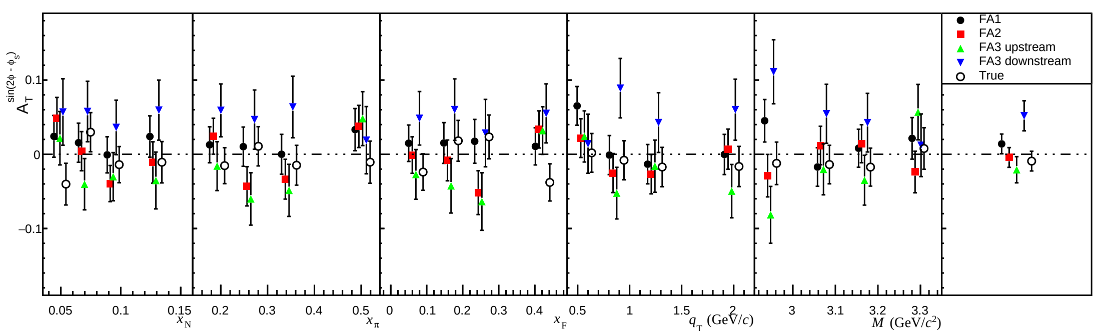

(c)

Figure 6.14: 2018 period-averaged J/ψ false asymmetries for the (a) Sivers, (b) pretzelosity, and (c) transversity TSAs. The extracted physics asymmetry is also shown for comparison.

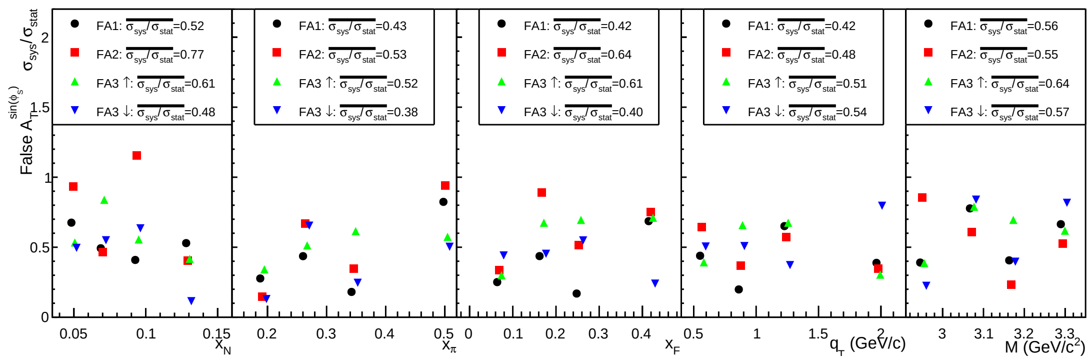

(a)

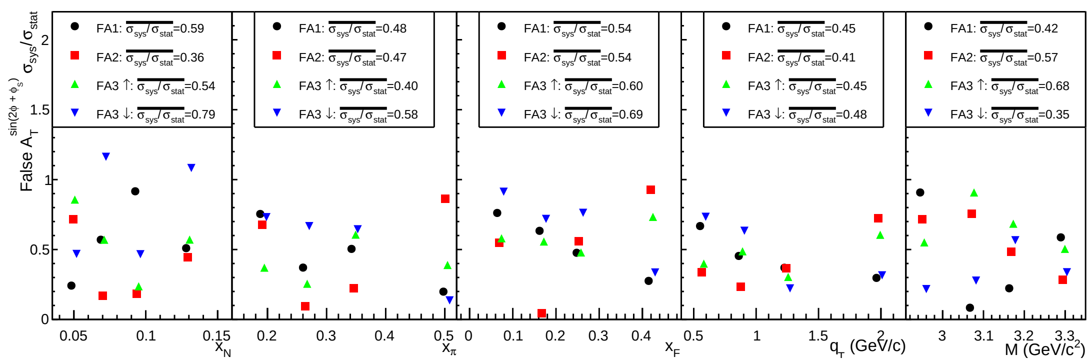

(b)

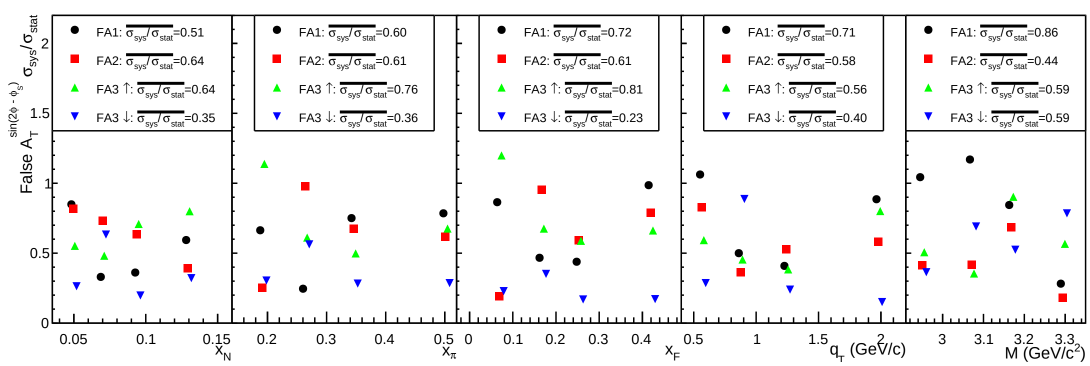

(c)

Figure 6.15: Systematic uceratintíes as a fraction of statistical uncertainties from false asymmetry tests for 2015 J/ψ (a) Sivers, (b) pretzelosity, and (c) transversity.

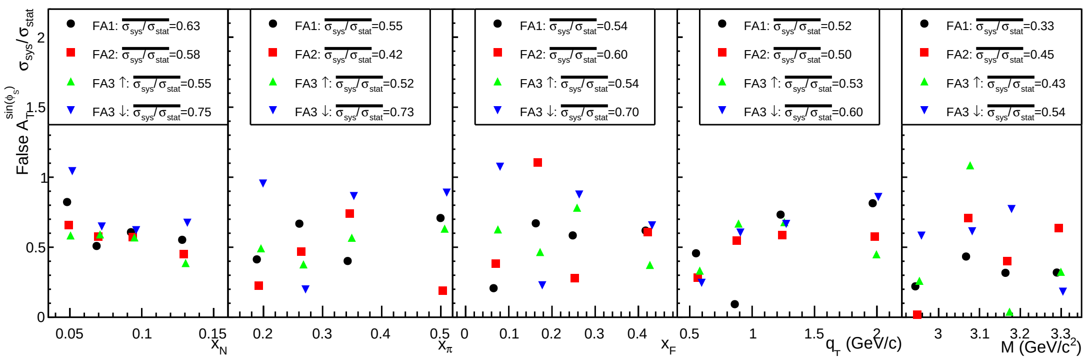

(a)

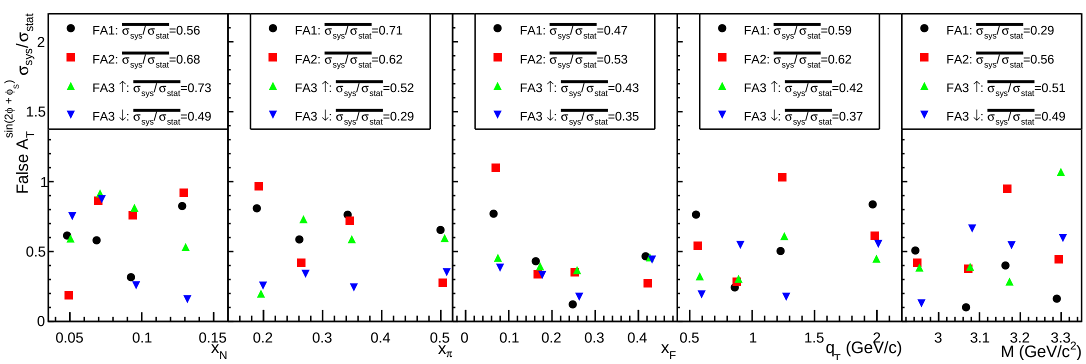

(b)

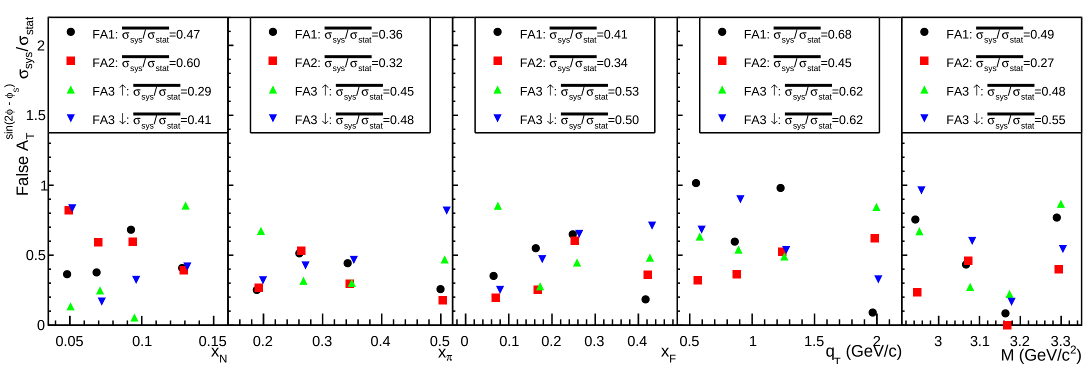

(c)

Figure 6.16: Systematic unceratinties as a fraction of statistical uncertainties from false asymmetry tests for 2018 J/ψ (a) Sivers, (b) pretzelosity, and (c) transversity.

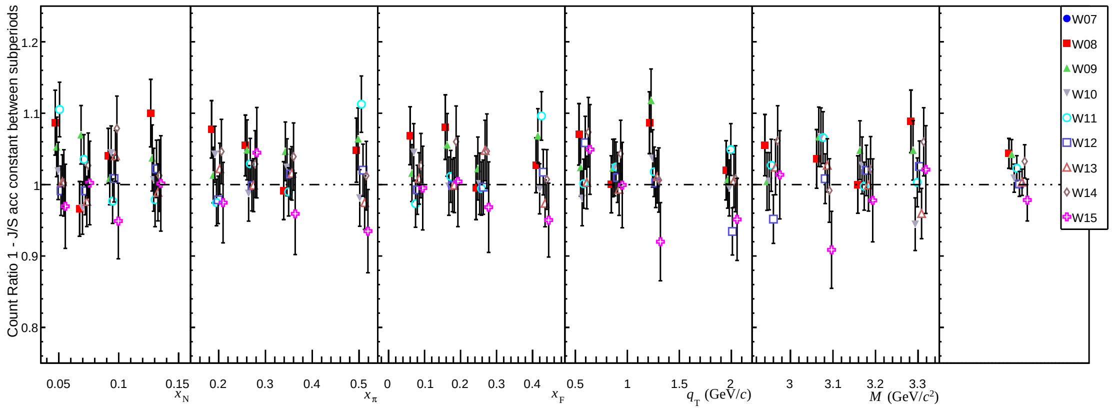

(a)

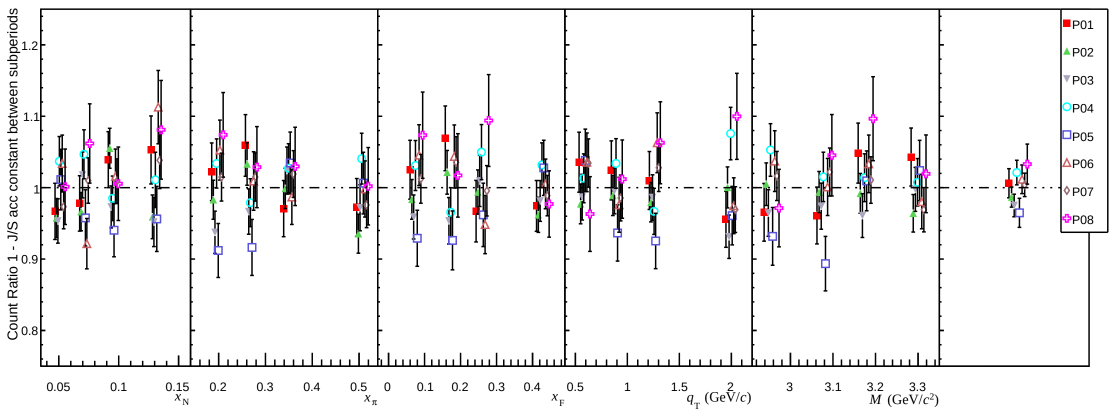

(b)

Figure 6.17: The false asymmetry ratio R_1 by period and kinematic bin from (a) 2015 and (b) 2018 J/ψ data. R_1 should equal one if the Jura/Saleve acceptance ratio is constant between subperiods.

Left-Right A_{N}

The same left-right false asymmetry ratios that were described in Sect. 5.3.4 will be tested here on J/ψ data in order to quantify the systematic uncertainty for A_{N}. As a reminder, the two ratios are

$$R_1 = \frac{N_\ell^{1+} N_\mathrm{r}^{2-} N_\ell^{1-} N_\mathrm{r}^{2+}}{N_\mathrm{r}^{1+} N_\ell^{2-} N_\mathrm{r}^{1-} N_\ell^{2+}} = \frac{a_\mathrm{J}^{1+} a_\mathrm{J}^{2-}}{a_\mathrm{S}^{1+} a_\mathrm{S}^{2-}} \frac{a_\mathrm{S}^{1-} a_\mathrm{S}^{2+}}{a_\mathrm{J}^{1-} a_\mathrm{J}^{2+}} \tag{6.4}$$

and

$$R_2 = \frac{N_\mathrm{r}^{1+} N_\ell^{1-} N_\ell^{2+} N_\mathrm{r}^{2-}}{N_\ell^{1+} N_\mathrm{r}^{1-} N_\mathrm{r}^{2+} N_\ell^{2-}} = \frac{a_\mathrm{S}^{1+} a_\mathrm{S}^{1-}}{a_\mathrm{J}^{1+} a_\mathrm{J}^{1-}} \frac{a_\mathrm{J}^{2+} a_\mathrm{J}^{2-}}{a_\mathrm{S}^{2+} a_\mathrm{S}^{2-}}. \tag{6.5}$$

The ratio R_1 should equal one if the Jura/Saleve acceptance ratio is equal between subperiods, or equivalently, between target polarization configuration. The ratio R_2 should equal one if the Jura/Saleve acceptance

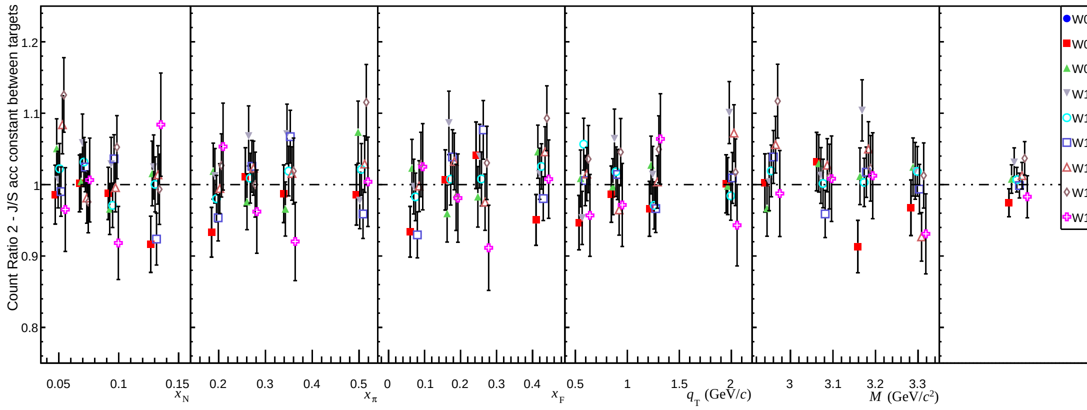

(a)

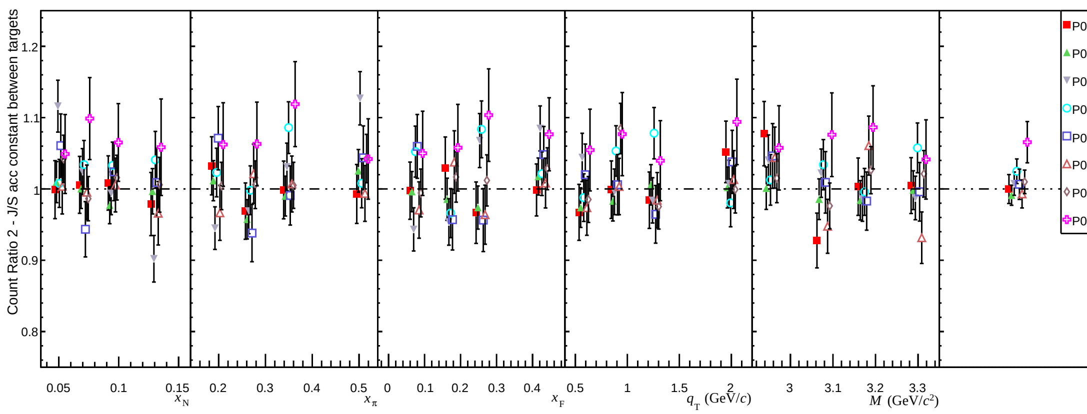

(b)

Figure 6.18: The false asymmetry ratio R_2 by period and kinematic bin from (a) 2015 and (b) 2018 J/ψ data. R_2 should equal one if the Jura/Saleve acceptance ratio is constant between target cells.

ratio is equal for each target cell. The values of R_1 and R_2 should lie within Gaussian distributions centered on one with widths equal to the respective statistical errors. Therefore, the systematic uncertainty due to R_1 and R_2 is calculated using the same formula from Sect. 5.3.4:

$$\begin{aligned} \frac{\sigma_{\text{sys}}}{\sigma_{\text{stat}}} &= 0 && \text{if} \quad |R_{1,2} - 1| < 0.68\, \sigma_{R_{1,2}} \\ \frac{\sigma_{\text{sys}}}{\sigma_{\text{stat}}} &= \sqrt{\frac{(R_{1,2}-1)^2}{\sigma^2_{R_{1,2}}} - 0.68^2} && \text{otherwise.} \end{aligned} \tag{6.6}$$

The period-by-period results for R_1 and R_2 are shown in Fig. 6.17 and 6.18 respectively. The systematic uncertainties from each ratio in each kinematic bin are shown in Fig. 6.19.

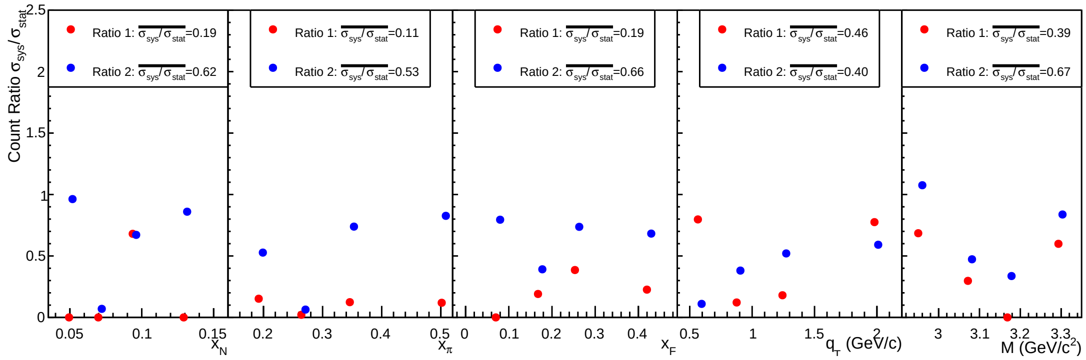

(a)

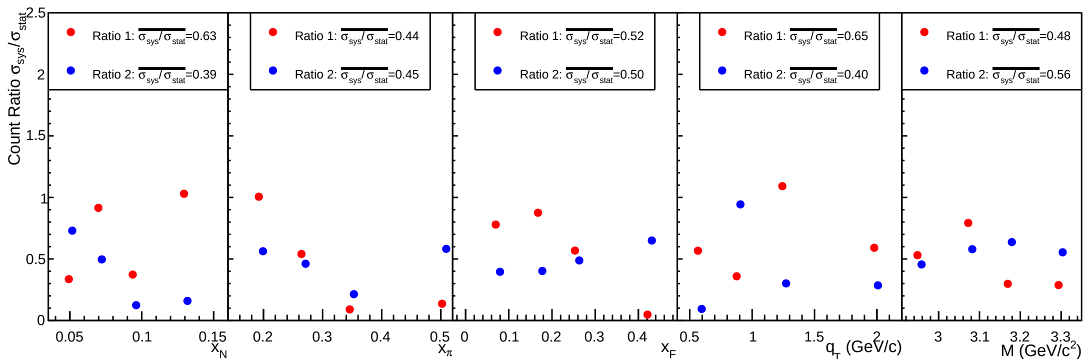

(b)

Figure 6.19: Systematic uncertainties as a fraction of statistical uncertainties due to false asymmetry ratios R_1 (red) and R_2 (blue) for J/ψ (a) 2015 and (b) 2018 $A_{\rm N}$ results.

6.3.5 Right-Left-Top-Bottom Test

The TSAs should be independent of where in the spectrometer the outgoing muon tracks pass through. The right-left-top-bottom (RLTB) test will be performed on the J/ψ TSAs (and just the top-bottom test will be performed on $A_{\rm N}$) as another way to quantify the impact of spectrometer effects on the asymmetry extraction. As a reminder from Sect. 5.3.5, 'top' refers to $\phi_{\mu_+} > 0$, 'bottom' to $\phi_{\mu_+} < 0$, 'left' to $\pi/2 < \phi_{\mu_+} < \pi$ or $-\pi < \phi_{\mu_+} < -\pi/2$, and 'right' to $0 < \phi_{\mu_+} < \pi/2$ or $-\pi/2 < \phi_{\mu_+} < 0$. The TSAs are compared between the right and left hemispheres as well as the top and bottom hemispheres. A systematic uncertainty is then calculated in each case:

$$\begin{aligned} \frac{\sigma_{\rm sys}}{\sigma_{\rm stat}} &= 0 && \text{if} \quad \alpha < 0.68 \\ \frac{\sigma_{\rm sys}}{\sigma_{\rm stat}} &= \sqrt{\alpha^2 - 0.68^2} && \text{otherwise,} \end{aligned} \tag{6.7}$$

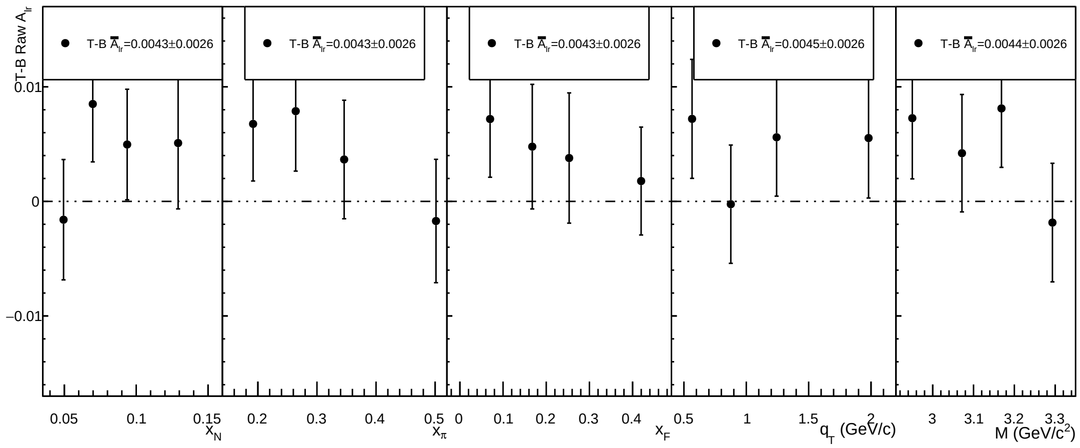

(a)

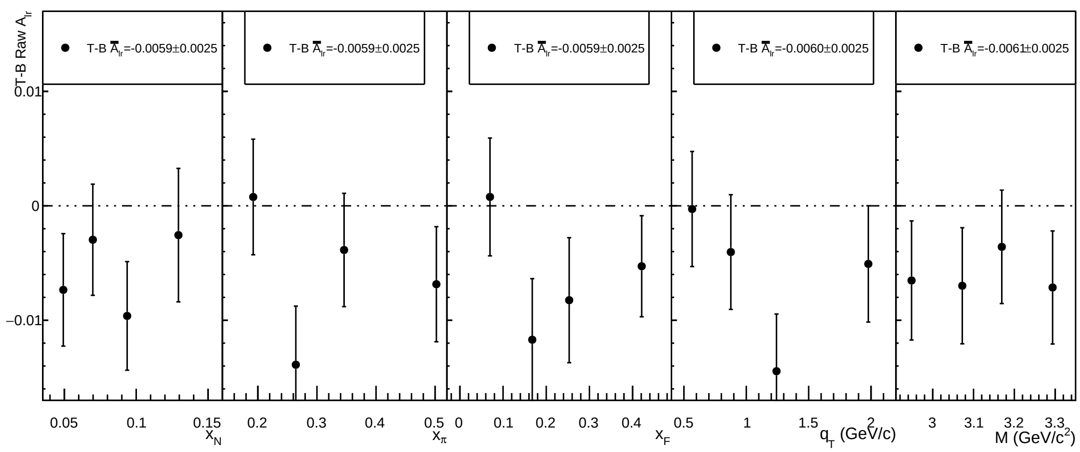

(b)

Figure 6.20: Period-averaged difference between A_N in the top and bottom hemisphers of the spectrometer for J/ψ (a) 2015 and (b) 2018 data.

where

$$\alpha = \frac{|A_{\text{top(left)}} - A_{\text{bottom(right)}}|}{\sqrt{\sigma^2_{\text{top(left)}} + \sigma^2_{\text{bottom(right)}}}}. \tag{6.8}$$

Figure 6.20 shows the period-averaged differences of $A_{\rm N}$ calculated in the top and bottom hemispheres. Figures 6.22 and 6.23 show period-averaged differences between the TSAs calculated in the top and bottom and right and left hemispheres in 2015 and 2018 respectively. The percent systematic uncertainties on $A_{\rm N}$ from the top-bottom test are shown in Fig. 6.21. The systematic uncertainties from the top-bottom and right-left comparisons are shown in Fig. 6.24 and Fig. 6.25 respectively for the Sivers, pretzelosity, and transversity TSAs.

The RLTB test is correlated with the previously described false asymmetry tests. Therefore, the method described in Sect. 5.3.5 is also used here to quantify an overall systematic uncertainty due to 'false asymmetries'. First, the uncertainties are averaged over each kinematic bin for each variable in order to average over statistical fluctuations. Then, the averages from each of the five kinematics are averaged together. Finally, the largest average is assigned to be the systematic uncertainty due to false asymmetries. The kinematic-averaged and final uncertainty values are shown for each TSA and A_{N} in Tables 6.5-6.8.

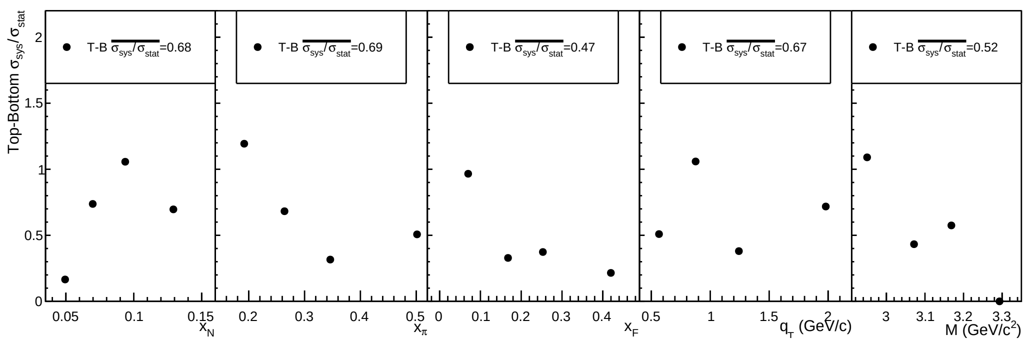

(a)

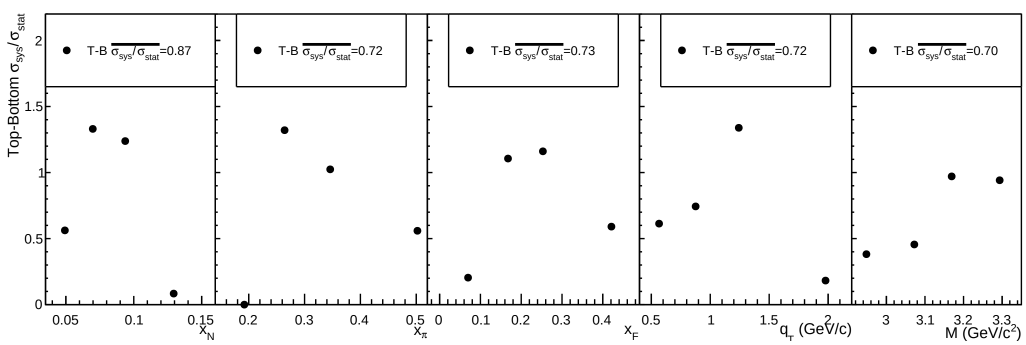

(b)

Figure 6.21: Systematic uncertainty for A_{N} due to the top-bottom test as a fraction of statistical uncertainty in J/ψ (a) 2015 and (b) 2018 data.

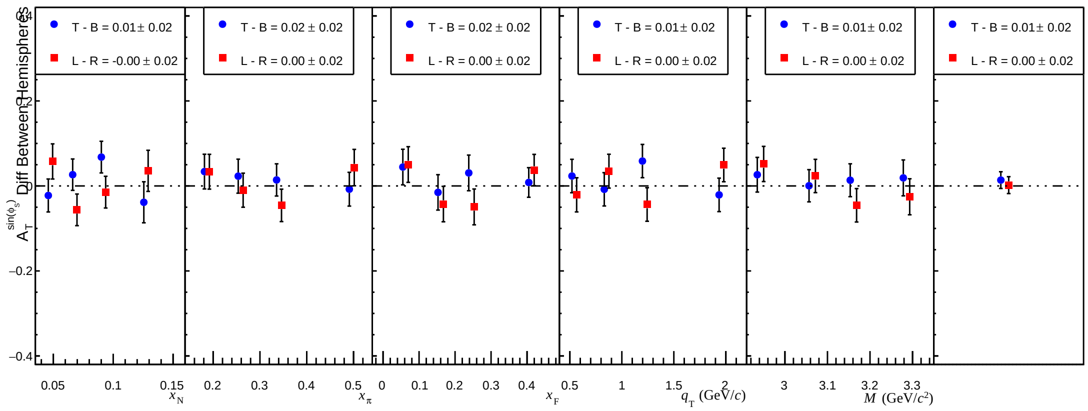

(a)

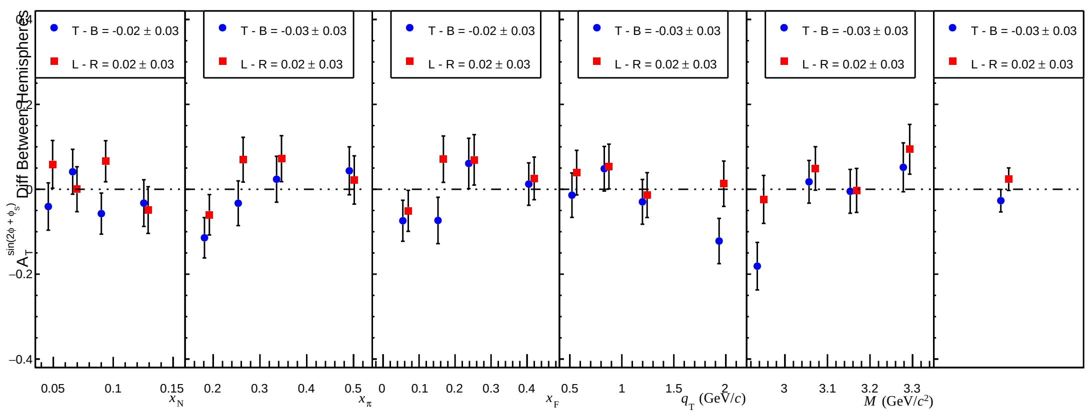

(b)

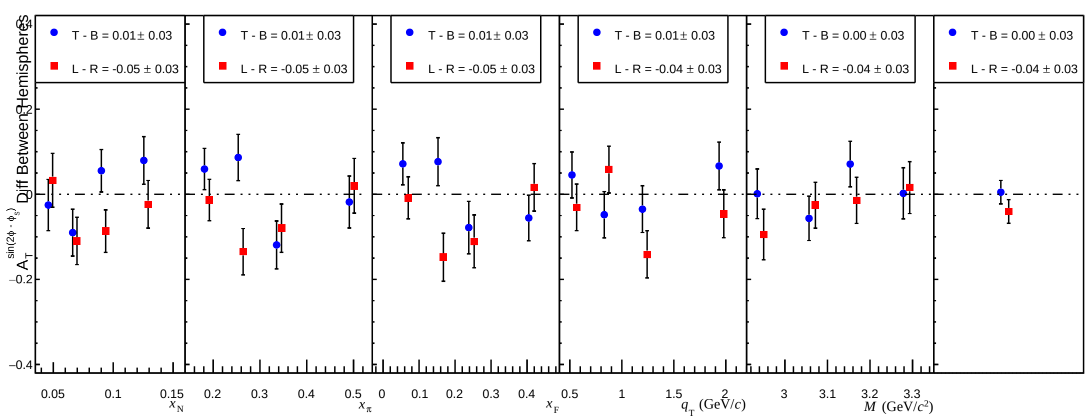

(c)

Figure 6.22: Period-averaged differences of the (a) Sivers, (b) pretzelosity, and (c) transversity TSAs between the top and bottom hemispheres (blue) and left and right hemispheres (red) in 2015 J/ψ data.

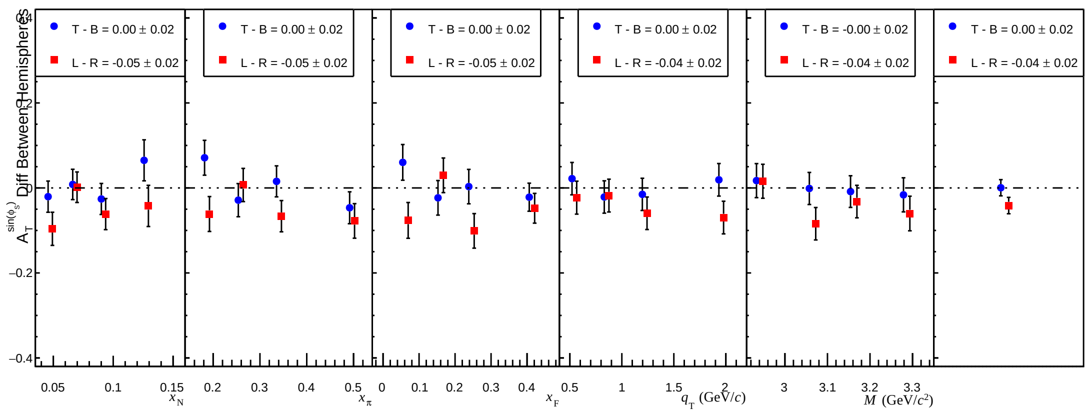

(a)

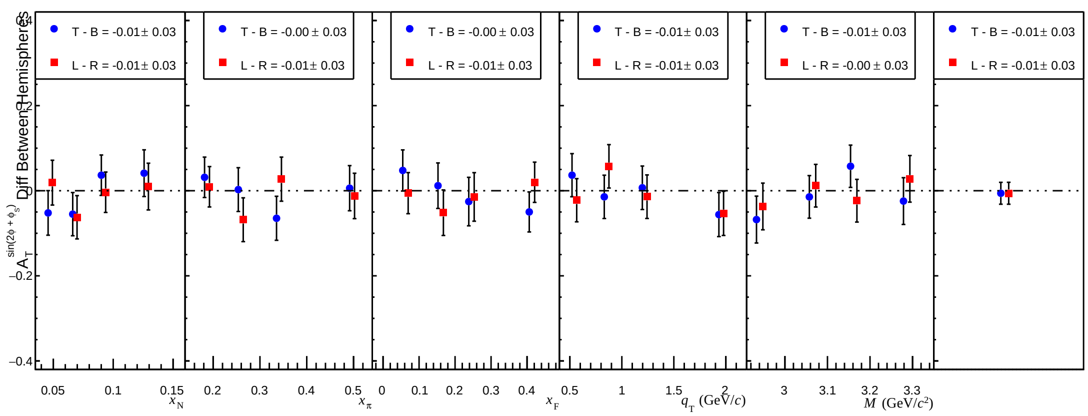

(b)

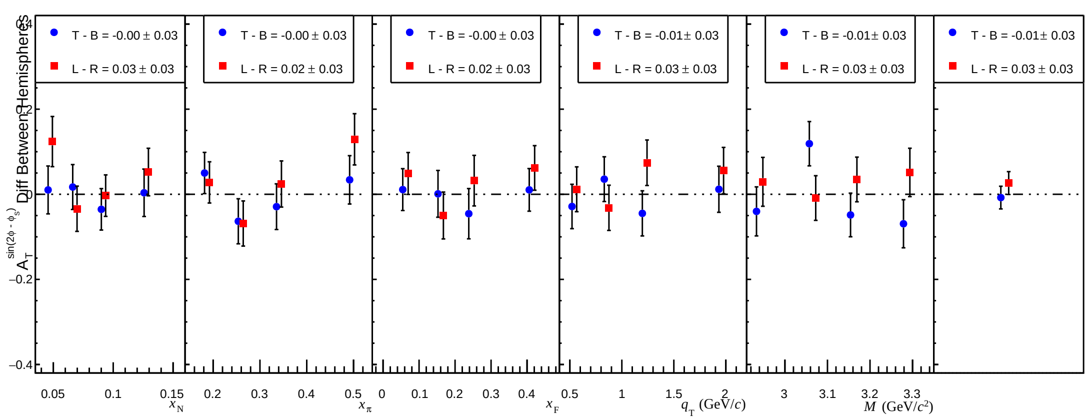

(c)

Figure 6.23: Period-averaged differences of the (a) Sivers, (b) pretzelosity, and (c) transversity TSAs between the top and bottom hemispheres (blue) and left and right hemispheres (red) in 2018 J/ψ data.

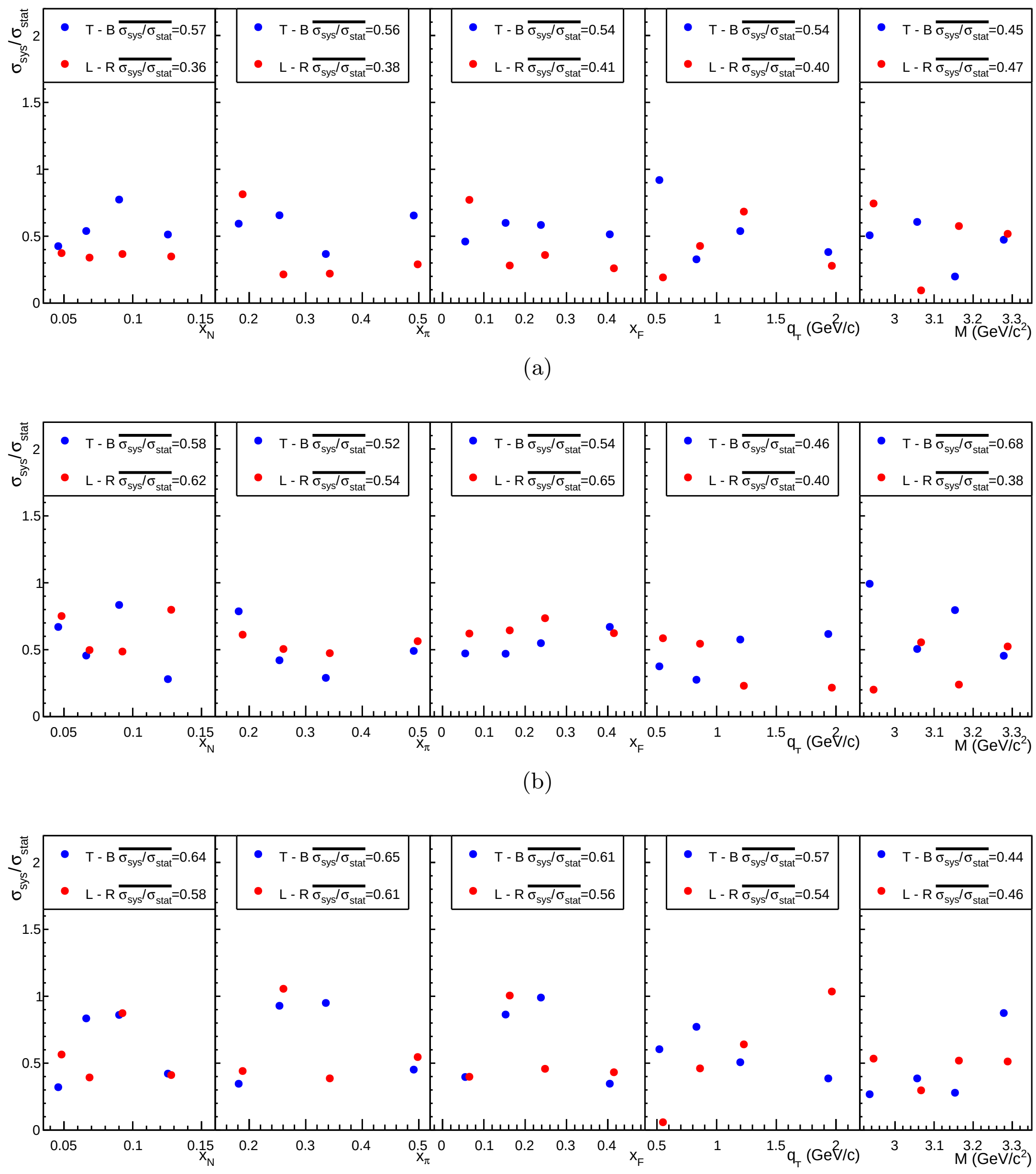

(a)

(b)

(c)

Figure 6.24: Systematic uncertainties due to the RLTB test as a fraction of statistical uncertainties for the (a) Sivers, (b) pretzelosity, and (c) transversity TSAs in 2015 J/ψ data.

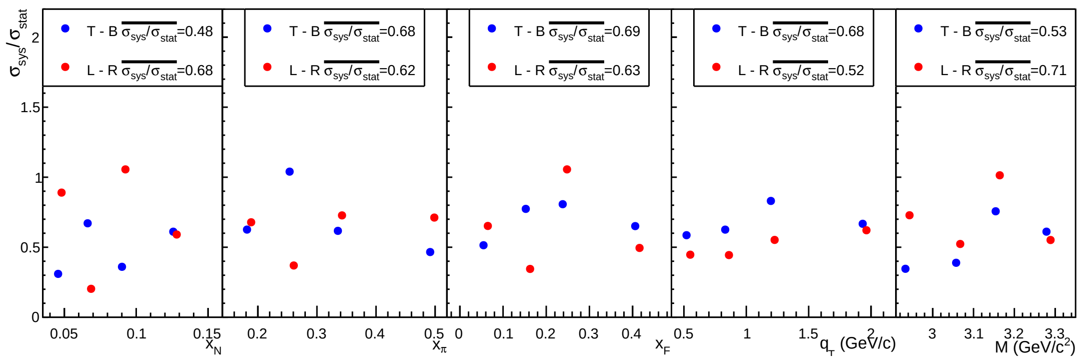

(a)

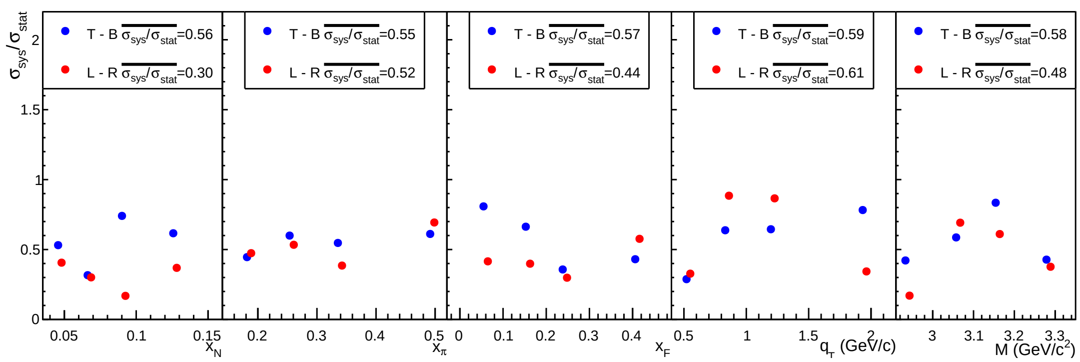

(b)

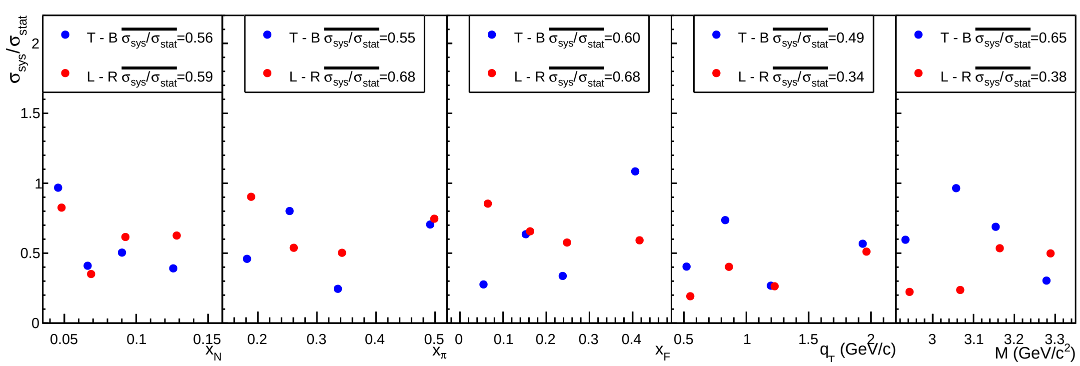

(c)

Figure 6.25: Systematic uncertainties due to the RLTB test as a fraction of statistical uncertainties for the (a) Sivers, (b) pretzelosity, and (c) transversity TSAs in 2018 J/ψ data.

Kinematic	**2015** $\sigma_{\text{sys}}/\sigma_{\text{stat}}$					
	FA1	FA2	FA3 1	FA3 2	RL	TB
x_N	0.52	0.77	0.61	0.48	0.36	0.57
x_π	0.43	0.53	0.52	0.38	0.38	0.56
x_F	0.42	0.64	0.61	0.40	0.41	0.54
q_T	0.42	0.48	0.51	0.54	0.40	0.54
$M_{\mu\mu}$	0.56	0.55	0.64	0.57	0.47	0.45
Average	0.47	***0.59***	0.58	0.47	0.40	0.53

Kinematic	**2018** $\sigma_{\text{sys}}/\sigma_{\text{stat}}$					
	FA1	FA2	FA3 1	FA3 2	RL	TB
x_N	0.63	0.58	0.58	0.75	0.68	0.48
x_π	0.55	0.42	0.52	0.73	0.62	0.68
x_F	0.54	0.60	0.54	0.70	0.63	0.69
q_T	0.52	0.50	0.53	0.60	0.52	0.68
$M_{\mu\mu}$	0.33	0.45	0.43	0.54	0.71	0.53
Average	0.51	0.59	0.58	***0.66***	0.63	0.61

Table 6.5: Average systematic uncertainty of J/ψ TSAs due to various false asymmetries, as a fraction of statistical uncertainty, for the Sivers TSA $A_{\mathrm{T}}^{\sin(\phi_{\mathrm{S}})}$. The values presented here are the average over the three bins of the identified kinematic variable. The average from each type of kinematic is averaged together in the last row, and the largest value (in bold italics) is the systematic uncertainty assigned to the results.

Kinematic	**2015** $\sigma_{\text{sys}}/\sigma_{\text{stat}}$					
	FA1	FA2	FA3 1	FA3 2	RL	TB
x_N	0.59	0.36	0.54	0.79	0.62	0.58
x_π	0.48	0.47	0.40	0.58	0.54	0.52
x_F	0.54	0.54	0.60	0.69	0.65	0.54
q_T	0.45	0.41	0.45	0.48	0.40	0.46
$M_{\mu\mu}$	0.42	0.57	0.68	0.35	0.38	0.68
Average	0.50	0.47	0.53	***0.58***	0.52	0.56

Kinematic	**2018** $\sigma_{\text{sys}}/\sigma_{\text{stat}}$					
	FA1	FA2	FA3 1	FA3 2	RL	TB
x_N	0.56	0.68	0.73	0.49	0.30	0.56
x_π	0.71	0.62	0.52	0.29	0.52	0.55
x_F	0.47	0.53	0.43	0.35	0.44	0.57
q_T	0.59	0.62	0.42	0.37	0.61	0.59
$M_{\mu\mu}$	0.29	0.56	0.51	0.49	0.48	0.58
Average	0.52	***0.60***	0.52	0.40	0.47	0.57

Table 6.6: Average systematic uncertainty of J/ψ TSAs due to various false asymmetries, as a fraction of statistical uncertainty, for the pretzelosity TSA $A_{\mathrm{T}}^{\sin(2\phi+\phi_{\mathrm{S}})}$. See the caption of Table 6.5 for more information.

Kinematic	**2015** $\sigma_{\text{sys}}/\sigma_{\text{stat}}$					
	FA1	FA2	FA3 1	FA3 2	RL	TB
x_N	0.51	0.64	0.64	0.35	0.58	0.64
x_π	0.60	0.61	0.76	0.36	0.61	0.65
x_F	0.72	0.61	0.81	0.23	0.56	0.61
q_T	0.71	0.58	0.56	0.40	0.54	0.57
$M_{\mu\mu}$	0.86	0.44	0.59	0.59	0.46	0.44
Average	***0.68***	0.58	0.67	0.39	0.55	0.58

Kinematic	**2018** $\sigma_{\text{sys}}/\sigma_{\text{stat}}$					
	FA1	FA2	FA3 1	FA3 2	RL	TB
x_N	0.47	0.60	0.29	0.41	0.59	0.56
x_π	0.36	0.32	0.45	0.48	0.68	0.55
x_F	0.41	0.34	0.53	0.50	0.68	0.60
q_T	0.68	0.45	0.62	0.62	0.34	0.49
$M_{\mu\mu}$	0.48	0.40	0.47	0.51	0.38	0.65
Average	0.48	0.42	0.47	0.50	0.53	***0.57***

Table 6.7: Average systematic uncertainty of J/ψ TSAs due to various false asymmetries, as a fraction of statistical uncertainty, for the transversity TSA $A_{\text{T}}^{\sin(2\phi-\phi_{\text{S}})}$. See the caption of Table 6.5 for more information.

Kinematic	**2015** $\sigma_{\text{sys}}/\sigma_{\text{stat}}$		
	R1	R2	TB
x_N	0.19	0.62	0.68
x_π	0.11	0.53	0.69
x_F	0.19	0.66	0.47
q_T	0.46	0.40	0.67
$M_{\mu\mu}$	0.39	0.67	0.52
Average	0.27	0.58	***0.61***

Kinematic	**2018** $\sigma_{\text{sys}}/\sigma_{\text{stat}}$		
	R1	R2	TB
x_N	0.64	0.39	0.87
x_π	0.44	0.45	0.72
x_F	0.52	0.50	0.73
q_T	0.65	0.40	0.72
$M_{\mu\mu}$	0.48	0.56	0.70
Average	0.54	0.46	***0.75***

Table 6.8: Average systematic uncertainty of J/ψ TSAs due to various false asymmetries, as a fraction of statistical uncertainty, for A_{N}. See the caption of Table 6.5 for more information.

6.3.6 Other $\sin(n\phi_S)$ Amplitudes with Odd n

As mentioned in Sect. 4.3, the left-right asymmetry A_N is related to all the $\sin(n\phi_S)$ amplitudes with odd n. Only the case where $n = 1$ should be physical, but it needs to be checked whether any of the other amplitudes are sizeable. This was done using the EWUML method. In the high mass DY case (Sect. 5.3.6), some of the amplitudes with $n > 1$ were found to be different from zero by at least 1σ (Fig. 5.27). These large amplitudes provided a possible explanation for the differences observed between A_N and $A_T^{\sin(\phi_S)}$ in the high mass case (Fig. 5.8). The $\sin(n\phi_S)$ amplitudes up to $n = 9$ are shown for the J/ψ case in Fig. 6.26. When averaged over kinematic bins, the non-physical amplitudes are consistent with zero. This is consistent with the fact that no significant difference was observed between A_N and $A_T^{\sin(\phi_S)}$ in Fig. 6.7.

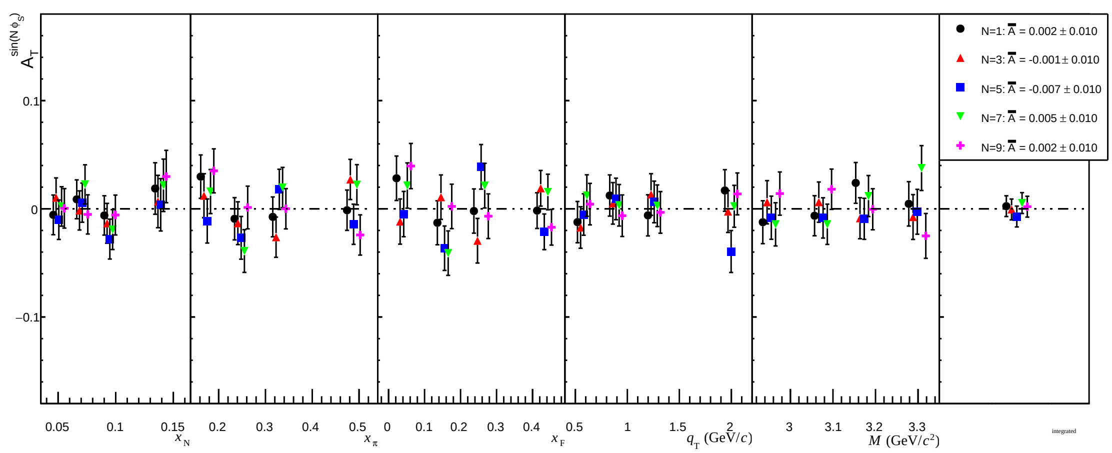

(a)

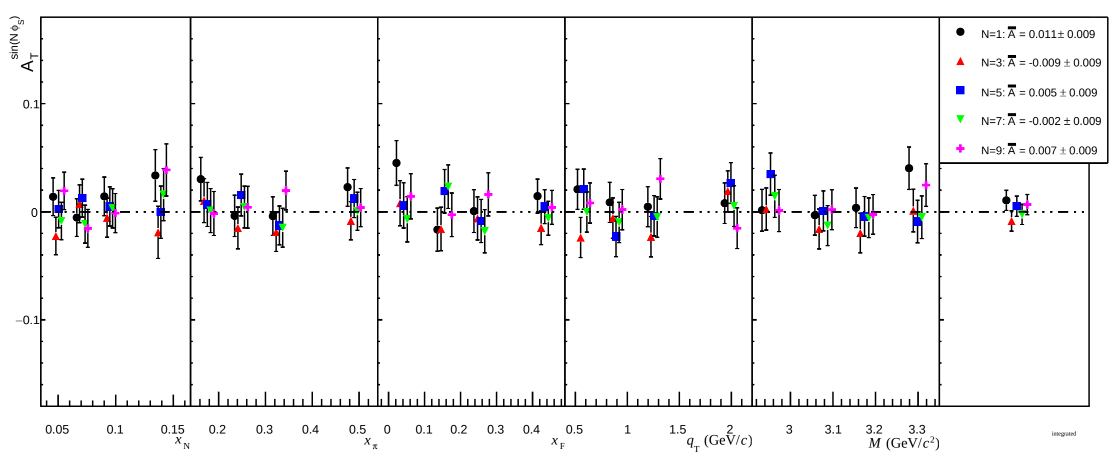

(b)

Figure 6.26: Different $\sin(n\phi_S)$ amplitudes with odd n up to $n = 9$ in J/ψ (a) 2015 and (b) 2018 data.

6.3.7 Period Compatibility

The J/ψ TSA results from each period are compared to see if they are statistically compatible. Disagreement would suggest that changes in the spectrometer setup and acceptance could be influencing the measurements. Fig. 6.27-6.29 show the results of the Sivers, pretzelosity, and transversity TSAs respectively by period for 2015, 2018, and the combination of both years. A constant fit is applied to the points from each period, and in all three cases the reduced χ^2 indicates that there is no significant period dependence. Fig. 6.30 shows the A_{N} results by period. Again, the reduced χ^2 of the constant fit indicates statistical compatibility between periods. Additionally, the disagreement between the first and second halves of 2018 that was observed in the high mass DY case is not observed in the J/ψ case. Therefore, no systematic uncertainty is assigned to any of the TSAs due to time dependence.

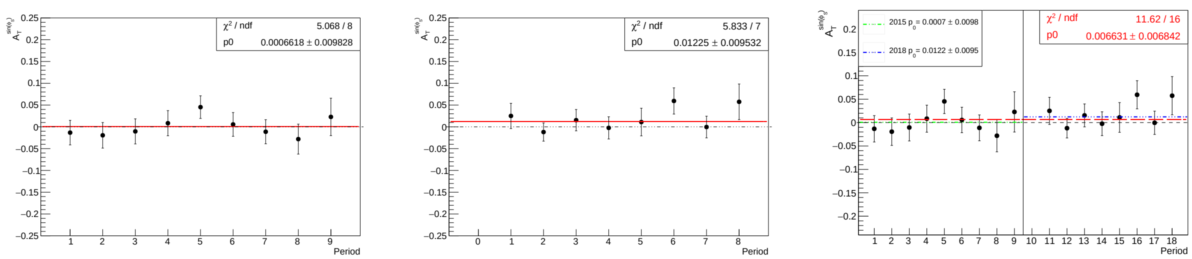

(a) (b) (c)

Figure 6.27: J/ψ Sivers TSA $A_{\mathrm{T}}^{\sin(\phi_{\mathrm{S}})}$ by period in (a) 2015, (b) 2018, and (c) both years combined. The χ^2 values of the constant fits indicate that the results within a single year as well as between years are statistically compatible.

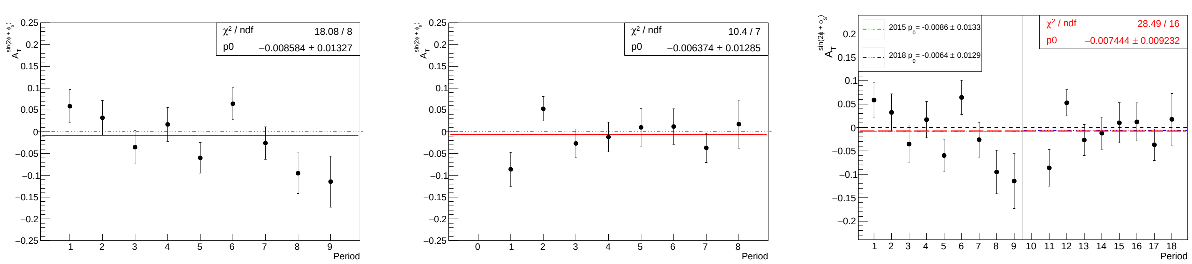

(a) (b) (c)

Figure 6.28: J/ψ Pretzelosity TSA $A_{\mathrm{T}}^{\sin(2\phi+\phi_{\mathrm{S}})}$ by period in (a) 2015, (b) 2018, and (c) both years combined. The χ^2 values of the constant fits indicate that the results within a single year as well as between years are statistically compatible.

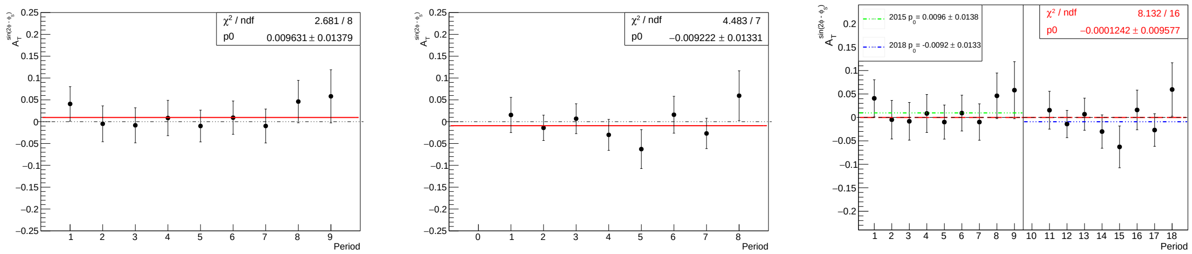

(a) (b) (c)

Figure 6.29: J/ψ Transversity TSA $A_{\mathrm{T}}^{\sin(2\phi-\phi_{\mathrm{S}})}$ by period in (a) 2015, (b) 2018, and (c) both years combined. The χ^2 values of the constant fits suggest that the results within a single year as well as between years are statistically compatible.

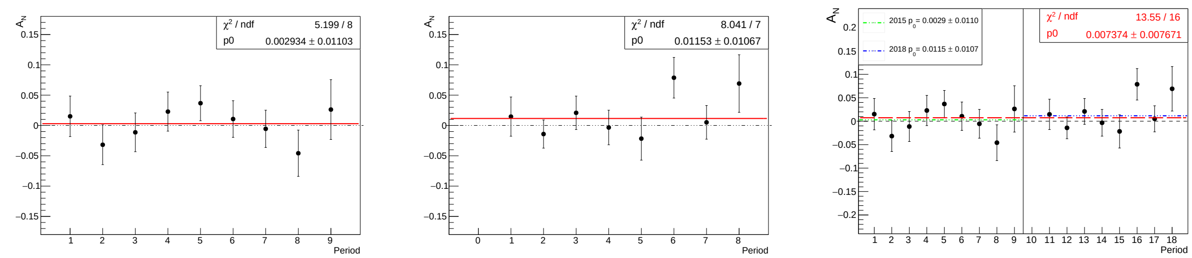

(a) (b) (c)

Figure 6.30: J/ψ A_{N} by period in (a) 2015, (b) 2018, and (c) both years combined. The χ^2 values of the constant fits indicate that the results within a single year as well as between years are statistically compatible.

6.3.8 Total Systematic Uncertainty

As in the high mass case, the dilution, polarization, and depolarization factors have inherent multiplicative uncertainties. The uncertainty of the polarization factor does not change with the invariant mass range, while the dilution factor uncertainty can depend on mass range. However, it turns out that the total multiplicative uncertainty is the same in the J/ψ case as in the high mass DY: 11%.

The systematic uncertainty contribution from each additive source is shown as a fraction of statistical uncertainty in Table 6.9. The overall average TSA and A_{N} results with systematic uncertainty bands are shown in Fig. 6.31 and 6.32 respectively.

6.4 Interpretation of Results

The COMPASS TSA results from J/ψ production in pion-proton collisions will be discussed further in this section. The most interesting results are the J/ψ Sivers TSA and A_{N} result. As discussed in Sect. 2.7, Ref. [106] predicted a large A_{N} amplitude in these COMPASS J/ψ events assuming quark-antiquark annihilation as the dominant J/ψ production mechanism (Fig. 2.36). The J/ψ A_{N} result in Fig. 6.32 is much

Systematic Uncertainty	2015 $\langle\sigma_{\rm sys}/\sigma_{\rm stat}\rangle$			
	$A_{\rm T}^{\sin(\phi_S)}$	$A_{\rm T}^{\sin(2\phi+\phi_S)}$	$A_{\rm T}^{\sin(2\phi-\phi_S)}$	$A_{\rm N}$
Period Compatibility	0.00	0.00	0.00	0.00
Left-Right Event Migration	N/A	N/A	N/A	0.01
False Asymmetries	0.6	0.6	0.7	0.6
Total	**0.6**	**0.6**	**0.7**	**0.6**

Systematic Uncertainty	2018 $\langle\sigma_{\rm sys}/\sigma_{\rm stat}\rangle$			
	$A_{\rm T}^{\sin(\phi_S)}$	$A_{\rm T}^{\sin(2\phi+\phi_S)}$	$A_{\rm T}^{\sin(2\phi-\phi_S)}$	$A_{\rm N}$
Period Compatibility	0.00	0.00	0.00	0.00
Left-Right Event Migration	N/A	N/A	N/A	0.004
False Asymmetries	0.65	0.60	0.60	0.75
Total	**0.65**	**0.60**	**0.60**	**0.75**

Table 6.9: Overall systematic uncertainty percentages for each TSA from J/ψ data.

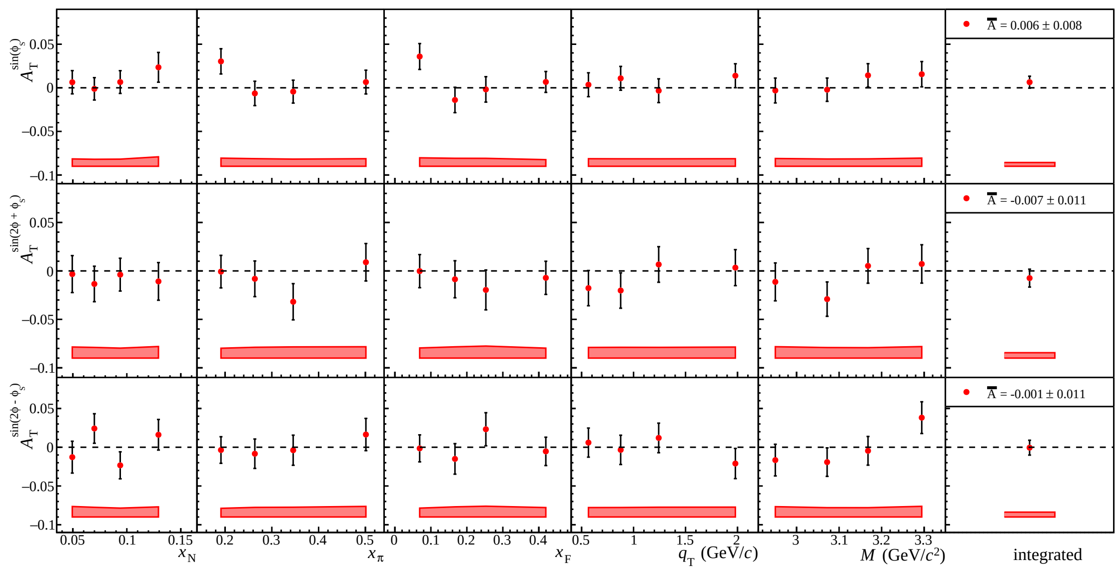

Figure 6.31: TSA J/ψ results averaged over 2015 and 2018 with systematic uncertainty bands, in various kinematic bins and extracted over the entire kinematic range. The first row is the Sivers TSA, the second is pretzelosity, and the third is transversity. The errors printed in the right-most panels are the combined systematic and statistical uncertainties.

smaller than that prediction, suggesting that gluon-gluon fusion is indeed an important channel of J/ψ production at COMPASS kinematics. This is consistent with the recent studies in Refs [97] and [102]. The Sivers TSA and $A_{\rm N}$ results are slightly positive, though still consistent with zero at less than 1σ even with the large number of events (over 40 times that of the high mass DY sample). Looking at the $x_{\rm N}$ dependence, the positive sign of the asymmetry is coming from the events in the highest $x_{\rm N}$ bin. This suggests that gluon-gluon fusion is the dominant J/ψ production mechanism except at the highest $x_{\rm N}$ values probed by COMPASS, where quark-antiquark annihilation becomes increasingly important.

If gluon-gluon fusion is the dominant mechanism, then the Sivers TSA and $A_{\rm N}$ amplitudes in J/ψ data

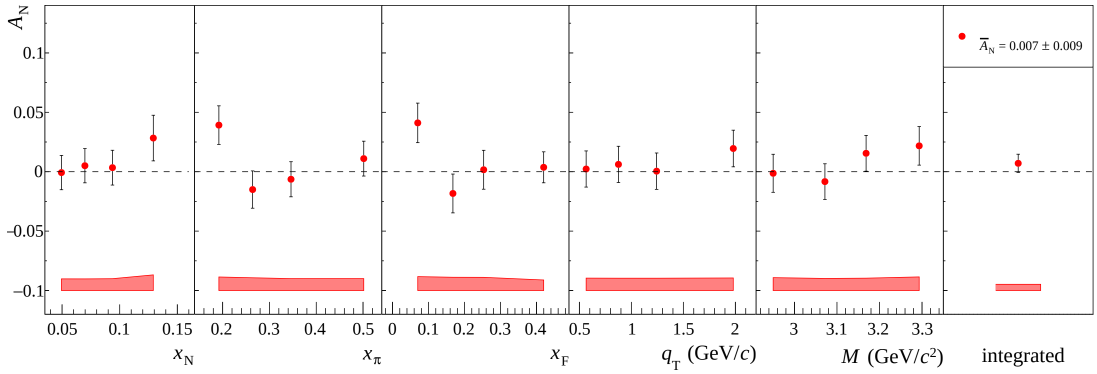

Figure 6.32: A_{N} J/ψ results averaged over 2015 and 2018 with systematic uncertainty bands, in various kinematic bins and extracted over the entire kinematic range. The error printed in the right-most panel is the combined systematic and statistical uncertainty.

provide information about the gluon Sivers function and can be compared to the results from PHENIX and COMPASS presented in Sect. 2.7. The small Sivers amplitude consistent with zero found in J/ψ events from pion-proton collisions is in agreement with the PHENIX A_{N} results (Fig. 2.34) from direct photon production and π^0/η production in polarized proton-proton collisions. A larger non-zero amplitude like those found in photon-gluon fusion and J/ψ leptoproduction at COMPASS (Fig. 2.35) was not observed.

The pretzelosity and transversity TSAs should also be related to gluon TMDs if gluon-gluon fusion is dominant. This could explain why the transversity amplitude is equal to zero in the J/ψ case while it is negative to a level of 2σ in the Drell-Yan case. The pretzelosity TSA is also consistent with zero, though it tends to be slightly negative. The fact that the transversity and pretzelosity amplitudes are zero in J/ψ production could suggest that the gluons in the proton are not transversely polarized.

Chapter 7

Conclusion and Outlook

Various experiments are currently working to better understand the transverse-momentum-dependent (TMD) structure of the nucleon. The COMPASS experiment at CERN is currently the only experiment designed to measure semi-inclusive deep inelastic scattering (SIDIS) data and Drell-Yan (DY) data using essentially the same apparatus, making it extremely well suited to test the (non-)universality of the TMD parton distribution functions (PDFs). In 2015 and 2018 COMPASS collected DY data using a 190 GeV/c negative pion beam and a transversely polarized proton target. The author of this thesis was one of the primary analyzers responsible for extracting transverse-spin-dependent asymmetries (TSAs) from the most up-to-date COMPASS DY data in order to provide new inputs to the study of TMD PDFs.

The author managed the productions of the 2015 and 2018 COMPASS data with the newest inputs, which included DC05 calibrations performed by the author. She checked the integrity and reliability of the newly reconstructed data, and carefully evaluated systematic uncertainties. The analysis resulted in the final Sivers-, pretzelosity-, and transversity-related TSA results from the total high mass DY 2015+2018 COMPASS data set. A_{N} was also extracted as an alternative approach for studying the Sivers TMD. These final DY TSA and A_{N} results are presented for the first time in this thesis and are currently in preparation for publication. The new results favor the Sivers sign change hypothesis to a level of 1.5σ. Due to high levels of background in the dimuon event sample at COMPASS, only the 'high mass' range from 4.3 to 8.5 GeV/c^2 can reasonably be used in the DY analysis. This greatly limits the available statistics. This lack of statistics could potentially be improved by using machine learning techniques as an alternative method for separating DY events from background.

The author of this thesis also extracted TSAs and A_{N} from the J/ψ events in the 2015 and 2018 COMPASS data samples. There are two possible leading-order J/ψ production mechanisms in pion-proton collisions: quark-antiquark annihilation and gluon-gluon fusion. In the first case, TSAs from the J/ψ events in COMPASS 2015+2018 data would provide more information about quark TMDs, with much higher statistics than that available in the high mass DY range. In the latter case, TSAs from the COMPASS J/ψ events would provide access to so-far poorly understood gluon TMDs. This thesis presents for the first time the TSAs extracted from the total 2015 and 2018 sample of J/ψ events. The Sivers, A_{N}, pretzelosity, and transversity amplitudes are all small, less than 1σ from zero. Comparing to the theory, this suggests that gluon-gluon fusion is important at COMPASS kinematics, and that gluon TMDs are small or consistent with zero. The first official release of these J/ψ TSAs is currently in progress. One possible avenue for further exploration would be to extract TSAs from other types of meson production occurring at COMPASS, such as the ψ' meson.

Though not discussed in this thesis, another avenue of exploration possible with the COMPASS DY data is the study of pion TMD PDFs, particularly the pion Boer-Mulders function. The pion Boer-Mulders function has been studied briefly at COMPASS [119], but not in very great detail. In general, pion TMDs are much less studied than proton TMDs, and further exploration will be very valuable. After the final COMPASS data-taking campaign in 2022, the apparatus will be upgraded and used by the new AMBER collaboration. One aspect of the AMBER physics program [120] will be to take DY measurements with both positive and negative pion beams. This data will be useful for further studies of pion substructure, including TMD PDFs and sea quark distributions.

Bibliography

[1] E. Rutherford, "The scattering of α and β particles by matter and the structure of the atom," *Phil. Mag.*, 1911, 21(125):669–688, doi:10.1080/14786440508637080.

[2] E. Rutherford and J. Nuttall, "Scattering of α particles by gases," *Phil. Mag.*, 1913, 26(154):702–712, doi:10.1080/14786441308635014.

[3] J. Chadwick, "Possible existence of a neutron," *Nature*, 1932, 129:312, doi:10.1038/129312a0.

[4] M. Gell-Mann, "A schematic model of baryons and mesons," *Phys. Lett.*, 1964, 8(3):214–215, doi:10.1016/S0031-9163(64)92001-3.

[5] G. Zweig, "An SU_3 model for strong interaction symmetry and its breaking; Version 2," , CERN-TH-412, 1964, pp. 22–101, URL `https://cds.cern.ch/record/570209`.

[6] R. Feynman, "Very high-energy collisions of hadrons," *Phys. Rev. Lett.*, 1969, 23(24):1415–1417, doi:10.1103/PhysRevLett.23.1415.

[7] C. Yang and R. Mills, "Conservation of isotopic spin and isotopic gauge invariance," *Phys. Rev.*, 1954, 96(1):191–195, doi:10.1103/PhysRev.96.191.

[8] J. Bjorken, "Asymptotic sum rules at infinite momentum," *Phys. Rev.*, 1969, 179(5):1547, doi:10.1103/PhysRev.179.1547.

[9] J. Bjorken and E. Paschos, "Inelastic electron-proton and γ-proton scattering and the structure of the nucleon," *Phys. Rev.*, 1969, 185(5):1975, doi:10.1103/PhysRev.185.1975.

[10] H. Fritzsch, M. Gellmann, and H. Leutwyler, "Advantages of color octet gluon picture," *Phys. Lett. B*, 1973, 74(4):365–368, doi:10.1016/0370-2693(73)90625-4.

[11] H. Politzer, "Reliable perturbative results for strong interactions?" *Phys. Rev. Lett.*, 1973, 30(26):1346, doi:10.1103/PhysRevLett.30.1346.

[12] D. Gross and F. Wilczek, "Ultraviolet behavior of non-abelian gauge theories," *Phys. Rev. Lett.*, 1973, 30(26):1343, doi:10.1103/PhysRevLett.30.1343.

[13] EMC Collaboration, "A measurement of the spin asymmetry and determination of the structure function g1 in deep inelastic muon-proton scattering," *Phys. Lett. B*, 1988, 206(2):364–370, doi: 10.1016/0370-2693(88)91523-7.

[14] R. Jaffe and A. Manohar, "The g_1 problem: deep inelastic electron scattering and the spin of the proton," , 1990, 337(3):509–546, doi:10.1016/0550-3213(90)90506-9.

[15] X. Ji, "Gauge-invariant decomposition of nucleon spin," *Phys. Rev. Lett.*, 1997, 78(4):610, doi:10.1103/PhysRevLett.78.610.

[16] COMPASS Collaboration, "Final COMPASS results on the deuteron spin-dependent structure function g_1^d and the Bjorken sum rule," *Phys. Lett. B*, 2017, 769:34–41, doi:10.1016/j.physletb.2017.03.018.

[17] COMPASS Collaboration, "Leading and next-to-leading order gluon polarization in the nucleon and longitudinal double spin asymmetries from open charm muoproduction," *Phys. Rev. D*, 2013, 87(5):052018, doi:10.1103/PhysRevD.87.052018.

[18] L. Dick, et al., "Spin effects in the inclusive reactions $\pi^\pm + p(\uparrow) \to \pi^\pm +$ anything at 8 gev/c," *Phys. Lett. B*, 1975, 57(1):93–96, doi:10.1016/0370-2693(75)90252-X.

[19] M. Burkardt and B. Pasquini, "Modelling the nucleon structure," *Eur. Phys. J. A*, 2016, 52(6):161, doi:10.1140/epja/i2016-16161-7.

[20] M. Perdekamp and F. Yuan, "Transverse spin structure of the nucleon," *Annu. Rev. Nucl. Part. Sci.*, 2015, 65:429–456, doi:10.1146/annurev-nucl-102014-021948.

[21] V. Barone and P. Ratcliffe, *Transverse Spin Physics*, (World Scientific Publishing Co. Pte. Ltd. 2003), ISBN 981-238-101-5.

[22] M. Breidenbach, et al., "Observed behavior of highly inelastic electron-proton scattering," *Phys. Rev. Lett.*, 1969, 23(16):935, doi:10.1103/PhysRevLett.23.935.

[23] Particle Data Group, "Review of particle physics," *Phys. Rev. D*, 2018, 98(3):030001, doi:10.1103/PhysRevD.98.030001.

[24] C. Callan and D. Gross, "High-energy electroproduction and the constitution of the electric current," *Phys. Rev. Lett.*, 1969, 22(4):156, doi:10.1103/PhysRevLett.22.156.

[25] NNPDF Collaboration, "Parton distributions for the LHC run II," *Journal of High Energy Physics*, 2015, (4), doi:10.1007/JHEP04(2015)040.

[26] HERMES Collaboration, "Measurement of parton distributions of strange quarks in the nucleon from charged-kaon production in deep-inelastic scattering on the deuteron," *Phys. Lett. B*, 2008, 666(5):446–450, doi:10.1016/j.physletb.2008.07.090.

[27] SMC Collaboration, "Polarised quark distributions in the nucleon from semi-inclusive spin asymmetries," *Phys. Lett. B*, 1998, 420:180–190, doi:10.1016/S0370-2693(97)01546-3.

[28] COMPASS Collaboration, "Flavour separation of helicity distributions from deep inelastic muon-deuteron scattering," *Phys. Lett. B*, 2009, 680(3):217–224, doi:10.1016/j.physletb.2009.08.065.

[29] Y. Dokshitzer, "Calculation of the structure functions for deep inelastic scattering and $e+$ $e-$ annihilation by perturbation theory in quantum chromodynamics," *Sov. Phys. JTEP*, 1977, 46:641–653, URL `http://www.jetp.ras.ru/cgi-bin/dn/e_046_04_0641.pdf`.

[30] V. Gribov and L. Lipatov, "Deep inelastic e p scattering in perturbation theory," *Sov. J. Nucl. Phys.*, 1972, 15:781–807.

[31] G. Altarelli and G. Parisi, "Asymptotic freedom in parton language," *Nucl. Phys. B*, 1977, 126(2):298–318, doi:10.1016/0550-3213(77)90384-4.

[32] D. Boer and P. Mulders, "Time-reversal odd distribution functions in leptoproduction," *Phys. Rev. D*, 1998, 57:5780–5786, doi:10.1016/S0550-3213(96)00648-7.

[33] P. Mulders and R. Tangerman, "The complete tree-level result up to order $1/Q$ for polarized deep-inelastic leptoproduction," *Nucl. Phys. B*, 1996, 461:197–237, doi:10.1016/0550-3213(95)00632-X.

[34] D. Sivers, "Single-spin production asymmetries from the hard scattering of pointlike constituents," *Phys. Rev. D*, 1990, 41:83–90, doi:10.1103/PhysRevD.41.83.

[35] S. Brodsky, D. Hwang, and I. Schmidt, "Initial-state interactions and single-spin asymmetries in Drell-Yan processes," *Nucl. Phys. B*, 2002, 642:344–356, doi:10.1016/S0550-3213(02)00617-X.

[36] S. Brodsky, D. Hwang, and I. Schmidt, "Final-state interactions and single-spin asymmetries in semi-inclusive deep inelastic scattering," *Phys. Lett. B*, 2002, 530:99–107, doi:10.1016/S0370-2693(02)01320-5.

[37] J. Collins, "Leading-twist single-transverse-spin asymmetries: Drell–Yan and deep-inelastic scattering," *Phys. Lett. B*, 2002, 536:43–48, doi:10.1016/S0370-2693(02)01819-1.

[38] J. Ralston and D. Soper, "Production of dimuons from high-energy polarized proton-proton collisions," *Nucl. Phys. B*, 1979, 152(1):109–124, doi:10.1016/0550-3213(79)90082-8.

[39] G. Miller, "Densities, parton distributions, and measuring the nonspherical shape of the nucleon," *Phys. Rev. C*, 2007, 76(6):065209, doi:10.1103/PhysRevC.76.06520.

[40] A. Bacchetta, et al., "Semi-inclusive deep inelastic scattering at small transverse momentum," *JHEP*, 2007, 2:093, doi:10.1088/1126-6708/2007/02/093.

[41] V. Barone, S. Melis, and A. Prokudin, "Boer-mulders effect in unpolarized SIDIS: An analysis of the COMPASS and HERMES data on the cos2ϕ asymmetry," *Phys. Rev. D*, 2010, 81(11):114026, doi:10.1103/PhysRevD.81.114026.

[42] S. Arnold, A. Metz, and M. Schlegel, "Dilepton production from polarized hadron hadron collisions," *Phys. Rev. D*, 2009, 79(3):034005, doi:10.1103/PhysRevD.79.034005.

[43] A. Kotzinian, "Description of polarized $\pi^- + N$ Drell-Yan processes," , 2010, URL `https://wwwcompass.cern.ch/compass/notes_public/2010-2.pdf`.

[44] D. Boer and W. Vogelsang, "Drell-Yan lepton angular distribution at small transverse momentum," *Phys. Rev. D*, 2006, 74(1):014004, doi:10.1103/PhysRevD.74.014004.

[45] C. Riedl, "Probing nucleon spin structure in deep-inelastic scattering, proton-proton collisions and Drell-Yan processes," *Acta Phys. Pol. B*, 2022, 53:5–A2, URL `https://www.actaphys.uj.edu.pl/R/53/5-A2/pdf`.

[46] HERMES Collaboration, "Azimuthal distributions of charged hadrons, pions, and kaons produced in deep-inelastic scattering off unpolarized protons and deuterons," *Phys. Rev. D*, 2013, 87(1):012010, doi:10.1103/PhysRevD.87.012010.

[47] COMPASS Collaboration, "Measurement of azimuthal hadron asymmetries in semi-inclusive deep inelastic scattering off unpolarised nucleons," *Nucl. Phys. B*, 2014, 886:1046–1077, doi:10.1016/j.nuclphysb.2014.07.019.

[48] A. Moretti, "Azimuthal asymmetries in unpolarized semi-inclusive deep inelastic scattering at COMPASS," *IL NUOVO CIMENTO C*, 2021, 44(2-3):61, doi:10.1393/ncc/i2021-21061-2.

[49] CLAS Collaboration, "Measurement of semi-inclusive π^+ electroproduction off the proton," *Phys. Rev. D*, 2009, 80:032004, doi:10.1103/PhysRevD.80.032004.

[50] M. Anselmino, et al., "Transversity and Collins functions from SIDIS and e^+e^- data," *Phys. Rev. D*, 2007, 75:054032, doi:10.1103/PhysRevD.75.054032.

[51] NA10 Collaboration, "Angular distributions of muon pairs produced by negative pions on deuterium and tungsten," *Z. Phys. C*, 1988, 37:545–556, doi:10.1007/BF01549713.

[52] E615 Collaboration, "Experimental study of muon pairs produced by 252-gev pions on tungsten," *Phys. Rev. D*, 1989, 39:92, doi:10.1103/PhysRevD.39.92.

[53] Y. Lien and A. Chumakov, "Measurement of target spin (in)dependent asymmetries in dimuon production in pion-nucleon collisions at COMPASS," *Proceedings for the XXVIII International Workshop on Deep-Inelastic Scattering and Related Subjects, Stony Brook University, New York, USA, 12-16 April 2021*, submitted to *SciPost Physics Proceedings*.

[54] W. Chang, R. McClellan, J. Peng, and O. Teryaev, "Lepton angular distributions of fixed-target Drell-Yan experiments in perturbative QCD and a geometric approach," *Phys. Rev. D*, 2019, 99:014032, doi:10.1103/PhysRevD.99.014032.

[55] HERMES Collaboration, "Azimuthal single- and double-spin asymmetries in semi-inclusive deep-inelastic lepton scattering by transversely polarized protons," *JHEP*, 2020, (12):010, doi:10.1007/JHEP12(2020)010.

[56] B. Parsamyan, "New target transverse spin dependent azimuthal asymmetries from COMPASS experiment," *Eur. Phys. J Special Topics*, 2008, 162:89–96, doi:10.1140/epjst/e2008-00780-1.

[57] B. Parsamyan, "Transverse spin dependent azimuthal asymmetries at COMPASS," *Journal of Physics Conference Series*, 2011, 295(1):012046, doi:10.1088/1742-6596/295/1/012046.

[58] B. Parsamyan, "Six "beyond collins and sivers" transverse spin asymmetries at COMPASS," *Phys. of Part. and Nucl.*, 2014, 45:158–162, doi:10.1134/S106377961401078X.

[59] COMPASS Collaboration, "Sivers asymmetry extracted in SIDIS at the hard scales of the Drell-Yan process at COMPASS," *Phys. Lett. B*, 2017, 770:138–145, doi:10.1016/j.physletb.2017.04.042.

[60] JLab Hall A Collaboration, "Measurement of "pretzelosity" asymmetry of charged pion production in semi-inclusive deep inelastic scattering on a polarized He-3 target," *Phys. Rev. C*, 2014, 90(5):055209, doi:10.1103/PhysRevC.90.055209.

[61] S. Bastami, et al., "The Drell-Yan process with pions and polarized nucleons," *JHEP*, 2021, (2):166, doi:10.1007/JHEP02(2021)166.

[62] C. Lefky and A. Prokudin, “Extraction of the distribution function $h_{1T}^{\perp}$ from experimental data,” *Phys. Rev. D*, 2015, 91(3):034010, doi:10.1103/PhysRevD.91.034010.

[63] JLab Hall A Collaboration, “Single spin asymmetries in charged pion production from semi-inclusive deep inelastic scattering on a transversely polarized He-3 target at $Q^2 = 1.4 - 2.7$ GeV^2,” *Phys. Rev. Lett.*, 2011, 107(7):072003, doi:10.1103/PhysRevLett.107.072003.

[64] COMPASS Collaboration, “First measurement of transverse-spin-dependent azimuthal asymmetries in the Drell-Yan process,” *Phys. Rev. Lett.*, 2017, 119(11):112002, doi:10.1103/PhysRevLett.119.112002.

[65] COMPASS Collaboration, “Collins and Sivers asymmetries for pions and kaons in muon–deuteron DIS,” *Phys. Lett. B*, 2009, 673(2):127–135, doi:10.1016/j.physletb.2009.01.060.

[66] COMPASS Collaboration, “Collins and Sivers asymmetries in muonproduction of pions and kaons off transversely polarised protons,” *Phys. Lett. B*, 2015, 744:250–259, doi:10.1016/j.physletb.2015.03.056.

[67] STAR Collaboration, “Azimuthal transverse single-spin asymmetries of inclusive jets and charged pions within jets from polarized-proton collisions at $\sqrt{s} = 500$ GeV,” *Phys. Rev. D*, 2018, 97:032004, doi:10.1103/PhysRevD.97.032004.

[68] JAM Collaboration, “Origin of single transverse-spin asymmetries in high-energy collisions,” *Phys. Rev. D*, 2020, 102(5):054002, doi:10.1103/PhysRevD.102.054002.

[69] Belle Collaboration, “Measurement of azimuthal asymmetries in inclusive production of hadron pairs in e^+e^- annihilation at $\sqrt{s} = 10.58$ GeV,” *Phys. Rev. D*, 2008, 78(3):032011, doi:10.1103/PhysRevD.78.032011.

[70] Belle Collaboration, “Azimuthal asymmetries of back-to-back $\pi^{+/-} - (\pi^0, \eta, \pi^{+/-})$ pairs in e^+e^- annihilation,” *Phys. Rev. D*, 2019, 100(9):092008, doi:10.1103/PhysRevD.100.092008.

[71] BABAR Collaboration, “Measurement of Collins asymmetries in inclusive production of charged pion pairs in e^+e^- annihilation at BABAR,” *Phys. Rev. D*, 2014, 90(5):052003, doi:10.1103/PhysRevD.90.052003.

[72] BABAR Collaboration, “Collins asymmetries in inclusive charged KK and $K\pi$ pairs produced in e^+e^- annihilation,” *Phys. Rev. D*, 2015, 92(11):111101, doi:10.1103/PhysRevD.92.111101.

[73] BESIII Collaboration, “Measurement of azimuthal asymmetries in inclusive charged dipion production in e^+e^- annihilations at $\sqrt{s} = 3.65$ GeV,” *Phys. Rev. Lett.*, 2016, 116(4):042001, doi:10.1103/PhysRevLett.116.042001.

[74] D. Pitonyak, "Comprehensive study of SSAs within the JAM global analysis framework," *APS April Meeting 2022, New York, 9-12 April 2022*, URL `https://apsapril22.onlineeventpro.freeman.com/sessions/23882355/subsession/33060225/H11`.

[75] R. Klem, et al., "Measurement of asymmetries of inclusive pion-production in proton-proton interactions at 6 and 11.8 GeV/c," *Phys. Rev. Lett.*, 1976, 36(16):929, doi:10.1103/PhysRevLett.36.929.

[76] E925 Collaboration, "Measurement of analyzing powers of π^+ and π^- produced on a hydrogen and a carbon target with a 22 GeV/c incident polarized proton beam," *Phys. Rev. D*, 2002, 65(9):092008, doi:10.1103/PhysRevD.65.092008.

[77] FNAL E581/704 Collaboration, "Comparison of spin asymmetries and cross sections in π^0 production by 200 GeV polarized antiprotons and protons," *Phys. Lett. B*, 1991, 261(1-2):201–206, doi:10.1016/0370-2693(91)91351-U.

[78] FNAL E704 Collaboration, "Analyzing power in inclusive π^+ and π^- production at high x_F with a 200 GeV polarized proton beam," *Phys. Lett. B*, 1991, 264(3-4):462–466, doi:10.1016/0370-2693(91)90378-4.

[79] BRAHMS Collaboration, "Single-transverse-spin asymmetries of identified charged hadrons in polarized pp collisions at $\sqrt{s}$=62.4 GeV," *Phys. Rev. Lett.*, 2008, 101(4):042001, doi:10.1103/PhysRevLett.101.042001.

[80] STAR Collaboration, "Measurement of the transverse single-spin asymmetry in $p^\uparrow + p \to W^\pm/Z^0$ at RHIC," *Phys. Rev. Lett.*, 2016, 116(13):132301, doi:10.1103/PhysRevLett.116.132301.

[81] O. Eyser, "Transverse single-spin asymmetries and cross section of weak bosons in $p+p$ collisions at $\sqrt{s} = 510$ GeV," *Proceedings for the Particles and Nuclei International Conference 2021, Online, 5-10 Sept. 2021*, submitted to *Proceedings of Science*.

[82] M. Bury, A. Prokudin, and A. Vladimirov, "Extraction of the Sivers function from SIDIS, Drell-Yan, and $W^\pm/Z$ data at next-to-next-to-next-to leading order," *Phys. Rev. Lett.*, 2021, 126(11):112002, doi:10.1103/PhysRevLett.126.112002.

[83] RHICf Collaboration, "Transverse single-spin asymmetry for very forward neutral pion production in polarized $p+p$ collisions at $\sqrt{s}$=510 GeV," *Phys. Rev. Lett.*, 2020, 124(25):252501, doi:10.1103/PhysRevLett.124.252501.

[84] STAR Collaboration, "Measurement of transverse single-spin asymmetries of π^0 and electromagnetic jets at forward rapidity in 200 and 500 GeV transversely polarized proton-proton collisions," *Phys. Rev. D*, 2021, 103(9):092009, doi:10.1103/PhysRevD.103.092009.

[85] PHENIX Collaboration, "Transverse momentum dependent forward neutron single spin asymmetries in transversely polarized $p + p$ collisions at $\sqrt{s}$=200 GeV," *Phys. Rev. D*, 2021, 103:032007, doi: 10.1103/PhysRevD.103.032007.

[86] M. Bury, A. Prokudin, and A. Vladimirov, "Extraction of the Sivers function from SIDIS, Drell-Yan, and $W^{\pm}/Z$ boson production data with TMD evolution," *JHEP*, 2021, (5):151, doi:10.1007/JHEP05(2021)151.

[87] M. Echevarria, Z. Kang, and J. Terry, "Global analysis of the Sivers functions at NLO+NNLL in QCD," *JHEP*, 2021, (1):126, doi:10.1007/JHEP01(2021)126.

[88] A. Bacchetta, F. Delcarro, C. Pisano, and M. Radici, "The 3-dimensional distribution of quarks in momentum space," *Phys. Lett. B*, 2022, 827:136961, doi:10.1016/j.physletb.2022.136961.

[89] J. Lansberg, "New observables in inclusive production of quarkonia," *Physics Reports*, 2020, 889:1–106, doi:10.1016/j.physrep.2020.08.007.

[90] H1 Collaboration, "Inelastic production of J/ψ mesons in photoproduction and deep inelastic scattering at HERA," *Eur. Phys. J. C*, 2010, 68(3-4):401–420, doi:10.1140/epjc/s10052-010-1376-5.

[91] Y.-Q. Ma, Y.-J. Zhang, and K.-T. Chao, "QCD corrections to $e^+e^- \to J/\psi + gg$ at B factories," *Phys. Rev. Lett.*, 2009, 102(16):162002, doi:10.1103/PhysRevLett.102.162002.

[92] M. Schub, et al., "Measurement of J/ψ and ψ' production in 800 GeV/c proton-gold collisions," *Phys. Rev. D*, 1995, 52(3):1307–1315, doi:10.1103/PhysRevD.52.1307.

[93] M. Kramer, "Quarkonium production at high-energy colliders," *Prog. in Part. and Nucl. Phys.*, 2001, 47(1):141–201, doi:10.1016/S0146-6410(01)00154-5.

[94] F. Maltoni, et al., "Analysis of charmonium production at fixed-target experiments in the NRQCD approach," *Phys. Lett. B*, 2006, 638(2-3):202–208, doi:10.1016/j.physletb.2006.05.010.

[95] R. Nelson, R. Vogt, and A. Frawley, "Narrowing the uncertainty on the total charm cross section and its effect on the J/ψ cross section," *Phys. Rev. C*, 2013, 87(1):014908, doi:10.1103/PhysRevC.87.014908.

[96] J. Lansberg, H. Shao, N. Yamanaka, Y. Zhang, and C. Noûs, "Complete NLO QCD study of single- and double-quarkonium hadroproduction in the colour-evaporation model at the Tevatron and the LHC," *Phys. Lett. B*, 2020, 807:135559, doi:10.1016/j.physletb.2020.135559.

[97] W. Chang, J. Peng, S. Platchkov, and T. Sawada, "Constraining gluon density of pions at large x by pion-induced J/ψ production," *Phys. Rev. D*, 2020, 102(5):054024, doi:10.1103/PhysRevD.102.054024.

[98] PHENIX Collaboration, "Probing gluon spin-momentum correlations in transversely polarized protons through midrapidity isolated direct photons in $p^{\uparrow}+p$ collisions at $\sqrt{s}=200$ GeV," *Phys. Rev. Lett.*, 2021, 127(16):162001, doi:10.1103/PhysRevLett.127.162001.

[99] PHENIX Collaboration, "Transverse single-spin asymmetries of midrapidity π^0 and η mesons in polarized $p+p$ collisions at $\sqrt{s}=200$ GeV," *Phys. Rev. D*, 2021, 103(5):052009, doi:10.1103/PhysRevD.103.052009.

[100] COMPASS Collaboration, "First measurement of the Sivers asymmetry for gluons using SIDIS data," *Phys. Lett. B*, 2017, 772:854–864, doi:10.1016/j.physletb.2017.07.018.

[101] J. Matousek, "Gluon-induced Sivers-like asymmetries at COMPASS," *NICA-workshop – Gluon content of proton and deuteron with the Spin Physics Detector at the NICA collider, JINR (remote), 30 Sept. - 1 Oct. 2020*, URL `https://wwwcompass.cern.ch/compass/publications/talks/t2020/NICA_SPD2020_matousek.pdf`.

[102] C. Hsieh, et al., "NRQCD analysis of charmonium production with pion and proton beams at fixed-target energies," *Chin. J. Phys.*, 2021, 73:13–23, doi:10.1016/j.cjph.2021.06.001.

[103] M. Anselmino, U. D'Alesio, S. Melis, and F. Murgia, "Constraints on the gluon Sivers distribution via transverse single spin asymmetries at midrapidity in $p^{\uparrow}p\to\pi^0x$ processes at BNL RHIC," *Phys. Rev. D*, 2006, 74(9):094011, doi:10.1103/PhysRevD.74.094011.

[104] U. D'Alesio, F. Murgia, and C. Pisano, "Towards a first estimate of the gluon Sivers function from A_{N} data in *pp* collisions at RHIC," *JHEP*, 2015, 9:119, doi:10.1007/JHEP09(2015)119.

[105] PHENIX Collaboration, "Measurement of transverse-single-spin asymmetries for midrapidity and forward-rapidity production of hadrons in polarized $p+p$ collisions at $\sqrt{s}=200$ and 62.4 GeV," *Phys. Rev. D*, 2014, 90(1):012006, doi:10.1103/PhysRevD.90.012006.

[106] M. Anselmino, V. Barone, and M. Boglione, "The Sivers asymmetry in Drell-Yan production at the J/ψ peak at COMPASS," *Phys. Lett. B*, 2017, 770:302–306, doi:10.1016/j.physletb.2017.04.074.

[107] Riccardo Longo, *Measurement of the spin effects in the Drell-Yan process at the COMPASS experiment*, University of Torino, PhD thesis, 2018.

[108] P. Abbon, et al., "The COMPASS experiment at CERN," *Nucl. Instrum. Meth. in Phys. Sect. A*, 2007, 577(3):455–518, doi:10.1016/j.nima.2007.03.026.

[109] P. Abbon, et al., "The COMPASS setup for physics with hadron beams," *Nucl. Instrum. Meth. in Phys. Sect. A*, 2015, 779:69–115, doi:10.1016/j.nima.2015.01.035.

[110] COMPASS Collaboration, "COMPASS-II Proposal," , CERN-SPSC-2010-014, 2010, URL `http://cds.cern.ch/record/1265628`.

[111] S. Wallner, et al., "CEDAR PID using the likelihood approach for the hadron-beam," , 2017, URL `https://wwwcompass.cern.ch/compass/notes_public/2017-1.pdf`.

[112] V. Andrieux, et al., "The large COMPASS polarized solid ammonia target for Drell-Yan measurements with a pion beam," *Nucl. Inst. and Methods in Phys. Research A*, 2022, 1025:166069, doi:10.1016/j.nima.2021.166069.

[113] A. Abragam and M. Goldman, "Principles of dynamic nuclear polarisation," *Reports on Progress in Physics*, 1978, 41(3):395–467, doi:10.1088/0034-4885/41/3/002.

[114] Marco Meyer-Conde, *Measurement of absolute Drell-Yan cross-sections using a 190-GeV π beam at the COMPASS-II experiment*, Universite Paris Saclay, PhD thesis, 2019.

[115] C. Riedl, private communication.

[116] Robert Heitz, *Transverse momentum dependent nucleon structure from pions impinged on a transversely polarized proton target*, University of Illinois Urbana-Champaign, PhD thesis, 2019.

[117] I. Kenyon, "The Drell-Yan process," *Rep. Prog. Phys.*, 1982, 45(11):1261–1315, doi:10.1088/0034-4885/45/11/002.

[118] NA3 Collaboration, "Experimental J/ψ hadronic production from 150 to 280 GeV/c," *Z. Phys. C*, 1983, 20(2):101–116, URL `https://link.springer.com/content/pdf/10.1007/BF01573213`.

[119] COMPASS Collaboration, "Measurement of p_T-weighted sivers asymmetries in leptoproduction of hadrons," *Nucl. Phys. B*, 2019, 940:34–53, doi:10.1016/j.nuclphysb.2018.12.024.

[120] AMBER Collaboration, "Proposal for measurements at the M2 beam line of the CERN SPS – Phase 1," , CERN-SPSC-2019-022, 2019, URL `http://cds.cern.ch/record/2676885`.